Mechanical characterisation and modelling of statistically representative granular materials subjected to impact loading



Francesco De Cola

Exeter College

University of Oxford

A thesis submitted for the degree of

Doctor of Philosophy

Hilary Term, 2017

Acknowledgements

To my beloved father Gianfranco... in loving memory of you! I feel an urge to thank you for your guidance and love. I owe it all to you!

My special thanks goes to my loving wife Adelaide. Thank you for encouraging me to succeed in life and being by my side every step of my life. Many thanks also to my mother Enza and my brother Fabrizio, who provided me through moral and emotional support.

I am heartily thankful to prof. Nik Petrinic and Dr. Ettore Barbieri for their encouragement, patient guidance and supervision. I also want to thank prof. Penumadu for his precious scientific guidance and all the people at University of Tennessee and EMI Fraunhofer.

Moreover, I would like to thank the Solid Mechanics Group at Oxford and, in particular, all the Impact Engineering Group.... each and every one of you contributed to make my time in Oxford unforgettable (one of the best experiences of my life)... I love you guys.

Finally, I would like to thank the Defense Threat Reduction Agency, not only for providing the funding which allowed me to undertake this research, but also for giving me the opportunity to attend conferences and meet so many interesting people.

Mechanical characterisation and modelling of statistically representative granular materials subjected to impact loading

Francesco De Cola, Exeter College, University of Oxford
For the degree of D.Phil. in Engineering Science, Hilary Term 2017

ABSTRACT

Granular materials are used in several industrial processes involving natural and man-made materials at a vast range of length scales, such as mining, extraction, and handling of rocks and sand, as well as in agricultural and pharmaceutical industry. They are also widely adopted in civil and military applications (e.g. earthquakes, penetration of projectiles, stress waves attenuation) because of their ability to dissipate energy and attenuate shock loading. However, despite the wide-spread use, the comprehension of their mechanical behaviour at high strain rates is still limited.

The main aim of this research is to provide a better understanding of the mechanics of granular materials and to develop a combined experimental/numerical capability to characterise and simulate the effects of high velocity excitations on the boundaries of granular domains and the consequent motion and deformation at high rates of strain. The achievement of this goal requires the knowledge of both meso-structural properties (i.e. initial density, wetness and confinement conditions) and the effects of micro-scale parameters (i.e. grain sizes and shapes, grains microstructure) upon the behaviour of granular assemblies. For this reason, attention is initially focused on the development of novel algorithms capable of correctly representing real meso-structures of granular materials, and on the estimation of their Representative Volume Elements. Subsequently, high strain rate experiments are conducted for a comprehensive mechanical characterisation of different types of sand and to evaluate the effect of micro-scale phenomena and rate dependency on the mechanical response of granular materials subjected to impact loading.

In particular, after having assessed the geometric characteristics of given granular media, modelling tools for the generation of numerical samples that are statistically

representative of real granular materials are developed. Two new efficient algorithms for the geometrical packing of spheres, able to concurrently assign total number of particles and radii distributions, are proposed. Then, a novel Voronoi-based method is presented to model a wide range of particles shapes. The obtained polyhedral grains are proved to successfully reproduce the relevant microscopic features of many naturally occurring granular media. The statistically representative packings thus generated are then used in Discrete Element simulations, which are executed to help designing experiments for the characterisation of granular materials at the meso-scale and to establish the dimensions of the Representative Volume Element of the investigated sands to be used in large-scale laboratory tests and multiscale simulations. A comprehensive experimental campaign on both single grains and granular assemblies at meso-scale is executed to gain insight into the complex behaviour of granular materials subjected to high strain rates and to produce valuable data for future calibration and validation of rate dependent constitutive models. The adoption of ad-hoc sample sizes allowed for the achievement of an improved dynamic equilibrium condition and enhanced reproducibility of the results with respect to what existing in literature. Additionally, a deeper understanding of the role of particles fracture on the behaviour of granular materials is gained by exploiting a number of conventional (microscopy) and novel (sound measurements) experimental techniques for in-situ and post-mortem analysis of samples subjected to a wide spectrum of rates of deformation. Finally, once identified - through experiments - the central role of micro-scale phenomena (grains failure) on the mechanical response of sand, a new mass-conserving modelling methodology capable of capturing the grains comminution happening during dynamic loading of granular materials is introduced, thus extending the range of applicability of DEM to dynamic phenomena.

List of Publications

The work presented in this thesis extends from research articles either published or submitted for publication by the author prior to completion of his DPhil. A detailed list is shown below.

Journal Papers

1. De Cola, F., Falco, S., Barbieri, E., and Petrinic, N. (2015) "New 3D geometrical deposition methods for efficient packing of spheres based on tangency". *Int. J. Numer. Meth. Engng*, 104: 1085-1114

2. De Cola, F., Pellegrino, A., Barbieri, E., Penumadu, D., Petrinic, N. (2016) "Void ratio based representative volume element for modelling the high strain rate behaviour of granular materials". *International Journal of Impact Engineering*, 91: 46-55

3. Pellegrino, A., De Cola, F., Dragnevski, K., Petrinic, N. (2016) "The Dynamic Response of Etnean Sand and the Effect of Its Impingement on Ti-6Al-4 V Alloy". *Journal of Dynamic Behavior of Materials*, 2:438-451

4. Falco, S., De Cola, F., Petrinic, N. (2017) "A method for the generation of 3D representative models of granular based materials". *Int. J. Numer. Meth. Engng*, doi: 10.1002/nme.5521

5. Falco, S., Jiang, J., De Cola, F., Petrinic, N. (2017) "Generation of 3D polycrystalline microstructures with a conditioned Laguerre-Voronoi tessellation tech-

nique". *Computational Material Science*, 136: 20-28.

6. De Cola, F., Quino, G., Dragnevski, K., Petrinic, N. "Sound Measurements and imaging of sand grains failure during in-situ compression tests". Submitted to *Geotechnique*.

7. De Cola, F., Pellegrino, A., Glöβner, C., Penumadu, D., Petrinic, N. "Effect of particle morphology, compaction, and confinement on the high strain rate behaviour of sand". *Experimental Mechanics*, DOI: 10.1007/s11340-017-0331-x.

Conference Papers

1. De Cola, F., Pellegrino, A., Barbieri, E., Penumadu, D., Petrinic, N. (2016) "A novel consolidation-based representative volume element for granular materials and its application for the characterization of the mechanical response of sand during impact loading", *Procedia Structural Integrity*, 2: 2905-2912.

2. De Cola, F., Bombace, N., Falco, S., Petrinic, N. (2017) "Concurrent adaptive mass-conserving comminution of granular materials using rigid elements", *Proceedings of the 7th International conference on Discrete Element Methods, Springer Proceedings in Physics.*, 1143-1152.

Poster Presentations / Talks

1. De Cola, F., Pellegrino, A., Petrinic, N. "Experimental observation of the influence of the grains shapes on the rate dependent behavior of Quartz sand". 8th International Congress of Croatian Society of Mechanics, 1-2 October 2015, Opatija, Croatia

2. De Cola, F., Bombace, N., Falco, S., Petrinic, N. "Concurrent adaptive mass-conserving comminution of granular materials using rigid elements", 7th International Conference on Discrete Element Methods, 1-4 August 2016, Dalian,

China

3. De Cola, F., Barbieri, E., Pellegrino, A., Petrinic, N. "Multiscale modelling and simulation of penetration phenomena", poster presented at the DTRA 2014 Basic Research Technical Review; Springfield, Virginia, USA; July 2014

4. De Cola, F., Petrinic, N. "High strain rate characterisation of Euroquartz sand using Long-Split-Hopkinson-Pressure-Bar apparatus", poster presented at the DTRA 2015 Basic Research Technical Review; Springfield, Virginia, USA; July 2015

5. De Cola, F., G. Quino, K. Dragnevski, N. Petrinic. "Acoustic measurements and imaging of sand grains failure during in-situ compression tests", 4th LIMA Users Meeting, Dept. of Engineering Science, Oxford, 20th April 2016

6. De Cola, F., Petrinic, N. "Acoustic Measurements applied to granular media: causes of rate dependency", 3rd Defence seminar on the high strain rate properties of soils and granular media, DSTL Porton Down, Wiltshire, UK, 9th December 2016

Contents

1 Introduction **1**

1.1 Background and motivation 1

1.2 Aim and objectives 5

1.3 Research strategy 6

1.4 Thesis outline 7

2 Literature Review **8**

2.1 Granular materials 8

2.2 Basic properties and controlling parameters 9

2.2.1 Granulometry 9

2.2.1.1 Particles size 10

2.2.1.2 Particles shape 11

2.2.2 Mineralogy 12

2.2.3 Presence of liquid phase 13

2.2.4 Packing properties 14

2.3 High rate applications of granular materials 15

2.3.1 Mechanical characterisation: Split Hopkinson Pressure Bar . . 16

2.3.1.1 Long Split Hopkinson Pressure Bar (LSHPB) 17

2.3.1.2 Pulse shaping 19

2.3.1.3 Effect of confining pressure, initial consolidation state and moisture content on the high strain rate behaviour of sand 20

2.3.2 Strain rate dependent behaviour of sand 22
2.4 Representative Volume Element of granular materials 24
2.5 Non Destructive Techniques applied to granular media 27
2.5.1 Acoustic Emission 28
2.6 Numerical methods for simulating granular media 29
2.6.1 Continuum and discontinuous methods 29
2.6.2 Discrete Element Method 30
2.6.2.1 Contact mechanics and time integration schemes . . 31
2.6.2.2 Simulation of grain comminution in DEM 34
2.7 Generation of numerical discrete statistically representative samples . 36
2.7.1 Spherical particles 36
2.7.1.1 Geometrical packing 38
2.7.1.2 Mechanical packing 39
2.7.2 Polyhedral particles 40
2.8 Summary 42

3 New three-dimensional geometrical deposition methods for packing spheres based on tangency 44

3.1 Planar-spiral deposition method 45
3.2 3D-clew deposition method 53
3.2.1 Primary spiral positioning technique 55
3.2.2 Secondary ”4-spheres-tangency” positioning technique 59
3.2.3 Subsequent levels 61
3.3 Results and discussion 63
3.3.1 Properties of the geometrical aggregate 66
3.3.1.1 Geometrical monodisperse assembly 67
3.3.1.2 Geometrical polydisperse assembly 67
3.3.1.3 Comparison of the geometrical methods 69
3.3.2 Gravity-assisted packing 69

3.3.2.1 DE simulations of monodisperse assemblies 70
3.3.2.2 DE simulations of polydisperse assembly 71
3.3.3 Summary of the results 72
3.4 Generation of loose aggregates: effect of friction on the mechanical packing 76
3.4.1 Results and discussion 78
3.5 Summary 79

4 A method for the generation and packing of representative polyhedral grains 81

4.1 Grain generation 82
4.2 Definition of the shape descriptors 85
4.2.1 Bounding sphere evaluation 86
4.2.2 Evaluation of the minimum volume enclosing ellipsoid 87
4.3 Packing algorithm 89
4.4 Computational cost and scalability 89
4.5 Parametric study of the models 91
4.5.1 Effect of ρ and H_k on the shape descriptors 91
4.5.2 Consolidation state of the packings 94
4.6 Representativeness of real granular materials 95
4.6.1 Shape descriptors 95
4.6.2 Validation 97
4.7 Summary 102

5 Definition of void ratio based Representative Volume Elements for granular materials 103

5.1 Numerical computation of the void ratio within the sample 104
5.2 Numerical estimation of the RVE: Ottawa sand 109
5.3 Experimental verification 118

5.4 Definition of the RVE for Ottawa sand in a loose configuration 123
5.4.1 Mechanical consolidation 123
5.4.2 Results and Comments 124
5.5 Summary 126

6 Characterisation of the effect of morphology, moisture content, compaction and confinement on the mechanical response of sand to impact loading 128

6.1 Sand materials and types of confinement 129
6.1.1 Ottawa, Q-Rok and Euroquartz Sand 129
6.1.2 Containers for lateral confinement of sand specimens 131
6.2 Procedure for the preparation of samples 133
6.2.1 Preparation of dense samples 134
6.2.2 Preparation of medium dense samples 135
6.2.3 Preparation of loose samples 135
6.2.4 Preparation of wet samples 135
6.3 Experimental Characterisation 136
6.3.1 Effect of the initial consolidation state 138
6.3.2 Effect of the grain shape 143
6.3.3 Effect of coating and inter-granular friction 145
6.3.4 Effect of the confinement 148
6.3.5 Combined effect of strain rate, shape and confinement 150
6.3.6 Effect of water content 152
6.3.6.1 Combination of the effects of morphology and water content 155
6.4 Summary 157

7 The development of sound measurements for the evaluation of the rate sensitivity of granular materials 159

7.1 Sound Measurements and imaging of sand grains failure during in-situ compression tests . . . 160
7.2 Experimental procedure . . . 161
7.2.1 Proposed method . . . 161
7.2.2 Materials and experimental set-up . . . 161
7.2.3 Post processing protocol . . . 164
7.3 Results and discussion . . . 167
7.3.1 Mechanical characterisation . . . 168
7.3.2 Correspondence of bursts and cracking events . . . 170
7.3.3 Time domain characteristics . . . 172
7.3.4 Single grains cracking versus sliding/rotations . . . 173
7.3.5 Effect of size, material and shape on single grain fracturing: frequency domain . . . 175
7.3.6 SM applied to granular assemblies: limitations of the technique 177
7.4 Sound Measurements on sand assemblies at different rates of loading . 179
7.4.1 Materials and containers . . . 180
7.4.2 Experimental set-up . . . 181
7.4.3 Results and observations . . . 183
7.4.3.1 Mechanical characterisation . . . 183
7.4.3.2 Sound measurements . . . 184
7.4.3.3 Time location of grain crushing during uniaxial compression tests . . . 186
7.5 Summary . . . 191

8 Concurrent adaptive mass-conserving comminution of granular materials using rigid elements 194

8.1 Implementation . . . 195
8.1.1 Spawning Method . . . 195
8.1.2 Failure Criterion . . . 196

8.1.3 Laguerre Voronoi Tessellation of the domain 196
8.1.4 Generation and arrangement of new fragments 197
8.2 Examples and Results 204
8.2.1 Mass loss and number of daughter particles: comparison with other existing methods 204
8.2.2 Effect of the size of the daughter particles 205
8.3 Summary 206

9 Conclusions and suggestions for future work 208
9.1 Generation and packing of statistically representative granular samples 209
9.2 Definition of Representative Volume Elements for granular materials . 210
9.3 Characterisation of the mechanical response of sand to impact loading 211
9.4 Discrete modelling of the comminution process during uniaxial compression of granular materials 213

List of Figures

1.1 Examples of granular materials: (a) building materials [3] , (b) pharmaceutical products [4], (c) food [5] 2

1.2 Examples of high rate applications of granular materials: (a) mine blasting [6], (b) earthquake [7], (c) projectile penetration [8] 2

1.3 Example of multiscale framework for granular materials 3

2.1 PDF (a) and CDF (b) representing the sizes distribution, taken from [10] 11

2.2 Classification of granular media based on the grains sizes 11

2.3 Split Hopkinson Pressure Bar set-up 17

2.4 Rise time and shape of the incident pulse; (a) no pulse-shaper, (b) with pulse-shaper 19

2.5 Comparison of the stress-strain curve of sand in uniaxial compression at low and high strain rates [53] 23

2.6 Schematic representation of the effect of the strain rate on the stress-strain curve of sand during uniaxial compression (taken from Whitman et al. [57]) 23

2.7 Mechanical deposition methods 40

3.1 Example of the planar deposition algorithm using spheres with three different radii: R_1, $R_2 = 2R_1$, $R_3 = 3R_1$ 46

3.2 Flowchart of the planar deposition algorithm 47

3.3 Deposition of the second circle on the second layer or positioning of the generic circle $S_{i,L}$ with respect to its neighbours 47
3.4 Deposition of the first circle of a new ring 49
3.5 Layer produced with the planar algorithm 51
3.6 Layer produced with the planar algorithm with a very wide radii distribution R_1, $R_2 = 10R_1$, $R_3 = 100R_1$ 51
3.7 Examples of concave and convex layers produced with the planar approach 52
3.8 Two different 3D planar assemblies based on the planar spiral deposition method, respectively in perspective and orthographic view . . . 52
3.9 Flowchart of the 3D-clew deposition method 54
3.10 Definition of the angles μ and η (a) and of the components of the vector $\mathbf{V}$ in the Cartesian coordinate system (b) 56
3.11 First two spheres of the 3D-clew assembly 56
3.12 Positioning of the following particles in the 3D-clew method 57
3.13 Transformation of coordinate system in the 3D-clew method 58
3.14 Second level around the initial sphere in the 3D-clew method 59
3.15 4 spheres tangency condition 60
3.16 First spheres of a subsequent level in the 3D-clew method 62
3.17 Assembly produced with the 3D-clew deposition method 62
3.18 Frontal and prospective view of a cubic 3D-clew geometrical assembly 63
3.19 Imaginary boxes defined to evaluate the correct void ratio, accounting for walls and free surface effects 64
3.20 Zone used to calculate the correct void ratio; d_i is the dimension of the fictitious box and D of the real one 64
3.21 Examples of monodisperse a) - b) and polydisperse c) - d) assemblies 66
3.22 Summary of the results for monodisperse assemblies 73
3.23 Summary of the results for polydisperse assemblies 74

3.24 Scalability of the 3D-clew geometrical method; computer architecture reported in footnote 2, pag.64 75

3.25 Effect of friction angles on the distribution of void ratio after mechanical packing 78

3.26 Mean values and standard deviations of the void ratios obtained varying the friction angle, and comparison with maximum (e_{max}) and minimum (e_{min}) experimental values reported in Chapter 6 79

4.1 Flowchart of the algorithm for the generation of assemblies of arbitrarily shaped particles 83

4.2 Aggregate of Voronoi cells 84

4.3 Frontal (top) and isometric (bottom) view of (a) an assembly stretched of (b) 25%, (c) 50%, and (d) 100% 85

4.4 3D clew packing of the spheres ($e \approx 0.8$) and corresponding inscribed grains ($e \approx 4.3$) 90

4.5 Distribution of S, ψ_w and ψ for different values of ρ 92

4.6 Variation of ψ, ψ_w and S with ρ 92

4.7 Variation of ψ, ψ_w and S with ρ, for different values of H_k 94

4.8 Variation of the void ratio with ρ 95

4.9 Comparison of the properties of real and numerically generated granular materials 96

4.10 Visual comparison of numerically generated (bottom) and tomography scans [191, 89] (top) of single sand grains 97

4.11 Comparison of numerically generated (dotted line) and experimentally measured (continuous line) size distributions of Q-Rok sand 98

4.12 Comparison of numerically generated (dotted line) and experimentally measured (continuous line) slenderness values of Q-Rok sand 99

4.13 Comparison of the experimental and numerical probability distribution functions of the length, width, and thickness of Alabama limestone particles 100
4.14 Comparison of the experimental and numerical probability distribution functions of sphericity and slenderness of Alabama limestone particles 101

5.1 Two-dimensional schematic representation of the three dimensional effect of the wall and free surfaces on the RVE 105
5.2 Schematic representation of the variation of the height of the fictitious volume 106
5.3 Schematic representation of the variation of all the dimensions of the fictitious volume 106
5.4 Possible intersections between boundaries and spheres 107
5.5 Qualitative distribution of the void ratio within granular materials, varying the dimension (d) of the imaginary volume with respect to the real container (D) 109
5.6 SEM images of grain shapes of Ottawa (a) and Q-Rok (b) sand . . . 110
5.7 Flowchart of the iterative algorithm for the calculation of the RVE . . 112
5.8 Three different initial and final assemblies produced with the combination of geometrical deposition method and mechanical method based on the application of gravity 113
5.9 Example of the Kinetic Energy of the system during the deposition . 113
5.10 Void ratio for three different numerical samples with 5000 particles, varying the dimension of the imaginary box (d) with respect to the real one (D) 114
5.11 Void ratio for three different numerical samples with 10000 particles, varying the dimension of the imaginary box (d) with respect to the real one (D) 115

5.12 Void ratio for three different numerical samples with 15000 particles, varying the dimension of the imaginary box (d) with respect to the real one (D) 116
5.13 Void ratio for different numerical samples with 15000 and 20000 particles, varying the dimension of the imaginary box (d) with respect to the real one (D) 117
5.14 Schematic of sand specimen confined in a steel tube 119
5.15 Forces at the sample-bars interfaces 120
5.16 Force equilibrium and strain rate in dry, dense Ottawa sand, $L = 10$ mm 121
5.17 Force equilibrium and strain rate in dry, dense Ottawa sand, $L = 6$ mm 121
5.18 Upper and lower limit of the experimental variation (over 5 tests) of the stress-strain curves of Ottawa sand at high strain rate ($1400s^{-1}$) and void ratio $e = 0.56$ for samples of length $L = 6$ mm 122
5.19 Upper and lower limit of the experimental variation (over 5 tests) of the stress-strain curves for samples smaller than the RVE with $L/D = 0.1$ 122
5.20 Void ratio for three different numerical samples of loose Ottawa sand with 5000 particles, varying d/D 124
5.21 Void ratio for three different numerical samples of loose Ottawa sand with 10000 particles, varying d/D 125
5.22 Void ratio for different numerical samples of loose Ottawa sand with 15000 and 20000 particles, varying d/D 125

6.1 Size distribution of (a) Ottawa, (b) Q-Rok, and (c) Euroquartz sand . 130
6.2 Comparison between the different shapes: (left) Q-Rok, (centre) Euroquartz Siligran $0.125 - 0.71$ and (right) Ottawa sand 131
6.3 Schematic of (a) stainless steel confinement and (b) latex confinement 132
6.4 Support for the containers 133
6.5 LSHPB set-up 133

6.6 Definition of the main zones of the stress-strain curve (in black) obtained during uniaxial compression tests and corresponding strain rate curve (in red); in the cartoons, the elastic deformation is represented with an overlap between grains 137
6.7 Effect of the initial consolidation state on Ottawa sand at (a) $1600s^{-1}$ and (b) $600s^{-1}$ in a rigid confinement 139
6.8 Confined modulus for the three initial void ratios (a), and effect of the initial consolidation state on the salient points of the stress (b) - strain (c) curves for Ottawa sand 140
6.9 Effect of the initial consolidation state on Q-Rok sand at (a) $1600s^{-1}$ and (b) $600s^{-1}$ 141
6.10 Confined modulus for the three initial void ratios (a) and effect of the initial consolidation state on the salient points of the stress (b) - strain (c) curves for Q-Rok sand 141
6.11 Effect of the initial consolidation state on Euroquartz sand at $1600s^{-1}$ 142
6.12 Confined modulus for the three initial void ratios (a) and effect of the initial consolidation state on the salient points of the stress (b) - strain (c) curves for Euroquartz sand 142
6.13 Effect of the grains shape at (a) $600s^{-1}$ and (b) $1600s^{-1}$ 144
6.14 Effect of the grains shape on confined modulus (a), stress (b) and strain (c) at $600s^{-1}$ 144
6.15 Effect of the grains shape on confined modulus (a), stress (b) and strain (c) at $1600s^{-1}$ 145
6.16 Effect of the drying process on the dense coated Euroquartz sand at high strain rate 146
6.17 Effect of the drying process on confined modulus (a), stress (b) and strain (c) for coated Euroquartz sand 146
6.18 Effect of coating on (a) dense and (b) loose Euroquartz sand 147

6.19 Effect of coating on (a) confined modulus, (b) stress and (c) strain of loose Euroquartz sand 148
6.20 Effect of the deformable confinement (a) on the response of the three types of sand at $1000s^{-1}$ and zoom-in at low strains (b) 149
6.21 Salient values of stress and strain of the three types of sand in a deformable confinement 150
6.22 Effect of the strain rate on the mechanical behaviour of (a) dense Q-Rok, (b) Euroquartz and (c) Ottawa sand in deformable containers . 151
6.23 Example showing the effect of the strain rate on the values of stress of dense Q-Rok sand in deformable containers 151
6.24 Combined effects of shape and confinement at a lower strain rate . . . 152
6.25 Moisture effect on initially dried, dense Euroquartz sand at high strain rate 153
6.26 Effect of the moisture content on (a) confined modulus, (b) stress and (c) strain of dense Euroquartz sand at high strain rate 153
6.27 Effect of the moisture content on initially dried, dense Ottawa sand at high strain rate 154
6.28 Effect of the moisture content on the confined modulus of dense Euroquartz sand at high strain rate 155
6.29 Effect of the moisture - comparison between Ottawa and Q-Rok dense sand at high strain rate 156
6.30 Effect of the moisture content on the confined modulus of dense Ottawa and Q-Rok sand at high strain rate 156

7.1 Size distribution of Volcanic sand 162
7.2 Grain shapes for Ottawa (a), Q-Rok (b), and Volcanic sand (c) with 20X magnification 162
7.3 Metallic container and glass cover for in-situ tests on sand (dimensions in mm) 163

7.4 In-situ testing procedure 164
7.5 Extraction of the fracture events from the waveform of the signal (a) and definition of an event (b) 164
7.6 Definition of counts per event (Hits) and cumulative counts per event 165
7.7 Typical examples of rise time (a) and duration (b) of a burst event . 166
7.8 Example of Frequency-Time distribution analysis 167
7.9 Box plot of force at failure for different types of sand grains 168
7.10 Box plot of displacement at failure for different types of sand grains . 169
7.11 Typical force - displacement curve for brittle materials 170
7.12 Test 1 - Ottawa sand grain. Comparison between SM, force-time curve (left), and microscopy (right): initial configuration (a), subsequent fractures (b and c) and complete crushing (d) 170
7.13 Test 2 - Ottawa sand grain. Comparison between SM, force-time curve (top) and microscopy (bottom): initial configuration (a), subsequent fractures (arrows in b - f), and complete crushing (g) 171
7.14 Test 1 - Waveform (a) and extraction of SM events (b) 172
7.15 Amplitude (a), duration (b) and rise time (c) of the three events . . . 173
7.16 Test 3 - Insensitivity of SM to rotations during uniaxial compression test. Comparison between SM, force-time curve (top) and microscopy (bottom): initial configuration (a), subsequent fractures (b - f) and final crushing (g) 174
7.17 Uniaxial compression of Q-Rok sand grain: initial configuration (a), subsequent fractures (b and c) and final crushing (d) 175
7.18 Uniaxial compression of Volcanic sand grain: initial configuration (a), subsequent fractures (b and c) and final crushing (d) 176
7.19 Effect of grain shape and chemical composition on the fracture of single sand grains 177
7.20 Effect of the grain size on the fracture of single sand grains 177

7.21 Initial assembly of Ottawa sand grains 178
7.22 Assembly - Comparison between SM, force-time curve (top) and microscopy (bottom): initial configuration (a), subsequent fractures (b and c) 178
7.23 Assembly of the different components of the container (a) and cross-sectional view (b) 180
7.24 Axial-torsion hydraulic Instron 8854 testing device 182
7.25 Example of speckle pattern used for DIC on anvil and sand container 182
7.26 Effect of the strain-rate on dense (a) and loose (b) Ottawa sand . . . 183
7.27 Effect of the strain-rate on dense (a) and loose (b) Q-Rok sand 184
7.28 Cumulative counts per event (logarithmic scale) on Ottawa sand in dense and loose consolidation states at different loading rates 185
7.29 Cumulative counts per event (logarithmic scale) on Q-Rok sand in dense and loose consolidation states at different loading rates 185
7.30 Grains fracture location in dense (a) and loose (b) Ottawa sand at $v = 0.02\ mm/s$ 187
7.31 Grains fracture location in loose Ottawa sand at (a) $v = 20\ mm/s$ and (b) $v = 0.02\ mm/s$ 188
7.32 Grains fracture location in dense (a) Q-Rok and (b) Ottawa sand at $v = 0.02\ mm/s$ 189
7.33 Grains fracture location in loose Q-Rok sand at (a) $v = 0.02\ mm/s$ and (b) $v = 2\ mm/s$ 190

8.1 Flowchart showing the spawning method 195
8.2 Laguerre Voronoi tessellation: a) granular packing, b) corresponding tessellation of the domain, c) superimposition of packing and tessellation 197
8.3 Representation of the 3D-clew deposition method for the spawning of daughter particles 198

8.4 Different cases for the point-to-plane distance d_i; the white colour indicates the portion of volume within the cell 198
8.5 Clockwise and anti-clockwise connectivity of the face and consequent direction of the normal 200
8.6 Example of daughter particle intersecting the boundary (left) and geometrical definition of the deposition angle α (right) 201
8.7 Example of scaling of the daughter particle (left) and definition of the new radius x of the scaled particle C_n (right) 202
8.8 Estimation of the position x of C_n (left) and zoom-in of the geometrical construction (red triangle) used to estimate x (right) 202
8.9 Examples of spawning in Voronoi cells: a) polyhedral shape, b) spherical shape, c) elongated shape 203
8.10 Example of packing with fractured particles 204
8.11 Number of particles with certain mass loss a) and number of daughter particles b) for different consolidation states 205
8.12 Number of particles with certain mass loss a) and number of daughter particles b) for different radii of the daughter particles 206

Chapter 1

Introduction

This chapter presents background information and motivation for research. It also sets aims and objectives of this dissertation.

1.1 Background and motivation

A small speck of sand on the seashore is not different (from a physical and chemical prospective) from a boulder made of the same material next to it, except for its extensive properties (i.e. mass, volume). However, an *aggregate* of sand grains of mass and volume comparable to the boulder would show a significantly different mechanical behaviour when subjected to external loads. While the boulder behaves like a solid, the sand aggregate can exhibit different physical states (from solid to gas-like) depending on the relative motion of particles within the assembly. For this reason they are considered an unusual form of matter. Materials which show such behaviour are defined *granular media*. Their *macroscopic* physical, chemical and mechanical properties are consequence of the *micro-scale* interaction between grains.

Granular media are widely diffused on Earth: they cover about 90% of its solid surface in the form of sand or clay (with grains of dimensions in the order of micrometers), stones, and rock blocks (from centimetres to tens of meters) [1]. Moreover, they are the second most used type of materials in industry after water [2] and find application in many different sectors, ranging from construction, mining, chemistry,

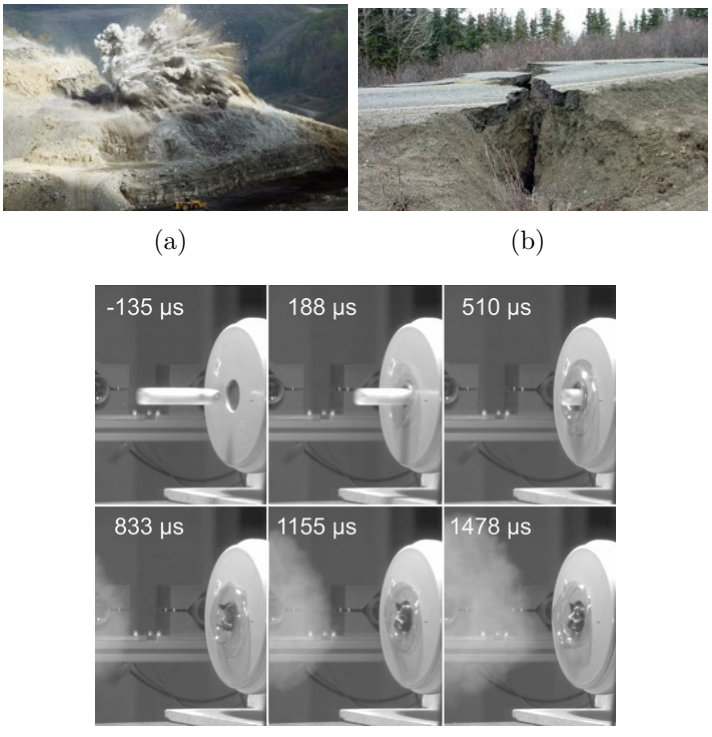
physics, pharmacy, but also in food and agricultural industry (Figure 1.1).



(a) (b) (c)

Figure 1.1: Examples of granular materials: (a) building materials [3] , (b) pharmaceutical products [4], (c) food [5]

Geo-materials are also widely adopted in civil construction and military applications (Figure 1.2) because of their high potential to attenuate shock loading, disperse momentum and dissipate kinetic energy when subjected to rapid loading (explosions, earthquakes, ballistic impacts).



(a) (b)

(c)

Figure 1.2: Examples of high rate applications of granular materials: (a) mine blasting [6], (b) earthquake [7], (c) projectile penetration [8]

Despite the increasing adoption of such materials in highly dynamic applications, the understanding of their mechanical behaviour at high strain rate is still very limited since they show characteristics which are not yet fully understood, thus requiring additional experimental and numerical investigations.

From predictive simulations point of view, in the recent years, particular attention is given to the development of numerical approaches, defined as *multiscale simulations*, able to capture fundamental features at multiple length and time scales and able to offer an improved correspondence between numerical models and reality. These approaches are particularly useful in case of systems, like granular media, where processes happening at a certain scale govern their behaviour across several larger scales (small scale-separation) [9]. In this case, multiple models should be adopted at different length and time scales. Using exclusively continuum models for such materials would induce noticeable approximations in the results.

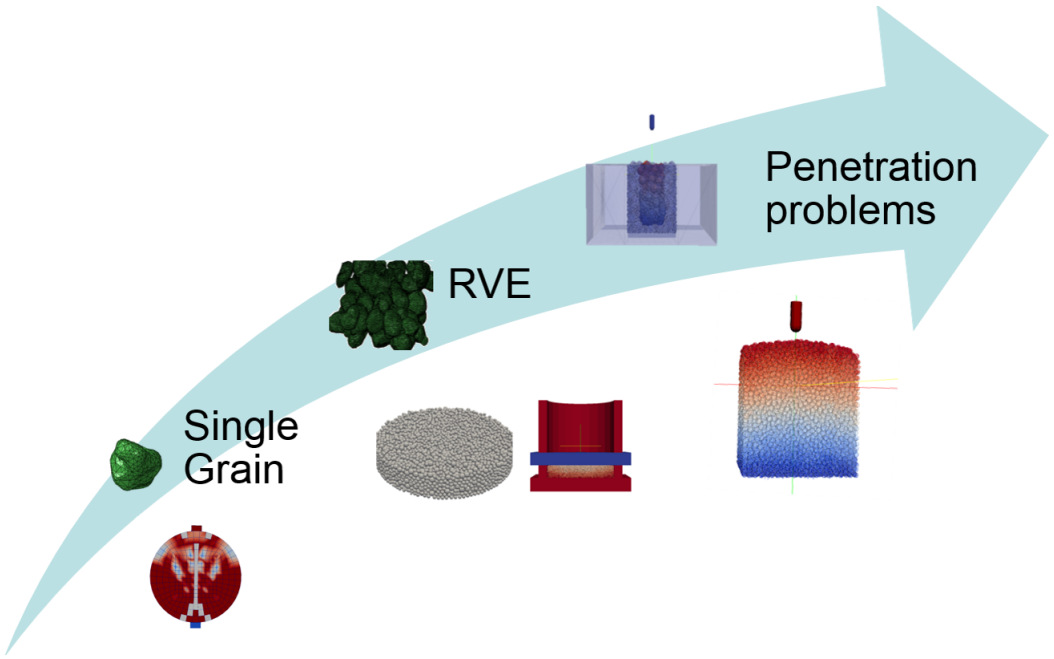


Figure 1.3: Example of multiscale framework for granular materials

Figure 1.3 shows an example of multiscale approach that could be employed, for instance, to simulate projectile penetration into granular materials. In this case, at least three representative length scales should be identified: micro-scale models,

used to represent the features and mechanical behaviour of the single sand grains; meso-scale models, statistically representative of the bulk and able to reproduce the interaction between grains; finally, fully homogenised macro-scale models that explicitly reproduce the interaction between the projectile and the continuum. The three length scales could be bridged either in a hierarchical (one-way communication between scales, where the behaviour at the bottom scale is homogenised at the upper scale) or concurrent sense (solving all scales simultaneously, constantly exchanging information between them).

However, the adoption of multiscale frameworks for simulating granular materials is still very limited. In fact, most of the available models for granular media ignore the aforementioned small scale-separation, adopting either continuum approaches (thus ignoring their intrinsic discontinuous nature) or fully discrete modelling techniques (where all particles are represented as distinct elements interacting through contacts). The former approach, even being more computational efficient, inevitably leads to approximations that can affect the correctness of the results. The latter one, instead, requires relevant computational power.

The limited adoption of multiscale approaches is due to the lack of statistically representative models at each length scale. Therefore, further numerical investigations are required. Particular attention should be paid to the definition of models able to statistically represent the single grains features (at the micro-scale) and their interaction at the meso-scale, before moving to larger scales.

From an experimental prospective, instead, the complex nature of granular materials induce uncertain and sometimes contradictory results. This is due to the strong inter-dependency of the parameters controlling their mechanical response (e.g. consolidation state, particles sizes and shapes, moisture contents, etc.) and to the complexity of the techniques generally adopted for their characterisation. Additional experimental studies at the grain (micro-scale) and assembly level (meso-scale) are needed to shed light onto the convoluted mechanical behaviour of granular media.

This research effort will eventually lead to a more complete understanding of their basic physics and to the development of engineered granular materials with enhanced mechanical properties.

The work presented in this thesis was part of a wider research effort titled "Multi-Scale Penetration Mechanics of Projectiles through Granular Media using Neutron and X-Rays", funded by the American Defence Threat Reduction Agency (DTRA), and carried out by the author in collaboration with the University of Tennessee and the EMI-Fraunhofer Institute. Its main aim was to develop a better understanding of the basic science and mechanics associated with the application of rapidly applied loads and to develop predictive numerical tools.

1.2 Aim and objectives

The main aim of the conducted research was to achieve better understanding of the response of granular materials to impact loading, by:

1. systematic experimental characterisation of the rate dependent behaviour of granular materials;

2. development of new approaches for the numerical generation of statistically representative particles and assemblies of real granular materials

As a consequence, the specific objectives of this thesis are:

- to develop numerical capability to generate statistically representative shapes and sizes of particles of real granular materials and their assemblies;

- to define the Representative Volume Element (RVE) for use in experimental characterisation of granular assemblies to dynamic loading and in numerical simulations of granular media;

- to offer a comprehensive experimental characterisation of granular materials at high strain rate;

- to improve the understanding of the effect of fracture of individual grains upon the mechanical response of granular assemblies; and

- to establish the building blocks of future multi-scale modelling capability for simulation of impact and penetration into sand.

1.3 Research strategy

A research strategy has been defined to achieve the objectives set in the previous section.

Firstly, in order to correctly model real granular materials, geometrical methods able to generate statistically representative numerical samples, in terms of shapes and sizes of single grains, need to be developed.

Such numerical models are then used to study the dimensions of Representative Volume Elements (RVE) of granular materials to be adopted in experiments or in multiscale simulations. Therefore, a numerical procedure for the estimation of the RVE of granular materials needs to be defined.

The definition of the RVE sets the dimensions of the samples to be used in a full experimental high rate characterisation of different types of sand at high strain rates, by means of a be-spoke Split Hopkinson Pressure Bar. The experimental characterisation aims at identifying and quantifying the effect of grain mineralogy, granulometry, confinement, moisture content and combination of these factors on the mechanical response of sand.

Additionally, Non-Destructive-Techniques (based on acoustics) are employed to detect single sand grain fracture during the execution of uniaxial compression tests. They need to be calibrated against microscopy during in-situ compression tests to verify their ability to capture the desired phenomena. They are then employed to study the effect of grains failure on the mechanical response of granular materials and to verify the existence of rate dependency.

Finally, providing that the central role of grains fracture on the mechanical behaviour of granular materials is experimentally verified, a numerical method for modelling the grain comminution in dynamic Discrete Element Simulations will be developed.

1.4 Thesis outline

This thesis is organised as follows. Chapter 2 presents a review of all relevant published work and identifies the open research questions that are addressed in subsequent chapters. Chapter 3 introduces two innovative geometrical methods for the generation of densely packed spherical assemblies that statistically represent - in terms of numbers and size distributions - real granular materials. The effect of grains shape will be introduced in Chapter 4, where a novel three dimensional geometrical approach based on a modified Voronoi tessellation technique is used to generate representative polyhedral particles. Chapter 5 presents a method for the numerical estimation of RVEs of granular media. Chapter 6 reports a comprehensive experimental characterisation of different types of sand at high rates of deformation, based on the adoption of RVE-based sample sizes. It identifies and quantifies the role of many inter-dependent parameters on the mechanical response of granular media, to be used for future integration in rate dependent constitutive models. Chapter 7, instead, introduces a new non-destructive experimental technique called Sound Measurements (SM), which is employed to verify the strain rate dependency and the effect of grain crushing on the mechanical behaviour of sand, when compressed at different loading rates. The SM are also used for the time location of cracking events during uniaxial compression tests of granular materials. Finally, once the central role of grains comminution on the mechanical response of granular materials has been experimentally identified, Chapter 8 introduces a new modelling approach to improve the mass-conservation during grain comminution in discrete element simulations. Conclusions and recommendation for future works are presented in Chapter 9.

Chapter 2

Literature Review

The current literature on granular materials subjected to impact loading, which underpins the work presented in this thesis, is reviewed in this chapter. First, a general description of granular media will be given. Then, the focus will be moved into applications in which granular media are loaded at high rates. Typical experimental techniques and devices for high strain rate characterisation of mechanical performances will be presented, together with state-of-the-art experimental observations of the mechanical behaviour of granular materials subjected to dynamic loading. Later on, attention will be focused on the numerical methods typically adopted for simulating granular media, on the algorithms for generating statistically representative models of granular materials and on the definition of Representative Volume Elements of granular media.

2.1 Granular materials

Granular materials are assemblies of a large number of discrete solid particles with interstitial voids filled with gases or liquids. They are characterised by negligible thermodynamic effects and their mechanical, physical and chemical properties derive from their microscopic features (e.g. single grain shape, sizes, chemical composition, etc.) and from the inelastic, non-linear, frictional interactions between grains. This class of materials presents an exceptional energy dissipation capability due to the

grains interaction.

Granular media are often in meta-stable states of equilibrium and they can be activated by several types of loading conditions (vibrations, pulses, motion of interstitial fluids, etc.). Unlike continuous materials, the stress generated by the application of external loads propagates from the point of application - on the boundaries - to the inside through defined paths, called *force chains*.

When subjected to external loads, granular materials can exhibit different states of matter. They are disordered at the grain level but behave like a solid or a fluid at the macroscopic level, exhibiting phenomena like arching and segregation. In some cases, their behaviour can mutate from solid, via liquid, to gas-like physical states in the very same process (e.g. the liquefaction processes happening during avalanches) [10]. All the aforementioned definitions and observations prove the unique nature of this not fully understood material.

2.2 Basic properties and controlling parameters

The complex behaviour of sand is controlled by the interaction of many parameters, describing its physical *nature* and *state*. The *nature* of the sand is generally represented by material and geometrical properties such as grain-size distribution, grains shape and mineralogy among others. On the contrary, its *physical state* represents the conditions under which the sand exists and it generally refers to the way the particles interact (packing properties).

Further description of the main parameters controlling the mechanical behaviour of granular materials is given in the following sections.

2.2.1 Granulometry

Granular materials are polydisperse assemblies of grains with very different geometrical features. The term *granulometry* is generally adopted to indicate geometrical attributes of the single sand grains such as size distributions and shapes.

Most of the mechanical properties of the grains and packings are conditioned by their granulometry. Whilst the size distribution influences both the force at the grain level and the inter-particle packing mechanisms, the shapes of the grains affect several properties of the assembly such as: the variability of the consolidation state, the bulk stiffness, the friction angle and the liquid bridging [11].

Granular media undergo diverse physical, chemical and biological processes that drastically influence their granulometry [10]. As a matter of fact, sizes and shapes of the grains are consequences of the chemical composition, formation mechanisms, depositional environments and transportation (wind or water) of the considered granular media.

In terms of formation mechanisms, a large portion of granular media comes from physical weathering actions and breakdown due to the development of fractures into rocks or from chemical weathering acts and erosion caused by water and air (ionisation, oxidation and dissolution of some of the chemical constituents). In other cases, granular materials are generated from volcanic activities. Depositional environments and transportation mechanisms, instead, strongly affect the shapes of the grains. For instance, grains of glacial and fluvial deposits are generally sharp and angular, whilst those of aeolian deposits are rounded and present smooth surfaces.

2.2.1.1 Particles size

The particle sizes are generally defined by an equivalent representative dimension, corresponding to the diameter of an ideal object that has the same geometrical properties (area or volume) as the real one. They are generally measured using sieving techniques, light-scatter measurements or microscopy analysis [10]. Among these, the most widely adopted technique is the *sieving*. The granular samples are passed through standard sieves with successfully smaller mesh sizes. The mass of the material retained in each sieve is determined and then used for the estimation of the cumulative percentage of mass passing each sieve.

The size distributions are mathematically expressed by either probability density functions (PDF - Figure 2.1a) or cumulative distribution functions (CDF - Figure 2.1b).

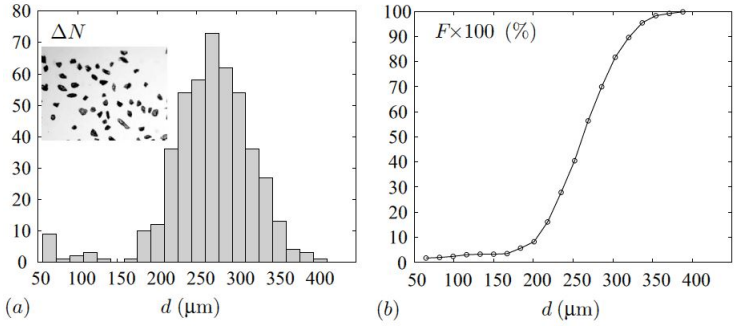


Figure 2.1: PDF (a) and CDF (b) representing the sizes distribution, taken from [10]

Particles sizes are also used to classify the granular materials. Figure 2.2 shows the ranges of sizes according to the British Standards BS 5930:1981 - Site Investigation.

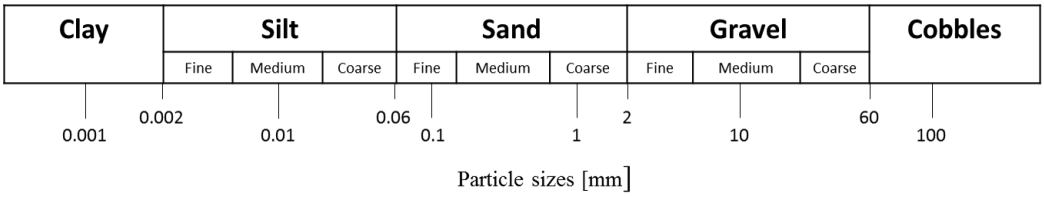


Figure 2.2: Classification of granular media based on the grains sizes

In this thesis, both sieving and microscopy-based techniques are used to measure the size distributions of the considered granular materials, expressed in terms of CDF. More detailed information will be presented in the next sections.

2.2.1.2 Particles shape

Physical phenomena such as inter-granular friction and grains locking are strictly due to the morphology of the grains. Bulky particles, for instance, can have angular, rounded, flat or elongated shapes.

Several investigations [12, 13, 14] defined numerical parameters to describe the morphology of single sand grains. Wadell [12] identified three main independent

properties to unequivocally describe the morphology of the particles: *form*, *roundness*, and *surface texture* (i.e. roughness). These three properties can be classified in terms of relative importance with respect to the particle size. The form is a first order property that defines the proportions of the grain; the roundness, which indicates the angularity of the corners, ranks second in the order of importance of the shape properties; finally, the surface texture describes the roughness of the surfaces. Each of those properties can be expressed by several parameters, also defined as *shape descriptors*, which are described in [13]. All these mathematical parameters are based on the definition of representative geometrical entities. For instance, the ellipticity is defined as the length-to-width ratio of the grain, whilst the circularity as the ratio between the square of the perimeter and the projected area [10].

Detailed information on the definition and computation of shape descriptors expressing the form of the grains will be presented in Chapter 4.

Experimental techniques are usually used to determine the shapes of the grains. One common and easy technique is based on the post-processing of images taken with the microscope, which provides planar measures of the shape descriptors. On the other hand, 3D shape descriptors can be measured using 3D scanner techniques (e.g. X-ray, neutron imaging) combined with surface mesh reconstruction software [15, 16] or destructive techniques (e.g. serial sectioning) [17].

2.2.2 Mineralogy

The term mineralogy generally indicates the study of chemistry and crystal structure of minerals. In the context of this thesis, it refers to the chemical composition of the single sand grains and the chemical processes to which they are exposed. The main constituent of most of the existing types of sand is silicon dioxide SiO_2 [18]. Nevertheless, impurities such as clay minerals (kaolinite and illite), iron oxides and heavy metals can be found in most of the natural occurring granular media. Sand made of up to 99% of SiO_2 is defined *silica sand*. In other cases, the sand can be

generated from organic sources and contain coral and shell fragments or it can derive from volcanic events, presenting high content of basalts and obsidian. In this work, silica and volcanic sand are analysed and used as reference materials. Further description of their specific mineralogy will be provided in Chapter 6 and 7.

The chemical composition strongly affects several properties of the grains: colour, elastic properties, comminution and crushability. For example, a white colour indicates a high content of organic substances or quartz, a black or dark green colour characterises the volcanic sand, whilst red and yellow colours are generally due to the presence of iron. As a consequence of their chemical composition, silica sand shows lower crushability index and better elastic properties than volcanic sand.

2.2.3 Presence of liquid phase

Granular media are either two or three-phase materials. Dry sand is a two-phase material, made of solid particles and pore air. It represents an example of non-cohesive system, showing only repulsive contact forces between grains. Another example of two-phases material is represented by fully saturated samples. In this case, the interstitial voids are completely filled with water. A partially saturated sample is, instead, a three-phase material composed of solid particles, pore water and air. The presence of water introduces adhesion forces and, as a consequence, cohesive effects between grains [19]. Moreover, it should also play a role in the variation of the frictional behaviour of sand. For low water content, a lubrication of the contact points between grains should yield a reduction of the inter-granular friction.

The *water content* (S_w), also known as *gravimetric water content* or *moisture content*, is defined as the ratio of the mass of water m_w to the mass of solids m_s into the considered volume:

$$S_w = \frac{m_w}{m_s} \tag{2.1}$$

An alternative definition for the water content is the *volumetric water content*,

which is the ratio between the volume of water and total volume available [18]. The gravimetric water content can be converted to volumetric one by multiplying it for the specific gravity of the sand.

Depending on the ease and speed at which water moves within the granular sample with respect to the duration of the loading, either drained or undrained conditions can be achieved [20]. In *drained conditions*, water can freely flow in or out of the sample during the application of the load. This generally happens when the load is slowly applied and it results in no variation of the water pressure. *Undrained conditions* are achieved when the water remains trapped within the inter-granular voids. This happens when changes in loads occur more rapidly than water can flow inside the medium, causing changes in the water pore pressure.

In this work, undrained conditions will be evaluated in Chapter 6.

2.2.4 Packing properties

Granular materials are assemblies of particles whose behaviour strongly depends upon the characteristics of the packing. Due to their discrete nature, granular materials can be found at different densities for the same amount of soil. Moreover, the very same material (same granulometry and mineralogy) differently packed would produce a significantly different response to mechanical loading. Many parameters such as void ratio, porosity, and relative density are used to describe the consolidation state of the considered granular material. The void ratio is defined as the ratio of the volume of voids V_v to the volume of solids V_s [18] as follows

$$e = V_v/V_s \tag{2.2}$$

Another equivalent parameter, largely used in soil mechanics, is the porosity (n). It is defined as the ratio between the volume of voids and the total volume of the soil V_{tot}:

$$n = V_v/V_{tot} \tag{2.3}$$

The two definitions are linked by the following

$$\begin{aligned} n &= e/(1+e) \\ e &= n/(1-n) \end{aligned} \tag{2.4}$$

Every soil system can exist at different consolidation states, ranging between a densest and loosest configuration. These extreme consolidation states are characterised, respectively, by minimum (e_{min}) and maximum (e_{max}) void ratios. For intermediate consolidation states, the concept of relative density (D_r) is widely adopted [21]. It is generally defined as

$$D_r = \frac{e_{max} - e}{e_{max} - e_{min}} \tag{2.5}$$

2.3 High rate applications of granular materials

Geo-materials, like sands and soils, are widely used in civil engineering and they are as such of significant relevance to defence applications. Most of these applications are particularly related to the high potential of granular materials to attenuate shock loading, disperse momentum and dissipate kinetic energy when subjected to rapidly applied loads (such as those arising from earthquakes [22], explosions [23], or projectile penetration [24]).

In the last decades, geo-materials have been sporadically characterised at high strain rate due to the difficulties associated with their complex nature and with the complexity of the experimental techniques required to fulfil this task. The next sections report the relevant literature about high rate characterisation of granular materials.

2.3.1 Mechanical characterisation: Split Hopkinson Pressure Bar

Several experimental techniques have been developed to measure the mechanical properties of materials at different strain rates. The most common techniques are summarised in Table 2.1.

Strain Rate		**Technique-Behaviour**
Low strain rate	$10^{-8} < \dot{\varepsilon} < 10^{-5}$	Creep behaviour, creep laws
	$10^{-5} < \dot{\varepsilon} < 10^{-3}$	Quasi-static tests, Hydraulic servo-controlled machines
Intermediate strain rate	$\dot{\varepsilon} < 10^{-1}$	Specialised hydraulic servo-controlled machines
	$\dot{\varepsilon} < 10^{0}$	Pneumatic-hydraulic or gas-driven machines
	$\dot{\varepsilon} < 10^{1}$	Drop-weight machines
High - Very high strain rate	$10^{2} < \dot{\varepsilon} < 10^{4}$	Split Hopkinson Bar (SHB)
	$\dot{\varepsilon} > 10^{4}$	Plate impact techniques

Table 2.1: Experimental techniques for materials characterisation at different strain rates

Among the experimental techniques for high rate mechanical loading, the Split Hopkinson Pressure Bar (SHPB) is the experimental apparatus most commonly adopted for the evaluation of the high strain rate behaviour of solid materials [25, 26, 27]. The SHPB was originally invented by Kolsky [27, 28] and it is composed of a projectile and two bars sandwiching a specimen of the material being characterised. The projectile, accelerated by compressed air, impacts the input bar, thus generating a stress pulse. This pulse travels through the input bar until it reaches the specimen. At the interfaces between sample and input bar, due to the impedance mismatch between the two, part of the signal is transmitted and part reflected. The transmitted wave travels through the specimen into the output bar.

The variation of the compressed air pressure defines the magnitude of the stress pulse that is delivered to the input bar. The time history of the stress waves travelling through the input and output bars is measured using calibrated strain gauges placed

on their surface at different locations. The measured voltages are converted into stresses via calibration. High strain rate experiments are considered valid only when the dynamic force equilibrium conditions are achieved within the sample [29].

2.3.1.1 Long Split Hopkinson Pressure Bar (LSHPB)

The modified Split Hopkinson Pressure Bar adopted in this thesis is longer than the usual set-up and includes input and output bars made of Ti64, 2.8 m long and 20 mm in diameter. Both bars were supported by low-friction polymeric circular bearings (with a support distance of 40 cm), in order to avoid sagging, buckling and any undesired lateral movement, as well as to ensure the alignment between bars and specimen. The schematic of the adopted set-up is shown in Figure 2.3.

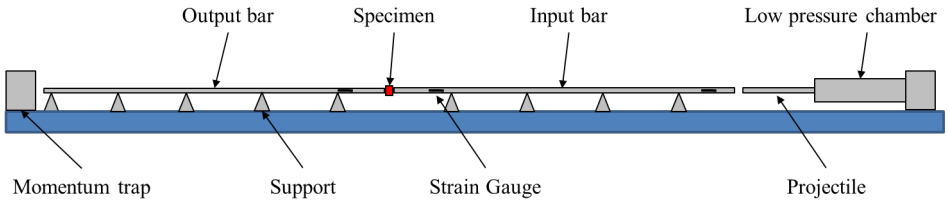


Figure 2.3: Split Hopkinson Pressure Bar set-up

The adoption of a longer projectile enables longer test duration, hence allowing for the analysis of a wider spectrum of strains with respect to what existed in literature. Gerlach et al. [30] presented a clear comparison between the pulses achieved using a similar set-up and the classical ones. A regular SHPB with a projectile of 500 mm generates a pulse with a duration of about 0.2 ms while a more than five times longer pulse (1.1 ms) can be obtained using this new configuration. The stress pulses are measured by means of strain gauges placed in selected sections of the bars. The signals are amplified by means of high-speed signal amplifiers and recorded by high-frequency digital oscilloscopes. The strain rate, strain, and stress histories in the specimen are calculated according to the one-dimensional wave analysis [27] using the recorded bar-surface strain signals, as follows:

$$\dot{\varepsilon}(t) = \frac{C_0}{L_s}[\varepsilon_i(t) - \varepsilon_r(t) - \varepsilon_t(t)] \tag{2.6}$$

$$\varepsilon(t) = \int_0^T \dot{\varepsilon}(t)dt = \frac{C_0}{L_s}\int_0^T [\varepsilon_i(t) - \varepsilon_r(t) - \varepsilon_t(t)]dt \tag{2.7}$$

$$\sigma(t) = \frac{A_0}{2A_s}E_0[\varepsilon_i(t) + \varepsilon_r(t) + \varepsilon_t(t)] \tag{2.8}$$

where L_s is the length of the sample, ε_i (t), ε_r (t) and ε_t (t) represent, respectively, the incident, reflected and transmitted strain histories. A_0 and A_s are the cross sectional area of bars and specimen; E_0 and C_0 are Young's modulus and elastic wave speed of the material of the bars.

The results obtained from the SHPB experiments are considered valid only when the sample is in dynamic equilibrium conditions. In this case:

$$\varepsilon_i(t) + \varepsilon_r(t) = \varepsilon_t(t) \tag{2.9}$$

Adopting this equivalence, eqs. (2.6), (2.7) and (2.8) can be simplified as:

$$\dot{\varepsilon}(t) = -2\frac{C_0}{L_s}\varepsilon_r(t) \tag{2.10}$$

$$\varepsilon(t) = -2\frac{C_0}{L_s}\int_0^T \varepsilon_r(t)dt \tag{2.11}$$

$$\sigma(t) = \frac{A_0}{A_s}E_0\varepsilon_t(t) \tag{2.12}$$

Generally, the achievement of constant strain rate and dynamic equilibrium conditions are enhanced by reducing the length of the sample. However, a too short

specimen might introduce uncertainties in the homogeneity of granular media. Another approach for the improvement of the dynamic equilibrium conditions relies on the adoption of pulse-shaping techniques.

2.3.1.2 Pulse shaping

In an ideal SHB test, the sample should be in a dynamic stress equilibrium and deform at a nearly constant rate of strain over most of the duration of the experiment [29]. However, materials like sand are highly discontinuous media, characterised by very low wave propagation speed [31]. When the stress wave propagation speed is low and the loading rate is very high, dynamic equilibrium conditions may not be achieved during the duration of the test. The achievement of a slowly rising incident pulse (Figure 2.4) would minimise the dispersion, allow for the achievement of dynamic stress equilibrium within the sample and enhance the strain rate constancy during the tests [32, 33, 34, 35].

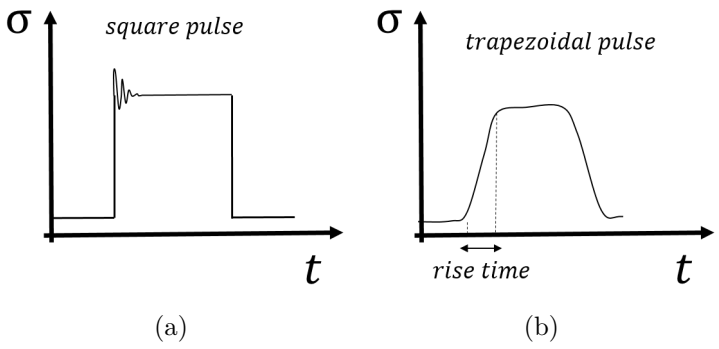


Figure 2.4: Rise time and shape of the incident pulse; (a) no pulse-shaper, (b) with pulse-shaper

For this last reason, over the years, the original SHPB setup underwent many changes and improvements, aiming to extend its range of applications to all those materials characterised by low wave propagation speed. Christensen et al. [36], for instance, used strikers with truncated cone to shape the incident wave. In other cases, strikers with hemispherical tips (with a large radius) were adopted to shape the incident pulse [33]. A more complex technique relies on the adoption of a third

low-strength bar mounted in front of the incident bar [37]. However, the most widely adopted method to facilitate dynamic equilibrium consists in interposing a sacrificial, highly deformable material between projectile and input bar [32, 38, 39]. During the impact, the deformation of the sacrificial material shapes the incident stress wave, modifying its rising time. Typical materials used for this purpose are: copper, brass, aluminium, plexiglass, paper, cardboard [32, 40]. However, one drawback of this method is the substantial reduction of the maximum achievable strain rate (at low strains) as a consequence of the increment in the rise time of the incident stress wave. Therefore, the choice of the optimal pulse-shaper for granular materials is a trade-off between improvement of dynamic equilibrium conditions and achievement of the highest possible strain rate.

2.3.1.3 Effect of confining pressure, initial consolidation state and moisture content on the high strain rate behaviour of sand

The dynamic behaviour of granular materials has been sporadically investigated in the last decades because of its complex nature and the limited available experimental techniques. The mechanical behaviour of sand is strongly influenced by many parameters such as initial consolidation state, confining pressure, moisture content, strain rate, intergranular friction and grain shape [10]. A comprehensive review of the most relevant high strain rate results on sand and experimental techniques is presented in [41].

Most of the existing studies attempted to address the behaviour of different granular materials without properly controlling all the parameters involved in the process. Therefore, these publications mostly provided information on the overall behaviour of certain types of sand rather than the results of systematic parametric studies aimed at understanding the effects of each key parameter and their combination upon the mechanical response of granular media.

The current literature primarily addresses the mechanical response of dry sand specimens within *rigid containers* subjected to impact loading, using conventional

SHPB [42, 43, 44]. Rigid containers provide quasi-uniaxial strain conditions, whilst the adoption of softer lateral confinements would allow for higher radial strain, resulting in quasi-uniaxial stress conditions. The study of the effects of the confinement generally relies on high rate triaxial tests [45, 46] or on the adoption of more compliant, semi-rigid containers (made of aluminium, brass or PMMA) [47, 46]. In particular, [47] offers a detailed study of the compressive response of dry sand by adopting a modified SHPB. This work showed the effects of two initial consolidation states, of the strain rate and of the type of confinement on the mechanical response of one specific kind of sand. The adoption of higher confinement pressures and consolidation states induced stiffer mechanical responses due to the increased frictional resistance, whilst the strain rate has been proved to have negligible effect on the behaviour of granular materials. In all cases the confining pressure is only marginally reduced, thus investigating a relatively narrow range of confining conditions. As a result, the response of nearly-unconfined sand has not been investigated much. Only Pierce [48] tried to innovate the use of confining pressure in SHPB by placing the samples in a deformable membrane submerged in pressurised water.

The effect of moisture content has been also investigated. Felice et al. [49] conducted experiments, by using a classical SHPB, on wet clayey sand, varying water contents, dimensions of the samples and loading rates. Later on, Vereyra et al. [50] showed the effect of moisture on the stress-strain behaviour of three different kinds of sand, at different strain rates, by means of a conventional SHPB. Only recently, Martin et al. [46] and Barr et al. [51] presented a detailed study of the moisture effects on the high strain rate behaviour of sand carrying out an experimental campaign on a modified SHPB. They all showed that the response of wet sand under high strain rates of loading is basically undrained, even when drainage is permitted. They also proved that partially saturated samples are more compliant than dry sand and that their stiffness decreases with increasing saturation. This behaviour is explained by the reduction of friction between grains and with the boundaries due to water. At

high saturation levels the response is essentially governed by the fluid that completely fills the interstitial voids, producing a lock-up of the mechanical response. Nevertheless, the reviewed literature did not provide detailed information on the influence of initial consolidation state, grains morphology, mineralogy and confining pressure on the high rate behaviour of partially saturated granular media. Moreover, it has been observed that the results found in literature are mainly qualitative and that the data available do not provide enough information for the development of physically based macroscopic rate dependent constitutive models.

Attention should be also drawn to the effect of grain crushing on the dynamic response of granular materials. This factor has been rarely investigated in literature and it has been generally estimated by means of *post-mortem sieving* analysis. Farr et al. [52] reported the effect of dynamic loading on the fracture of grains during SHPB compression tests. They proved that, at given initial void ratio, the rate of particles breakage reduces with the loading rate because of the time-dependent nature of particle crushing. However, it is worth noting that the time-dependent nature of grains fracture should be dependent upon the granulometry and mineralogy of the particles, factors that have not yet been addressed in the literature.

2.3.2 Strain rate dependent behaviour of sand

Another important aspect to consider for the correct characterisation of granular materials is the variation of their mechanical behaviour with the speed at which the load is applied, also known as *rate effect*.

The main difference between quasi-static and high rate tests is in the way the sand fails. In slow tests, shear bands appear and the sand rearranges itself during failure. At higher rates (HR) of deformation, instead, the sand keeps flowing throughout the entire test in the form of viscous flow [41]. These differences can be better explained by looking at the two governing mechanisms happening during the uniaxial compression of granular materials: particle crushing and rearrangement of particles (as the particle

sliding is strongly affected by the inter-granular friction). As a matter of fact, both grain fracture and inter-granular friction are sensitive to the rate of application of the axial load.

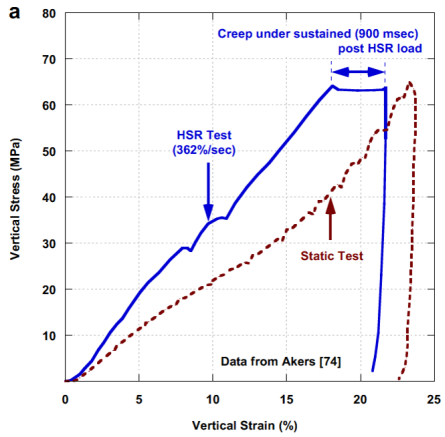


Figure 2.5: Comparison of the stress-strain curve of sand in uniaxial compression at low and high strain rates [53]

Several authors [53, 54, 55, 56] measured a stiffer mechanical response (higher confined modulus) when testing granular materials at higher strain rates (Figure 2.5).

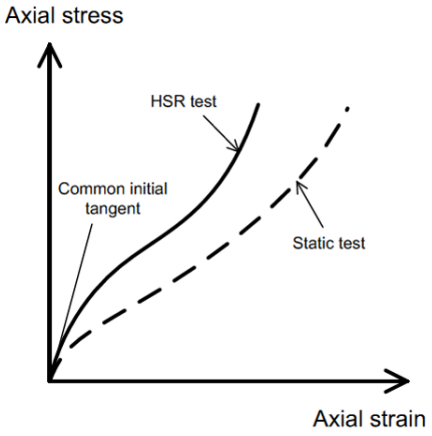


Figure 2.6: Schematic representation of the effect of the strain rate on the stress-strain curve of sand during uniaxial compression (taken from Whitman et al. [57])

Figure 2.6 shows a schematic representation of the effect of the rate of deformation on the mechanical response. At very low strains (less than 1%), the static and HR

responses have a similar stiffness. At higher strains, HR exhibit a higher stiffness than static tests as the particles have less time to rearrange themselves during the application of the load. Moreover, at high stress levels and HR, there should also be less particle breakage, as it is a time-consuming phenomenon.

Nevertheless, other authors found a less significant - almost negligible - effect of the strain rate on the mechanical response of sand [58, 59].

These controversial results can be explained in the considerable scatter in the experimental data due either to the variation in the test conditions (e.g. difference in initial consolidation state, mineralogy, grain shapes, etc.) or to the incorrect choice of the dimensions of the sample that, if smaller then the RVE, fail to represent the integral response of the tested granular media (see Section 2.4 for further discussion). For example, Farr [60] showed that the presence of fines in sand, which can fill interstitial voids, reduces drastically the rate effects. Song et al.[47] and Kabir et al.[45] reported insignificant strain rate effect on the stress-strain curve of sand, for stress magnitude of 200 MPa. Despite this observation, post-mortem analysis reported a noticeable decrease in the number of broken particles, confirming the time-dependency of the grain fracture process. The concurrent presence of time-dependent grain crushing and time-independent stress-strain curves might mean a reduced effect of the grain crushing on the overall mechanical response of sand at high strain rate.

Therefore, these limited and sometimes controversial observations hinder the drawing of any definite conclusion on the strain-rate dependency. There is, hence, a clear need for further research in this area.

2.4 Representative Volume Element of granular materials

A representative length scale is one of the first considerations when characterising and simulating the behaviour of solid materials subjected to mechanical loading. When considered macroscopically, some materials appear homogeneous. However, at

a smaller length scale, it is often possible to identify diffused or discrete discontinuities, associated with the material's heterogeneous micro- or nano-structure corresponding to voids, cracks, grains or crystals, molecules, dislocations, atoms. It is well known that every macroscopic property of an intrinsically heterogeneous and discontinuous medium is the consequence of its microscopic structure [10]. Modelling an apparently homogeneous material without taking into account its structure at the smaller scale would yield inaccurate results, unless its behaviour is comprehensively characterised experimentally at the larger scale. Granular materials are highly heterogeneous assemblies whose response to mechanical loading is strongly affected by the distribution of grain sizes and shapes, as well as the consolidation state, moisture content, surface roughness, inter-particles interactions and several other parameters [41, 61, 62]. At certain larger scales, even highly heterogeneous and discontinuous assemblies - such as powders, sands and gravels - can exhibit homogeneous behaviour, which can be modelled and experimentally characterised by using equivalent continuum mechanics approaches. This poses a requirement upon the smallest Representative Volume Element (RVE) of materials and loading conditions under consideration. Several definitions of RVE are available in literature. For example, [63] defines the RVE as the volume representing the entire system and its heterogeneity, including its regions of disorder. In [64], the RVE is defined as the volume used to determine the corresponding effective properties of a given material to be adopted in a homogenised macroscopic model. Therefore, the dimensions of the representative volume element should be large enough to contain statistically representative information about its microstructure while describing the behaviour of the macroscopic body. When the sample is smaller than the RVE, the measurements of any physical property start to vary thus resulting in uncertainty of the obtained experimental results. Physical and geometric properties such as density, particle size distribution, and void ratio or porosity are often used to determine the RVE [65, 66, 67]. In other cases, mechanical parameters such as elastic modulus, shear modulus, stress fluctuations are taken into

account [68, 69, 70].

No information is available in literature about the relationship between RVE of granular materials and sample sizes to be used in experiments at elevated strain rates such that the response to rapidly applied loading can be successfully characterised ensuring dynamic equilibrium. The choice of a particular type of sand unequivocally defines the *nature* of the material (i.e. size distribution, grain shape and moisture content, as explained in Section 2.2). Therefore, only the effect of the initial consolidation state (i.e. *state* of the material), which affects considerably the dynamic mechanical response of granular materials [61, 62], needs to be defined. In fact, the very same granular medium, if subjected to external loading without controlling its initial consolidation state, could provide very different results, similarly to what would happen when testing different materials. Therefore, the initial void ratio (e) should be considered as the key control state parameter for obtaining the RVE that can be adopted in high strain rate compression tests using the Split Hopkinson Pressure Bar. However, no evidence of similar studies has been found in literature.

Most of the experimental work on the mechanical characterisation of granular material does not take into account the definition of the RVE. The estimation of the dimensions of the sample to be used in SHPB tests is often based on conventions or obtained by trial and error procedures. Kabir et al. [45] presents an example of preliminary definition of the sample dimensions using high-speed cameras to define the smallest volume characterised by uniform deformation. However, no check of the correct representation of the initial consolidation state of the sample is conducted. Moreover, according to the existing literature, it is common practice to adopt granular samples with a very short thickness during SHPB experiments [41, 71, 72] to obtain higher strain rates and enhance the dynamic equilibrium within the sample, which is otherwise difficult to obtain because of the low wave propagation speed in granular media [10, 31, 73]. For instance, references [49, 74] use specimens with a slenderness L/D lower than 0.2 to carry out Hopkinson pressure bar experiments on saturated

sand. Also [50, 71, 75] adopt samples with very low L/D values.

Therefore, further studies on the definition of the RVE for granular materials are clearly justified by the aforementioned observations.

2.5 Non Destructive Techniques applied to granular media

As already mentioned in the previous sections, conventional post-mortem destructive methods have been extensively used to study the influence of grains fracture on the mechanical behaviour of granular materials [76, 77, 78, 79, 80, 81]. Nonetheless, the aforementioned techniques cannot give real time information on the studied phenomena (e.g. identification of the spatial and time location of the cracking events) and they are not able to unequivocally capture and reveal the micro-processes taking place during fracture.

More information on the micro-phenomena happening during grain fracturing can be obtained by employing non-destructive 3D imaging techniques such as microscopy, X-ray or neutron tomography imaging [82, 83, 84, 85]. These methods offer detailed results in terms of spatial resolution, but are characterised by reduced speculation windows (few square centimetres) and limited time resolution (even though they can reach acquisition rates of several tens of Hertz). Such limits reduce their adoption for large-scale or dynamic problems. Moreover, because of their complexity, these techniques are characterised by very high installation and testing costs and time-demanding analysis. Imaging techniques have been widely adopted for visual post-mortem inspection and characterisation of samples [84, 85, 86]. Only more recently, despite their limits, they have been employed for real-time filming of cracking phenomena [83, 87, 88, 89].

2.5.1 Acoustic Emission

Another existing non-intrusive experimental technique, based on the qualitative and quantitative evaluation of the sounds emitted during the application of an external load, is the Acoustic Emission technique (AE). The AE are transient elastic waves (audible and sub-audible sounds), resulting from the release of strain energy following irreversible microstructural changes in the material, such as fracture processes, crack jumps, strain localisation, leaks, friction, dislocations, etc. [90]. This technique can be defined as *passive* because it usually identifies defects while they develop during the tests. The waves generated within the whole volume of interest travel to the free surface, where contact piezoelectric sensors capture them. The sensors, coupled to the surface using special couplant (gel or glue), produce a voltage/time output that is recorded and analysed. AE has been successfully applied to investigate the fracture mechanics of rocks [91, 92], concrete [93], composites [94], soils and sand [86, 95], as well as friction and wear phenomena [96]. It has also been adopted to deliver useful information on size and location of cracks within brittle materials [97]. Recently, AE has also been applied in the study of fragmentation processes in single sand grains [98]. Differently from conventional methods, AE can detect events happening at not only failure stage (catastrophic failure) but also micro *noises* due to the initiation and development of cracks. However, with AE being simultaneously sensible to fracture and sliding/rotation of the grains [90, 98, 99, 100], it is extremely difficult to tell about the nature of the recorded events. Various works showed the need for additional post-processing (filtering or frequency analysis) of the collected data to infer the nature of each emission [90, 99]. The AE technique presents some drawbacks when used to study grain fracture mechanisms. Firstly, the smallest commercially available probe is generally much bigger than the size of a typical granular Representative Volume Element. This implies that the sensor needs to be mounted on the testing machine with obvious problems in case of miniaturised in-situ devices (i.e. the probe cannot fit into the testing apparatus). Furthermore, the measured

signal is averaged depending on the size of the sensor. This leads to a loss of accuracy and sensitivity when it comes to studying the fracture at grain level.

For all the aforementioned reasons, the identification of alternative NDTs would be particularly beneficial to the geo-mechanical community.

2.6 Numerical methods for simulating granular media

The noteworthy complexity of the experimental approach, in terms of reproducibility of the results, control of boundary conditions, isolation and analysis of the relevant parameters affecting the mechanical behaviour of granular materials, is overcome by the introduction of numerical methods. In contrast to experiments, numerical modelling can determine the influence of each key physical parameter on the response of granular media, offering a deeper insight into their mechanical behaviour.

Nevertheless, the simulation of physical problems requires the introduction of idealisations and simplifications of the problem (e.g. geometry, boundary conditions, loading conditions, etc.) that, in turn, affect the correctness of the results. Depending on the nature and on the level of desired simplification of the problem, numerical methods can be classified into continuous and discontinuous methods.

2.6.1 Continuum and discontinuous methods

Discontinuous materials when observed at relatively large scales (bigger than the correspondent RVE) can be treated as a continuum. This happens when discontinuities (e.g. particles, voids, dislocations) have sizes much smaller than the characteristic length of the problem to be solved. Continuous media can be modelled recurring to rheological constitutive laws that define the response of a material, at a given length scale, subjected to external constraints [101]. The constitutive laws, together with *a priori* physical balance principles (e.g. conservation of mass, energy, preservation of momentum) form a set of partial differential or integral governing equations that

are, generally, solved numerically. One of the most commonly adopted method is the Finite Element Method (FEM). The correct prediction of the system behaviour by means of FEM requires the calibration of the chosen constitutive model and the definition of many mechanical parameters such as Lame' constants, friction and dilatancy angles, and so on.

The FEM has been extensively used to predict the behaviour of granular materials and many constitutive laws have been proposed [21, 102, 103]. However, considerable approximation in the results are introduced when the local behaviour of grains (fracture of grains and inter-grain friction) is ignored or when simulating large material deformations [104]. Adaptive meshing techniques can be employed to solve the latter, but they still fail to describe inhomogeneities (local variation of the packing density and single grain phenomena). For solving problems of Mechanics of Discontinua [105], several alternative numerical methods have been developed in the last decades.

2.6.2 Discrete Element Method

In 1970s, Cundall and Strack [106] developed a numerical tool alternative to continuum methods, called Distinct/Discrete Element Method (DEM), to solve problems of granular and rock mechanics.

DEM is a family of numerical techniques that solves mechanics problems exhibiting large discontinuous material and geometrical behaviour.

DEM explicitly model each discrete particle of an assembly and, as a result of their interaction through contact, it computes the kinematics of the bodies by solving Newton's equations of motion. The particles were originally represented by *rigid* disks and spheres, thus simplifying the mathematical representation of the contact mechanics. Recently, more complex geometries (cluster of particles, eroded spheres, polyhedrons, etc.) have been used [107, 108, 109]. However, the adoption of complex shapes leads to the employment of more sophisticated and computational expensive contact interaction algorithms. This issue has been partially solved thanks to the

advancements in computing power. Further discussion on the shape representation will be presented in Section 2.7.

Some of the advantages of DEM over FEM are: the accurate representation of microscopic features of granular media (grains shapes and sizes) and of the soil fabric (consolidation state, variation in packing density), the identification of the effective stress between grains and the ability to capture the behaviour of granular media without recurring to complex constitutive models. On the other hand, DEM simulations could require significant computational power, depending on the adopted contact models, size of the problem (number of particles in the domain) and simulation time.

2.6.2.1 Contact mechanics and time integration schemes

By convention, a DEM algorithm involves three main stages:

1. Contact detection
2. Contact interaction or resolution (calculation of contact tractions and forces)
3. Time integration scheme to solve Newton's second law equations.

Contact detection or geometric intersection search is a preparation step to the solution of the contact mechanics used to find whether two or more particles are in contact. Once the contact is detected, the relative distance and velocities are computed. A review of contact detection algorithms is provided by Kockara et al. [110].

The partial geometrical overlap between contacting bodies is used to evaluate the contact forces acting on the bodies in the *contact resolution* phase. One method to evaluate these induced tractions is based on the penalty approach [111]. It is able to model the correct contact stiffness and to capture the wave propagation within the granular media. This approach is also called *soft body* approach and it assumes that the small allowed overlap reproduces the deformation happening at the contact point.

Various contact force models are available in literature [112] to simulate both normal and tangential contact. In this thesis, the Hertz-Mindlin contact law will be extensively used. In the normal direction, a non linear Spring-Dashpot model based on Hertz law is used to model the interaction force.

Given two particles of, respectively, radii R_1 and R_2, overlapping by a distance δ, with Young's modulus E_1 and E_2 and Poisson's ratio ν_1 and ν_2, an equivalent radius R^* and elastic modulus E^* can be computed as follows

$$\frac{1}{E^*} = \frac{1-\nu_1^2}{E_1} + \frac{1-\nu_2^2}{E_2} \tag{2.13}$$

$$\frac{1}{R^*} = \frac{1}{R_1} + \frac{1}{R_2} \tag{2.14}$$

The normal contact force is the sum of an elastic F_{ne} and inelastic F_{nd} (dissipative) term

$$F_n = F_{ne} + F_{nd} \tag{2.15}$$

Knowing the normal overlap δ_n between particles, the elastic component of the force is given by

$$F_{ne} = \frac{4}{3} E^* \sqrt{R^*} \delta_n^{3/2} \tag{2.16}$$

and the dissipative part is

$$F_{nd} \propto \beta_n V_n^{rel} \tag{2.17}$$

where V_n^{rel} represents the relative normal velocity and β_n the normal damping coefficient.

The tangential component of the contact force F_t can be represented as a serial non-linear spring with a dashpot and slider rheological model and, as for the normal component, it can be divided into an elastic and dissipative part

$$F_t = F_{te} + F_{td} \tag{2.18}$$

The elastic part F_{te} represents a linear relationship between force and incremental relative tangential displacement Δ_t

$$F_{te} = -S_t \Delta_t \tag{2.19}$$

The tangential stiffness $S_t = 8G^* \sqrt{R^* \delta_n}$ is a function of the equivalent shear modulus G^*, which is defined similarly to eq. (2.13) and it depends upon the normal overlap. The dissipative part of the tangential force is differently defined depending on whether sliding occurs. If no sliding happens (i.e. $F_t < \mu F_n$), the dissipative component of the force will be

$$F_{td} \propto \beta_t V_t^{rel} \tag{2.20}$$

Otherwise, the tangential force will be limited by

$$F_t = \mu F_n \tag{2.21}$$

Once all forces and moments applied to the i-th particle are known, the translation and rotational motion can be evaluated by solving Newton's equations

$$m_i \ddot{\mathbf{x}}_\mathbf{i} = m_i \mathbf{g} + \sum_{j=1}^{N} \mathbf{f}^\mathbf{n}_\mathbf{i,j} \tag{2.22}$$

and

$$I_i \dot{\theta}_\mathbf{i} = \sum_{j=1}^{N} \mathbf{f}^\mathbf{t}_\mathbf{i,j} \mathbf{r}_\mathbf{i,j} \tag{2.23}$$

where N is the total number of particles, m_i and I_i are mass and moment of inertia of the i-th particle, $\ddot{\mathbf{x}}_\mathbf{i}$ and $\dot{\theta}_\mathbf{i}$ are the linear and angular acceleration, $\mathbf{g}$ is the gravity, $\mathbf{f}^\mathbf{n}_\mathbf{i,j}$ and $\mathbf{f}^\mathbf{t}_\mathbf{i,j}$ are the normal and tangential contact forces and $\mathbf{r}_\mathbf{i,j}$ is the distance between point of application of the tangential force and centre of the particle.

This set of equations are integrated in time by using explicit schemes [113], which are *conditionally stable*. Therefore, every time step in the simulation has to be lower than a fixed threshold called *critical time step* [114], which is function of the highest frequency in the system and its damping.

2.6.2.2 Simulation of grain comminution in DEM

As Section 2.3 showed, comminution (reduction in size of solid materials obtained by particle breakage) has a striking effect on the mechanical response of granular materials. Therefore, it has to be also captured in the numerical simulations of granular materials subjected to impact loading. However, the standard DEM does not allow crushing since it relies upon the adoption of rigid particles that cannot neither deform nor break.

Over the years, different methods have been proposed to model the fracture of particles in DEM simulations. A detailed review can be found in [115]. It also showed several typical applications and proved the improvements obtained by introducing grain comminution with respect to standard DEM simulations. The methods to introduce comminution in DEM simulations can be classified in two main groups. The first class uses *grain clusters* to model the single particle, with bond strength proportional to the fracture stress [116]. Since every particle has to be modelled as an agglomerate of many smaller spheres, this method becomes impractical when simulating large domains [117] and, additionally, it cannot reproduce the effect of particle size on particle crushing. The second group of methods, called *multigenerational approach*, replaces each failed particle with a new generation of smaller grains. This is done only for those particles that reach a given stress threshold (failure stress), thus drastically reducing its computational cost when compared against the first method. All the aforementioned reasons led to a wider adoption of the second approach, initially in two dimensions [118] and, later on, in three dimensions [119, 120], which can *successfully reproduce the mechanical behaviour of granular materials subjected*

to different loading conditions. Nevertheless, the adoption of the multigenerational approach requires several further modelling assumptions, which prompted the generation of many variations of the very same numerical method. Among these, the choice of the particle spawning procedure is of utmost importance. It establishes the relationship between failed particle and newly added smaller particles (daughters) in terms of their number and relative position. Furthermore, this choice strongly affects the mass conservation between generations, as a new generation of daughters cannot fit into the volume of the failed particle: the spatial volume of the daughter particles together with the void between them is larger than the volume of the mother particle [117]. Even in this case, two main modelling strategies have been adopted. On one hand, a strict mass conservation is enforced by substituting the failed particle with a cluster of overlapping spheres. This strategy is not without problems: forcing the overlap between particles generates undesirable local pressure spikes that, in turn, badly affect the contact force computation and the resulting particle's velocity. On the other hand, a broken particle is replaced with a cluster of non-overlapping spheres [117]. In this case, no fictitious contact forces are generated but the mass conservation is not entirely fulfilled. In [121], in order to reduce the mass loss in 2D problems, some of the remainder fragments were placed in the free voids surrounding the mother particle. However, filling the nearby voids requires a time-consuming local void search that drastically reduces the effectiveness of such method. In some engineering applications, where mass control and mass flow rates are key parameters (dynamic problems, impact on granular media, explosions, etc.), mass conservation is very important and none of the two multigenerational approaches presented could be applied. Therefore, further studies would be required to extend the range of applicability of multigenerational method to the simulation of impact phenomena.

2.7 Generation of numerical discrete statistically representative samples

Many natural (powders, silts, sands and gravels) and artificial materials (e.g. sintered ceramics, foams) consist of aggregates of particles showing different sizes and shapes. The packing of particles is, therefore, of utmost significance in further understanding the behaviour of granular materials and in improving industrial procedures, such as sedimentation, compactioning and sintering [122, 123, 124]. Even the atomic structure of several materials (e.g. amorphous metals and semiconductors, simple liquids, glasses and "doped" materials [125, 126, 127, 128, 129]) are studied creating statistically representative packings of hard particles.

Despite the fact that all the macroscopic properties of granular materials are characterised by the strong influence of both sizes and shapes of the grains [130, 131], very often these two effects are analysed separately. The effect of the grain size distribution is reproduced by modelling polydisperse assemblies of perfectly *spherical particles*. The shapes of the grains are, instead, generally taken into account by either grouping [132] or eroding spheres [133].

2.7.1 Spherical particles

The packing of spherical particles – and in particular the definition of the densest possible arrangement in $3D$ – has been diffusively studied with analytical [134, 135], experimental [123, 126] and numerical [136, 137, 138] approaches.

For two-dimensional problems, the maximum admissible relative density of monodisperse packing (packing fraction) has been defined analytically in ancient times, and it was found to be equal to 0.6 (i.e. void ratio corresponding to 0.67). For three dimensional assemblies, instead, the problem of the definition of the densest agglomerate of spheres was firstly assessed by Kepler in 1611, with the identification of the face centered cubic (FCC) arrangement of spheres as the densest monodisperse assembly possible (i.e. "Kepler conjecture" [139]). Several decades later, Gauss [134]

and C. Hales [135] proved the validity of the Kepler's theory, defining the maximum relative density of monodisperse aggregates equal to 0.74 (i.e. minimum void ratio of 0.35). For polydisperse assemblies, the packing density is function of the particle size distribution and it appears that there is no analytical estimation of the closest packing fraction as a function of the distribution of radii.

The experimental approach, instead, allows for the measurement of the properties of assemblies consisting of spheres with any possible distribution of radii. However, they present significant incertitude in the estimation of some parameters, such as the number of contacts, void ratio or density in an assembly. Experimental measurement of the packing fraction of monodisperse systems are presented in [124, 140], whilst [141] shows results on polydisperse agglomerates.

The numerical approach finally grants the possibility to understand the role of key physical parameters (e.g. density, void ratio, coordination number), overcoming the extreme complexity of the experimental tests in spite of a simplified interpretation and modelling of the reality.

Computational methods, capable of generating statistically representative particle assemblies, are the key for successful simulations of experimentally observed and quantified behaviour of granular materials. In the last decades several numerical algorithms have been developed to simulate the packing mechanism and the samples generation [1]. These can be classified into *mechanical* and *geometrical* algorithms. The mechanical methods consist in solving the initial boundary-value mechanical problem (IBVP) for the entire assembly, hence mimicking the physical behaviour of the particles. The geometrical methods, instead, create assemblies with defined properties in terms of packing density and given dimensions. The geometrical methods generally do not reproduce physically stable (e.g. in mechanical equilibrium) assemblies of particles but they have the advantage of a sensibly lower computational cost than the mechanical ones. Typically, the computational time required by geometrical algorithms is about three orders of magnitude smaller than gravitational deposition

using micro-mechanical approaches [1].

In the following sections, the two categories are described and further classified.

2.7.1.1 Geometrical packing

The geometrical methods place particles inside a given domain using geometric assumptions. They usually require a computational time sensibly lower than mechanical methods. The geometrical methods can be divided in two sub-categories. One is based on the pre-assignation of the distribution of radii (varying the number of spheres in the assembly), whilst the second one is based on the assignation of the total number of particles to be placed in the domain (thus varying the radii distribution to fit them into the assembly).

In the first case, radii are statistically representative of a possible range of particle sizes. Examples of methods falling under this category are: the membrane [142] and the ballistic (or sequential) methods [141, 143, 144].

The membrane approach randomly places particles within a given volume, ensuring no overlap. Their positions are readjusted when an overlap between particles is detected. The process ends when it is not possible, after a given number of attempts, to find a new position without overlaps. This method ensures full control over the size distribution but, since it does not ensure contact between particles, it cannot neither achieve the highest packing densities nor uniform spatial density distribution.

Ballistic or sequential methods add each particle to a pre-existing substrate, one after another, without overlaps. An example of sequential algorithm of particular interest for the topic of the current research is the one proposed by Lo et al. [144]. The method assigns the initial position of each new sphere as tangent to a pre-existing particle, allowing, then, for the descending rotation of such sphere (with different mechanisms) along preferred directions, until it reaches the lowest possible position.

Examples of methods with no pre-assignment of the distribution of radii are the Lily-Pond method [145], the concurrent (or collective) methods [146], and the

Delaunay triangulation based methods [147].

The Lily-Pond method fixes the centres of the particles and then increases the radius of each particle – with constant growth rate – until the contact of two neighbouring particles is detected. The concurrent or collective methods, instead, place all the particles at the same time within the given domain. These algorithms start with a random distribution of particles of zero size (points), then – for each point – a sphere is allocated with a radius r equal to half of the distance to the nearest neighbour. The process is repeated until all the points are replaced with spheres of finite radii. The method presented in [147], instead, is based on the generation of background meshes, using the Delaunay tessellation, that are filled with spheres, whose radii depend directly on the mesh size. In this case, each sphere is assigned by solving numerically (with geometric inversion) a five spheres tangency problem, represented by a system of four equations. Those approaches, as the Lily-Pond methods and the concurrent methods, ensure limited control over the size distribution of the particles.

Geometrical methods, as opposed to the mechanical ones, are inadequate to reproduce the initial stress state in granular media and to generate systems in static or dynamic physical equilibrium as they do not take into account the history of the system.

2.7.1.2 Mechanical packing

The mechanical methods assemble pre-assigned particles within a confined domain by simulating physical phenomena, such as the effect of electro-magnetic or gravitational fields (e.g. DEM [148, 149], Molecular Dynamics (MD) [150]). They are generally classified in:

- Pouring methods (first two pictures from left in Figure 2.7)

- Sedimentation or collective methods (last two pictures from left in Figure 2.7).

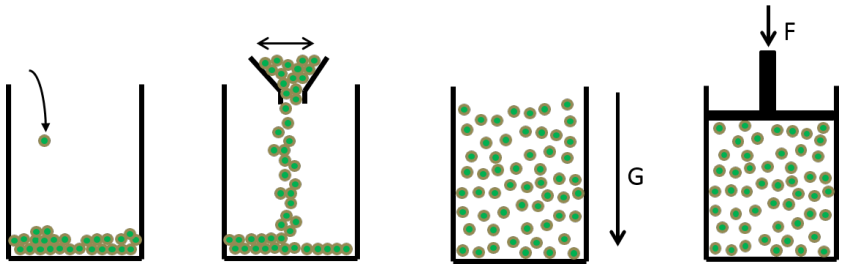


Figure 2.7: Mechanical deposition methods

The pouring methods place particles inside the volume either singularly, with an initial velocity and/or acceleration, or pour them from an initial position, using a funnel or a nozzle and producing a desired mass flow [151]. In the sedimentation or collective method, instead, all the particles are placed a-priori inside the volume and they are compacted by applying gravity or tractions along certain boundaries, or a combination of the two [152].

The literature review conducted so far pinpointed the clear computational advantages of geometrical packing methods with respect to the mechanical ones. Nevertheless, it also identified the lack of geometrical algorithms able to concurrently assign the total number of particles and the size distribution of the desired assembly. This would enable a better control of the properties of the packings by the user, thus improving the representativeness of the numerical samples.

2.7.2 Polyhedral particles

The macroscopic properties of granular assemblies (e.g. void ratio, coordination number, mechanical response) are strongly influenced by the morphology of the grains. Therefore, the generation of statistically representative numerical samples requires the correct modelling, among other things, of the shape of the grains.

Although the challenge of defining representative particle size distributions has been successfully addressed by numerous authors [1, 153], the correct representation of the shape of the particles still presents some challenges.

Most of the approaches developed during the past decades adopt regular shapes,

thus guaranteeing simplicity in the definition of both geometry and contact between grains. However, they are generally scarcely representative of real granular materials. The adopted shapes can be either basic geometrical entities, such as spheres [1], ellipsoids [154], regular polyhedra [155], or a combination of basic geometries (e.g. sphero-cylinders) [156].

More complex and arbitrary shaped geometries can be obtained by assembling [107, 108] or eroding [157] base geometries, such as spheres. Other alternative techniques, able to represent a wide range of shapes with less information, imply the use of superquadrics [158, 159] or the extraction of Fourier descriptors from Fourier spectra available for specific structures [160]. However, the complexity of the shape generation process required by these methods explains their relatively limited adoption.

The adoption of the Voronoi tessellation technique to generate polyhedral grains would provide a compromise between the simplicity of the grains shapes and the computational cost. The Voronoi tessellation divides the space into arbitrarily shaped convex polyhedral cells with planar faces and straight edges that have been proved to fairly represent the microstructures of real materials [161, 162]. Aurenhammer [163] offer a more detailed description of the Voronoi tessellation technique.

The Voronoi tessellation has been proposed in several variants to offer control over the sizes of the grains and the regularity of the packings obtained. This has been achieved by either imposing constraints on the nuclei seeding procedure (e.g. Poisson [164], Hardcore [165], Extended Hardcore [166]) or introducing different definitions of the distance (e.g. Centroidal [167], Laguerre [168]).

Despite the proven ability of the Voronoi technique to generate samples with ad-hoc size distributions and shapes resembling real polyhedral grains, none of the existing methods provide the user with full control over the size distributions of the generated grains. Moreover, they have been sporadically and unsuccessfully used to generate samples with statistically representative shapes.

Additionally, the Voronoi tessellation produces tight packings of polyhedral bodies

that have to be disorderly rearranged to reproduce real granular matter. Whilst several geometrical approaches have been proposed for the packing of spherical particles (Section 2.7.1), the difficulty of introducing geometrical constructions, for arbitrarily shaped particles, has limited the development of methods for the packing of non-spherical particles mainly to mechanical approaches. Also the definition of the initial configuration of mechanical simulations is generally based on sequential position operation that requires the verification of the overlap of each newly added particle with all the pre-deposited particles (e.g. [169]).

2.8 Summary

From the literature review, a number of limitations and open questions have been identified.

From a numerical prospective, there is the need for:

1. the identification of a viable method to reproduce mass-conserving grains comminution in DEM simulations

2. the development of geometrical packing algorithms to create statistically representative assemblies, concurrently assigning size distribution and total number of particles

3. the development of a numerical technique able to provide grains with user-controlled statistically representative shapes

4. the definition of representative volume elements for granular media to be used in experiments and large scale simulations

On the other hand, from an experimental prospective:

1. a comprehensive parametric study aimed at understanding the effects of each key parameter and their combination on the mechanical behaviour of sand, at wider ranges of strain;

2. characterisation of nearly unconfined sand (effect of highly compliant confinements)

3. study of the effect of inter-granular friction and grain crushing during uniaxial compression of sand

4. study of the combined effect of moisture content, grains morphology, mineralogy and consolidation state

5. verification of the rate effect on granular media and influence of microscopic single grains features on it

The above points provided the justification and basis for the new developments presented in the following chapters.

Chapter 3

New three-dimensional geometrical deposition methods for packing spheres based on tangency

The literature review, as reported in Section 2.7.1, showed the lack of methods able to simultaneously assign the number of particles to be placed inside a given volume and their size distribution. The aim of this chapter [1] is to present two new geometrical deposition methods, based on tangency between neighbouring spherical particles, able to fulfil this task. These methods allow for the generation of polydisperse assemblies with *a-priori* assigned distribution of radii whose void ratios and coordination numbers are comparable with the outcomes of the mechanical approaches.

One of the main novelties proposed in this work arises form the implementation of the tangency condition between particles within the two proposed geometrical methods, in which the position of each new sphere is adjusted rotating it randomly around a central one (without any pre-defined preferential direction of rotation).

The first method, named *planar spiral deposition method*, generates layers of particles stacked-up to create $3D$ aggregates. Similar results have been obtained by Feng et al. [170] for the packing of 2D disks imposing a linear, rather than a spiral,

[1] Part of this chapter has been reprinted from the International Journal of Numerical Methods in Engineering, Vol. 104/12, F. De Cola, S. Falco, E. Barbieri, N. Petrinic, "New 3D geometrical deposition methods for efficient packing of spheres based on tangency", 1085-1114, Copyright (2015), with permission from the Wiley and Sons, Inc.. Both planning and implementation of the work were conducted by the first author, with the others in advisory role.

tangential deposition. This method is extremely fast and best suited for assemblies with a reduced particle size variation, whilst it might generate localised voids for polydispersed assemblies with a wide range of radii. Given the shape of the output, it can be used to simulate constant particle flows through funnels or nozzles. In this case, the mass flow rate is adjusted by changing the number of particles placed in each single layer.

The second proposed method, called $3D$-*clew deposition method*, places particles in a three-dimensional manner, tangentially spiralling around the central sphere mimicking a clew of yarn. It is more computationally expensive than the planar spiral method, but it can produce statistically representative packing of polydisperse spheres with arbitrary size distribution of the particles.

Both methods provide accurate predictions in terms of void ratio and coordination number of dense packings as well as a sensible reduction of the computational cost required, in comparison to DEM simulations.

3.1 Planar-spiral deposition method

The underlying principle of the planar-spiral deposition algorithm can be briefly described as:

1. Generation of a set of particles using an arbitrarily assigned distribution of radii;

2. Positioning each particle tangent to two prepositioned ones; thus producing a layer of particles in an outwards anticlockwise spiral manner (Figure 3.1a);

3. Loose stacking the layers to create a $3D$ assembly. The distance between the two neighbouring layers is given by the sum of two largest radii in respective layers, to avoid overlaps between layers (Figure 3.1b).

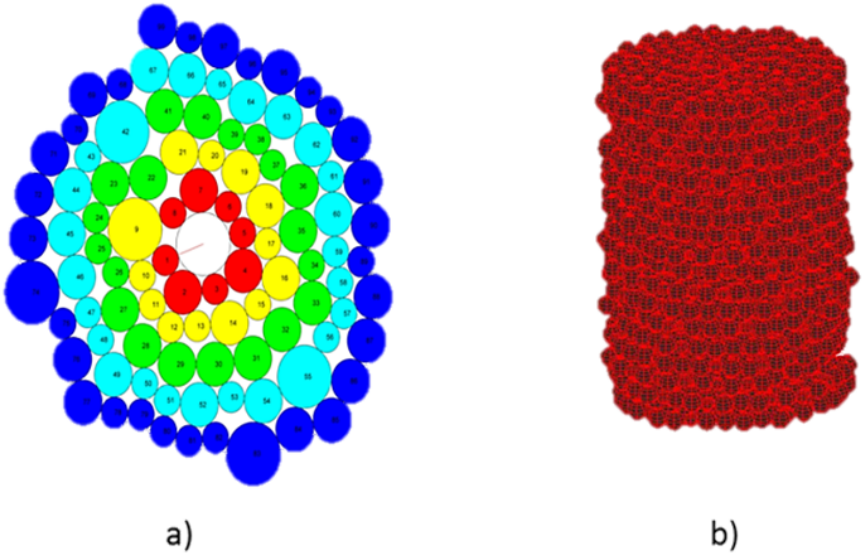


Figure 3.1: Example of the planar deposition algorithm using spheres with three different radii: R_1, $R_2 = 2R_1$, $R_3 = 3R_1$

The flowchart in Figure 3.2 summarises the algorithm for the generation of a single layer. The generic nomenclature $S_{i,L}$ (or $S_{j,L}$) identifies the i^{th} (or j^{th}) particle in the L^{th} ring.

Since the distribution of radii is assigned a-priori and all the centres lay on the same plane (i.e. planar deposition), each particle requires only two additional conditions to be fully defined, such as the tangency with other two pre-positioned particles. Obviously, the tangential approach cannot be applied for the first two circles on each layer, which are placed respectively ($S_{1,1}$) at the origin of the local coordinate system, and ($S_{1,2}$) tangentially to $S_{1,1}$ along a direction, with respect to the x axis, defined by a random initial angle α_1 as represented in Figure 3.3.

The coordinates of the centre of $S_{1,2}$ are expressed in eq. (3.1):

$$\begin{cases} x_{S_{1,2}} = (r_{S_{1,1}} + r_{S_{1,2}})cos(\alpha_1) \\ y_{S_{1,2}} = (r_{S_{1,1}} + r_{S_{1,2}})sin(\alpha_1) \end{cases} \tag{3.1}$$

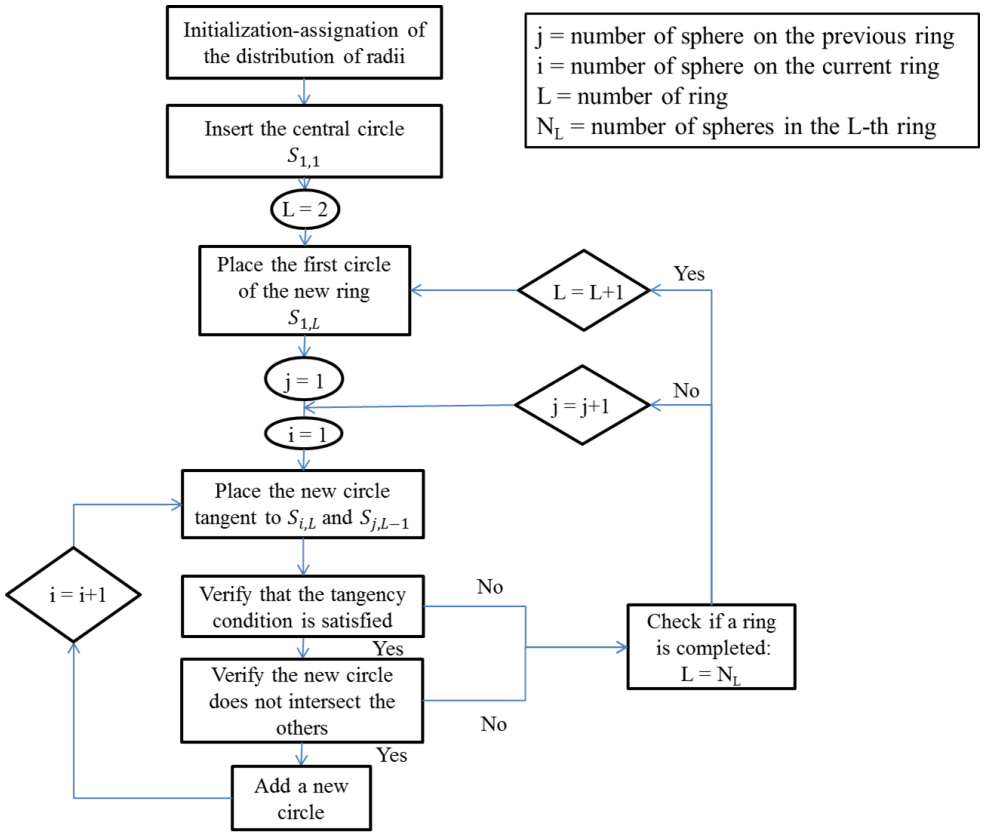


Figure 3.2: Flowchart of the planar deposition algorithm

All other circles on the same ring are placed, in an anticlockwise manner, around the same initial particles until it is not possible to insert an additional one around $S_{1,1}$ without overlapping other existing particles.

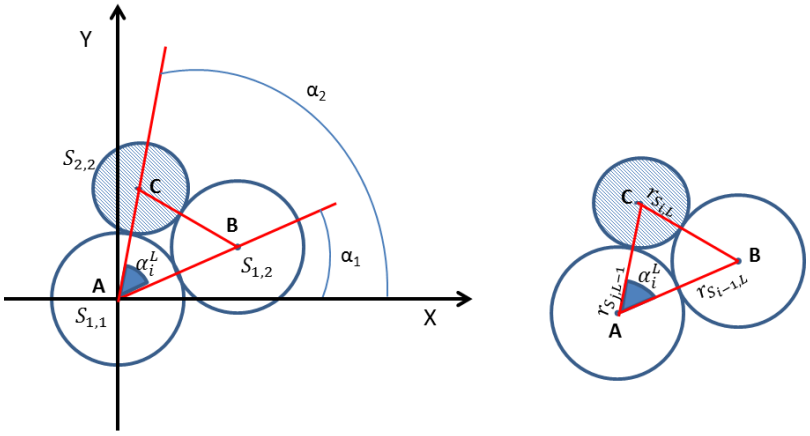


Figure 3.3: Deposition of the second circle on the second layer or positioning of the generic circle $S_{i,L}$ with respect to its neighbours

The position of the centre of the new circle $S_{i,L}$, tangent to the previous circle $S_{i-1,L}$ on the same layer and to the j^{th} circle $S_{j,L-1}$ in the previous layer, is defined by the angle α_i^L and by the radii of the three circles involved, as reported in Figure 3.3. The angle is calculated applying the *law of cosines* to the triangle having as vertices the centres of the three circles (ABC in Figure 3.3):

$$BC^2 = AB^2 + AC^2 - 2 \cdot AB \cdot AC \cdot cos\alpha_i^L \tag{3.2}$$

Expressing the edges of the triangle as sum of the radii, we can rewrite eq. (3.2) as:

$$\begin{aligned}(r_{S_{i-1,L}} + r_{S_{i,L}})^2 = (r_{S_{j,L-1}} + r_{S_{i-1,L}})^2 + (r_{S_{j,L-1}} + r_{S_{i,L}})^2 + \\ - 2 \cdot (r_{S_{j,L-1}} + r_{S_{i-1,L}}) \cdot (r_{S_{j,L-1}} + r_{S_{i,L}}) \cdot cos\alpha_i^L\end{aligned} \tag{3.3}$$

After solving the special products and simplifying where possible, the previous equation becomes:

$$\begin{aligned}(r_{S_{j,L-1}} + r_{S_{i-1,L}}) \cdot (r_{S_{j,L-1}} + r_{S_{i,L}}) \cdot cos\alpha_i^L = \\ r^2_{S_{j,L-1}} + r_{S_{j,L-1}} \cdot r_{S_{i-1,L}} + r_{S_{j,L-1}} \cdot r_{S_{i,L}} - r_{S_{i-1,L}} \cdot r_{S_{i,L}}\end{aligned} \tag{3.4}$$

Accordingly

$$cos\alpha_i^L = \frac{r^2_{S_{j,L-1}} + r_{S_{j,L-1}} \cdot r_{S_{i-1,L}} + r_{S_{j,L-1}} \cdot r_{S_{i,L}} - r_{S_{i-1,L}} \cdot r_{S_{i,L}}}{\left(r_{S_{j,L-1}} + r_{S_{i-1,L}}\right) \cdot \left(r_{S_{j,L-1}} + r_{S_{i,L}}\right)} \tag{3.5}$$

Therefore the coordinates of the new centre are:

$$\begin{cases} x_{S_{i,L}} = x_{S_{j,L-1}} + \left(r_{S_{j,L-1}} + r_{S_{i,L}}\right) cos(\alpha_i) \\ y_{S_{i,L}} = y_{S_{j,L-1}} + \left(r_{S_{j,L-1}} + r_{S_{i,L}}\right) sin(\alpha_i) \end{cases} \tag{3.6}$$

where:

$$\alpha_i = \alpha_{i-1} + cos^{-1}\left(cos\alpha_i^L\right) \tag{3.7}$$

The same procedure is applied to place subsequent particles around the central one $S_{j,L-1}$ until a new circle overlaps with an existing one. The presence of overlap indicates the saturation of the central particle (i.e. there is no space to add a new circle around $S_{j,L-1}$), and another circle has to become the new central one. The new central particle can either be the subsequent entity on the ring $L-1$ (i.e. $S_{j+1,L-1}$ as shown in Figure 3.4b), or – in case $S_{j,L-1}$ is the last of the ring $L-1$ – the first particle of the following ring (i.e. $S_{1,L}$, as shown in Figure 3.4a).

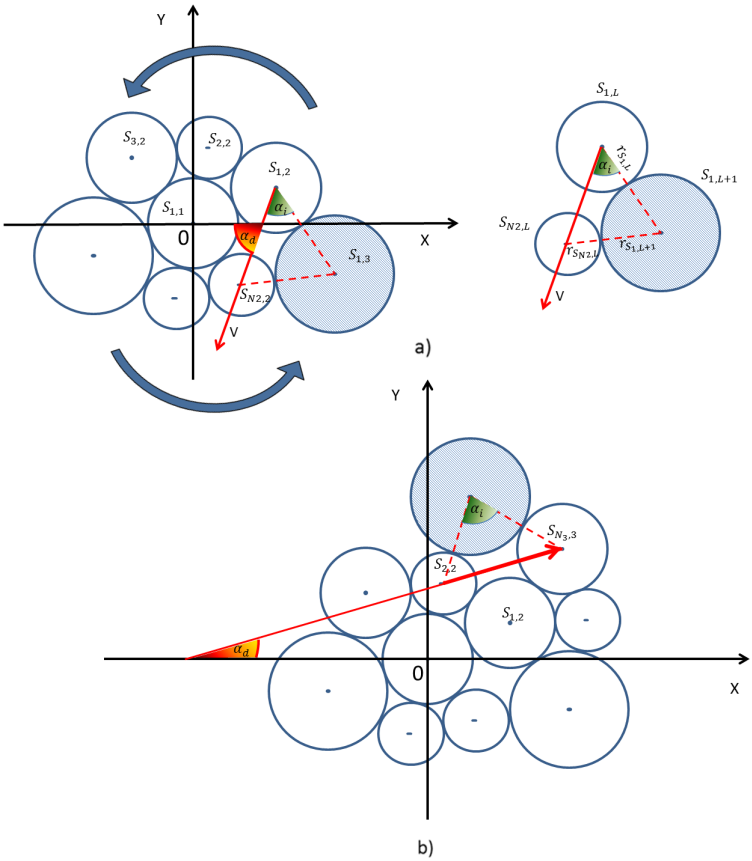


Figure 3.4: Deposition of the first circle of a new ring

The position of the new circle, $S_{1,L+1}$, is defined with respect to the direction of the vector $\mathbf{V}$, connecting the new central and the last added circle (Figure 3.4a). The angle the vector $\mathbf{V}$ forms with the x-axis is defined as:

$$\alpha_d = cos^{-1}\left(\frac{\mathbf{V}\cdot e_x}{|\mathbf{V}|}\right) \tag{3.8}$$

where e_x is the unit vector along the x-axis.

Expressing eq. (3.8) in terms of cartesian coordinates

$$\alpha_d = cos^{-1}\left(\frac{x_{S_{NL,L}} - x_{S_{1,L}}}{|\mathbf{V}|}\right) \tag{3.9}$$

where:

$$|\mathbf{V}| = \sqrt{\left(x_{S_{NL,L}} - x_{S_{1,L}}\right)^2 + \left(y_{S_{NL,L}} - y_{S_{1,L}}\right)^2} \tag{3.10}$$

Now, the angle for the deposition of the new circle $S_{1,L+1}$ defined with respect to the direction of $\mathbf{V}$, called α_i and shown in Figure 3.4a and Figure 3.4b, is defined using the law of cosines

$$cos\alpha_i = \frac{|\mathbf{V}|^2 - \left(r_{S_{NL,L}} + r_{S_{1,L+1}}\right)^2 + \left(r_{S_{NL,L}} + r_{S_{1,L}}\right)^2}{2\cdot|\mathbf{V}|\cdot\left(r_{S_{1,L+1}} + r_{S_{1,L}}\right)} \tag{3.11}$$

The final deposition angle α of the particle $S_{1,L+1}$, with respect to the x axis, is defined as the sum of the two angles just evaluated and it is shown in eq. (3.12).

$$\alpha_{S_{1,L+1}} = \alpha_d + \alpha_i \tag{3.12}$$

The illustrated procedure to generate the first ring can be repeated an arbitrary number of times, until the desired dimension of the assembly is reached (Figure 3.5).

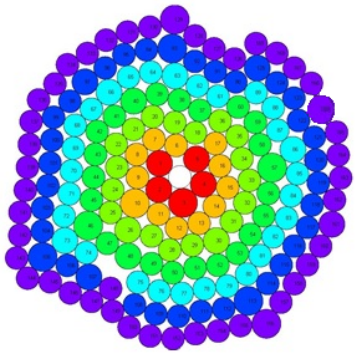


Figure 3.5: Layer produced with the planar algorithm

Figure 3.5 shows an example of a planar distribution of particles affected by the presence of localised voids and by the formation of preferential directions of growth, which affects the achievement of totally random assemblies. However, the adoption of subsequent mechanical consolidation simulations allows for the attainment of an increased randomness of the final three-dimensional assembly.

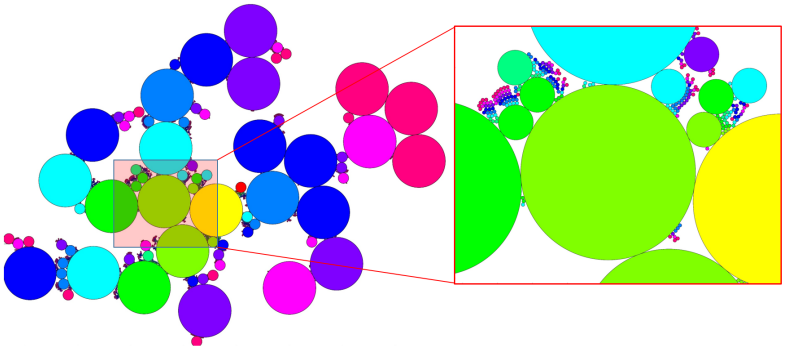


Figure 3.6: Layer produced with the planar algorithm with a very wide radii distribution R_1, $R_2 = 10R_1$, $R_3 = 100R_1$

Figure 3.6 proves, instead, the robustness of the method and its ability to generate highly polydisperse media (characterised by a very wide size distribution) such as powders, colloidal particles or natural occurring gravels and sands.

Nonetheless, the adoption of the planar approach to simulate polydisperse assemblies results in the generation of very loose packings, as demonstrated and explained

in Section 3.3.1.2.

The final assemblies can also be shaped by discarding all the circles outside user-defined boundaries (Figure 3.7).

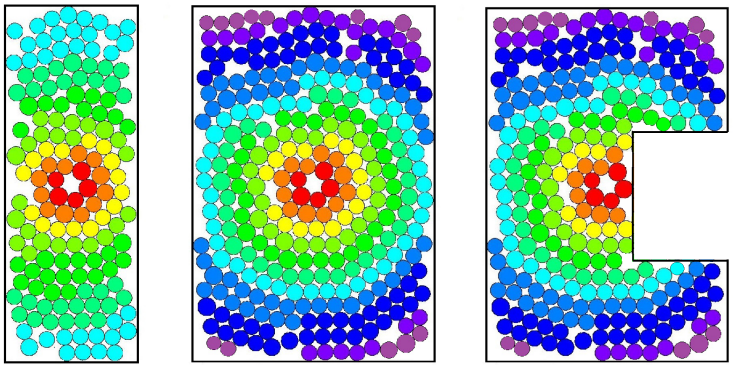


Figure 3.7: Examples of concave and convex layers produced with the planar approach

The obtained two dimensional layers can be seen as sections across the centre of spheres tangent to each other along their equatorial circumferences. The layers can be stacked up parallel to each other to generate three-dimensional assemblies. The distance between two neighbouring layers is defined as the sum of the radii of the biggest spheres of each layer, hence assuring the absence of overlaps.

Two examples of the final assembly are shown in Figure 3.8.

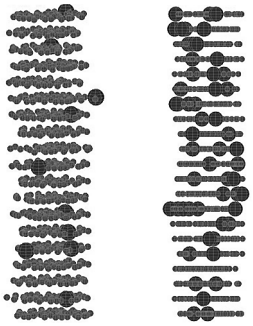


Figure 3.8: Two different 3D planar assemblies based on the planar spiral deposition method, respectively in perspective and orthographic view

The approach presented is an extremely efficient method to produce three-dimensional assemblies of spheres. However, the properties of the packing (e.g. void ratio, coordination number) depend strongly on the variance of the size of the spheres. In par-

ticular, the planar spiral deposition method provides accurate predictions for quasi-monodisperse assemblies.

3.2 3D-clew deposition method

The planar deposition method is evidently limited, as it imposes sub-optimal inter-layer void space for sets of spheres with a wide distribution of radii (as shown in Figure 3.8). As a result of this, a new $3D$ deposition method, based on three-dimensional tangency condition between neighbouring spheres, is proposed. This new method places the particles around the central sphere in a three-dimensional spiral manner, mimicking a clew of yarn. The spheres are inserted sequentially and their position is determined by imposing the tangency with at least two spheres in the assembly. Contrary to the planar approach presented in Section 3.1, in this method the agglomerate has no preferential growth directions. Moreover, there is no concentration of voids – of the type observed between the planes of the aggregates generated with the planar deposition approach – in the case of non-uniform distribution of radii.

The underlying principles of the current algorithm are:

1. Generation of a set of particles using an assigned distribution of radii;
2. The particles are added, one by one, imposing the tangency of the new entity with two already existing spheres, creating a spiral-spool of spheres;
3. To reach higher densities, after completing the deposition, new spheres are added using a 4 sphere-tangency condition;
4. The distance between the newly added sphere and the already placed ones is checked to avoid any possible overlap.

The algorithm implemented to generate the $3D$ deposition is described in Figure 3.9. The two separate deposition techniques (i.e. *primary spiral* and secondary 4-*spheres tangency* depositions) are described respectively in Section 3.2.1 and Section

3.2.2. In the framework of the three-dimensional deposition method, each particle is defined using two subscripts: i to identify the particle and L for the level to which the particle belongs to. Therefore, $S_{i,L}$ is the i^{th} particle in the L^{th} level. The subscript j is used as a counter on the level $(L-1)$. The very first step for the generation of the aggregate is the definition of the distribution of the radii of the spherical particles. The capability of defining the radii a-priori allows for the generation of samples statistically representative of real granular media. Each sphere in the domain is defined by the radius and by the three Cartesian coordinates of its centre (i.e. each sphere has four degrees of freedom). Therefore, four conditions have to be imposed. The first is resolved by choosing the radius from a distribution, whilst the other three are imposed by tangency condition. The next two sections describe two competing $3D$-clew deposition techniques, both based on the tangency condition, concurrently used for the generation of spherical particles assemblies.

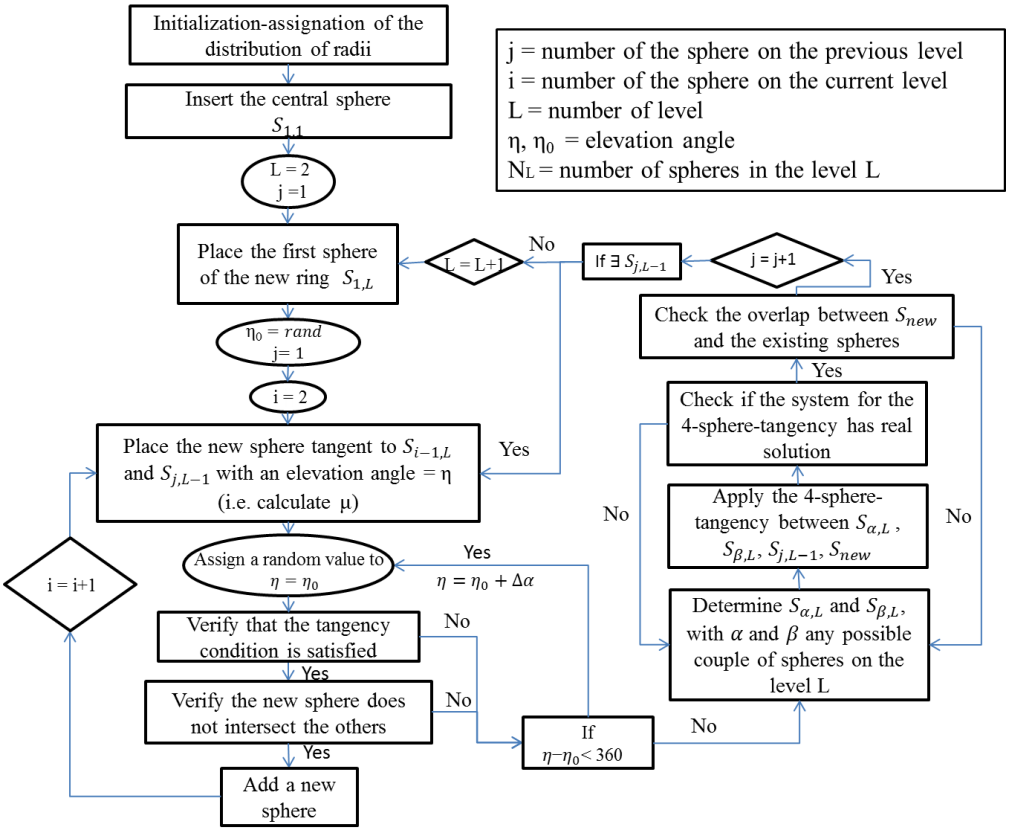


Figure 3.9: Flowchart of the 3D-clew deposition method

3.2.1 Primary spiral positioning technique

The centre of the generic new sphere is defined by the two angles μ and η as graphically explained in Figure 3.10 (i.e. conical coordinate system [171]). The generic vector $\mathbf{V}$, linking the origin of the coordinate system O with the generic point Q, can be defined as:

$$\mathbf{V} = \overrightarrow{OQ} = Q_x\mathbf{i} + Q_y\mathbf{j} + Q_z\mathbf{k} \tag{3.13}$$

The angle μ is the angle between the x-axis and the vector $\overrightarrow{OQ}$, whilst η is the angle between the planes π (plane XY) and Π (plane defined by the vectors $\overrightarrow{OQ}$ and $\overrightarrow{OP}$).

The components of the vector $\mathbf{V}$ are:

$$\begin{cases} Q_x = |\mathbf{V}| cos\mu \\ Q_y = |\mathbf{V}| sin\mu \cdot cos\eta \\ Q_z = |\mathbf{V}| sin\mu \cdot sin\eta \end{cases} \tag{3.14}$$

The first sphere $S_{1,1}$ (O in Figure 3.11) is arbitrarily placed in the three-dimensional space. The origin of the "global" rectangular coordinate system is imposed coincident with the centre of such sphere, which is considered to be the only particle belonging to the first layer. The second sphere $S_{1,2}$ (P_1 in Figure 3.11) is the first sphere of the second layer. The position of $S_{1,2}$ is imposed by the arbitrary definition of the angles α_x and α_z, respectively azimuthal and elevation angles in spherical coordinates [171], as defined in Figure 3.11.

Considering that the magnitude of the vector $\mathbf{V}$ (in Figure 3.11) is equal to the sum of the radii of the two considered spheres, the coordinates of the centre of P_1 are:

$$\begin{cases} x_{P_1} = x_{j,L-1} + \left(r_{j,L-1} + r_{i,L}\right) cos\alpha_z \cdot cos\alpha_x \\ y_{P_1} = y_{j,L-1} + \left(r_{j,L-1} + r_{i,L}\right) cos\alpha_z \cdot sin\alpha_x \\ z_{P_1} = z_{j,L-1} + \left(r_{j,L-1} + r_{i,L}\right) sin\alpha_z \end{cases} \tag{3.15}$$

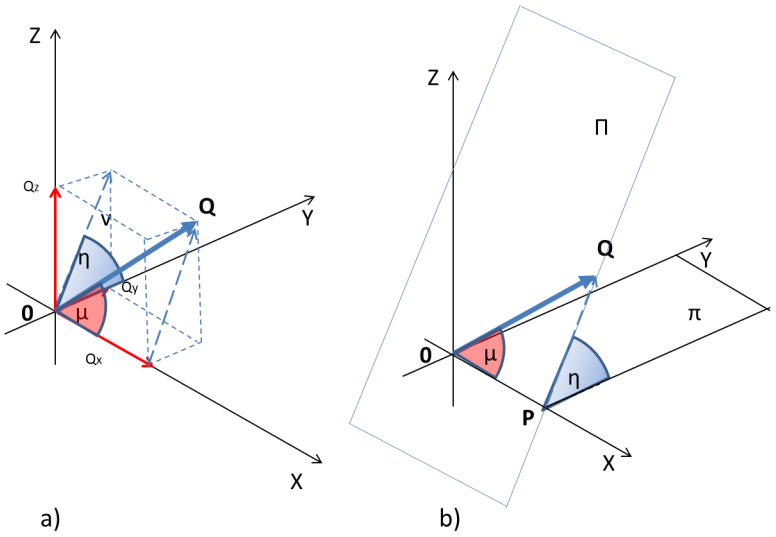


Figure 3.10: Definition of the angles μ and η (a) and of the components of the vector $\mathbf{V}$ in the Cartesian coordinate system (b)

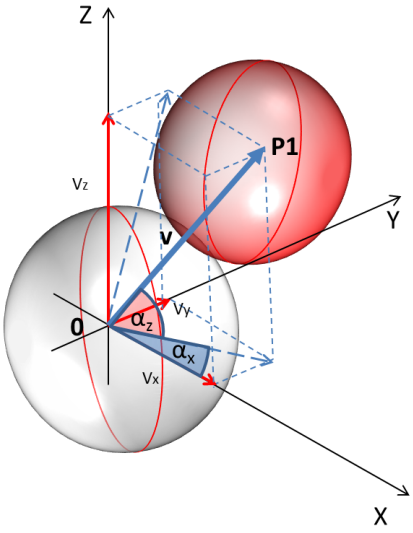


Figure 3.11: First two spheres of the 3D-clew assembly

Every possible new particle should not overlap any other particles already placed in the assembly. The Eulerian distance between the centres of two spheres is used to ensure this. The position of the centre of each new particle $S_{i,L}$ in the same layer (P_2 in Figure 3.12) is defined imposing the tangency with the two spheres that already exist $S_{i-1,L}$ and $S_{j,L-1}$ (O and P_1 in Figure 3.12).

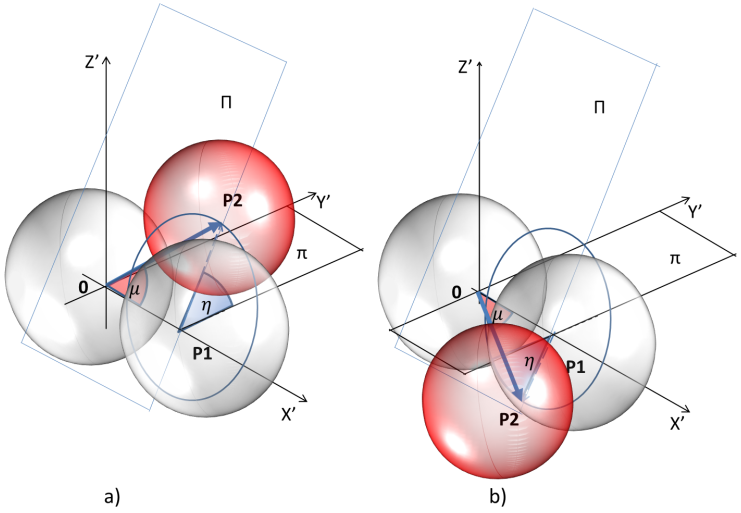


Figure 3.12: Positioning of the following particles in the 3D-clew method

Defining the magnitude of the two vectors $\overrightarrow{OP_1}$ and $\overrightarrow{OP_2}$ in terms of their radii

$$\left\|\overrightarrow{OP_1}\right\| = r_{j,L-1} + r_{i-1,L} \tag{3.16}$$

$$\left\|\overrightarrow{OP_2}\right\| = r_{j,L-1} + r_{i,L} \tag{3.17}$$

the angle μ between them can be evaluated using the cosine law and applying the same simplifications adopted for eq. (3.2):

$$\mu_i = cos^{-1}\left(\frac{r_{j,L-1}^2 + r_{i-1,L}\cdot r_{j,L-1} + r_{j,L-1}\cdot r_{i,L} - r_{i-1,L}\cdot r_{i,L}}{\left\|\overrightarrow{OP_1}\right\|\cdot\left\|\overrightarrow{OP_2}\right\|}\right) \tag{3.18}$$

The tangency condition defines the angle μ but it is not sufficient to fix the position of the new sphere P_2, whose centre could be placed anywhere on the base circumference of a cone with a fixed half opening angle equal to μ (i.e. around the blue circle in Figure 3.12). The angle η has to be chosen to univocally define the position of the new sphere. In Figure 3.12a and Figure 3.12b, two possible diametrical opposite positions of the new sphere P_2 are shown. The initial $\eta = \eta_0$ is chosen randomly, thus ensuring the casual deposition of particles around the central one in a *clew of*

yarn manner. The overlap with the other existing spheres has to be checked before inserting, for good, the new sphere. The same procedure is applied to all the other spheres $S_{j,L-1}$ on the same level $L-1$ as central particles (O in Figure 3.12). In order to use the eqs. (3.16)-(3.18), valid in the local coordinate system ($X'Y'Z'$) centred on the sphere O and with the x-axis pointing to the last added sphere, a change of reference system is required. Looking at Figure 3.13c, the new sphere to be inserted is P_3, which is tangent to O and P_2 (in general P_2 is the sphere $S_{i-1,L}$). The rotation of frame of reference is required so that the X'-axis points to the sphere P_2.

Starting from the initial coordinate system (XYZ in Figure 3.13) two rotations are required to end up in the final configuration ($X'Y'Z'$ in which the eqs. (3.16)-(3.18) are valid): one rotation α around the Z-axis as shown in Figure 3.13a and a subsequent one, equal to an angle β, around the new y-axis as in Figure 3.13b. The rotation matrix is

$$R = R_y \cdot R_z = \begin{bmatrix} cos\beta & 0 & sin\beta \\ 0 & 1 & 0 \\ -sin\beta & 0 & cos\beta \end{bmatrix} \begin{bmatrix} cos\alpha & -sin\alpha & 0 \\ sin\alpha & cos\alpha & 0 \\ 0 & 0 & 1 \end{bmatrix} \tag{3.19}$$

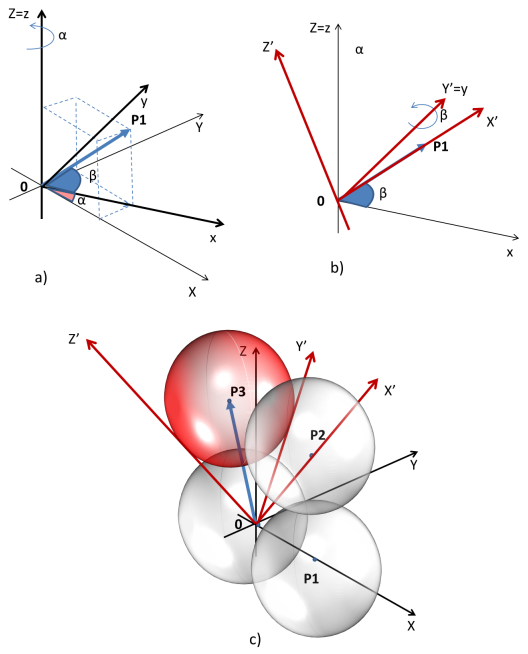


Figure 3.13: Transformation of coordinate system in the 3D-clew method

When the position of the new sphere is defined in the local coordinate system $(X'Y'Z')$, it is converted in global coordinates applying the opposite rotation with respect to R, before being inserted. For each new particle, the overlap is checked against all the other spheres belonging to the current and previous layers. If the sphere cannot be inserted because of the overlapping condition, another attempt is done adding the increment $\Delta\eta$ to the angle η (defined in Figure 3.12).

$$\eta = \eta + \Delta\eta \tag{3.20}$$

When $\eta = \eta_0 + 360^o$ the layer is completed (Figure 3.14) but it is possible to reach a higher density adding more spheres in the available free space, using a 4 sphere-tangency technique.

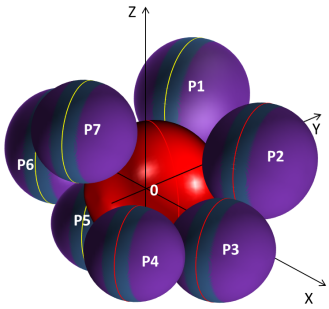


Figure 3.14: Second level around the initial sphere in the 3D-clew method

3.2.2 Secondary "4-spheres-tangency" positioning technique

Each sphere in the space is defined by the radius and by the three Cartesian coordinates of its centre, i.e. four conditions have to be assigned to fix unequivocally its position. Because of the a-priori assignation of the radii, only three more conditions are required. These three conditions are obtained imposing the simultaneous tangency between three already existing particles (one of them is always the central sphere $S_{j,L-1}$ in the previous level) and the new one, as shown in Figure 3.15. This procedure has to be applied to all the particles in the just completed level, using all the possible combinations of three neighbouring spheres.

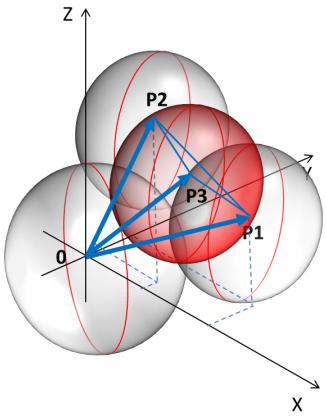


Figure 3.15: 4 spheres tangency condition

Defining a system of distances between each of the three existing particles and the new one, the unknown variables to be defined are the three coordinates x, y, z of the centre of the new sphere.

$$\begin{cases} (x-x_1)^2+(y-y_1)^2+(z-z_1)^2=(r+r_1)^2 \\ (x-x_2)^2+(y-y_2)^2+(z-z_2)^2=(r+r_2)^2 \\ (x-x_3)^2+(y-y_3)^2+(z-z_3)^2=(r+r_3)^2 \end{cases} \tag{3.21}$$

The symbolic solution of eq. (3.22) produces an explicit expression for each of the coordinates of the new sphere in the form

$$\begin{cases} x=f(x_1,y_1,z_1,x_2,y_2,z_2,x_3,y_3,z_3,r,r_1,r_2,r_3) \\ y=f(x_1,y_1,z_1,x_2,y_2,z_2,x_3,y_3,z_3,r,r_1,r_2,r_3) \\ z=f(x_1,y_1,z_1,x_2,y_2,z_2,x_3,y_3,z_3,r,r_1,r_2,r_3) \end{cases} \tag{3.22}$$

In this manner, even though the coordinates and the radii of the pre-existing spheres change in each iteration, there is no need of solving numerically the system (3.22). This can presents two kinds of solutions: $(x, y, z) \in \mathbb{R}$, if the new inserted particles respects all the requirements previously presented, or $(x, y, z) \notin \mathbb{R}$, if the particle does not fulfil the tangent conditions. Hence, all the solutions with an imaginary part are discarded. Additionally, the non-overlapping of the new sphere with any of the other pre-existing ones is verified. If any overlap is detected the sphere is discarded and a new triple is used.

3.2.3 Subsequent levels

When the first level is completed (i.e. no more particles can be added), the second one is started (yellow spheres in Figure 3.16). The central sphere, around which the new layer is developed, is the first sphere $S_{1,L-1}$ of the previous level $L-1$ (P_1 in Figure 3.16). When no more spheres can be placed around that particle, the following sphere on the same level is chosen $S_{2,L-1}$ (P_2 in Figure 3.16), and so on. When all the spheres on the level $L-1$ are surrounded by new particles, the current level is exhausted and a new one is started. Every first sphere of a new level requires the random update of the direction cosines used in eq. (3.15) and when there is overlap, the direction cosines are changed, considering all the possible combinations of α_x and α_z

$$\begin{cases} 0^o < \alpha_x < 360^o \\ -90^o < \alpha_z < 90^o \end{cases} \tag{3.23}$$

In this way all the possible positions around the same sphere are scanned. The intersection with the spheres belonging to the current and previous layers is checked for each new particle. The entire process already defined for the second layer is repeated for all the spheres in the following layers. Because each new sphere $S_{i,L}$ (e.g. sphere P_9 in Figure 3.16), for the subsequent levels, is defined in a frame of reference parallel to the global one but centred in the j^{th} sphere of the layer $L-1$ (Sx, Sy, Sz are the coordinates of the new sphere in $X"Y"Z"$) a rigid translation into the global coordinate system is required:

$$\begin{cases} x_{i,L} = Sx + x_{j,L-1} \\ y_{i,L} = Sy + y_{j,L-1} \\ z_{i,L} = Sz + z_{j,L-1} \end{cases} \tag{3.24}$$

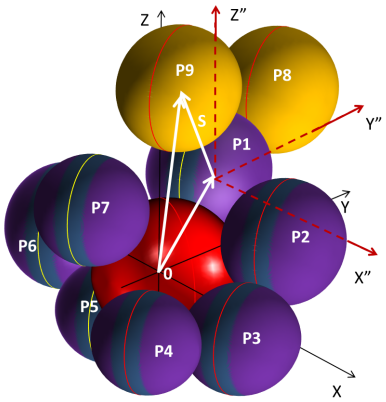


Figure 3.16: First spheres of a subsequent level in the 3D-clew method

Figure 3.17a shows an intermediate step in the deposition process of an unconfined aggregate of spheres with two (very) different radii, whilst Figure 3.17b represents the final state of the same aggregate. For displaying purposes each level is represented with a different colour. It is important to highlight the absence of concentrated voids of the kind observed for the planar deposition method for a similar distribution of radii.

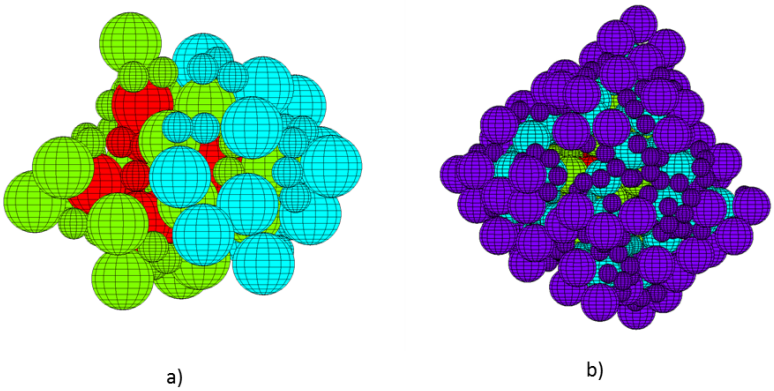


Figure 3.17: Assembly produced with the 3D-clew deposition method

The three-dimensional final assembly can be cropped into more regular geometries, as the cubic aggregate shown in Figure 3.18 or in more complex concave or convex 3D geometries adopting cropping procedures similar to what shown, for the planar case, in Figure 3.7. Furthermore, the cropped cubic aggregates can be adopted as unit cells for the application of periodic boundary conditions of the kind introduced,

for example, by Parrinello and Rahman [172] (in 2D) and extended to 3D by Henrich et al. [173].

With the $3D$-clew approach, an initial volume can be densely packed with spherical particles without using any mechanical approaches.

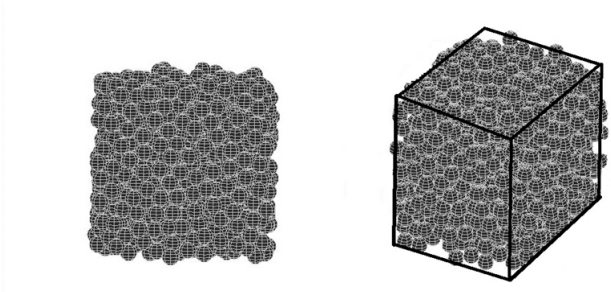


Figure 3.18: Frontal and prospective view of a cubic 3D-clew geometrical assembly

3.3 Results and discussion

The new algorithms have been tested intensively with the aim to generate assemblies of particles representative of those naturally occurring when assisted by gravity, such as gravel and sand or those obtained through power processing. The observations and quantitative evaluations of the developed algorithms are presented in this section. The void ratio is often used to characterise the assembly [174, 82] and it is defined as

$$e = \frac{V_v}{V_s} = \frac{V_{tot} - V_s}{V_s} = \frac{V_{tot}}{V_s} - 1 = \frac{1}{\rho} - 1 \tag{3.25}$$

where V_v is the volume of voids, V_s is the volume of solid, V_{tot} is the total volume of the assembly and ρ is the packing density. The void ratio can vary inside each single assembly and, additionally, it is strongly affected by the presence of the walls and of the free surfaces.

The walls of the container reduce the randomness of the particle distribution, imposing an ordered arrangement of the spheres against the fixed boundary. The presence of the free surface, instead, induces a noticeable fluctuation of the void ratio,

compared to the average value measured far away from the boundaries. For those reasons, the void ratio is computed evaluating the volume of solids inside fictitious cubic boxes. The dimension d_i of the boxes is increased from a size equal to the radius of the smallest sphere to the dimension of the real domain D (Figure 3.19), starting from the centre of the samples.

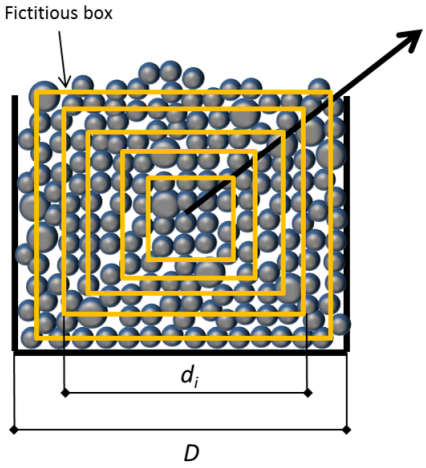


Figure 3.19: Imaginary boxes defined to evaluate the correct void ratio, accounting for walls and free surface effects

The curve of the void ratio in function of the dimension of the fictitious box (presented in Figure 3.20) shows the influence of the boundaries that induce the increase of the void ratio, which is not representative of the real properties of the assembly.

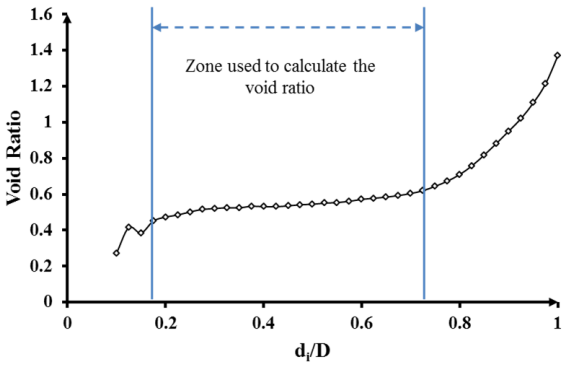


Figure 3.20: Zone used to calculate the correct void ratio; d_i is the dimension of the fictitious box and D of the real one

To exclude such effect as well as the fluctuations related to the use of a not representative volume (i.e. not enough particles in the box) the void ratio of the assembly is calculated as the portion of the curve that has a standard deviation less than 0.2.

Another parameter to consider is the coordination number Z, which defines the average number of contacts per particle

$$Z = \frac{\sum_{i=1}^{N} C_p}{N} \tag{3.26}$$

where C_p is the number of contacts per particle and N is the total number of particles in the sample. Moreover, Section 3.3.1 presents a comparison between the computational times[2], in both absolute and relative[3] value, required by the Planar and $3D$-clew method.

Section 3.3.2 shows the results for the DEM simulations using a non-parallelized code. In the following sections, two kinds of assemblies are tested:

1. Monodisperse assembly, with a mean radius of 0.352 mm for all the spheres and a total number of particles around 1000.

2. Polydisperse assembly, based on the distribution of radii: $0.52, 0.35, 0.12$ mm with different percentages. The total number of particles in the polydisperse case is around 2000 to guarantee the representativeness of all the three sets of particles.

The properties of mono and polydisperse assemblies generated with the two methods described in the previous sections are reported in Section 3.3.1. In Section 3.3.2, then, the outcomes of DEM mechanical simulations of gravity assisted packings are reported highlighting the effect of the initial particle arrangement. In particular, it

[2]All the simulations are performed on a Dell Precision T7600 workstation, with 2 quad-core Intel Xeon CPU E5-2630 processors and 64 GB of RAM

[3]The computational time is normalised against the average time required to generate 2000 spheres polydisperse assemblies with the 3D-clew deposition method (equal to 106 sec.)

is shown the noticeable reduction of the computational time required to reach mechanical equilibrium starting from assemblies generated with the methods presented in this chapter (both planar and $3D$-clew) with respect to DEM simulations starting from randomly positioned spheres. Finally, all the results are summarised in Section 3.3.3.

3.3.1 Properties of the geometrical aggregate

In the present section the assemblies produced with planar deposition and $3D$-clew methods are compared - both for monodisperse and polydisperse configurations - in terms of void ratio and computational time. All the samples have the same square base (i.e. 8 x 8 mm). Examples of the four different classes of aggregates are presented in Figure 3.21.

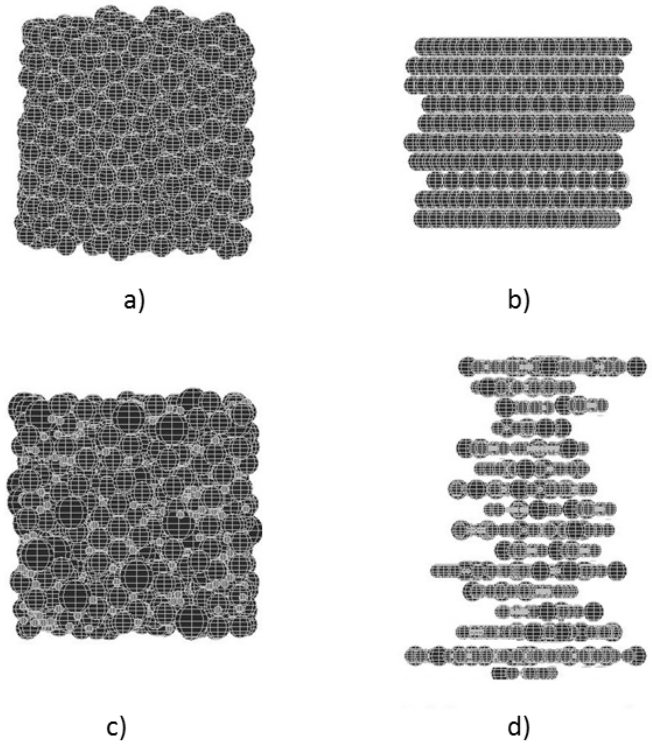


Figure 3.21: Examples of monodisperse a) - b) and polydisperse c) - d) assemblies

3.3.1.1 Geometrical monodisperse assembly

Table 3.1 and Table 3.2, respectively, summarise the results for the planar and the $3D$-clew geometrical approaches.

N° of Particles	e_{mean}	$e_{variance}$	**Time [sec]**	**Relative Time**
998	0.68	0.10	0.44	$4.2 \cdot 10^{-3}$
1016	0.68	0.09	0.46	$4.3 \cdot 10^{-3}$
998	0.67	0.10	0.43	$4.1 \cdot 10^{-3}$
998	0.68	0.10	0.44	$4.2 \cdot 10^{-3}$
1004	0.68	0.10	0.45	$4.2 \cdot 10^{-3}$
998	0.68	0.10	0.43	$4.1 \cdot 10^{-3}$
1004	0.68	0.09	0.45	$4.2 \cdot 10^{-3}$

Table 3.1: Results of the planar geometrical approach used for monodisperse assemblies

N° of Particles	e_{mean}	$e_{variance}$	**Time [sec]**	**Relative Time**
1071	0.85	0.02	85	0.81
1049	0.84	0.03	84	0.79
1041	0.89	0.04	84	0.79
1060	0.87	0.04	85	0.81
1035	0.85	0.02	83	0.78
1016	0.84	0.02	85	0.81
997	0.85	0.03	83	0.78

Table 3.2: Results of the 3D-clew geometrical approach used for monodisperse assemblies

The planar approach clearly shows to be more computationally efficient than the $3D$-clew approach, generating aggregates with lower average void ratios (0.68 instead of 0.85) and an higher standard deviation (0.1 instead of 0.03) due to the layered nature of the assembly that produces regions of concentrated voids (Figure 3.21b), which are absent in the assemblies generated with the $3D$-clew method (Figure 3.21a).

3.3.1.2 Geometrical polydisperse assembly

The considered polydisperse assemblies consist of three sets of spherical particles with different radii and given percentages, as reported in Table 3.3

Radii	Percentage
0.517 mm	7%
0.355 mm	36%
0.124 mm	57%

Table 3.3: Distribution of radii of the polydisperse assembly

Since the maximum size of the particles imposes the distance between subsequent layers in the planar geometrical approach, the polydisperse assemblies generated with this approach present concentrated voids in between the layers that are proportional to range of particle size (Figure 3.21d).

Table 3.4 and Table 3.5 report, respectively, the results for the planar and $3D$-clew approaches.

N° of Particles	e_{mean}	$e_{variance}$	**Time [sec]**	**Relative Time**
2021	2.7	0.5	1.7	$1.6 \cdot 10^{-2}$
2094	2.6	0.7	1.5	$1.4 \cdot 10^{-2}$
2084	2.2	0.8	1.5	$1.4 \cdot 10^{-2}$
2106	2.4	0.7	1.8	$1.7 \cdot 10^{-2}$
2045	2.5	0.8	1.9	$1.8 \cdot 10^{-2}$
2085	2.5	0.7	1.8	$1.7 \cdot 10^{-2}$
1982	2.6	0.8	1.5	$1.4 \cdot 10^{-2}$

Table 3.4: Results of the planar geometrical approach for polydisperse assemblies

N° of Particles	e_{mean}	$e_{variance}$	**Time [sec]**	**Relative Time**
1992	0.61	0.15	91	0.86
2013	0.55	0.17	87	0.82
1981	0.62	0.16	105	1.00
1956	0.59	0.10	120	1.13
2051	0.67	0.06	130	1.22
2022	0.63	0.17	122	1.15
1952	0.60	0.20	89	0.84

Table 3.5: Results of the 3D-clew geometrical approach for polydisperse assemblies

Similarly to monodisperse assemblies, the planar approach is more computationally efficient than the $3D$-clew approach. However, the effect of inter-layer void concentration increases noticeably the void ratio of the assemblies generated with the

planar approach ($e_{mean} \approx 2.5$), whilst the void ratio of the $3D$-clew approach remains low, thus generating compacted samples (Figure 3.21c).

3.3.1.3 Comparison of the geometrical methods

In conclusion, the planar approach is computationally more efficient than the $3D$-clew approach (i.e. up to 200 times faster), however the void ratio of the assemblies generated is strongly influenced by the distribution of particle radii. Therefore, the use of the planar deposition method is best suited for the packing of particles with narrow range of sizes.

The $3D$-clew method, instead, is scarcely affected by the size of the particles, both in terms of computational cost and void ratio predicted.

3.3.2 Gravity-assisted packing

In this section, the new geometrical algorithms are used to define the initial topologies for the mechanical simulation of gravity assisted packing of spherical particles. To achieve a mechanically stable system, the assemblies produced in Section 3.3.1 are imported in an in-house DEM code, DEST, and subjected to gravitational field. The adopted DE algorithm is based on the penalty approach, thus allowing for small overlap of the particles to calculate the contact forces. The overlap is carefully monitored to avoid erroneous estimations of the aggregate properties. In the simulations herein presented, the overlapping volume of each single particle never exceeds 0.3% of its volume, and can, therefore, be considered negligible. The material properties used in the simulation are the following:

Material	Quartz
Density	$2650\,kg/m^3$
E	$76\,GPa$
ν	0.31

Table 3.6: Material properties of the single particle for the DE simulation

The particles are poured in a cubic container whose base is equal to the base of

the geometrical packings (i.e. 8 x 8 mm).

In the next sections the results of the DEM simulations, adopting as starting configuration the assemblies generated with the newly developed geometrical approaches, are compared against DEM simulations starting from randomly distributed particles, showing a noticeable reduction of the computational time required to reach the mechanical equilibrium.

The randomly positioned particles are placed within a given volume with a brute force algorithm that only verifies the non-overlapping of the spheres. This method strongly depends on the initial volume, which is inversely proportional to the computational time and to the void ratio of the assembly.

3.3.2.1 DE simulations of monodisperse assemblies

This section reports the results for mechanically packed monodisperse assemblies obtained by using as initial configurations aggregates generated with: random (Table 3.7), planar (Table 3.8), and $3D$-clew (Table 3.9) geometrical approaches.

N° of Particles	e_{mean}	$e_{variance}$	**Time [min]**	**Relative Time**
1000	0.48	0.08	28	0.26
1000	0.47	0.07	29	0.27
1000	0.48	0.06	24	0.23
1000	0.46	0.10	28	0.26

Table 3.7: Results of DEM simulations of monodisperse assemblies, from random initial configuration

N° of Particles	e_{mean}	e_{varian}	**Time [min]**	**Relative Time**
998	0.45	0.03	16	0.15
1016	0.50	0.02	17	0.16
998	0.52	0.03	17	0.16
998	0.50	0.04	17	0.16

Table 3.8: Results of DEM simulations of monodisperse assemblies, from "planar geometrical" initial configuration

N° of Particles	e_{mean}	e_{varian}	Time [min]	Relative Time
1071	0.44	0.02	23	0.22
1049	0.46	0.02	21	0.20
1041	0.45	0.02	24	0.23
1060	0.45	0.02	19	0.18

Table 3.9: Results of DEM simulations of monodisperse assemblies, from "$3D$-clew" initial configuration

All the DEM simulations produce assemblies with comparable values of average void ratio and coordination number (i.e. $Z \approx 8$). However, the adoption of initial configurations generated with the planar geometrical approach allows to perform the mechanical simulations more efficiently, because of the lower initial void ratio. In particular, the adoption $3D$-clew approach initial assemblies leads to an increase of the computational time of about 30%, whilst simulations with random initial configurations require about 63% more time with respect to the planar approach.

3.3.2.2 DE simulations of polydisperse assembly

This section reports the results for mechanically packed polydisperse assemblies obtained by using as initial configurations aggregates generated with: random (Table 3.10), planar (Table 3.11), and $3D$-clew (Table 3.12) geometrical approaches.

N° of Particles	e_{mean}	$e_{variance}$	Time [min]	Relative Time
2000	0.46	0.05	360	3.40
2000	0.45	0.08	365	3.44
2000	0.42	0.04	420	3.96
2000	0.41	0.08	360	3.40

Table 3.10: Results of DEM simulations of polydisperse assemblies, from random initial configuration

N° of Particles	e_{mean}	e_{varian}	Time [min]	Relative Time
2021	0.49	0.02	380	3.58
2094	0.49	0.02	380	3.58
2084	0.44	0.04	345	3.25
2106	0.49	0.03	310	2.92

Table 3.11: Results of DEM simulations of polydisperse assemblies, from "planar geometrical" initial configuration

N° of Particles	e_{mean}	e_{varian}	Time [min]	Relative Time
1992	0.48	0.08	96	0.90
2013	0.50	0.06	118	1.11
1981	0.49	0.07	90	0.85
1956	0.49	0.06	100	0.95

Table 3.12: Results of DEM simulations of polydisperse assemblies, from "$3D$-clew" initial configuration

As for the monodisperse assemblies, the void ratios and the coordination numbers ($Z \approx 9$) of the three sets of mechanically compacted packings are very similar. In this case the adoption of initial configurations generated with the $3D$-clew geometrical approach results to be the best choice in terms of computational efficiency, given that the simulations adopting either the random or the planar geometrical initial configurations are over than 2.5 times more computationally expensive.

3.3.3 Summary of the results

Finally, in this section, all the results presented (for both mono and polydisperse assemblies) are summarised, comparing the outcomes of the purely geometrical approaches (i.e. planar and $3D$-clew) as well as of the DEM simulations with different initial configurations (i.e. random, planar, and $3D$-clew).

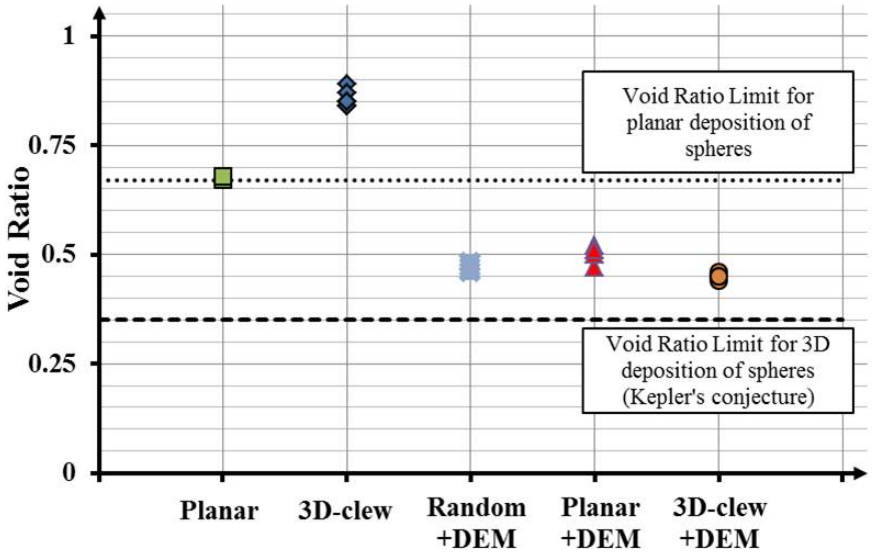


Figure 3.22: Summary of the results for monodisperse assemblies

Figure 3.22 shows the void ratio values for monodisperse assemblies for the five different sets of simulations. The planar geometric method produces assemblies with a void ratio ($e = 0.67$) extremely close to the minimum admissible value for monodisperse assemblies of spheres distributed on a plane [139] and lower than the $3D$-clew method. As highlighted in the previous sections, the different initial configurations have negligible effect on the void ratio of the assemblies consolidated mechanically ($e \approxeq 0.44 \div 0.5$), all relatively close to the Kepler conjecture ($e = 0.35$).

Figure 3.23, instead, shows the void ratio values of the polydisperse assemblies. In this case, the $3D$-clew method produces assemblies much denser than the planar deposition method and comparable to those obtained using DEM based simulations of gravity assisted compaction. Therefore, the $3D$-clew method can be applied on its own (i.e. without recurring to DE simulations) to produce dense aggregate, if the mechanical equilibrium of the aggregate is not strictly necessary.

The comparison of the computational costs of both the geometrical methods and the gravity assisted simulations with different initial configurations are summarised in Table 3.13, which reports the computational time required for the packing of 1000 monodisperse and 2000 polydisperse assemblies.

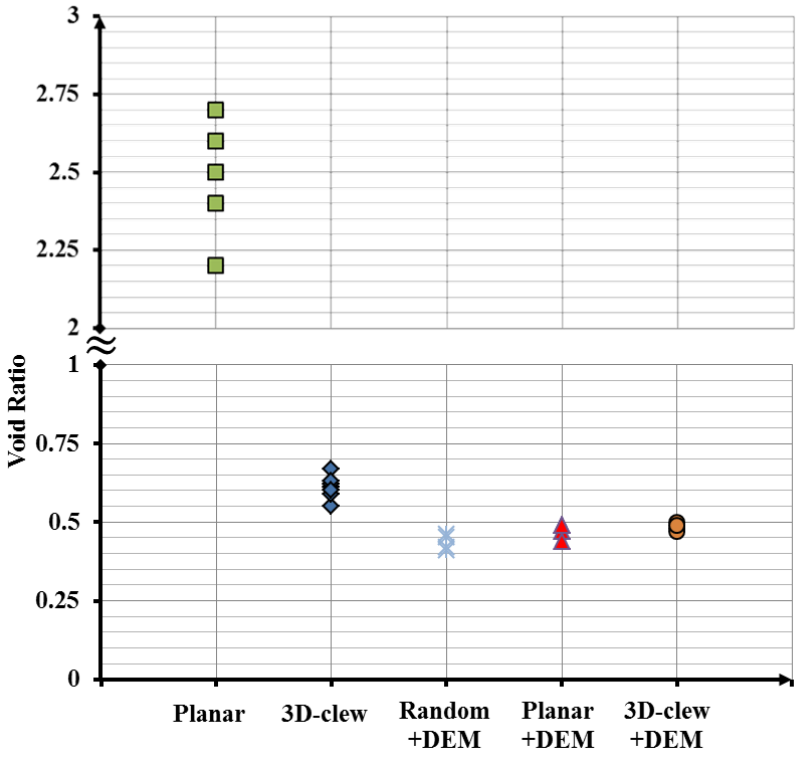


Figure 3.23: Summary of the results for polydisperse assemblies

Method	Monodisperse Time [min]	Polidisperse Time [min]
Planar	0.007 ± 0.001	0.027 ± 0.004
3D clew	4.7 ± 0.1	4.5 ± 0.7
DEM from Random	28 ± 2	360 ± 15
DEM from Planar	16 ± 1	340 ± 25
DEM from 3D-clew	21 ± 3	100 ± 10

Table 3.13: Average computational times for generating 1000 spheres monodisperse and 2000 spheres polydisperse assemblies using pure geometrical methods and to consolidate them using DEM

The results presented highlight the advantage of adopting the geometrical approaches to generate models of particle aggregates that can, eventually, be used as initial configurations for mechanical simulations. The advantage is further enhanced by the extremely high computational cost of the brute force method for the generation of random assemblies of particles, which - for the simulations presented - is several order of magnitude higher than the geometrical approaches developed. For

monodisperse assemblies, the adoption of initial configurations produced with the planar geometrical method grants a strong reduction of the computational cost of the mechanical simulation with respect to both the $3D$-clew (30% slower) and the random (63% slower) methods, without measurable differences in the final properties of the packing.

For polydisperse assemblies, instead, the initial configurations produced with the $3D$-clew method offers an even greater reduction of the computational cost of the mechanical simulations with respect to planar and random methods, both around 2.5 times slower.

The results demonstrate the high efficiency of the geometrical methods proposed to produce assemblies with void ratios comparable to the ones generated with gravity assisted compaction, as well as the the reduced computational cost of the combined use of mechanical and geometrical simulations.

Finally, Figure 3.24 shows the scalability of the $3D$-clew geometrical method, reporting the time required for the pure geometrical deposition of the assembly for different number of particles (n).

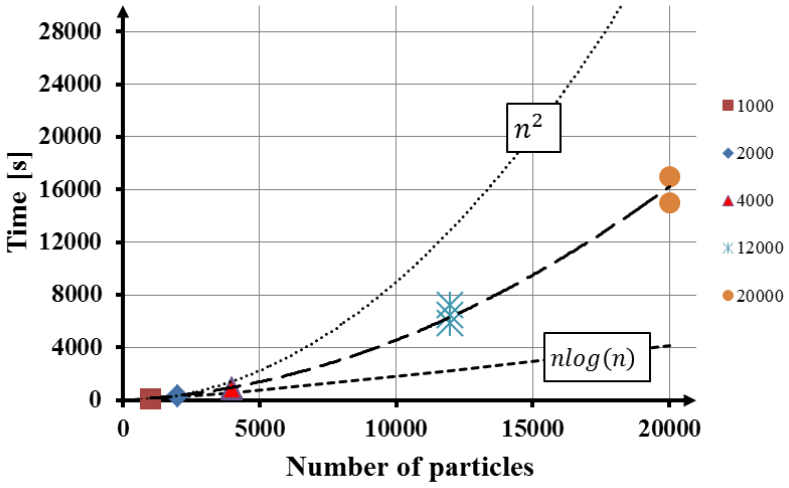


Figure 3.24: Scalability of the 3D-clew geometrical method; computer architecture reported in footnote 2, pag.64

Figure 3.24 demonstrates the robustness of the implemented code, and shows

that the computational cost trend lies between the $n \cdot log(n)$ and n^2 (i.e. *brute force* algorithm) curve. This shows the effectiveness of the selective choice of particles for the overlapping verification presented in Section 3.2.2. The efficiency of the method presented could be further improved implementing a binary tree search algorithm, of the kind presented by [105].

3.4 Generation of loose aggregates: effect of friction on the mechanical packing

The geometrical packing algorithms presented so far can efficiently generate dense samples. However, granular assemblies exist over a wide range of densities. Therefore, there is a clear need for the generation of numerical samples representative of looser granular assemblies.

Whilst generating dense numerical agglomerates starting from loose geometrical packings is trivial (it generally requires the application of prescribed boundary conditions during a subsequent mechanical packing that would mimic the consolidation process), the generation of loose samples from initial dense packings is not straightforward. The most common approach to achieve the latter, in literature, consists in varying the inter-particle friction during the mechanical packing [175, 176]. The presence of friction, indeed, maximises the void ratio by enhancing the inter-granular locking and the wall effect [109].

This section shows how a wide range of initial consolidation states can be generated by changing the value of the inter-granular friction in DEM based simulations of gravity assisted compaction.

All the following mechanical simulations have been carried out using the DEM open-software YADE [177].

The numerical samples consists of about 15000 spheres representing the Ottawa sand, with size distribution reported in Table 3.14.

Radius	Percentage
0.355 mm	7%
0.25 mm	76%
0.175 mm	17%

Table 3.14: Radii distribution of the Ottawa sand

The choice of this particular type of sand is justified by:

- prior knowledge of the experimental values of void ratio (e) [82], which range between 0.52 and 0.74;
- high sphericity of the grains, which can be properly modelled using perfect spheres.

The initial dense packing has been generated using the 3D-clew algorithm presented in Section 3.2.

The so generated sample is, then, imported in YADE for the subsequent mechanical packing: the particles are poured, under gravity, in a stainless steel cylindrical container of diameter equal to 20 mm.

The contact law adopted is based on the Hertzian-Mindlin theory, without viscosity and rotational friction. In fact, the tangential friction is generally predominant in case of relatively slow granular flows [178] (i.e. gravitational depositions) and it is enough to represent the frictional behaviour of the granular media under consideration.

In the following simulations, the angle of friction has been continuously changed from 0 (frictionless) to 40 degrees. The material properties of the Ottawa sand adopted in the simulations are reported in Table 3.15.

Density	2650 kg/m^3
Young's modulus	76 GPa
ν	0.3

Table 3.15: Material properties of the Ottawa sand adopted in the mechanical simulations

For simplicity's sake, the internal surfaces of the cylindrical box had the same frictional and elastic properties of the particles to be poured.

3.4.1 Results and discussion

As already explained in Section 3.3, the estimation of the void ratio representative of the consolidation state of the entire domain is computed using smaller fictitious boxes.

Figure 3.25 shows the curves of the void ratio in function of the dimension of the fictitious boxes (distribution of the void ratio within the sample) when changing the friction angle from 0 to 40 degrees.

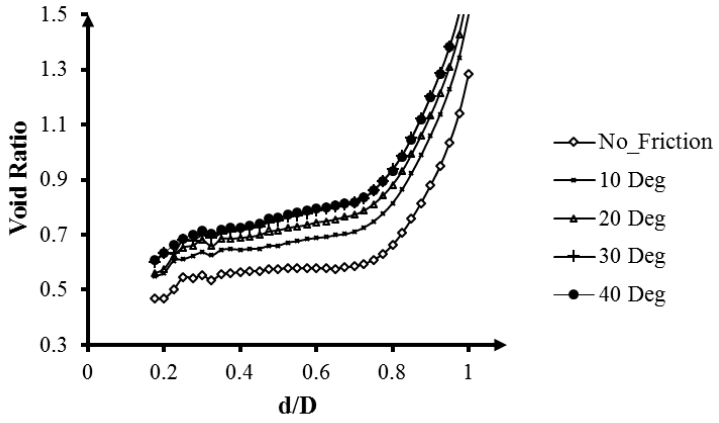


Figure 3.25: Effect of friction angles on the distribution of void ratio after mechanical packing

The tangential friction drastically affect the extension of the plateau region, which reduces with increasing angles of friction. For angles higher than 20 degrees, the plateau disappears. This proves the existence of a bigger scatter in the void ratio measurements that can be explained by the enhanced inter-granular locking. In fact, differently from frictionless systems, the inter-granular locking creates "defects" (i.e. disordered distributions of particles) in the packing, hindering the creation of homogenised samples.

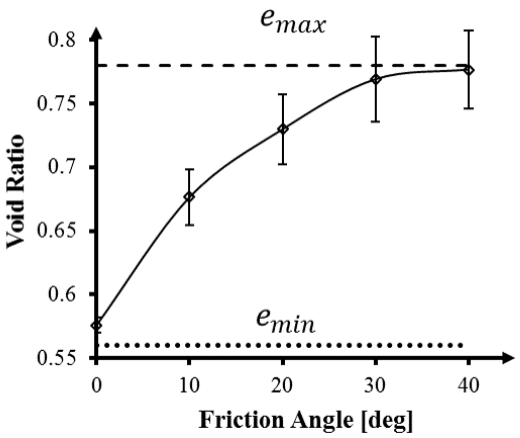


Figure 3.26: Mean values and standard deviations of the void ratios obtained varying the friction angle, and comparison with maximum (e_{max}) and minimum (e_{min}) experimental values reported in Chapter 6

Figure 3.26 shows the variation of void ratio with the friction angle. In particular, it reports the mean values (dots) and standard deviations (error bars) measured in the plateau zone of Figure 3.25 (for $0.4 < d/D < 0.7$) for each configuration. The plateau region is characterised by a maximum variation of the void ratio comparable to the experimental uncertainty (± 0.1), as explained in Chapter 5. The two dotted lines represents the maximum and minimum experimentally measured void ratios. This chart clearly shows how the entire experimental range of void ratios can be modelled by properly choosing the angle of friction, thus extending the applicability of the proposed geometrical packing algorithms to loose assemblies.

3.5 Summary

This chapter presented two new geometrical methods for monodisperse and polydisperse sphere packing able to concurrently reproduce total number of particles and their size distribution: *the planar geometrical deposition method*, based on tangency between spheres with co-planar centres, and the $3D$*-clew geometrical deposition method*, based on tangency between spheres in the three dimensional space. Thus generated assemblies were compared with further consolidated states achieved by means of DEM based simulations of gravity assisted compaction.

The planar deposition method generates dense packing of monodisperse particles with void ratios extremely close to the analytical limit for 2D depositions (i.e. Kepler conjecture), but the density of the assemblies decreases for polydisperse particles - given the layered nature of the method. The $3D$-clew method, instead, produces dense packing of both mono and polydisperse assemblies at the expense of the computational cost of the process.

The geometrically generated packings are compared with the results of gravity assisted simulations, showing comparable properties of the assemblies alongside a several times smaller computational time required.

Additionally, the geometrical methods developed can be used in combination with mechanical methods to efficiently produce dense packings in physical equilibrium. In particular, it has been shown that the adoption of the packing generated with the geometrical methods developed as initial condition of gravity assisted simulations reduces the computational cost up to 2.5 times, with respect to the same simulations starting from a random distribution of particles.

Finally, loose packing - representative of the experimentally measured consolidation state of granular materials - can be obtained by varying the angle of friction in simulations of mechanical consolidation under gravity.

Chapter 4

A method for the generation and packing of representative polyhedral grains

The literature review - in Section 2.7.2 - identified the need for an efficient numerical method able to model the real grains shape of granular materials in a user-controlled manner. As a matter of fact, all existing approaches were either difficult to implement or presented a questionable ability to reproduce real shapes.

This section presents an innovative method, based on the *Hardcore-Voronoi* tessellation technique, capable of generating randomly shaped convex grains that are representative of a wide range of natural and artificial granular materials.

The developed method provides full control over the sizes and shapes of the Voronoi cells by defining two tuning parameters: *hardcore radius* (ρ) and *stretching factor* (H_k).

It is worth mentioning that the presented work focuses on the generation of models representative of the *first order property* (i.e. form) of real materials. The effect of roundness (i.e. corner angularity) and texture (i.e. surface roughness) of the grains are generally considered to be of a lower order of importance [12].

A feedback loop on both the seeding of the Voronoi *nuclei* (i.e. Hardcore radius), and on the geometrical transformations of the tessellation (i.e. stretching of the grains) grants control over the *form* of the particles, as detailed in Section 4.1.

The 3D assemblies, generated using the modified Voronoi tessellation, are comprised of tightly packed grains without empty space between the cells. In order to reproduce real granular materials, the generated grains need to be packed in a disordered assembly. A computationally efficient geometrical packing approach is also proposed: the so-generated particles are enclosed in *bounding spheres*, which are assembled using the 3D-clew geometrical deposition approach presented in Chapter 3. The use of *minimum bounding spheres* (MBSs) to enclose the grains yields relatively dense packings. The proposed calculation of the MBSs and the ability of the adopted geometrical packing algorithm to minimise the void ratio of the aggregate guarantee the efficient generation of assemblies of polyhedral grains with controllable density. Additionally, the bounding spheres can be enlarged by introducing a scaling factor to produce less dense packings of particles. These can be used to create either granular inclusions or pores within a matrix, thus modelling materials ranging from foams to composites.

The developed methodology is summarised in the flowchart in Figure 4.1.

The *shape factors* of the numerical samples (i.e. *sphericity* ψ and *slenderness* S) are compared against experimentally measured values (Section 4.2), thus validating the proposed method.

4.1 Grain generation

Statistically representative models of granular materials are generated using a modified Voronoi tessellation technique.

Given a finite set of N *nuclei*, arbitrarily positioned in $\Re^3$, the Voronoi method tessellates the space into N *cells*, one per nucleus. Each cell consists of all points closer to its nucleus than to any other one in the domain:

$$\{R_{P_i}\} = \{x \in \Re^3 | d(\mathbf{P_i}, \mathbf{x}) \leq d(\mathbf{P_j}, \mathbf{x})\}\ j = 1, 2, ..., N : j \neq i \tag{4.1}$$

where $\mathbf{P_j}$ is the position of the j-th nucleus, R_{P_i} is the cell associated to the nucleus

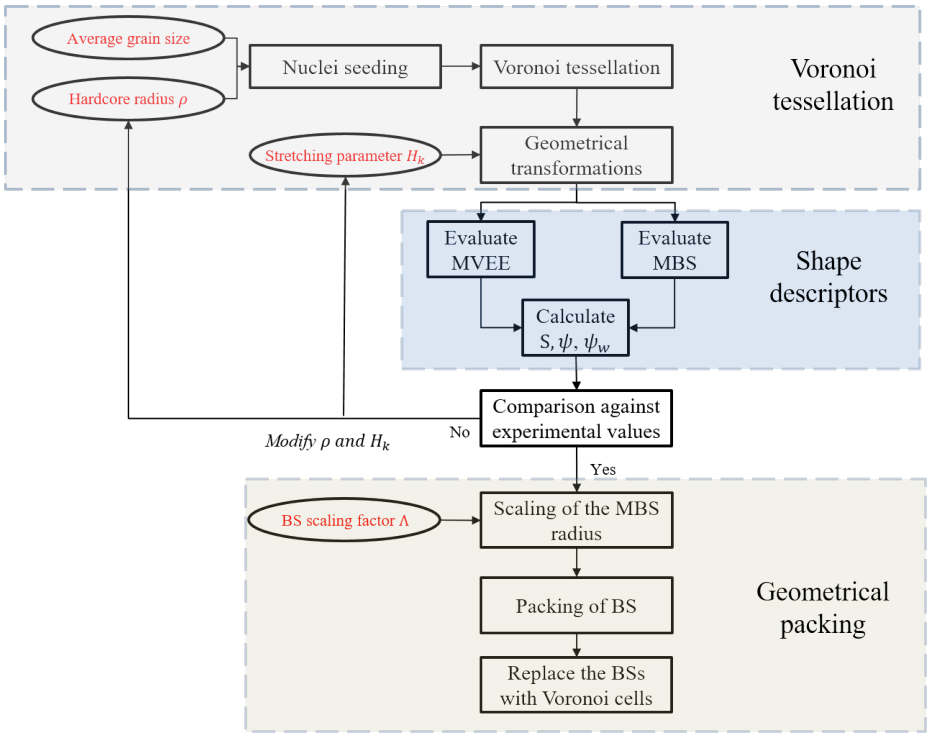


Figure 4.1: Flowchart of the algorithm for the generation of assemblies of arbitrarily shaped particles

$\mathbf{P_i}$, and $\mathbf{x}$ is the position of a generic point in $\Re^3$.

Among all the existing Voronoi-based methods, the Hardcore-Voronoi offers the opportunity to control the sphericity of the grains by varying a single scalar value: the *Hardcore radius* ρ. It represents the minimum distance between neighbouring nuclei during the seeding of the domain. This operation, in a three-dimensional space, can be expressed as:

$$|\mathbf{P_i} - \mathbf{P_j}| = \sqrt{\sum_{k=1}^{3} (P_{i_k} - P_{j_k})^2} > \rho \;\; \forall (i,j) = 1,2,...,N : j \neq i \tag{4.2}$$

As reported in [179], the typical grain size distributions of the Voronoi assemblies obtained with this method exhibits a bell-shaped curve that is not necessarily representative of real granular materials. However, the combination of multiple tessellations allows for the generation of assemblies with any desired size distribution, thus allowing for the reproduction of the actual features of real granular assemblies. An alternative way of generating real size distributions is represented by the weighted

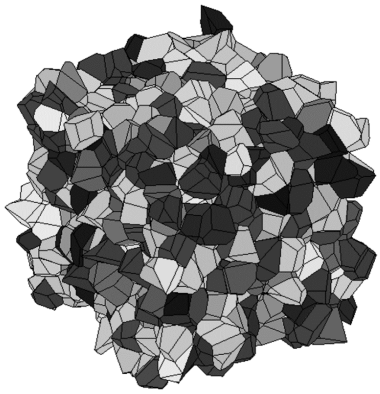


Figure 4.2: Aggregate of Voronoi cells

tessellation or Laguerre Voronoi diagram [180, 181].

Once the domain is tessellated, the cells in the outer part of the seeding domain are discarded to minimise the boundary effects on the grain morphology. An example of tightly packed Voronoi cells aggregate is presented in Figure 4.2.

The form of the so-obtained grains can be further manipulated by employing a *stretching* transformation of the cells, of the type presented in [166]. With this transformation, the vertices of the cells are translated according to the vector H_k to keep the volume of the cell constant, by stretching the grain along the arbitrary direction η and shrinking it in the perpendicular directions (ξ and ζ). The transformation can be expressed as:

$$P_{i_k}^S = (P_{i_k} - P_{0_k}) \cdot H_k \;\; \forall k = 1,2,3 \tag{4.3}$$

The components of the stretching vector in the shrinking directions (H_ξ and H_ζ), expressed in terms of stretching value (H_η) and dimensions of the seeding domain (L_η, L_ξ, and L_ζ), are:

$$H_{(\xi,\zeta)} = \frac{1}{L_{(\xi,\zeta)}} \sqrt{\frac{L_\xi L_\zeta}{H_\eta}} \tag{4.4}$$

Figure 4.3 shows an example of a group of grains stretched, along the generic direction k, of 25%, 50%, and 100% with respect to their original length. The resulting

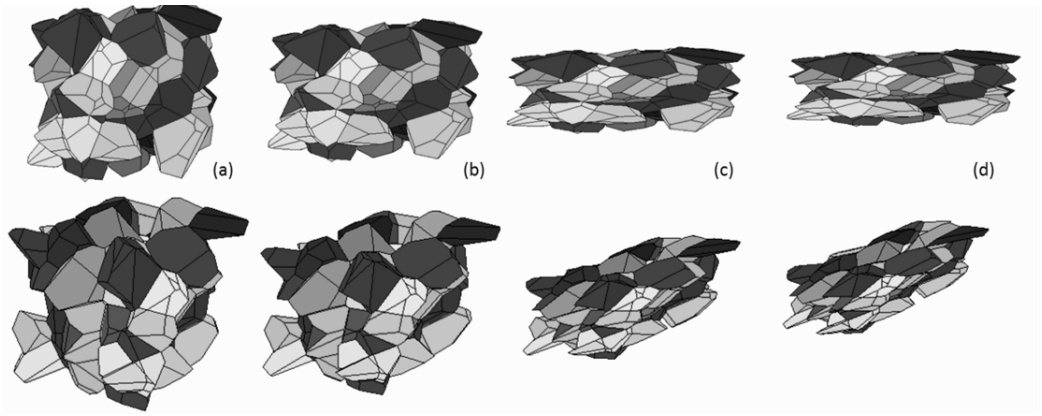


Figure 4.3: Frontal (top) and isometric (bottom) view of (a) an assembly stretched of (b) 25%, (c) 50%, and (d) 100%

effect of the variables ρ and H_k on *sphericity* and *slenderness* of the grains is presented in Section 4.5.1.

4.2 Definition of the shape descriptors

Numerous alternative definitions of shape descriptors can be found in literature to describe the shape of the grains (Section 2.2.1.2). The computation of the shape descriptors is based on the concepts of *minimum bounding sphere* (MBS) and *minimum volume enclosing ellipsoid* (MVEE). To allow for the validation of the numerical results against experimental measurements taken from different sources, the presented work adopts two alternative expressions of sphericity: the *classic sphericity* ψ and the *Wadell sphericity* ψ_w [12]. These are mathematically defined as:

$$\psi = \frac{V_p}{V_{cs}} \tag{4.5a}$$

$$\psi_w = \frac{A_p}{A_{cs}} \tag{4.5b}$$

where V_p and V_{cs} are respectively the volume of the particle and of the MBS, whilst A_p and A_{cs} represent the respective surface areas.

An alternative widely adopted definition of sphericity, the *intercept sphericity* ψ_I,

is based on the relations between the shortest (δ_{min}), the intermediate (δ_{med}), and the longest (δ_{Max}) radii of the MVEE:

$$\psi_I = \frac{\delta_{min} \cdot \delta_{med}}{\delta_{Max}^2} \tag{4.5c}$$

However, since [182] proved that $\psi_I \equiv \psi$ within an approximation of 2%, in this work the two quantities are considered equivalent.

Finally, the slenderness of each grain S is defined as the ratio between the maximum (δ_{Max}) and minimum (δ_{min}) axes of the MVEE [1].

$$S = \frac{\delta_{Max}}{\delta_{min}} \tag{4.6}$$

The definitions of MBS and MVEE are reported in the next two sections.

4.2.1 Bounding sphere evaluation

The calculation of the sphericity requires the knowledge of the radius of the smallest sphere that contains each grain. The evaluation of the minimum bounding sphere (MBS) of an irregular convex body (defined by its vertices) is a well-known problem of computational geometry and it is frequently adopted in many applications such as computer graphics and pattern recognition. The definition of the minimum bounding sphere has been addressed in several works [183, 184].

Let $k = \{X_1, X_2, ..., X_N\} = \{(x_1, y_1, z_1), ..., (x_N, y_N, z_N)\}$ be a set of N points in $\Re^3$. The minimum bounding sphere MBS_k exists, it is unique, and it represents the smallest sphere containing all points in k. The exact minimum bounding sphere is defined by its radius R_k, its centre c_k and it can be unequivocally computed by solving a quadratic optimisation problem of the kind below

$$\begin{cases} \min\limits_{c_k, R_k} R_k^2 \\ \|X_i - c_k\| \leq R_k^2 \ \ \forall i = 1, 2, 3, ..., N \end{cases} \tag{4.7}$$

The easiest way of solving the problem relies on the adoption of a *brute force* approach, which consists of building a sphere for each possible quadruplet of vertices

of the polyhedron and then compare their radii to find the minimum one. This approach requires a number of operations in the order of $O(n_v^5)$, therefore rapidly increasing with the number of vertices (n_v), making this method extremely inefficient in case of irregular polyhedra with high number of vertices. Recently, more efficient numerical iterative methods have been proposed to identify the MBS [185, 186].

The method adopted in this work defines the MBS in an incremental fashion. It is inspired by the so-called *move-to-front* approach presented, for the first time, by Welzl [184] and subsequently implemented in a fast and robust way by Gartner [187].

This method efficiently identifies the smallest subset of points $D = \{X_\alpha, X_\beta, X_\gamma, ..., X_\omega\} \subset k \in \Re^3$ that defines the minimum bounding sphere $MBS_k \equiv MBS_D$.

The procedure to find the MBS starts with the definition of a random subset of 2 points $D = \{X_\alpha, X_\beta\}$. The relative position of the points $k - \{D\}$ with respect to MBS_D is sequentially checked. If the generic point X_γ falls outside the sphere, the subset D is enlarged to include the point X_γ. The position of the points $k - \{D\}$ is checked against all the bounding spheres defined by the points in D that have X_γ on the boundary. The procedure is repeated until all points k are included in MBS_D.

The points are kept in an ordered list. Each new point to be checked is moved to the front of the list. Therefore, it will be processed earlier in the following iteration. From here, the name *move-to-front approach*. The proposed method grants a noticeable reduction of the required number of operations, from $O(n_v^5)$ of the *brute force* approach to $O(n_v)$ [187].

4.2.2 Evaluation of the minimum volume enclosing ellipsoid

The calculation of the minimum volume enclosing ellipsoid (MVEE) is needed for the definition of the slenderness of the grains.

Given a set k of N points in $\Re^3$, the corresponding MVEE can be computed by solving a minimisation problem of the kind:

$$\begin{cases} \min\limits_{c_k, E_k} det(E_k^{-1}) \\ (X_i - c_k)^T E_k (X_i - c_k) \leq 1 \ \ \forall i = 1, 2, ..., N \\ E_k > 0 \end{cases} \tag{4.8}$$

where c_k is the centre of the MVEE and E_k represents a symmetric positive definite $3x3$ matrix containing all the information regarding the shape of the ellipsoid.

Welzl [184] presented a method for the calculation of the MVEE similar to the one adopted for MBSs (defined in Section 4.2.1) that requires a number of operations still linearly proportional to n_v. However, the proportional constant for MVEE in three-dimensional problems ($\sim 81!$) is much higher than the one defined for spheres ($\sim$ 16!). For the aforementioned reason, this work adopts a more efficient - although approximated - method.

The algorithm used herein was initially proposed by Khachiyan [188], and subsequently improved by Moshtagh [189]. A change of variables in the definition of the ellipsoid makes eq. (4.8) a convex optimisation problem of the kind presented in eq. (4.9):

$$\begin{cases} \max\limits_{u_k} \log[\det(V(u_k))] \\ u_k \geq 0 \end{cases} \tag{4.9}$$

where $V(u_k) = Q\,\mathrm{diag}(u_k)\,Q^T$, and Q represents the *lifting* of the points X_i in the hyperplane $\Re^4$.

The adoption of a *conditional gradient ascent* method allows to solve eq. (4.9) by iteratively increasing u_k until the desired tolerance ε is reached:

$$(u_k^{new} - u_k^{old}) \leq \varepsilon \tag{4.10}$$

The results presented in this chapter are obtained using a tolerance $\varepsilon = 10^{-4}$.

4.3 Packing algorithm

The Voronoi diagram tessellates the space in tightly assembled cells, defining a continuum structure without voids between neighbouring grains. The granular materials, instead, are disordered assemblies of discrete particles. Therefore, the grains have to be repositioned *disorderly* to obtain representative models.

A geometrical packing of particles with complex polyhedral shapes can be obtained by initially assembling their corresponding bounding spheres (BSs), using the 3D-clew method presented in Section 3. The radius of the BSs is controlled by a scaling factor (Λ) to arbitrarily increase the radius of the MBSs, thus providing full control on the volume fraction of the granular particles and allowing for the generation of representative models of granular media. The densest possible geometrical packing (i.e. $BS \equiv MBS$) is obtained using the minimum scaling factor ($\Lambda = 1$).

Although the packing algorithm ensures the tangency between BSs, it does not guarantee the achievement of the densest configurations since the tangency between bounding spheres does not entail the contact between the inscribed polyhedral particles.

Denser samples, in physical equilibrium, can be obtained subsequently applying a mechanical packing method (e.g. DEM/FEM). The preliminary adoption of geometrical packing methods (reducing the distances between neighbouring particles) massively reduces the total computational time required for assembling the particles.

Figure 4.4 shows an example of how a polydisperse agglomerate of BSs is packed using the 3D-clew method and how, by inserting each grain in its corresponding BS, the final packing of polyhedral bodies is obtained.

4.4 Computational cost and scalability

The computational cost of the entire method is equal to the sum of the costs of three main operations: *generation of the Voronoi cells*, *evaluation of the MBSs*, and *geometrical packing*.

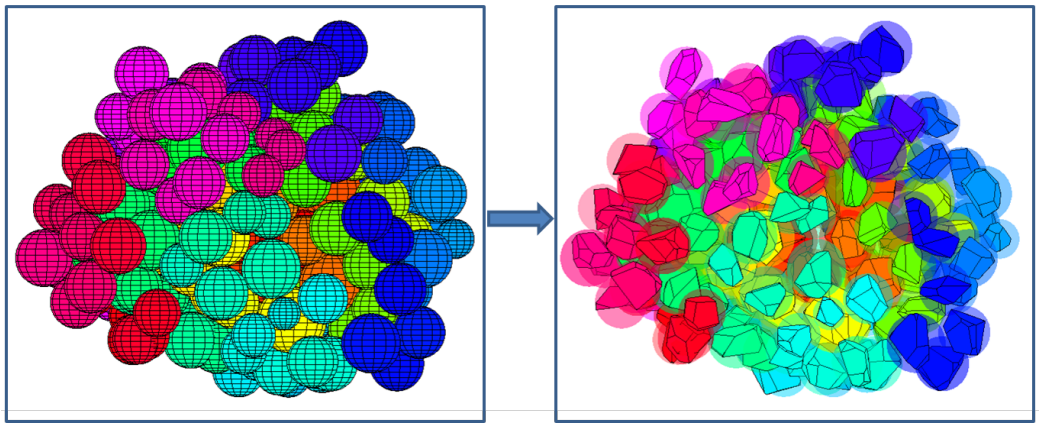


Figure 4.4: 3D clew packing of the spheres ($e \approx 0.8$) and corresponding inscribed grains ($e \approx 4.3$)

A noticeably reduced total computational cost is a consequence of the high efficiency of the methodologies presented to perform the three operations. For example, the approach developed presents two main advantages with respect to random deposition mechanical packing methods: the absence of contact checks between polyhedral bodies and the initial enhanced closeness between neighbouring particles. Both of them derive from the imposition of the tangency between *minimum bounding spheres* embedding the particles. Additionally, because of the relatively small scalability factor, the computational efficiency of the method enhances for high number of particles. Specifically, the computational cost of the generation of 3D Voronoi tessellations is in the order of $O(n \log v)$ [190], where v is the number of vertices in the tessellation and n is the number of cells. The calculation of the MBS of each grain, instead, has a computational cost equal to $O(n_v)$, with n_v equal to the number of vertices of each grain [187]. Consequently, the computational cost for an assembly composed of n particles is equal to $O(\sum_{i=1}^{n} n_v^i)$. However, granted that the calculation of the MBS of a particle is independent from the calculation of the other MBSs, the process can be parallelised reducing considerably the total computational time. Finally, the computational cost of the packing of spheres is between $O(n \log n)$ and $O(n^2)$, as reported in Section 3.3.3. Therefore, it ultimately depends upon the nature of the problem analysed, as well as on the level of parallelisation adopted.

4.5 Parametric study of the models

The ability of the developed method to reproduce, both in terms of particle shapes and consolidation state, an extremely wide range of morphologies is shown in this section.

In particular, Section 4.5.1 presents a parametric study of the effect of ρ and H_k on the shape descriptors. Then, Section 4.5.2 explains how the hardcore radius affects the consolidation state of the assembly.

4.5.1 Effect of ρ and H_k on the shape descriptors

The ability of the Hardcore Voronoi tessellation to control the grains shapes is demonstrated evaluating the shape descriptors of 8 sets of assemblies with hardcore radius ρ equal to 0, 0.125%, 0.25%, 0.375%, 0.5%, 0.625%, 0.75%, and 0.8% of the edge of the seeding domain. Four different grain assemblies per set are obtained by seeding 1500 nuclei in a cubic domain. As explained before, the external grains are discarded to minimise the effect of the boundaries on the cells shape, thus reducing the number of grains to about 800.

The curves in Figure 4.5 represent the effect of the Hardcore radius ρ on the frequency of occurrence of grains with equal shape descriptors. A smaller ρ reduces the peak value, whilst widening the distributions of all the shape descriptors. This trend becomes less evident for ρ smaller than 3.75%. On the contrary, high values of ρ produce more spherical particles with higher values of sphericity and lower of slenderness, thus inducing a regularisation of the Voronoi cells. The enhanced uniformity of shapes is also confirmed by the smaller standard deviations obtained for higher values of ρ.

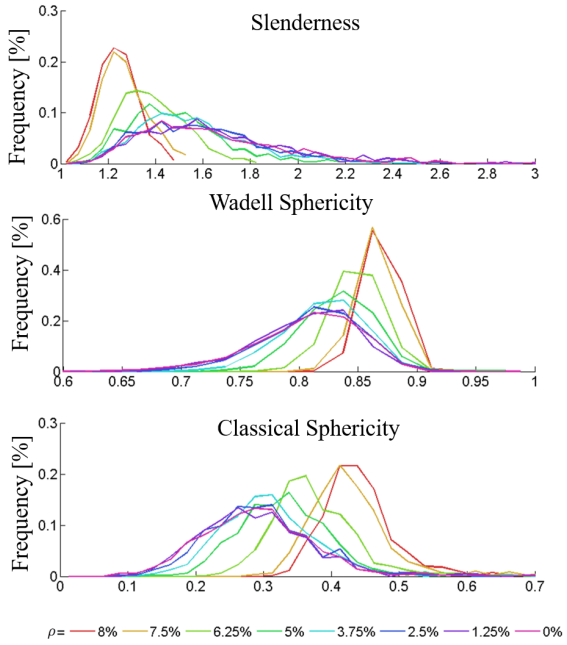


Figure 4.5: Distribution of S, ψ_w and ψ for different values of ρ

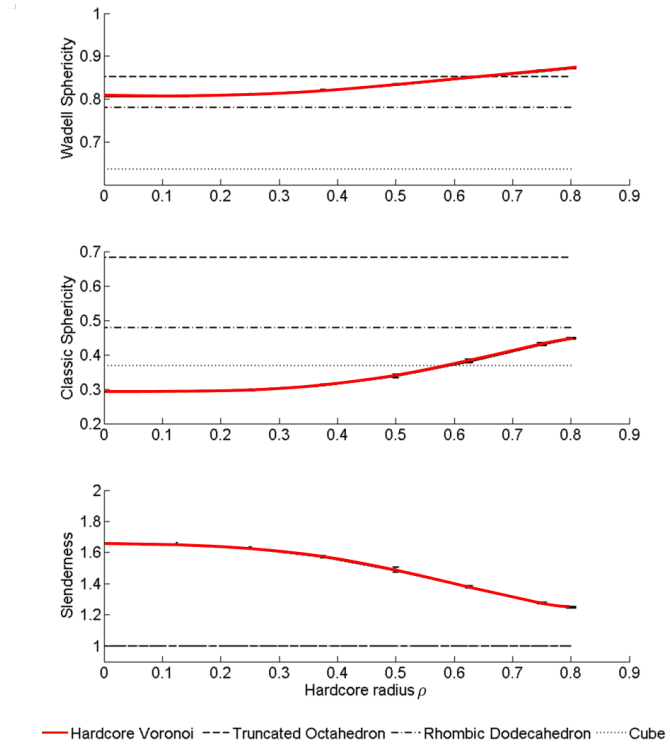


Figure 4.6: Variation of ψ, ψ_w and S with ρ

Figure 4.6 reports the mean values of the bell-shaped distributions presented in Figure 4.5.

Figure 4.6 clearly confirms that an increase in the values of the hardcore radius ρ yields higher values of sphericity whilst reducing the slenderness of the grains. The statistical variance of the results is graphically represented with error bars. The extremely reduced variance suggests that the chosen domains are statistically representative of the geometrical properties of the grains. For the sake of comparison, the shape descriptors obtained for the only three regular polyhedra able to uniformly tessellate the space are included into the graph; in particular, the three black dotted lines represent reference values of shape descriptors obtained when modelling the grains as cubes, rhombic dodecahedra, and truncated octahedra. Obviously, sphericity and slenderness equal to 1 would be measured for perfectly spherical particles.

Additional variability to the form of the grains can be achieved imposing the transformations reported in eq. (4.3) and eq. (4.4). The stretching of the grains along an arbitrary direction allows for the reproduction of elongated and pebble-like particles, increasing the range of reproducible granular materials. Figure 4.7 shows the effect of the stretching on the shape descriptors. The same granular assembly is stretched of 25%, 50%, and 100% (corresponding respectively to H_k equal to 1.25, 1.50, and 2.00) with respect to the original configuration.

As expected, H_k has an opposite effect than ρ on the shape descriptors. Higher slenderness and reduced sphericity, with a non-linear dependence over H_k, are measured for elongated grains. However, the effect of H_k upon the slenderness seems to be almost independent from the Hardcore radius, as the curves depicting the relations between ρ and S at different levels of transformation are nearly parallel to each other (Figure 4.7).

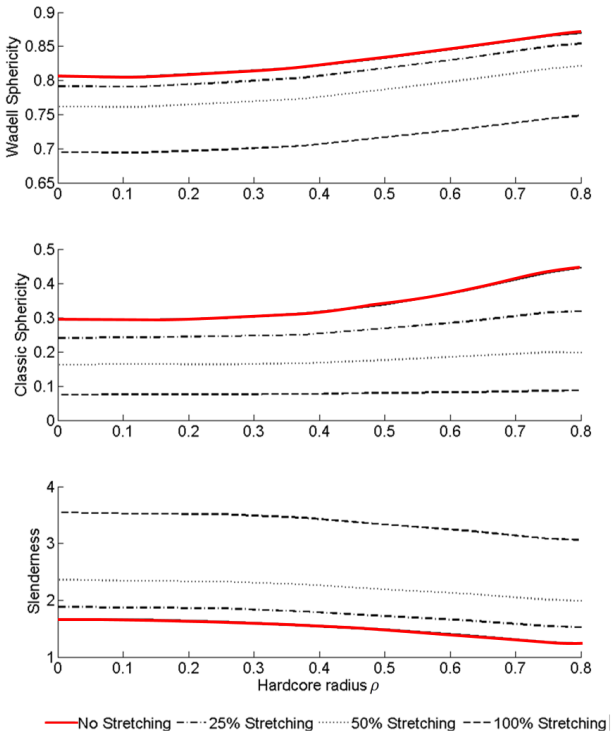


Figure 4.7: Variation of ψ, ψ_w and S with ρ, for different values of H_k

4.5.2 Consolidation state of the packings

As already done for spherical particles, the effectiveness of the geometrical packing procedure can be measured in terms of void ratio of the domain [82]. As explained in Section 3.3 and shown in Figure 3.19 and Figure 3.20, the consolidation states of the aggregates for different values of ρ (i.e. 0%, 0.125%, 0.25%, 0.375%, 0.5%, 0.625%, 0.75%, and 0.8%) is evaluated as an average of the void ratio values for fictitious boxes with sides comprised between 50% and 80% of the original domain edge. Figure 4.8 summarises the values of void ratio and relative variations for both the polyhedral particles (e_p) and the bounding spheres (e_{MBS}).

According to the definitions of MBS and void ratio, it is obvious that $e_p \geq e_{MBS}$ for any aggregate. Nevertheless, in light of the higher computational efficiency offered by the proposed methodology with respect to other packing techniques that perform contact checking between all bodies in the domain, the obtained values of void ratio

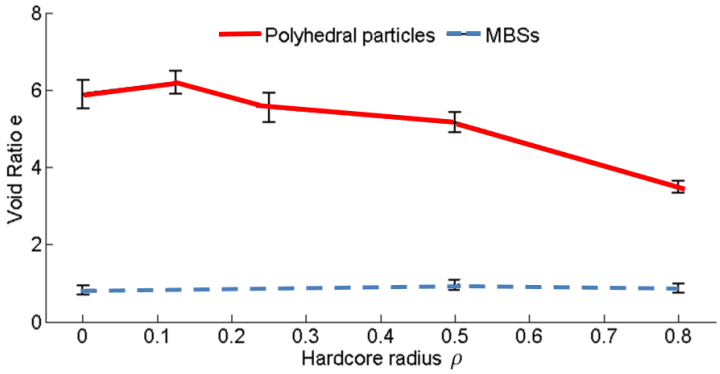


Figure 4.8: Variation of the void ratio with ρ

can still be considered acceptable. Further compaction can be applied to the models by employing mechanical packing methods to reduce the void ratio to values closer to the experimental measurements.

The void ratio (e) of the polyhedral particles reduces drastically with the increase in the *Hardcore radius*, whilst the e of the bounding spheres is independent from ρ. In particular, since the sphericity (in Figure 4.6) decreases when ρ increases, ψ could be interpreted as a direct measure of the difference between the void ratio of the assemblies made of polyhedrons and of the corresponding bounding spheres, with $e_p \to e_{MBS}$ for $\psi \to 1$.

4.6 Representativeness of real granular materials

In this section, the models are validated against experimental measurements of size distributions and shapes of real granular media, thus proving the capability of the presented methodology to reproduce an extremely wide spectrum of materials.

4.6.1 Shape descriptors

Figure 4.9 shows how the right combination of ρ and H_k allows for the generation of particles with an extremely wide range of shape descriptors, reproducing many

features observed in granular materials. The experimental data reported in Figure 4.9 are taken from [191][1] and [192, 193][2].

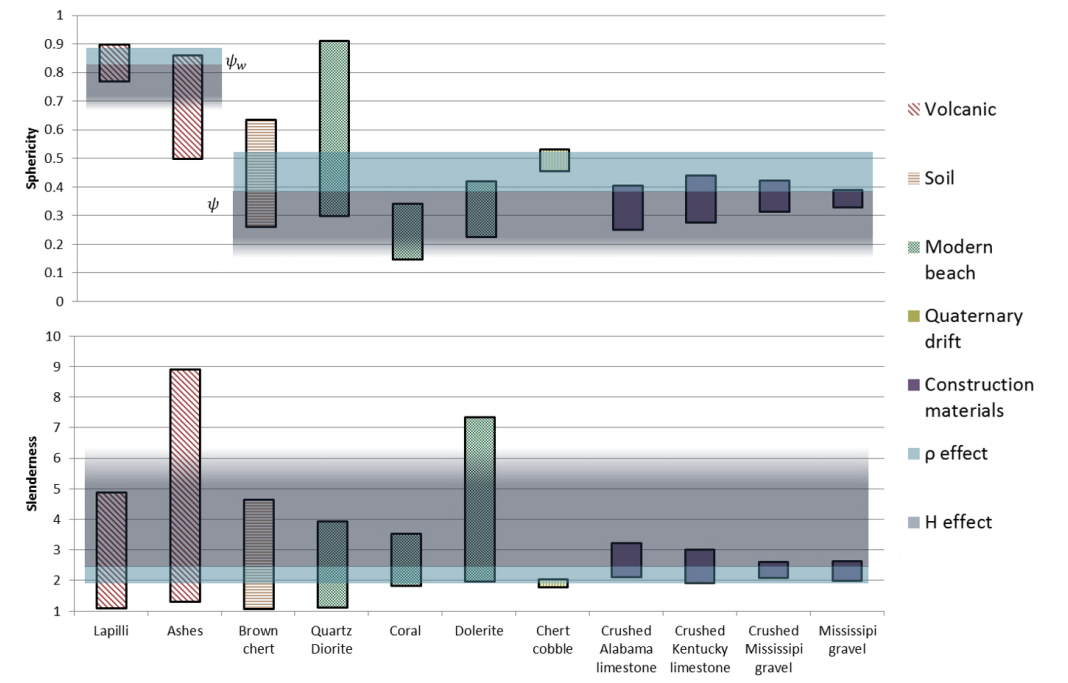


Figure 4.9: Comparison of the properties of real and numerically generated granular materials

The shaded areas in the picture represent the range of numerically obtained values of the shape descriptors, for given H_k (between 25% and 100%) and ρ (between 0 and 1). However, the adoption of higher values of stretching factor (inducing a reduction of the sphericity and increase of the slenderness) would increase the range of representativeness of the numerical grains. This comes at the cost of higher values of void ratio of the final geometrical assemblies, thus limiting the effectiveness of the presented packing method. Nevertheless, it is able to model most of the range of shape descriptors experimentally measured for natural and artificial materials (e.g. volcanic rocks and ashes, soil, sand, gravels).

Figure 4.10 shows a qualitative comparison of experimental images of real grains

[1]The values of S for the volcanic particles are inferred from the slightly different definitions of slenderness and flatness, leading to a slight overestimation of the real scatter.

[2]For these granular materials the classic sphericity ψ is reported because of the absence of measurements of the surface area.

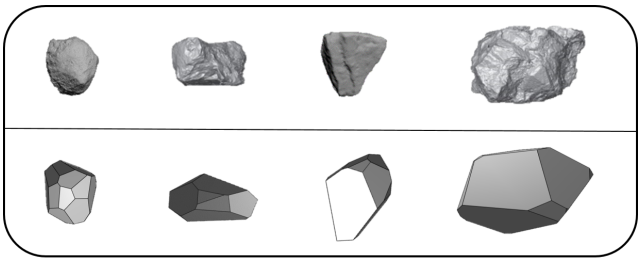


Figure 4.10: Visual comparison of numerically generated (bottom) and tomography scans [191, 89] (top) of single sand grains

against the polyhedral particles produced with the presented method. Even the visual comparison proves the ability of the method to reproduce the form of real granular materials. A quantitative validation of the models of granular media, instead, is reported in the next section.

4.6.2 Validation

This section presents two examples of quantitative validation, in terms of shape descriptors and size distributions, of the generated numerical models. The Q-Rok sand is used as reference material for a first validation test, since it represents a standard example (widely adopted in this thesis) of sand with polyhedral grains. Its size distribution is reported in Figure 6.1b. Several images of Q-Rok sand grains are captured using the Alicona Infinite Focus 3D profilometer with $20X$ magnification lens. The images are then analysed using the open source image processing program ImageJ, by employing contrast edge detection techniques on binary images. A built-in post-processing procedure allows for the identification of 2D shape descriptors such as circularity and slenderness of the grains [194]. Unfortunately, the experimentally measured circularity (obtained starting from 2D images) cannot be related to the numerically obtained three-dimensional sphericity of the grains. Therefore, only the slenderness and size distribution can be used for comparison with the experimental measurements.

The models are generated using the grain sizes reported in Table 4.1, with Hard-

core radius $\rho = 0.5$ and $H_\eta = 0.5$.

Radii [mm]	Percentage [%]
0.075	12
0.1	33
0.15	10
0.2	10
0.25	25
0.3	10

Table 4.1: Size distribution of Q-Rok sand given as an input to the model

Five different numerical samples, composed of about 1000 particles each, are used to generate statistics.

Figure 4.11 shows the comparison between experimental (continuous line) and numerical (dotted line) size distributions of the sample, expressed in terms of their cumulative distribution function (CDF).

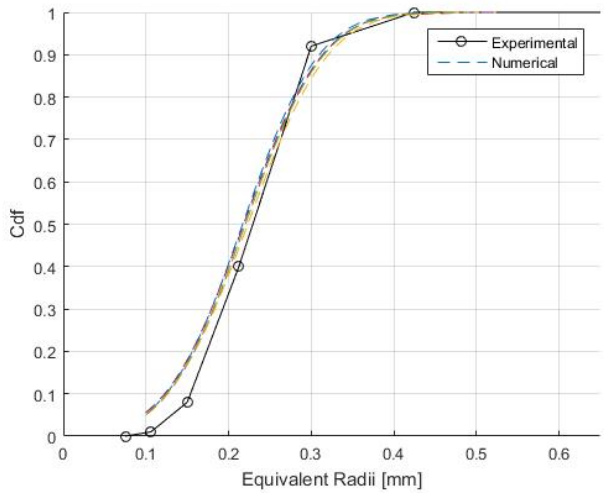


Figure 4.11: Comparison of numerically generated (dotted line) and experimentally measured (continuous line) size distributions of Q-Rok sand

The size distributions obtained for the five different numerical assemblies match the experimental measures (with root-mean-square error less than 11%) and do not show any particular variation between different samples, showing a good reproducibility of the results. Figure 4.12 shows, instead, the comparison in terms of slenderness.

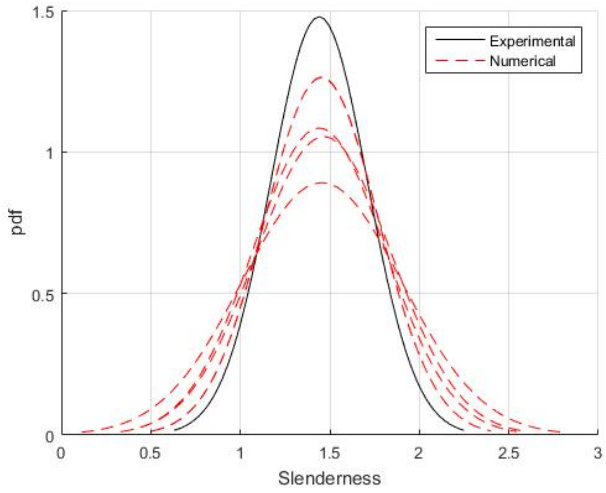


Figure 4.12: Comparison of numerically generated (dotted line) and experimentally measured (continuous line) slenderness values of Q-Rok sand

The numerical and experimental *PDF*s show good agreement in terms of mean values, proving the ability of the numerical models to represent the slenderness measured for Q-Rok sand. In this case, the choice of different numerical samples - obtained using the same input parameters - yields a noticeable variation in the standard deviations (from 1% up to 10%). An optimisation procedure should be implemented to further improve the matching between experimental and numerical measures. This will be topic of a future study.

To definitively prove that the proposed method can simultaneously capture the distributions of sizes and 3D shape descriptors (i.e. sphericity and slenderness), the experimentally measured properties of *Alabama limestone* grains reported in [193] are used for the second quantitative validation of the models.

In this case, the assemblies are obtained by combining three sets of polyhedral particles. In particular, each set consists of about 100 particles, with ρ equal to 3.75% of the domain edge. The same Hardcore radius is imposed to the three sets of Voronoi tessellations (i.e. $\rho = 3.75\%$ of the domain edge), whilst three different values of H_η (i.e. 2.18, 2.14, and 1.78) and H_ξ (i.e. 1.36, 2.00, and 1.67) are used.

Table 4.2 presents the results in terms of mean and variance of the probability

distribution function (PDF).

Parameter	Mean [193] (Experimental)	Variance [193] (Experimental)	Mean (Numerical)	Variance (Numerical)
$\delta_{max}[mm]$	29.65	7.19	29.26 ± 0.70	6.55 ± 0.20
$\delta_{med}[mm]$	21.67	3.41	20.92 ± 0.50	2.82 ± 0.25
$\delta_{min}[mm]$	12.37	3.45	12.92 ± 0.25	2.86 ± 0.13
$Sphericity(\Psi)$	0.31	0.11	0.34 ± 0.02	0.10 ± 0.003
$Slenderness(S)$	2.59	0.62	2.31 ± 0.09	0.45 ± 0.04

Table 4.2: Experimental and numerical measures of size and shape descriptors of Alabama limestone particles

An excellent agreement between experimental and numerical values both in terms of dimension of the particles and first order shape descriptors (i.e. sphericity and slenderness) is obtained.

Figure 4.13 provides a visual comparison between the sizes of the numerical particles and the experimentally measured dimensions of Alabama limestone.

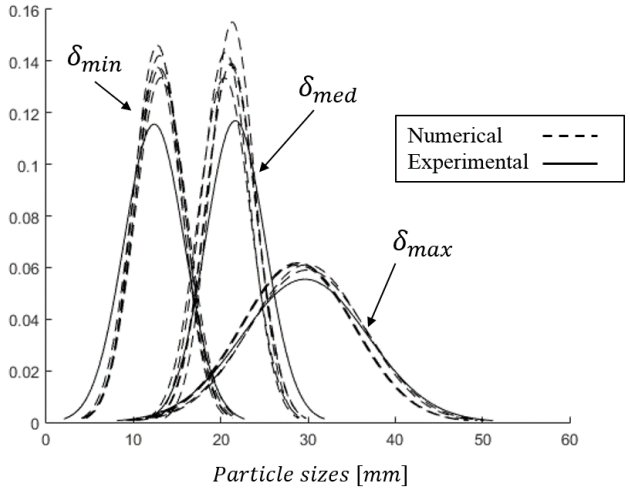


Figure 4.13: Comparison of the experimental and numerical probability distribution functions of the length, width, and thickness of Alabama limestone particles

The solid curves represent the *PDF* of the length, width, and thickness of the grains measured by Kuo et al. [193]. The dashed lines are the *PDFs* of the size of

the five numerical models. Both show a perfect agreement between experimental and numerical results.

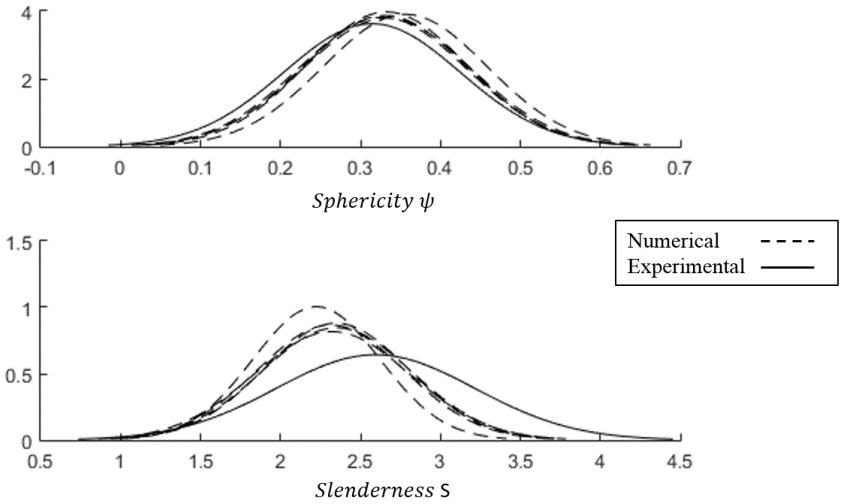


Figure 4.14: Comparison of the experimental and numerical probability distribution functions of sphericity and slenderness of Alabama limestone particles

Finally, Figure 4.14 visualises the capability of the method to also reproduce the form of real sand grains. The sphericity values of the numerically samples are in good agreement with the experimental ones. A clear mismatch is noticed, instead, for the slenderness of the grains. This is thought to be caused by the fact that, unlike sphericity, the experimental values of slenderness (S) were obtained by multiplying the measurements of flatness (F) and elongation (E) reported in [193], as shown in eq. (4.11)

$$S = E * F \tag{4.11}$$

where

$$S = \frac{\delta_{max}}{\delta_{min}} \quad E = \frac{\delta_{max}}{\delta_{med}} \quad F = \frac{\delta_{med}}{\delta_{min}} \tag{4.12}$$

The error propagation leads to a slight overestimation of the real scatter between numerical and experimental measures.

4.7 Summary

This chapter presents a novel method, based on a modified Hardcore Voronoi tessellation technique, for the generation and geometrical packing of arbitrarily shaped polyhedral particles statistically representative of real granular assemblies.

The range of representativeness of the Voronoi cells is further increased by conditioning the seeding of the domain (expressed in terms of *hardcore radius* ρ) and applying geometrical transformation (expressed in terms of *stretching* H_k) to the cells.

The numerical models are compared against real materials in terms of *shape descriptors* and size distributions, proving the ability of the method presented to cover a wide range of realistic shapes. The generated particles are then enclosed in bounding spheres and geometrically packed using the 3D-clew geometrical approach, thus creating chaotic assemblies. Additionally, the packing density of the particles can be adjusted by varying the radii of the bounding spheres.

The methodology developed guarantees the achievement of densely packed assemblies at extremely low computational costs when compared against serial deposition mechanical methods.

In terms of particle shape, the method can accurately reproduce a wide range of natural and synthetic granular media, as visually presented in Figure 4.9.

Chapter 5

Definition of void ratio based Representative Volume Elements for granular materials

The generation of numerical samples statistically representative of assemblies of discrete particles is only a starting point for the correct modelling of granular materials. In many cases, despite the discrete and heterogeneous nature at the micro-scale, granular media are homogenised before being adopted for the representation of the mechanical behaviour at larger scales. For example, both FE modelling (widely adopted for simulating the behaviour of granular materials at the macro-scale in multiscale frameworks) and the uniaxial elastic wave theory used in the experimental characterisation (by means of SHPB) rely on the hypothesis of continuum.

This justifies the importance of the definition of Representative Volume Elements (RVEs) to be used in both numerical and real experiments on granular materials.

In particular, Section 2.4 identifies the need for the definition of RVEs to set the dimensions of the samples to be used in the SHPB experiments on granular materials.

The work presented in this chapter [1] provides a method for the numerical computation of RVEs based on the correct representation of the initial consolidation state

[1]Part of this chapter has been reprinted from the International Journal of Impact Engineering, Vol. 91, F. De Cola, A. Pellegrino, E. Barbieri, D. Penumadu, N. Petrinic, "Void ratio based representative volume element for modelling the high strain rate behaviour of granular materials", 46-55, Copyright (2016), with permission from Elsevier. Both planning and implementation of the work were conducted by the first author, with the others in advisory role.

of granular materials. It states, for the first time in literature, the existence of a lower limit on the dimensions of the specimens to be used in high rate experiments. As a result, this work proves that it is not possible to use arbitrarily small samples in the experiments, since samples smaller than the RVE do not statistically represent the desired consolidation state of the medium. In addition, the adoption of samples whose dimensions are equal to the pre-determined RVE ensures an improved experimental repeatability of the results when compared against existing data [45].

5.1 Numerical computation of the void ratio within the sample

The generation of three-dimensional assemblies of grains, representing the sand samples under examination, is the first step required for the determination of the RVE. The correct numerical reproduction of experimental conditions implies the appropriate modelling of the microstructure of granular materials (in terms of grain size distribution, grain shape, and physical properties), confinement and boundary conditions. An in-house software (DEST - Discrete Elements Simulation Tools) is used to model the motion and interaction of 3D particles during their gravitationally assisted deposition and consolidation. Additional information on the Discrete Element methodology is reported in Section 2. This approach allows for numerous simulations to evaluate the final packing densities as a function of the granular media and deposition process. The detailed description of the adopted numerical method for the evaluation of the RVE is included in the next section. Once the numerical packing is generated, the variation of void ratio within the sample and its mean value have to be estimated. Moreover, it has to be verified whether the numerical values match the experimental ones, thus correctly reproducing the initial consolidation state of the packing. The definition of the RVE should take into account the variations of the packing density within the sample. In fact, the walls of the container induce an ordered distribution of particles in their vicinity while the particles, far from the

walls, are randomly arranged. As a result, the particles immediately close to the walls, typically within a distance of $2-4$ equivalent diameters, should not be considered statistically representative of the consolidation state of the medium [195, 196, 197].

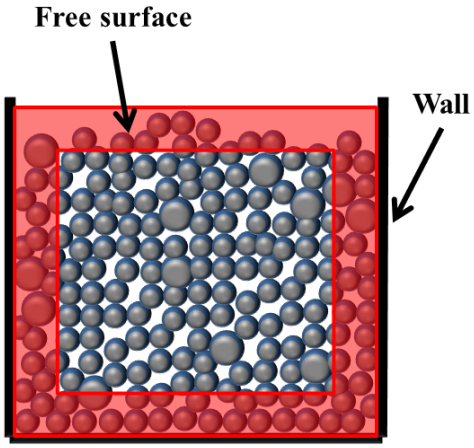


Figure 5.1: Two-dimensional schematic representation of the three dimensional effect of the wall and free surfaces on the RVE

For non-spherical particles, instead, the variation of local density due to the presence of the walls is less significant. In fact, non-spherical particles tend to generate a more random packing [198]. Furthermore, when only gravity is applied, the presence of the uneven free surface on the top of the samples (Figure 5.1) produces significant oscillations of the void ratio. The numerical approach used to compute the void ratio and its variation within the sample is based on eq. (5.1), which is obtained by rewriting eq. (2.2) as a function of the volume of particles V_s enclosed in a container of volume V_{tot}:

$$e = V_v/V_s = (V_{tot} - V_s)/V_s = V_{tot}/V_s - 1 \tag{5.1}$$

V_s and V_{tot} are numerically computed considering smaller fictitious volumes - which locally define V_{tot} in eq. (5.1) - enclosed in the real container and computing only the volume of the particles and their fractions V_s contained in them. This approach takes into account the effect of walls and free surface on the consolidation state. The fictitious volumes can be defined in two ways:

1. By gradually increasing their height (Figure 5.2), starting from the bottom of the real container. This approach assesses the variation of the consolidation state across the height of the sample.

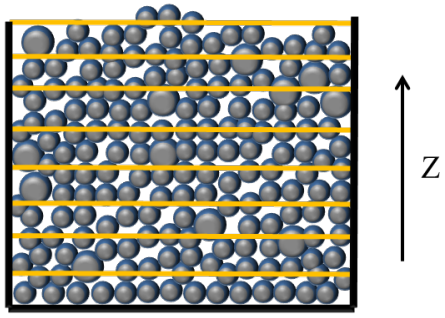


Figure 5.2: Schematic representation of the variation of the height of the fictitious volume

2. By simultaneously increasing all three spatial dimensions starting from the centre of the sample (Figure 5.3).

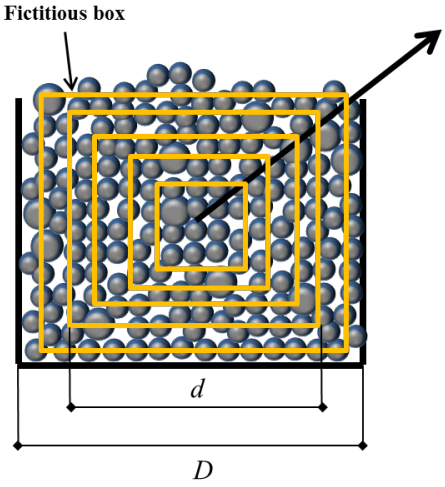


Figure 5.3: Schematic representation of the variation of all the dimensions of the fictitious volume

Both cases present six different configurations to be taken into account when computing the particle fractions contained in the virtual volumes (the fraction of particles comprised in the volume is coloured white in Figure 5.4). The ratio between d_0, the distance from the centre of the particle to the boundary, and the radius R of the particle delineates all possible locations (Figure 5.4a). The distance d_0 is positive

if the centre of the particle is inside the volume of interest.

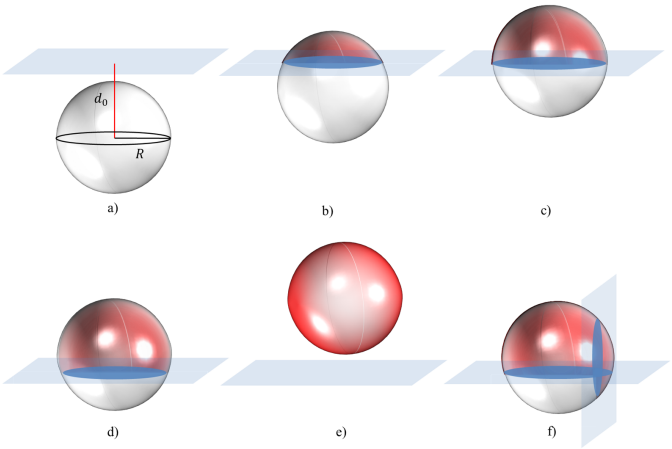


Figure 5.4: Possible intersections between boundaries and spheres

Table 5.1 summarizes the definitions of the volumes of particles taken into account in all configurations.

Ref. Figure	**Condition**	**Description**	**Definition of particle volume**
Figure 5.4a	$\frac{d_0}{R} > 1$	Spheres totally contained in the volume;	$V = V_{sph}$
Figure 5.4b	$0 < \frac{d_0}{R} < 1$	The sphere is inside with more than half of its volume;	$V = V_{sph} - V_{sph-cup} = \frac{4}{3}\pi R^3 - \pi d_0^2 \left(R - \frac{d_0}{3}\right)$
Figure 5.4c	$\frac{d_0}{R} = 0$	The centre of the sphere is on the boundary;	$V = \frac{V_{sph}}{2}$
Figure 5.4d	$-1 < \frac{d_0}{R} < 0$	Less than a half of the sphere is inside the volume;	$V = V_{sph-cup} = \pi (R - d_0)^2 \left(R - \frac{R-d_0}{3}\right)$
Figure 5.4e	$\frac{d_0}{R} < -1$	Spheres totally outside the volume;	$V = 0$
Figure 5.4f	–	The spheres intersects two corner of the box at the same time;	Procedure reported in the Appendix A in [199]

Table 5.1: Volume evaluation of the spheres contained in the fictitious volume

The void ratio e is computed for each considered fictitious volume (for different d/D, Figure 5.3), hence defining its variation within the sample. Figure 5.5 shows an example of the typical e vs d/D curves, depicting the effects of free-surfaces and boundaries upon the void ratio. These charts are obtained by varying the dimension (d) of the fictitious bounding volumes (within which the void ratio is computed) with respect to the dimension (D) of the real container.

Three different zones can be identified:

- ZONE ①: in this portion of the figure, the dimensions of the fictitious samples are comparable to the dimensions of the grains. Small volumes in the centre of the assembly contain only few voids and, consequently, the void ratio is very low.

- ZONE ②: in the central part of the plot the void ratio is not affected by the presence of walls and free surface. This portion of the chart is used to calculate the average void ratio and its standard deviation, adopted in the following analysis (Section 5.2).

- ZONE ③: the dimensions of the fictitious volume are comparable with those of the real container; the void ratio is very high because both the effects of free surface and walls are present.

Applying this numerical method for every packing, the mean value of the void ratio is computed and it is, then, used for the estimation of the RVE.

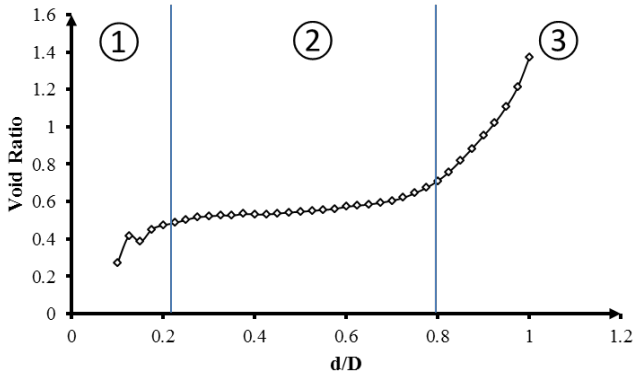


Figure 5.5: Qualitative distribution of the void ratio within granular materials, varying the dimension (d) of the imaginary volume with respect to the real container (D)

5.2 Numerical estimation of the RVE: Ottawa sand

In the past decades, the response of granular materials at high rates of strain (HR) by means of *Split Hopkinson Pressure Bar* experiments [29] has been extensively studied [41, 42, 45, 48, 71, 74, 200]. The main aim of this work is to demonstrate the existence, for the first time in literature, of a lower limit for the dimensions of the sample to be used in SHPB tests on granular materials and to present a numerical method for the computation of the RVE. Additionally, this work demonstrates that the adoption of specimen size comparable to the determined RVE improves the repeatability of the experimental results with respect to what is presented in literature. The numerical method for the calculation of the RVE presented in this chapter has to be considered as a general approach applicable to any kind of granular material. However, for the sake of simplicity, it has been adopted to define the RVE of a specific type of sand, the dry Ottawa sand in a dense initial consolidation state (corresponding to a void ratio of 0.56). Section 5.4, instead, will extend this approach to the estimation of RVEs for loose Ottawa sand. In order to define the minimum statistically representative sample at prescribed consolidation states, numerical simulations are conducted before carrying out the experiments.

The preparation of the sample is crucial for any experimentation on granular

materials since each test has to be representative of a fixed and reproducible consolidation state. Experimentally, specific consolidation procedures have been adopted to produce samples in initial dense consolidation state. The sand is dropped from a controlled height into a container and subsequently, it is compacted by tapping and compressing it (with a dropping weight of 240 g). A detailed description of the experimental preparation procedure will be presented in Section 5.3. The numerical simulations have to be representative of the experimentally achieved initial consolidation state. The Ottawa sand is composed of quasi-spherical grains, as visible in Figure 5.6.

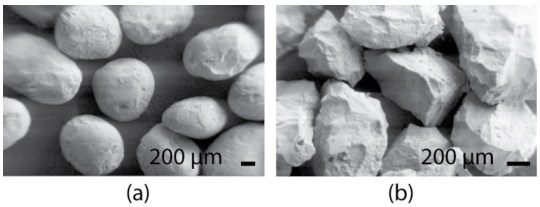


Figure 5.6: SEM images of grain shapes of Ottawa (a) and Q-Rok (b) sand

For this reason, the grains are modelled as spherical particles. Table 5.2 reports a discretisation of the experimental particle size distribution obtained by sieving. Table 5.3 lists the physical properties of the sand used in the simulations. All packing simulations are conducted using frictionless contact. This assumption is based on previous numerical studies [201, 202] which compared the results obtained by either using inter-particle friction or frictionless contact. It has been demonstrated that both approaches converge to the same solution when evaluating the consolidation state of very dense granular assemblies. Simulations carried out in presence of friction require the application of pressure loading and initial perturbative boundary conditions. On the contrary, the adoption of frictionless contact allows for the attainment of physically equilibrated densely packed granular systems exclusively by applying gravity [203, 204]. The assemblies considered in this study are consolidated under gravity and, therefore, no significant deformations are expected other than relatively small compliance along interacting surfaces of individual grains. Consequently, the particles

are modelled as rigid spheres that can overlap by the amount predictable by *Hertzian contact law*.

Radius	**Percentage**
0.355 mm	7%
0.25 mm	76%
0.175 mm	17%

Table 5.2: Radii distribution of the simulated sand particles

Material	Quartz
Density	2650 kg/m^3
E	76 GPa
ν	0.31

Table 5.3: Material properties of the Ottawa sand

The sand assemblies used in the simulations are packed by means of a combination of geometric deposition methods and mechanical approaches (application of gravity). Representative 3D geometrical packings of particles, based on the experimentally measured size distribution reported in Table 5.2, are generated using the *planar* packing algorithm detailed in Section 3.1 and in [153]. This geometric deposition method is based on the tangency between neighbouring particles and it can effectively consider poly-dispersity and different particle shape. This algorithm produces several parallel layers of particles, thus reproducing a prescribed mass flow through a funnel. The application of gravity, using the DEM, reproduces the pouring procedure required to have physically meaningful and stable systems (Figure 5.8). The RVE is calculated by means of the iterative procedure summarised in the flowchart in Figure 5.7. The starting point is the definition of the diameter of the container used in the experiments (point A in Figure 5.7). In this study, a stainless steel cylindrical container of diameter equal to 20 mm and 5 mm thick walls is used. The diameter D of the samples is equal to the diameter of the Split Hopkinson bar (20 mm) that will be used in the experiments and it respects the requirements for countering the effects of inertia and friction [29]. The thickness of the container is designed to resist applied

axial and resulting lateral stresses avoiding plastic deformation of the container and its lateral expansion.

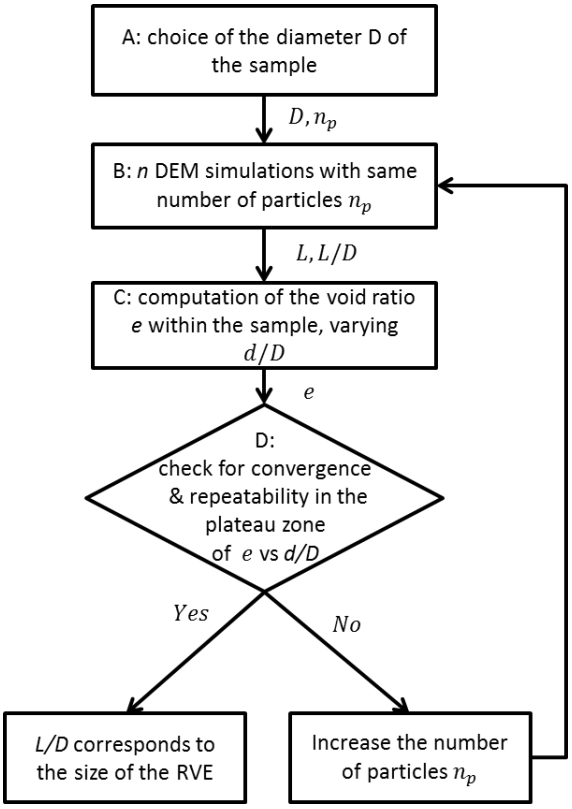


Figure 5.7: Flowchart of the iterative algorithm for the calculation of the RVE

Once the diameter is fixed, only the thickness of the sample along the direction of loading (L) needs to be defined. This depends, in turn, upon the amount of sand (m) to be poured in the container. From a numerical point of view, this is equivalent of fixing the number of particles to be included in the simulations. The first iteration of the process starts choosing an exploratory number of particles n_p equal to 5000. A number of n three-dimensional DEM simulations with same number n_p of particles are run, in analogy with repeated samples preparation in the experiments (point B in Figure 5.7). In our test case, 3 simulations per configurations are carried out (Figure 5.8). These are characterised by the same radii distribution but different arrangements.

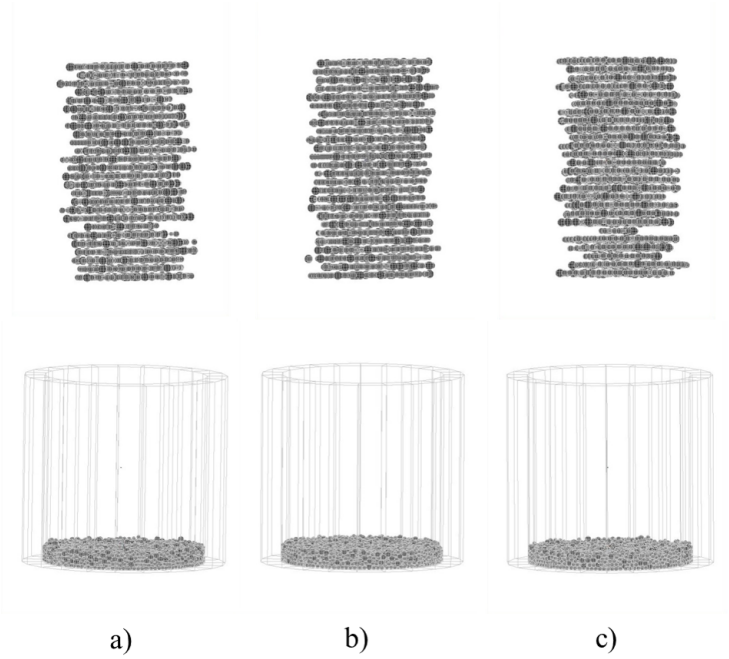


Figure 5.8: Three different initial and final assemblies produced with the combination of geometrical deposition method and mechanical method based on the application of gravity

The simulations are interrupted when the total kinetic energy of the system decreases to around 10^{-3} J, thus reproducing static equilibrium conditions (Figure 5.9).

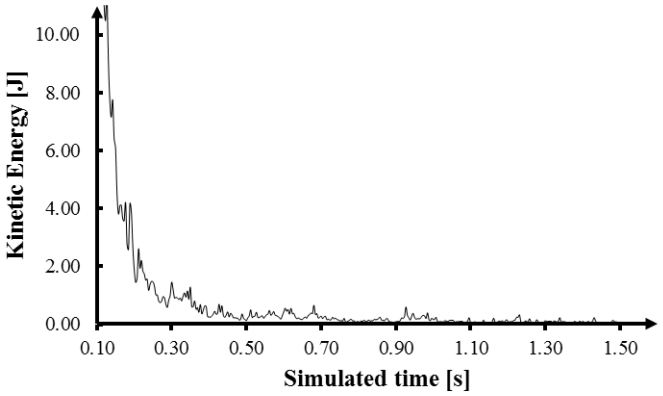


Figure 5.9: Example of the Kinetic Energy of the system during the deposition

At this stage, it is possible to measure the resulting length L of the sample in the loading direction and the corresponding slenderness (L/D). For the case of 5000 particles, the average length of the sample L after compaction is approximately 2.3 mm ($L/D = 0.12$), as reported in Table 5.4. Afterwards, the results of the simulations

are analysed to evaluate the mean value of the void ratio and its distribution within the samples (point C in Figure 5.7). For this purpose, the second procedure defined in Section 5.2 - based on the progressive increase of the dimensions of a virtual volume of interest (d, with diameter equal to length) - is used. The average values of the void ratio are extracted taking into account the portion of plot included between $d/D = 0.4$ and $d/D = 0.7$, characterised by a maximum variation of the void ratio of less than 0.1. Therefore, the void ratio resulting from each simulation is defined as the average value calculated in ZONE ②, as identified earlier in Figure 5.5. Table 5.4 reports the results obtained from the simulations in terms of void ratio and final height of the sample, after gravity is applied.

Sample	e_{mean}	$e_{variance}$	**Thickness L of the sample [mm]**
5000_1 mm	0.50	0.07	2.35
5000_2 mm	0.57	0.06	2.24
5000_3 mm	0.59	0.04	2.36

Table 5.4: Numerical results for the 5000 spheres simulations

Figure 5.10 summarizes the results obtained from the simulations of assemblies containing 5000 particles.

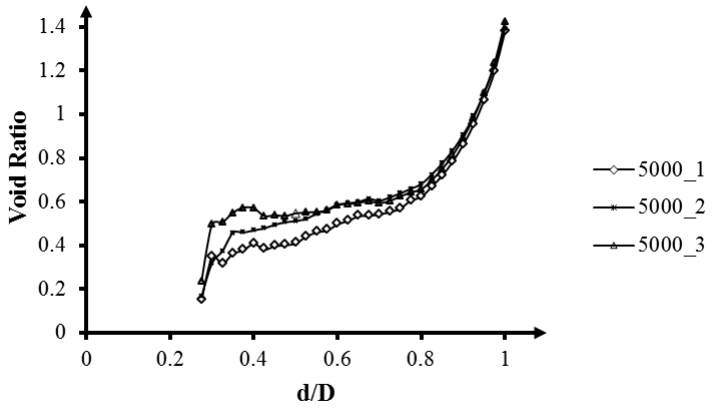


Figure 5.10: Void ratio for three different numerical samples with 5000 particles, varying the dimension of the imaginary box (d) with respect to the real one (D)

The charts produced by plotting the distribution of the void ratio within the sample (as in Figure 5.10) are used to conduct a convergence study to assess if the

considered samples are statistically representative of the consolidation state of the material under examination (point D in Figure 5.7). In case the graphs obtained for the n samples show repeatability and the plateau area is wide and horizontal (ZONE ② of Figure 5.5), the dimension L averaged from the n simulations determines the thickness of the specimen corresponding to the RVE. On the contrary, if the charts show significant scatter or the plateau region does not exist, the number of particles n_p (and consequently the specimen length L) has to be increased.

It is evident, observing Figure 5.10, that the curves do not show any plateau - as they exhibit a positive slope - and that the results obtained for the three samples are visibly different. The relevant scatter in the measurements demonstrates that the considered dimensions do not correspond to the RVE. Therefore, a second series of simulations containing 10000 particles is conducted. Table 5.5 and Figure 5.11 summarize the results of the simulations.

Sample	e_{mean}	$e_{variance}$	**Thickness L of the sample [mm]**
10000_1 mm	0.56	0.08	5.2
10000_2 mm	0.51	0.07	5.0
10000_3 mm	0.57	0.09	4.9

Table 5.5: Numerical results for the 10000 spheres simulations

Also in this case, the variation of void ratio among the three samples shows that the current volume cannot be considered as the RVE of the material.

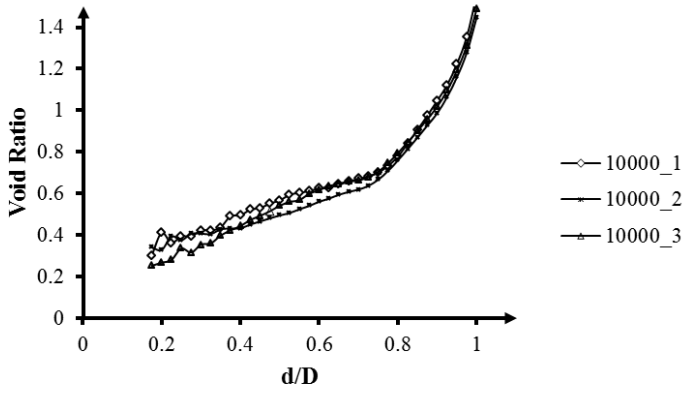


Figure 5.11: Void ratio for three different numerical samples with 10000 particles, varying the dimension of the imaginary box (d) with respect to the real one (D)

The dimensions of the samples are then further increased using 15000 particles in two different arrangements. Table 5.6 and Figure 5.12 report the outcomes of both simulations.

Sample	e_{mean}	$e_{variance}$	**Thickness L of the sample [mm]**
15000_1 mm	0.56	0.05	6.34
15000_2 mm	0.55	0.04	6.24

Table 5.6: Numerical results for the 15000 spheres simulations

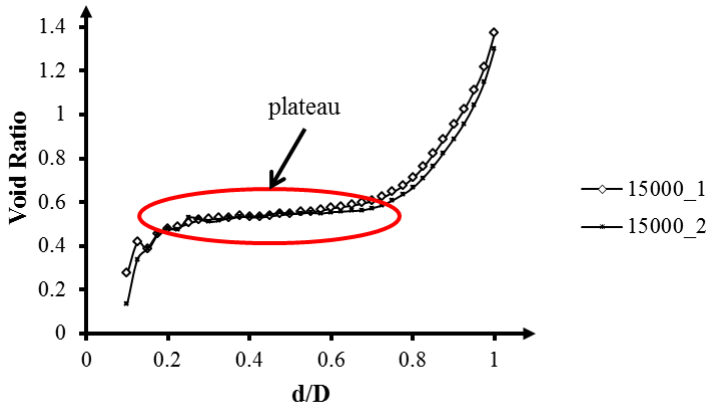


Figure 5.12: Void ratio for three different numerical samples with 15000 particles, varying the dimension of the imaginary box (d) with respect to the real one (D)

After compaction, the thickness of the samples containing 15000 particles is about 6.3 mm. The void ratio is nearly constant in a broader region ($0.2 < d/D < 0.8$) with a value approximately equal to 0.56. Despite the limited number of simulations, there is no significant scatter between the data obtained in these two numerical experiments. Therefore, the considered virtual sample, corresponding to a length of the sample in the loading direction L equal to 6.3 mm, is considered as the RVE. The thickness L of the obtained sample can be expressed in terms of average particle diameter ($\bar{d} \approx 0.5$ mm). In this case, the length of the representative sample is approximately 12 times the mean diameter $\bar{d}$. Obviously, many more simulations would have been required to define a statistical evidence of the correct definition of the RVE. However, X-ray computed tomography experiments [205] confirm our estimation of the RVE dimensions, thus proving the correctness of the numerical results obtained.

For completeness, a sample containing 20000 particles is considered. The application of gravity yields a sample of final height equal to 8.2 mm and void ratio equal to 0.56 (Table 5.7).

Sample	e_{mean}	$e_{variance}$	**Thickness L of the sample [mm]**
20000 mm	0.56	0.04	8.2

Table 5.7: Numerical results for the 20000 spheres simulations

In Figure 5.13, the curve representing the void ratio of the sample containing 20000 particles is superimposed to the curves shown in Figure 5.12. It is evident that the three curves are in perfect agreement. Therefore, the adoption of a volume of sand bigger than the RVE does not significantly modify the results in terms of void ratio.

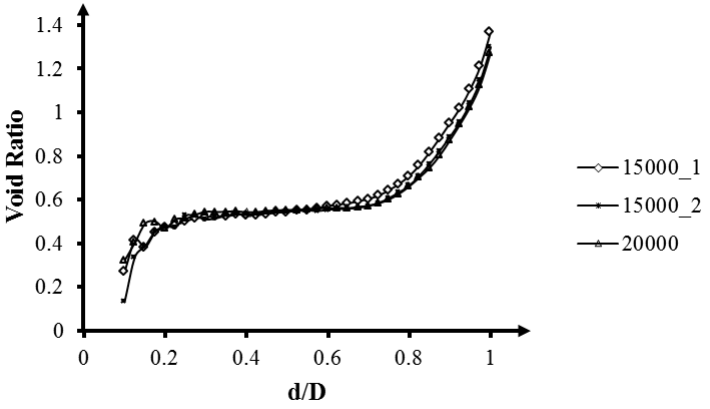


Figure 5.13: Void ratio for different numerical samples with 15000 and 20000 particles, varying the dimension of the imaginary box (d) with respect to the real one (D)

In conclusion, the RVE of the sand under investigation is considered to be a cylindrical sample of diameter and length equal to 20 mm and 6.3 mm respectively ($L/D \cong 0.3$). This is obtained for the specific compaction state and diameter of the container considered in this study. However, the method presented herein is intended to be a universally applicable numerical approach, which can be used for the estimation of RVE of any specific granular media.

5.3 Experimental verification

A series of laboratory Hopkinson bar compression experiments are conducted to assess the behaviour of Ottawa dry sand in its dense state ($e = 0.56$) at high strain rate. The Split Hopkinson Pressure Bar (SHPB) apparatus, used for the experiments, is presented in Section 2.3.1.1. Cardboard shims (436 g/m^2) of 1 mm thickness were used to reduce the high-frequency content in the signal, wave dispersion and Pochhammer-Chree oscillations. The velocity of the projectile is regulated by changing the pressure in the chamber. In these experiments, the projectile moves, before impact, at a speed of around 10 m/s. The first tests are conducted using cylindrical sand specimens characterized by a diameter equal to 20 mm and length equal to 10 mm, hence using a volume bigger than the calculated RVE.

A conservative estimate of the radial expansion of the container can be obtained by applying the *thin-wall cylindrical pressure vessel theory* (as $R/t = 20 > 5$, where R is the radius of the cylindrical container and t its thickness), assuming that:

- the applied load is considered hydrostatic ($\sigma_l = \sigma_r = p$)
- the applied pressure p is equal to the maximum axial stress measured during the tests.

In this case, the hoop stress σ_h is equal to

$$\sigma_h = \frac{\sigma_{max}\, R}{t} \tag{5.2}$$

with $\sigma_{max} = 120$ MPa. The radial expansion $\Delta_R = R\varepsilon_r = R\sigma_h/E$ is equal to 0.012 mm ($\varepsilon_r = 0.0012$), so three orders of magnitude less than the radius of the sample.

The porosity and void ratio definitions (see Section 2.4), used for the experiments is:

$$n = 100\left(1 - \frac{V_s}{V_{tot}}\right) = 100\left(1 - \left(\frac{m}{\rho_{sp}}\right)/V_{tot}\right) \tag{5.3}$$

Where V_s is the volume of solid particles, ρ_{sp} is the bulk density for the silica sand (equal to $2.65 g/cm^3$) and $V_{tot} = \frac{\pi D^2}{4} L$ is the available volume. The conversion from porosity n to void ratio e is done according to the second eq. in (2.4). Figure 5.14 illustrates the sample in its assembly. The two titanium anvils confine the sand within the cylinder and protect the input and output bars from indentation. A specimen filling procedure is established to obtain experimentally a fixed and reproducible void ratio. The amount m of sand required to obtain a given compaction is determined by means of a precision scale. The sand is then poured in the container using a funnel.

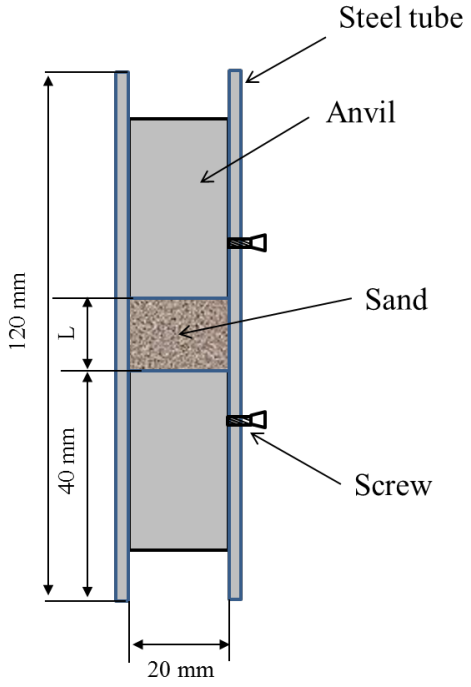


Figure 5.14: Schematic of sand specimen confined in a steel tube

The container is thereafter tapped five times on four diametrical points. The sand has to be further compressed using a dropping weight of a fixed mass (240 g) until it reaches the final required height L (measured by means of Vernier-callipers). The weight is dropped 10 times starting from a height of 10 cm. Further information and a detailed justification of the adopted protocol can be found in Section 6.2.1. A SHPB test is valid only if dynamic equilibrium conditions, within the specimens, are achieved during the experiment [29]. In fact, the mechanical response obtained

is representative of the whole specimen only when this condition is fulfilled. During SHPB tests the stress pulse is produced by the impact of a striker on the input bar. A perfect dynamic equilibrium would require several reflections of this stress wave along the specimen. Granular materials are characterised by a low wave propagation velocity [46, 71]. Consequently, the time required to achieve dynamic equilibrium is high. The dimensions of the sample need to be reduced as much as possible to allow multiple stress wave reflections within the specimen during the test. The time history of the forces at the interfaces between sample and bars (Figure 5.15) is obtained from the measurement data associated with the strain gauges positioned along the input and output bars. The comparison of these forces provides a measure of the dynamic equilibrium within the sample.



Figure 5.15: Forces at the sample-bars interfaces

Figure 5.16 shows such comparison for an experiment conducted on a sample of length equal to 10 mm. The two curves - representing the input (grey line) and output (black line) interfacial forces - are not parallel and do not overlap during the compaction phase of the specimen. This denotes a lack of dynamic equilibrium in the sample. As already said, the dynamic equilibrium conditions improve reducing the longitudinal dimensions of the specimen (i.e. reducing the length over diameter ratio L/D for a defined cross section). However, the minimum dimensions of the sample are dictated by the lower limit defined by the RVE, as previously explained.

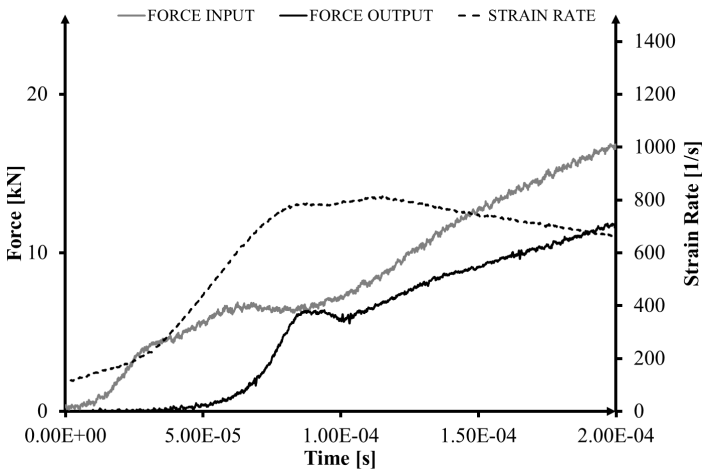


Figure 5.16: Force equilibrium and strain rate in dry, dense Ottawa sand, $L = 10$ mm

Figure 5.17 shows the time history of the forces at the interfaces between bars and sample for a specimen having dimensions equal to the RVE.

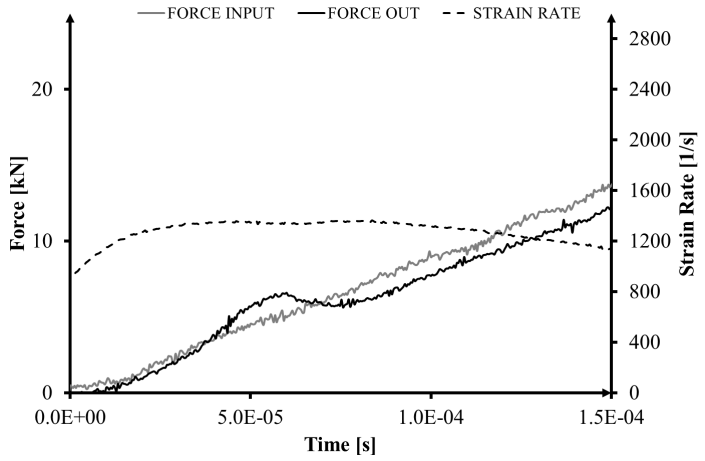


Figure 5.17: Force equilibrium and strain rate in dry, dense Ottawa sand, $L = 6$ mm

The dynamic equilibrium conditions are visibly improved with respect to the previous case. Furthermore, the strain rate (dotted line in Figure 5.17) is approximately constant for a large portion of the stress-strain curve. Figure 5.18 shows two stress-strain curves obtained using samples having dimensions corresponding to the RVE ($L = 6.3$ mm equivalent to a slenderness of the sample $L/D \cong 0.3$). The results obtained from a series of five tests, in a same initial consolidation state, are all included between the two curves depicted in Figure 5.18.

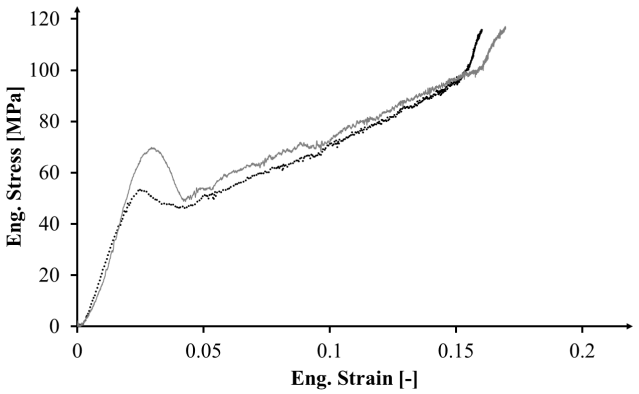


Figure 5.18: Upper and lower limit of the experimental variation (over 5 tests) of the stress-strain curves of Ottawa sand at high strain rate ($1400s^{-1}$) and void ratio $e = 0.56$ for samples of length $L = 6$ mm

This demonstrates that the choice of specimens having dimensions corresponding to the RVE produces also a significant improvement in the repeatability of the results, thus capturing better the mechanical behaviour of sand subjected to high strain rates.

It must be stressed that it is not possible to further improve the dynamic equilibrium in the sample reducing its dimensions below the RVE limit as this would affect the initial representative consolidation state. However, it is worthwhile mentioning that pulse-shaping techniques could additionally enhance the equilibrium conditions.

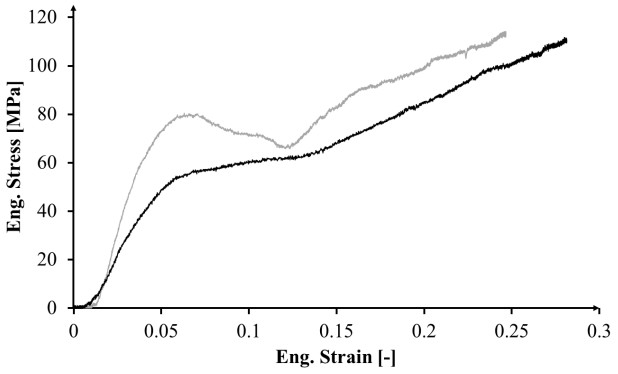


Figure 5.19: Upper and lower limit of the experimental variation (over 5 tests) of the stress-strain curves for samples smaller than the RVE with $L/D = 0.1$

Finally, for the sake of completeness and to demonstrably confirm the correct determination of the RVE, an additional series of 5 tests were carried out on specimens

of thickness equal to 2 mm ($L/D = 0.1$). All the corresponding stress-strain curves are comprised in between the two curves depicted in Figure 5.19. The adoption of samples smaller than the RVE affects the consistency of the void ratio within the specimen as demonstrated by the increased scatter in the obtained results (Figure 5.19).

5.4 Definition of the RVE for Ottawa sand in a loose configuration

The hypothesis of frictionless systems allows for the representation of Ottawa sand in a dense consolidation state, as shown in Section 5.2, for which the RVE sizes have been computed.

This section presents the procedure for calculating the Representative Volume Element for Ottawa sand in a loose configuration (with void ratio $e = 0.78$), which is then compared to what obtained for dense samples.

Even in this case, the RVE is calculated following the iterative procedure reported in Figure 5.7. The same initial geometrical packings presented in Section 5.2 (respectively with 5000, 10000, 15000 and 20000 particles) are now mechanically consolidated in a cylinder of diameter equal to 20 mm, applying friction. Again, 3 simulations per configuration presenting same radii distribution but different arrangements are carried out.

5.4.1 Mechanical consolidation

DEM based simulations of gravity assisted compaction have been carried out in YADE, using a non linear/non viscous elastic Hertz-Mindlin no-slip contact law. The tangential friction angle is set to 30 deg [206], whilst radii distribution and material properties of the Ottawa sand are reported, respectively, in Table 5.2 and Table 5.3. The internal surfaces of the cylindrical box present the same frictional and elastic properties of the sand particles. The simulations are interrupted when static

equilibrium conditions, characterised by low values of kinetic energy (as shown in Figure 5.9), are achieved.

5.4.2 Results and Comments

The variation of the void ratio within the sample is estimated by adopting the second procedure presented in Section 5.2, with the progressive variation of the dimensions of a fictitious box.

The first set of simulations considers 3 different assemblies composed of 5000 particles. Figure 5.20 shows the distribution of void ratio with respect to d/D.

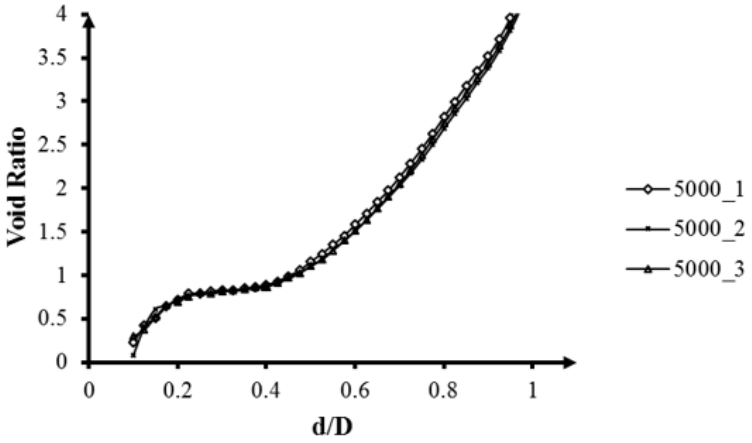


Figure 5.20: Void ratio for three different numerical samples of loose Ottawa sand with 5000 particles, varying d/D

On the contrary of what seen in Figure 5.10 for frictionless dense samples, there is a good repeatability in the plateau region (i.e. no relevant variations in the values of void ratio among the three different samples). However, the extension of the plateau zone is drastically reduced, showing a stronger variation of void ratio within each assembly and more noticeable boundary effects. These observations can be justified by the presence of intra-granular and particle-walls friction, as also explained in Section 3.4.

A second series of simulations with 10000 particles is conducted (Figure 5.21).

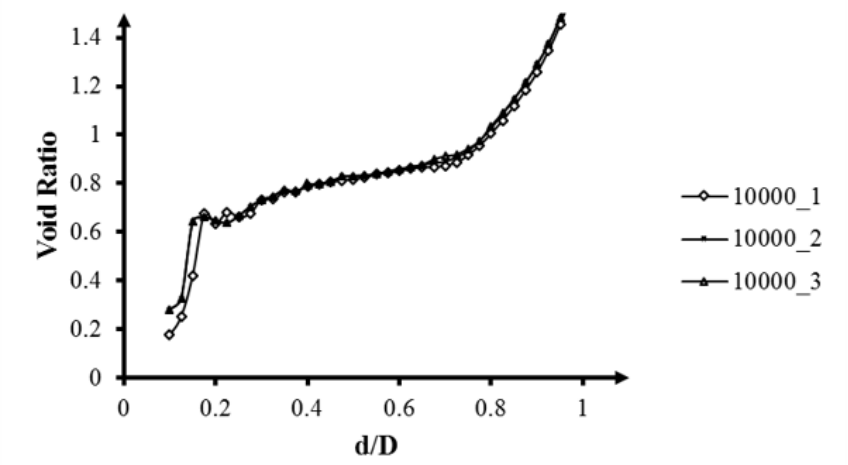


Figure 5.21: Void ratio for three different numerical samples of loose Ottawa sand with 10000 particles, varying d/D

In this case, even if the plateau is not perfectly horizontal (slightly different distributions of void ratio within each sample), it spreads for a wider range of d/D values and shows high reproducibility of the results among the three simulations (i.e. no scatter among different simulations).

Finally, simulations with 15000 and 20000 particles are conducted and reported in Figure 5.22.

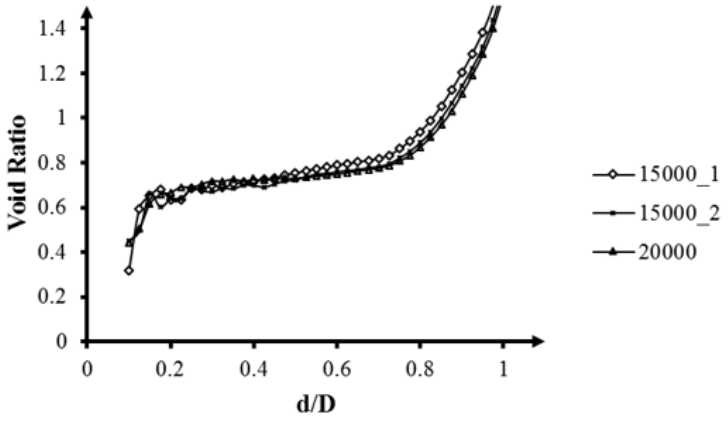


Figure 5.22: Void ratio for different numerical samples of loose Ottawa sand with 15000 and 20000 particles, varying d/D

The concurrent presence of a wide plateau and reproducible values of void ratio

among different simulations demonstrates that an RVE is comprised of a number of particles ranging between 10000 and 15000. Therefore, the presence of friction slightly reduces the RVE sizes to be adopted in mechanical experiments.

5.5 Summary

Achieving the dynamic equilibrium within the sample, at constant strain rates, is of utmost importance in experimental characterisation of the mechanical performance of any material when relying upon the Split Hopkinson bar apparatus. The most common approach used in literature to improve the dynamic equilibrium conditions is the reduction of the sample dimensions. However, such approach may have missed the important aspect of considering a representative volume element size. A rigorous characterisation of the high strain rate behaviour of granular materials requires careful consideration of the initial consolidation state of the particulate or granular assembly in order to achieve consistent results that represent the stress-strain behaviour of its continuum. Choosing an arbitrarily small sample would invalidate the correct representation of the initial compaction state. Therefore, it is necessary to evaluate the volume element representing the consolidation state of the tested granular material. This work demonstrates the effectiveness of using the Discrete Element Method for the estimation of the RVE, which is the smallest volume of sand that ensures the attainment of a compaction state consistent with the material under investigation in its continuum. A new numerical procedure for the definition of the RVE based on the estimation of the void ratio is presented. The RVE proposed is based on the phenomenological observation on the importance of initial geometric arrangement of granular materials captured using the void ratio parameter. This is an important descriptor of the initial consolidation state of assemblies that affects significantly the high strain rate behaviour. The representative volume element of the sand under consideration is determined using an iterative numerical procedure based on DEM simulations. The results obtained from the Split Hopkinson Pressure

Bar experiments, reported in this chapter, demonstrate that the achievement of the dynamic equilibrium, in samples of granular materials, strongly depends upon the RVE dimensions. The use of samples with dimensions comparable to the RVE enabled better repeatability of measurements when compared against results available in open literature. Finally, the presence of friction, for generating loose sample, induces smaller RVEs. Therefore, adopting samples equal to the RVE obtained for the densest possible initial consolidation state is a conservative approach when defining the dimensions of the specimens to be used in SHPB experiments on sand.

Chapter 6

Characterisation of the effect of morphology, moisture content, compaction and confinement on the mechanical response of sand to impact loading

The definition of representative models of granular materials and corresponding RVEs, presented in the previous chapters, can be used as building blocks for multiscale simulations. However, every numerical model needs to be calibrated and validated against real experiments. In particular, the execution of high rate experiments on granular materials is of utmost importance for the correct modelling and understanding of the dynamic behaviour of sand. The literature review (Section 2.3.1.3) proved the existence of a considerable gap in the characterisation of granular material subjected to impact loading. This is justified by their complex nature due to the simultaneous effect of many parameters on their mechanical behaviour (e.g. morphology and sizes of the grains, compaction, confinement, moisture contents, etc.). For instance, there are neither detailed studies on the effect of microscale properties such as grain shape and inter-grain friction nor researches aiming to appreciate the effects of the combination and interference of these parameters on the high strain rate mechanical response of sand. This chapter wants to fill the identified gaps, by presenting a comprehensive high strain rate characterisation of sand that addresses

the influence of grain shape, intergranular friction, confining pressure, initial consolidation state, water content, strain rate and possible combination of these on the stress-strain behaviour of granular materials. Differently from what found in literature, the experiments in this chapter are conducted by adopting the Long-SHPB apparatus described in Section 2.3.1.1. The main peculiarity of this set-up is the longer length of the projectile (2.7 m), which influences the duration of the incident pulse [29]. Its adoption enables longer pulses of higher magnitude to be applied to the sample under consideration. This allows for the achievement of higher strains than what currently existing in the literature. Moreover, based on the review of the existing works on pulse shaping and observations made in Section 2.3.1.2, the work herein presented is carried out by using a 1 mm thick cardboard shim ($436 g/m^2$). By doing so, the transmitted Pochhammer-Chree oscillations [39], caused by the high-frequency oscillation and by the coupling between axial and radial displacements in the sample (Poisson effect), are reduced without negatively affecting the maximum achievable strain rate. All the experiments reported in this work are conducted on bars and samples having same cross-sectional areas ($A_0 = A_s = 20$ mm). The length of the sand specimens adopted in this research are designed to improve the repeatability of the results whilst guaranteeing acceptable equilibrium conditions and constant strain rates. This is achieved by following the procedure presented in Chapter 5.

6.1 Sand materials and types of confinement

6.1.1 Ottawa, Q-Rok and Euroquartz Sand

Three types of Crystalline Silica sand were tested: Ottawa sand with round grain shape, Euroquartz Siligran - trocken $0.125 - 0.71$ mm with sub-rounded grains and Q-Rok sand with polyhedral grain shapes. Ottawa and Q-Rok sand were obtained from US Silica, Berkeley Springs, West Virginia. Their mineralogy is presented in Table 6.1.

Component	%
Quartz	99.7
Aluminium Oxide	< 0.1
Iron Oxide	< 0.1
titanium Oxide	< 0.1

Table 6.1: Mineralogy of the Ottawa and Q-Rok sand

Both Ottawa and Q-Rok sand passed #20 sieve (sieve opening = 0.84 mm) but were retained on #30 sieve (sieve opening = 0.6 mm). The measured size distributions of Ottawa and Q-Rok sand are reported in Figure 6.1.

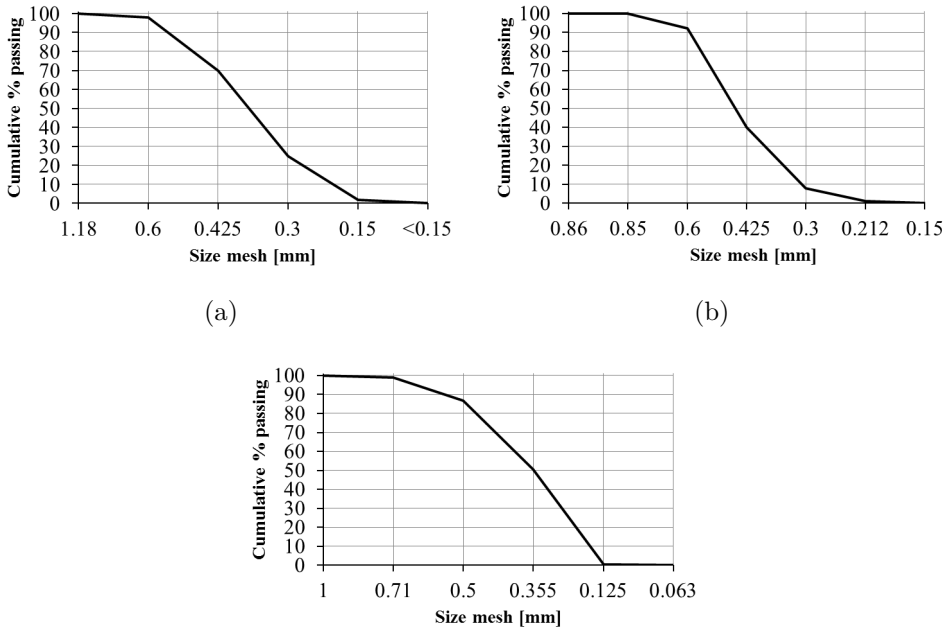


Figure 6.1: Size distribution of (a) Ottawa, (b) Q-Rok, and (c) Euroquartz sand

The specific gravity of both sands was 2.65 and their bulk density was equal to $1.6 g/cm^3$. Ottawa sand is a naturally occurring sand, whilst Q-Rok sand is obtained by crushing. Their hardness is equivalent to 7 Mohs. Euroquartz Siligran trocken sand was obtained by Euroquartz Gmbh (Germany). Table 6.2 shows its mineralogy.

Component	%
Quartz	99.6
Aluminium Oxide	< 0.2
Iron Oxide	< 0.1
titanium Oxide	< 0.1

Table 6.2: Mineralogy of Euroquartz sand

The Euroquartz sand passed #18 sieve (sieve opening = 1 mm) but retained on #25 sieve (sieve opening = 0.71 mm). The specific gravity of Euroquartz sand was 2.65 and its bulk density was equal to $1.6 g/cm^3$. Some of the following experiments were conducted using Euroquartz sand with grains coated by a thin layer of epoxy resin. The coating itself did not modify the distribution of sizes considered in Figure 6.1. A comparison between the shapes of the three types of sand, using microscopy, is shown in Figure 6.2.

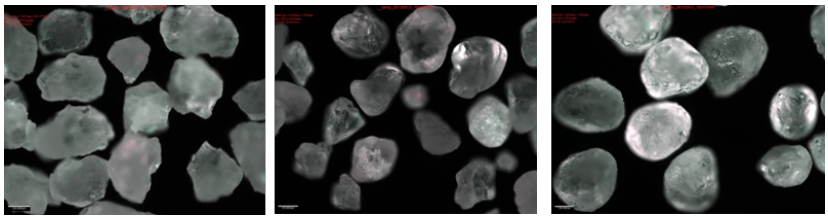


Figure 6.2: Comparison between the different shapes: (left) Q-Rok, (centre) Euroquartz Siligran $0.125 - 0.71$ and (right) Ottawa sand

6.1.2 Containers for lateral confinement of sand specimens

Appropriate confinements were designed to allow for the preparation and positioning of representative samples of sand within the LSHPB apparatus. Two configurations were adopted to test the sand under quasi-uniaxial stress and quasi-uniaxial strain conditions:

1. *Rigid confinement - Quasi-uniaxial strain condition.* A stainless steel cylinder, having internal diameter equal to the diameter of the bars (20 mm), length of 120 mm and thickness of the walls of 5 mm was used as a container. The thickness was determined in order to prevent any plastic deformation of the

container during compression testing (Figure 6.3a). The sand was constrained within the container using two cylindrical Ti64 anvils of diameter equal to 20 mm and length of 40 mm. The material and cross section chosen for the anvils were the same of the bars to ensure mechanical impedance matching, as confirmed by calibration tests. The anvils were also used to preserve the input and output bars from indentation/erosion by sand specimens.

2. *Deformable confinement - Quasi-uniaxial stress condition.* Deformable latex confinements, having same diameter of the bars and length equal to 10 mm, were used as a container. Also in this case, the sand was constrained using two Ti64 anvils as described above. The latex cylinder was sealed to the two anvils by means of adhesive tape. Figure 6.3-b depicts a schematic representation of the latex confinement.

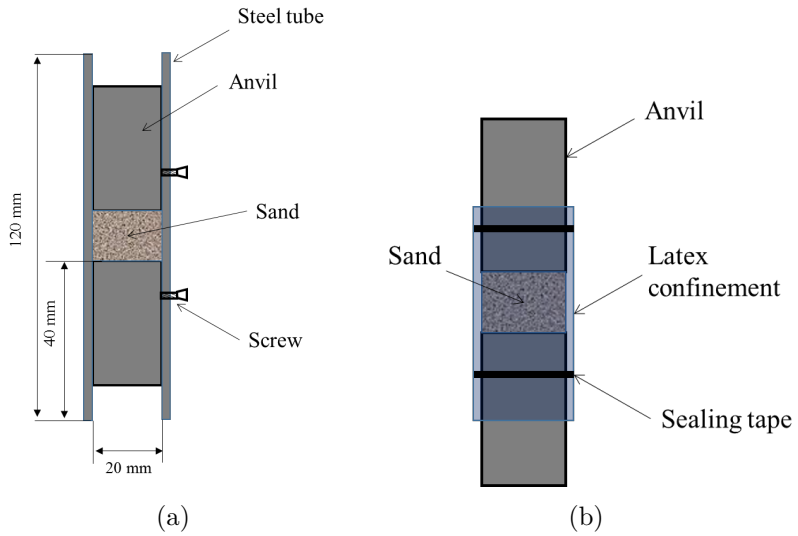


Figure 6.3: Schematic of (a) stainless steel confinement and (b) latex confinement

Both containers were positioned within an aluminium support to keep the cylinder in position and to avoid any misalignment between the two bars and the sample (Figure 6.4).

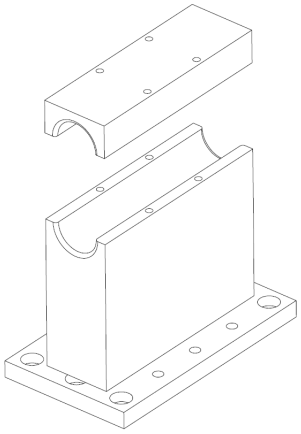


Figure 6.4: Support for the containers

The two anvils were constrained during the filling phase using two grub screws (similarly to [45]), until the cylindrical containment was placed between the two bars, in horizontal position (Figure 6.5).

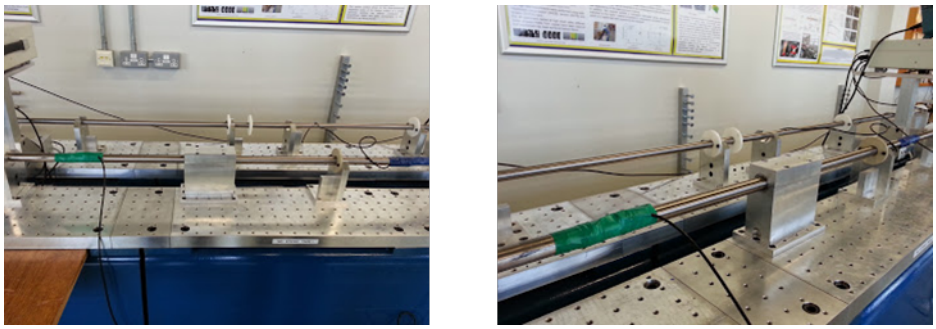


Figure 6.5: LSHPB set-up

The screws were removed before the execution of the test, once anvils and bars were in contact. The grub-screws replaced any adhesives. This approach ensured the contact and alignment between bars and anvils avoiding the input signal to be affected by the presence of any interfacial material.

6.2 Procedure for the preparation of samples

Most naturally occurring granular materials are random assemblies of discrete entities (grains) that interact through contacts. Their mechanical behaviour is strongly

dependent on both microscopic features of the medium (grains properties) and packing properties (consolidation state) [11, 207]. Therefore, differently from continuous materials, the control of the consolidation state is fundamental for a correct mechanical characterisation of the medium.

Two equivalent parameters representing the consolidation state are either the void ratio (e) or the porosity (n), as defined in eq. (2.2) and (2.3) in Section 2.4. The two variables are interdependent as expressed by eq. (2.4).

Each test has to be representative of a fixed and reproducible consolidation state. This section presents three different consolidation procedures [208] adopted to produce loose, intermediate and dense samples.

Both porosity and void ratio can be expressed in terms of bulk density of the silica sand (ρ_{sp}), total volume comprised between the two anvils (V_{tot}) and mass of sand (m) poured within the container as done in eq. (5.3). The sand samples used in the present work were cylinders with 20 mm diameter and 6 mm height. These dimensions were set following the procedure detailed in Chapter 5 and define the V_{tot} occupied by the sand. Once the bulk density and the sample volume were defined, the only remaining variable was the mass of the sand. The variation of the mass poured into the container allowed for the attainment of different void ratios.

6.2.1 Preparation of dense samples

Dense sand assemblies were characterised by a void ratio of 0.57 for Ottawa sand, 0.69 for Q-Rok and 0.56 for Euroquartz sand. The total amount of sand to pour into the container was measured using precision weighing scales. This quantity of sand was divided into three equal parts and the following procedure was repeated for each portion. First, the sand was poured into the container using a funnel. After that, the container was tapped five times on four diametrical points. Then, the sand was further compressed dropping ten times a weight with a fixed mass ($240g$) from a determined height until the final required length of the specimen was obtained.

6.2.2 Preparation of medium dense samples

The intermediate configuration, which corresponds to void ratios of 0.65 for Ottawa sand, 0.85 for Q-Rok and 0.72 for Euroquartz sand, was obtained via three consecutive steps. Firstly, the total amount of sand to pour in the container to achieve the given void ratio was measured using a precise set of weighing scales. This quantity of sand was poured into the container using a funnel. The funnel was then moved along the container with a constant velocity until its final height L was covered. Finally, the container was tapped ten times on each side on four diametrical points.

6.2.3 Preparation of loose samples

The preparation of loose samples, corresponding to void ratios equal to 0.78 for Ottawa sand, 1 for Q-Rok and 0.8 for Euroquartz sand, was achieved in two steps. The total amount of sand was measured using a weighing scale. Then, the sand was poured into the container by means of a funnel that was moved upwards until covering the length of the container. Table 6.3 summarises the void ratios obtained for the three types of sand in loose, intermediate and dense configurations. The scatter in the measured void ratios was less than 1%.

Type of sand	Loose consolidation	Intermediate consolidation	Dense consolidation
Ottawa	0.78	0.65	0.57
Q-Rok	1.00	0.85	0.69
Euroquartz	0.80	0.72	0.56

Table 6.3: Void ratio for the three types of sand

6.2.4 Preparation of wet samples

All procedures presented above refer to dry conditions. The procedures adopted for the preparation of wet assemblies were similar to the ones reported in the previous sub-sections. The sand was initially dried at 100° Celsius in a drying chamber for 2 days. Once dry samples of equal compaction were prepared, the desired volume of water was measured and injected in several positions of the sample using a 1 ml

syringe. Finally, water and dry sand were mixed thoroughly by using a metallic stick.

The water content of the different sand specimens is reported as the gravimetric water content (S_w):

$$S_w = \frac{m_w}{m_{sdried}} \tag{6.1}$$

Where m_w represents the volume of water added to the mass of dried soil (m_{sdried}). The values of gravimetric water content adopted in this research varied between 3% and 25%. The volumetric and gravimetric percentages of water injected in the Ottawa sand in an initial dense state is summarised in Table 6.4.

Mass of water [g]	0.096	0.192	0.384	0.640
Volumetric water content	15%	30%	60%	100%
Gravimetric water content	3%	6%	12%	20%

Table 6.4: Water contents adopted for the Ottawa wet dense sand

Table 6.5 and Table 6.6 summarise the water contents for Euroquartz and Q-rok sand respectively.

Mass of water [g]	0.18
Gravimetric water content	6%

Table 6.5: Water contents adopted for the Q-Rok wet dense sand

Mass of water [g]	0.096	0.192	0.384	0.640	0.800
Gravimetric water content	3%	6%	12%	20%	25%

Table 6.6: Water contents adopted for the Euroquartz wet dense sand

6.3 Experimental Characterisation

In this section, the results of experimental characterisation of the three types of sand are presented. The effects of initial consolidation state, shapes of the grains, coating, confinement, water content and their combination on their mechanical behaviour are considered.

Generally, four phases of compression response behaviour can be identified by observing the stress-strain curve obtained from SHPB experiments on sand specimens [200, 41], as illustrated in Figure 6.6:

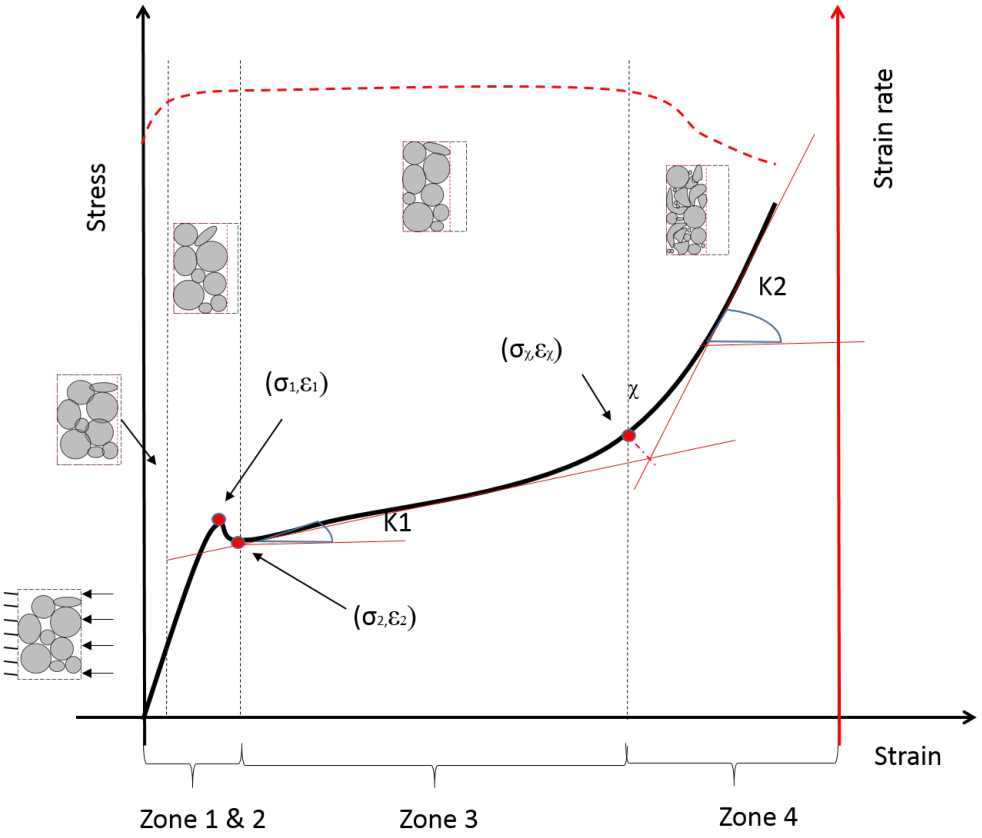


Figure 6.6: Definition of the main zones of the stress-strain curve (in black) obtained during uniaxial compression tests and corresponding strain rate curve (in red); in the cartoons, the elastic deformation is represented with an overlap between grains

- **Zone 1**: The grains deform elastically because the axial stress level is not high enough to exceed the static friction between individual sand grains, showing an initial elastic constrained modulus [200, 41]. The strain measurements obtained by means of the SHPB tend, in general, not to be reliable in this phase because of the lack of dynamic equilibrium.

- **Zone 2**: The stress exceeds the static friction causing the rolling and sliding of the particles in the intergranular voids and the subsequent deformation of the soil skeleton. The stress-strain behaviour in this region deviates from the initial

pseudo-elastic response and an apparent yield point can be detected. The values of the stress and strain corresponding to the apparent yield point (σ_1, ε_1) and to the following point of local minimum stress (σ_2, ε_2) are extensively reported in the following analysis.

- **Zone 3**: A denser state is produced by the rearrangement of sand grains into the voids, thereby more contacts between the grains occur. Relative movements become more difficult and a following "lock-up" is obtained.

- **Zone 4**: At high-stress levels, grains fragmentation followed by an additional contraction in the volume of the specimen are observed. The material exhibits a higher pseudo-elastic stiffness. Another relevant point reported in the following sections is χ (σ_χ and ε_χ).

A minimum number of three repeatable experiments per configuration were conducted. This number was increased to five tests per configuration when the repeatability of the results was outside the desired tolerance. For clarity, whenever appropriate, the number of individual results included in the following plots was reduced to a minimum.

The achievement of dynamic equilibrium and constant strain rate during the experiment is proved in Figure 5.17 in Section 5.3.

6.3.1 Effect of the initial consolidation state

The void ratio is one of the main parameters influencing the mechanical response of granular media subjected to compressive loading. Characterising the mechanical behaviour of a granular medium without controlling its initial consolidation state would alter the determination of its response [153, 209]. This section shows the effect of the initial consolidation state on the mechanical behaviour of three different types of sand when loaded compressively within a stiff lateral confinement (i.e. under nearly uniaxial strain conditions). Ottawa and Q-Rok sand were compressed at two differ-

ent strain rates ($600s^{-1}$ and $1600s^{-1}$) in order to characterise the interdependence between the effects of void ratio and strain rate on their mechanical response.

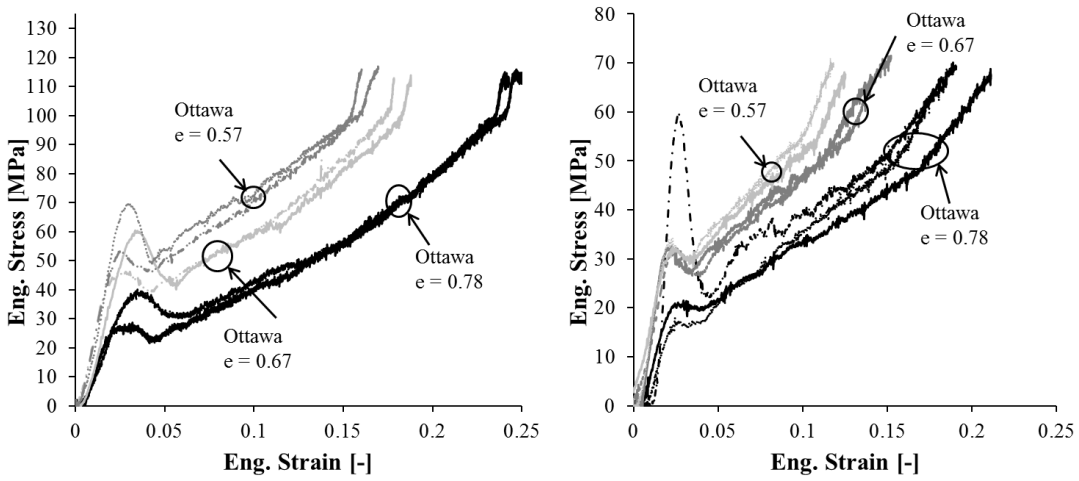
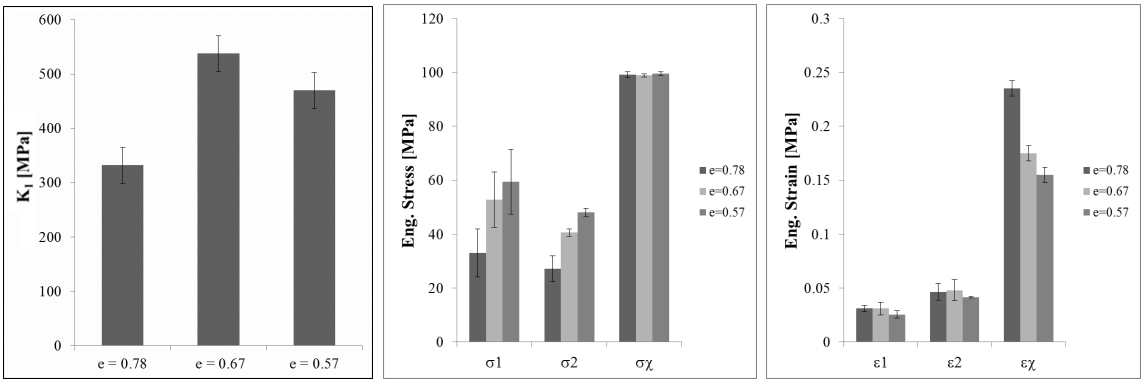


Figure 6.7: Effect of the initial consolidation state on Ottawa sand at (a) $1600s^{-1}$ and (b) $600s^{-1}$ in a rigid confinement

Figure 6.7a shows how the flow stress increased with the initial density (reduction of the void ratio), showing a strong dependence of the Ottawa sand behaviour upon the initial consolidation state [41, 45, 46]. This can be explained by the higher availability of voids in loose samples thus exhibiting a more compliant behaviour when compared to dense specimens. This trend persisted even at lower strain rates as deducible in Figure 6.7a and Figure 6.7b. The effect of the initial consolidation state upon the confinement modulus is shown in Figure 6.8a. The variation of the stiffness of the stress-strain curve (K1 in zone 3 of Figure 6.6) with the void ratio was not unequivocal. The Ottawa sand in its initial dense consolidation state ($e = 0.57$) presented an increased stiffness when compared with the loose configuration ($e = 0.78$), but lower than the value obtained for the intermediate configurations. Therefore, any correlation between the variation in the confinement modulus and the initial consolidation state does not constitute experimental evidence.



(a) (b) (c)

Figure 6.8: Confined modulus for the three initial void ratios (a), and effect of the initial consolidation state on the salient points of the stress (b) - strain (c) curves for Ottawa sand

A more explicit trend could be identified by comparing the variation of the relevant levels of stress and strain (see Figure 6.6 for notations) with the consolidation state (Figure 6.8b and Figure 6.8c). The apparent yield stress (σ_1) increased, as expected, with the relative initial density of the assembly, whilst the stress at the point χ (σ_χ) appeared to be unaffected by the consolidation state. On the contrary, the effect of the initial consolidation state on the strains was evident with ε_χ substantially decreasing when increasing the initial compaction.

A summary of all results illustrating the effect of the initial consolidation state on the mechanical response of Q-Rok sand at strain rates of $1600s^{-1}$ and $600s^{-1}$ is shown in Figure 6.9. The effect of the relative density on the confined modulus (K1) was evident (Figure 6.10a). Lower relative densities (moving from $e = 0.67$ to $e = 1$) produced a substantial decrease of K1. The comparison of the measured values of stress and strain around the apparent yield point did not allow for a straightforward conclusion on the effect of consolidation state for Q-Rok sand (Figure 6.10b and Figure 6.10c). This was mainly due to the high oscillations in the mechanical response present at low strains. However, the flow stress was clearly higher in sands with lower void ratios. The effect on the points χ was similar to the one observed for Ottawa sand: also for Q-Rok, the point χ moved to higher values of strain (higher ε_χ) for

lower compaction states. The stress σ_χ, instead, remained nearly constant. The effect of the consolidation state on the stress-strain curves did not change at lower strain rates, as it is evident in Figure 6.9b.

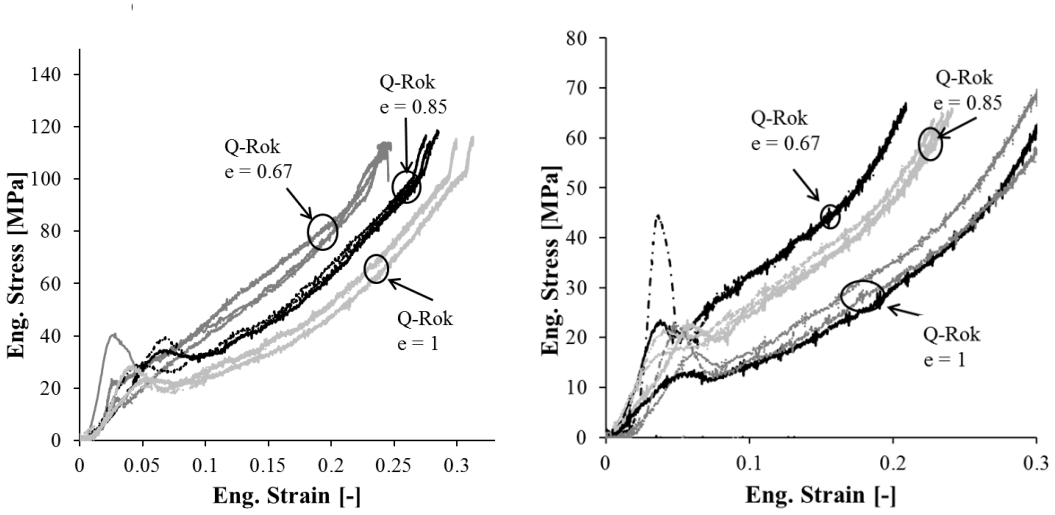


Figure 6.9: Effect of the initial consolidation state on Q-Rok sand at (a) $1600s^{-1}$ and (b) $600s^{-1}$

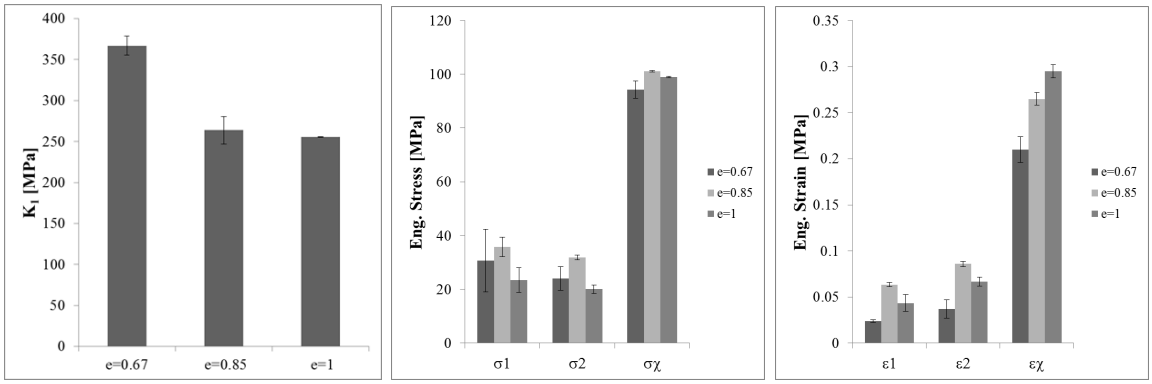


Figure 6.10: Confined modulus for the three initial void ratios (a) and effect of the initial consolidation state on the salient points of the stress (b) - strain (c) curves for Q-Rok sand

The response of Ottawa sand in a *loose* configuration (Figure 6.7a) and Q-Rok in its *more densely packed* state at strain rates of about $1600s^{-1}$ (Figure 6.9a) showed very similar results. This observation denotes the concurrent effects of initial consolidation state and grain morphology (spherical for Ottawa and polyhedral for Q-Rok)

on the mechanical response. Additional results showing exclusively the effect of the shape of the grains on the stress-strain curves will be presented in Section 6.3.2.

The effect of the consolidation state upon the response of Euroquartz sand at high strain rate ($1600s^{-1}$) is shown in Figure 6.11.

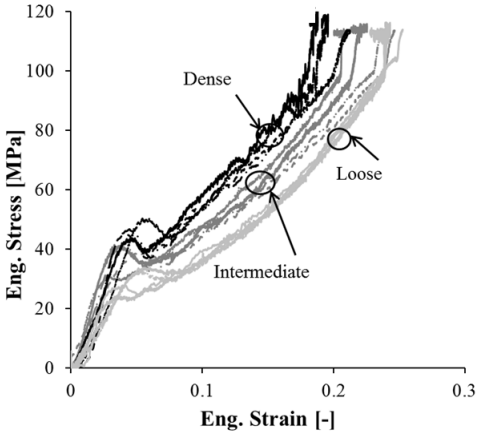
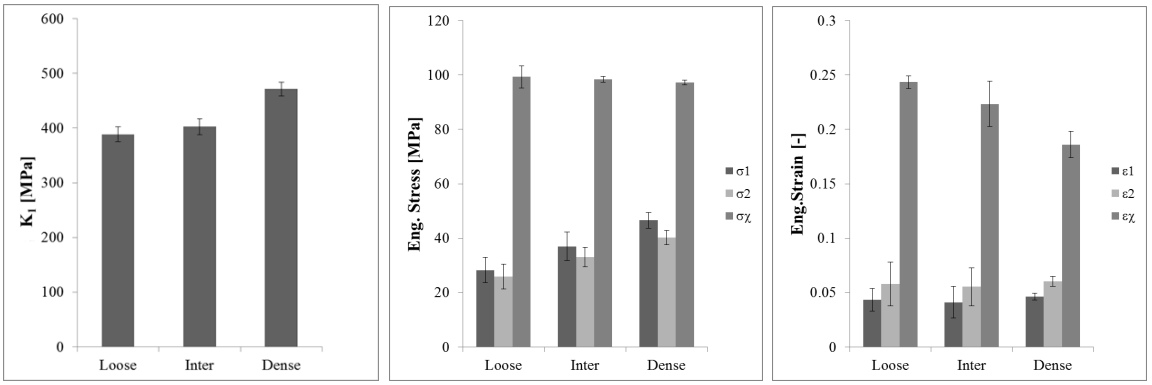


Figure 6.11: Effect of the initial consolidation state on Euroquartz sand at $1600s^{-1}$



(a) (b) (c)

Figure 6.12: Confined modulus for the three initial void ratios (a) and effect of the initial consolidation state on the salient points of the stress (b) - strain (c) curves for Euroquartz sand

As expected, the increase in the relative density of the tested sand produced higher flow stresses. Figure 6.12a shows, for Euroquartz sand, the effect of the initial consolidation state on the confined modulus K1. Also in this case, higher values of K1 were obtained for samples with higher initial relative density.

The point χ was characterised, for loose Euroquartz sand, by higher strains (ε_χ) and similar levels of stress (σ_χ) when compared to denser configurations (Figure 6.12b and Figure 6.12c). Moreover, denser samples produced higher apparent yield stresses but no significant variation in the corresponding strains.

Summarising, the mechanical response of dense granular material showed:

- Steeper confined modulus;
- Lower deformation at the point χ;
- Higher stresses, but similar strains, at the apparent yield point,

when compared to the response of loose samples.

6.3.2 Effect of the grain shape

The effect of the grains morphology on the mechanical response of sand is herein addressed. This section presents a direct comparison between Ottawa and Q-Rok sands characterised by, respectively, spherical and polyhedral grains. Two different strain rates were imposed to investigate any interaction between the rate of deformation and shape of the grains on the resultant mechanical response. Samples of both types of sand were prepared with equal void ratio to eliminate any possible influence of the consolidation state on the following analysis.

Figure 6.13 shows the effect of the grain shape on the stress-strain curve at intermediate and high strain rate. The Ottawa sand, composed of spherical grains, exhibited a steeper but less extended stress-strain curve when compared to the Q-Rok sand. During the compaction phase (zone 3 in Figure 6.6), the deformation of the granular material is mainly due to the rearrangement and fracture of the grains. When a polyhedral grain is compressed, the rough edges produce a local stress concentration leading to an anticipated failure. For a spherical grain, instead, higher forces are required to reach the failure condition. Thereby, the Q-Rok sand, composed of polyhedral grains, was compressed up to higher engineering strains but it

was characterised by a lower flow stress when compared to the Ottawa sand. This is shown in Figure 6.14b and Figure 6.14c, where σ_2 and σ_χ were higher for Ottawa sand than for Q-Rok sand. On the contrary, ε_2 and ε_χ were higher for Q-Rok sand.

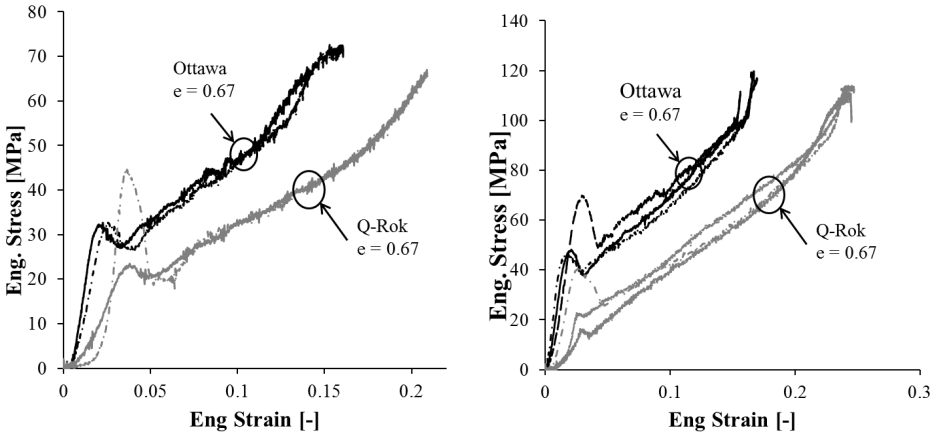


Figure 6.13: Effect of the grains shape at (a) $600s^{-1}$ and (b) $1600s^{-1}$

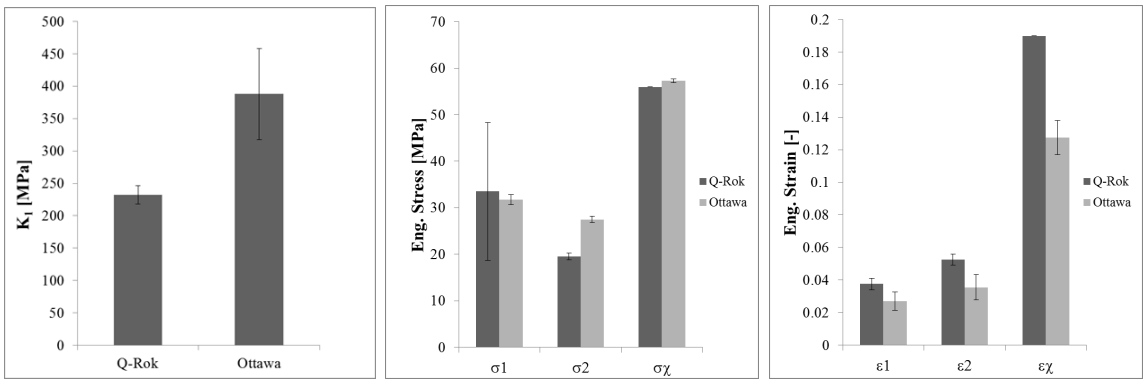
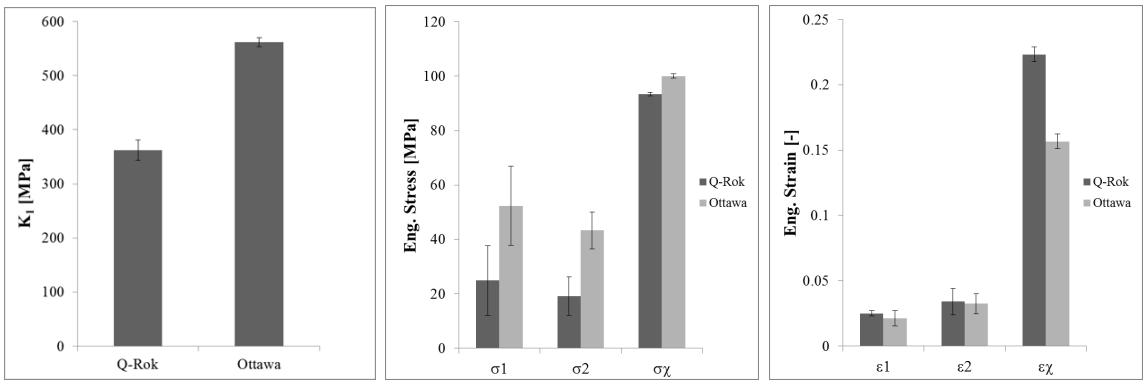


Figure 6.14: Effect of the grains shape on confined modulus (a), stress (b) and strain (c) at $600s^{-1}$

All the observations made so far on the effect of the grain shape apply also to tests conducted at higher strain rates ($1600s^{-1}$), as shown in Figure 6.13b and Figure 6.15.



(a) (b) (c)

Figure 6.15: Effect of the grains shape on confined modulus (a), stress (b) and strain (c) at $1600s^{-1}$

In conclusion, sands with spherical grains can withstand higher levels of stress while undergoing lower deformations compared to sands with polyhedral grains. This effect is mainly due to the fracture of grains that is strongly dependent on the grain shape [200, 210].

6.3.3 Effect of coating and inter-granular friction

The mechanical behaviour of sand under quasi-uniaxial strain compressive loading is also influenced by the surface properties of the grains as they mutually interact through contact. Therefore, the influence of these properties on the overall response of the material needs to be addressed. In this section, the stress-strain curves, obtained from natural Euroquartz sand, are compared with those obtained testing coated Euroquartz sand. The grains were coated using a thin and uniform layer of epoxy resin. After being coated, the sand was dried in an oven at 100°C for 24 hours before testing.

Figure 6.16 shows the effect of the drying process on the response of dense coated Euroquartz sand. When dried, the coating undergoes a change of its material properties (epoxy resin is a thermo-softening resin) that results in the modification of the overall response of the granular assembly.

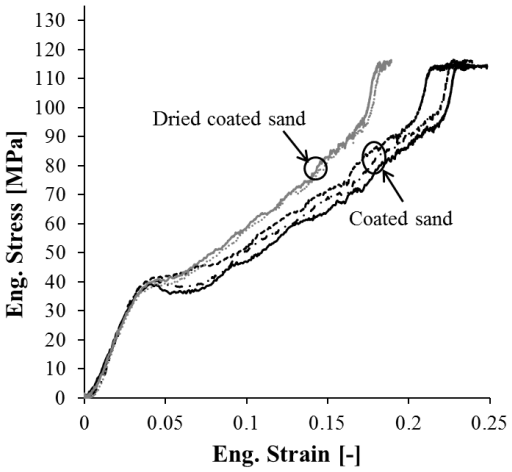
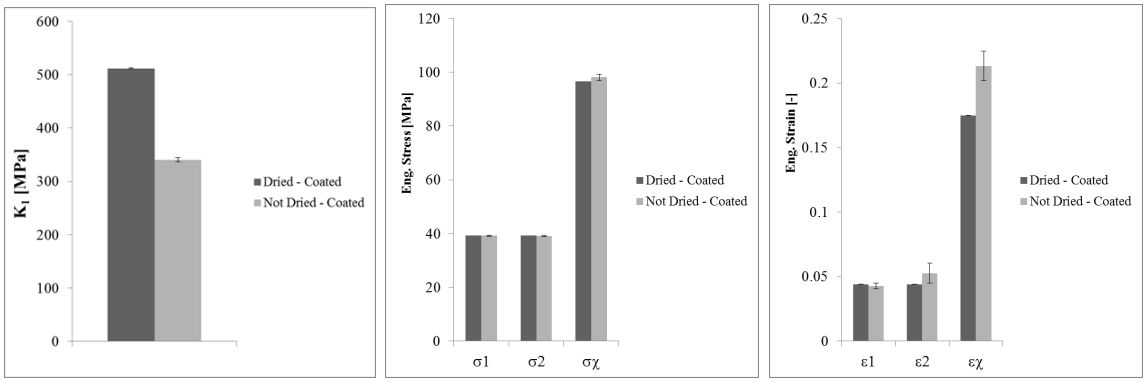


Figure 6.16: Effect of the drying process on the dense coated Euroquartz sand at high strain rate

The variation in the confined modulus due to the drying process was evident. The diagram shown in Figure 6.17a quantifies the increase of K1 when the coated sand was dried. The drying process resulted in a reduction of the maximum deformation but it did not affect the measured stresses (Figure 6.17b and Figure 6.17c). This behaviour could be explained by the variation of the surface properties of the grains due to the heating process.



(a) (b) (c)

Figure 6.17: Effect of the drying process on confined modulus (a), stress (b) and strain (c) for coated Euroquartz sand

Following, the behaviour of dried coated sand was compared to the natural occurring sand in order to appreciate the combination of the effects of surface properties

and initial consolidation state. Figure 6.18a compares the mechanical response of natural and coated Euroquartz sand in a dense initial configuration.

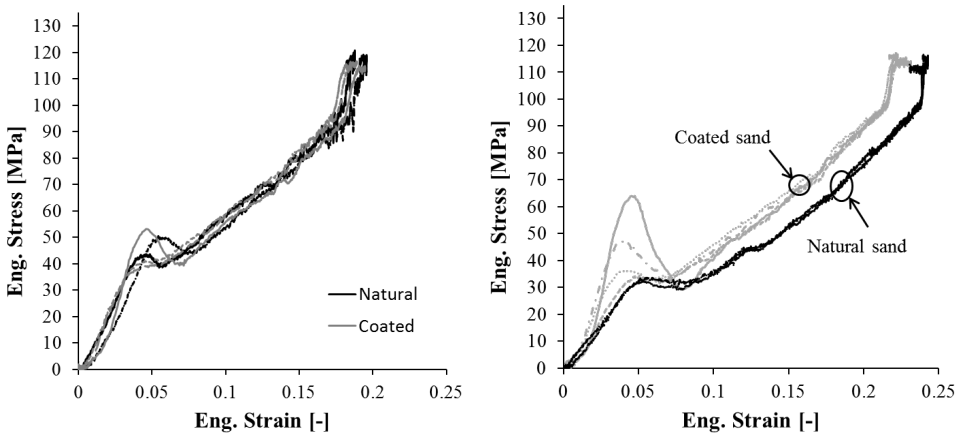


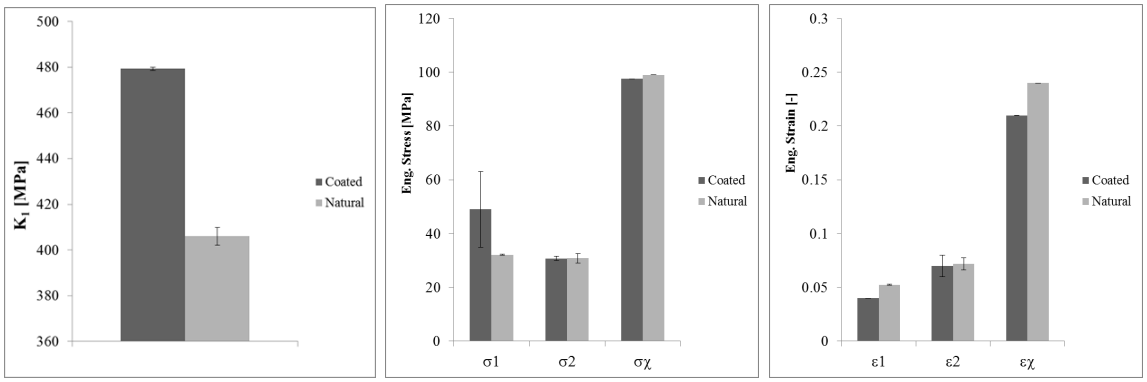
Figure 6.18: Effect of coating on (a) dense and (b) loose Euroquartz sand

When the sand was tightly packed, the variation of surface properties did not influence its mechanical response. Figure 6.18b, instead, presents the effect of the coating on the response of Euroquartz sand in a loose consolidation state. In this case, the effect was noticeable. The coating induced an increase in the confined modulus of the sand making it less compliant in compression (Figure 6.19a).

The coating produced a general stiffening of the mechanical response. Hence, at equal loading conditions the coated sand was characterised by lower compression strain. However, there was no significant variation in the characteristic stress levels (Figure 6.19b and Figure 6.19c). This behaviour could be explained by the increase of the intergranular friction due to the presence of the coating.

Summarising, the surface properties of the grains affected the response of the sand under compressive loading in quasi-uniaxial strain conditions. The effect of friction was only evident in loose configurations, having the grains more freedom of movement than in dense packing configurations. The increase of friction enhanced the inter-granular locking, producing an increase in the stiffness of the material (during

the compaction phase) and a reduction of the maximum compression strain.



(a) (b) (c)

Figure 6.19: Effect of coating on (a) confined modulus, (b) stress and (c) strain of loose Euroquartz sand

6.3.4 Effect of the confinement

The investigation of the compressive mechanical behaviour of granular materials under quasi-uniaxial stress conditions requires the use of containments opposing negligible resistance to radial deformations. Latex confinements (described in detail in Section 6.1.2) were used for this purpose. In this case, the sand was free to expand radially because of the very low resistance imposed by the latex to radial deformations (low confining pressures). Figure 6.20 shows the comparison between the experimental results obtained on three types of sand, in a dense compaction state, compressed at a strain rate of $1000s^{-1}$ using rigid (quasi-uniaxial strain) and deformable containers (quasi-uniaxial stress). Q-Rok sand was more compliant than the other two types of sand in both conditions. Ottawa and Euroquartz sands presented same levels of stress for strains lower than 0.1, regardless the type of confinement adopted. At higher strains, Ottawa sand exhibited a higher flow stress then Euroquartz sand. The compressive stress-strain behaviour of sand confined in deformable containers appeared to be very different with respect to the one constrained in a rigid confinement.

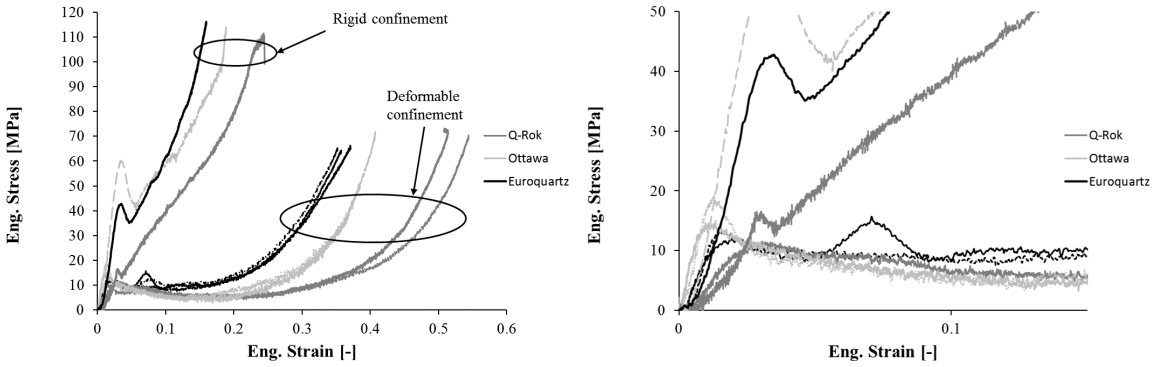
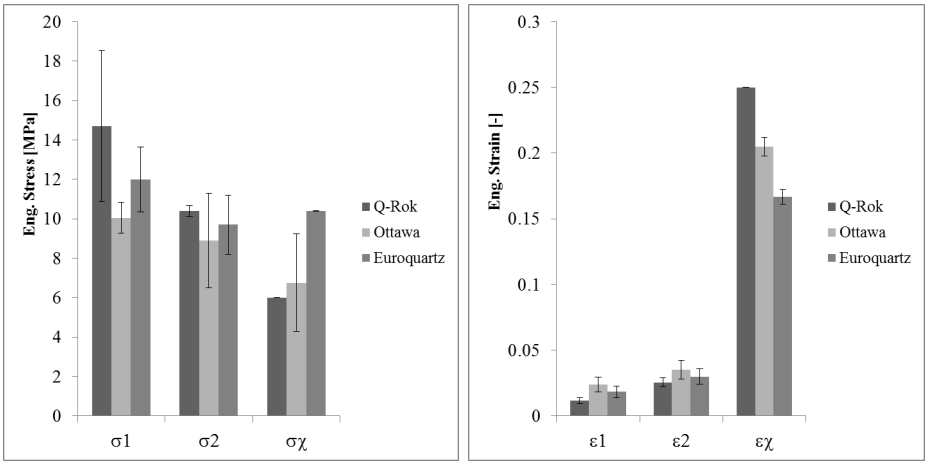


Figure 6.20: Effect of the deformable confinement (a) on the response of the three types of sand at $1000s^{-1}$ and zoom-in at low strains (b)

The initial pseudo-elastic response, due to the elastic recoverable deformation of the grains, was similar in both configurations. Also, the position of the apparent yield point was unaffected by the type of confinement. Therefore, for very low deformations, the mechanical behaviour was not influenced by the confining pressure. For engineering strains larger than 5%, the sand tested in a quasi-uniaxial stress condition exhibited lower flow stresses when compared to the sand constrained into a rigid confinement. Figure 6.21 shows the relevant stress and strain values for the three types of sand investigated, confined in deformable containers. The adoption of the LSHPB allowed for the achievement of larger deformations, thus speculating the compressive behaviour of the sand at strains higher than those usually achieved in literature. The type of confinement affected the confined modulus, as this portion of the stress-strain curve primarily depends upon the reorganisation of the grains and on their fragmentation. The reduction of the confining pressure modified the reorganisation process and, consequently, the overall behaviour. For engineering strains larger than ε_χ the slope of the curves exhibited an upsurge, with stiffness similar to the one of the initial pseudo-elastic response (zone 1 in Figure 6.6). This could be due to the fragmentation of the grains during compression. At this stage, most of the grains are plausibly fractured. Consequently, the response of the sand becomes

equivalent to the response of an assembly, of much smaller grains, that is able to sustain larger stresses without further comminution (size effect).



(a) (b)

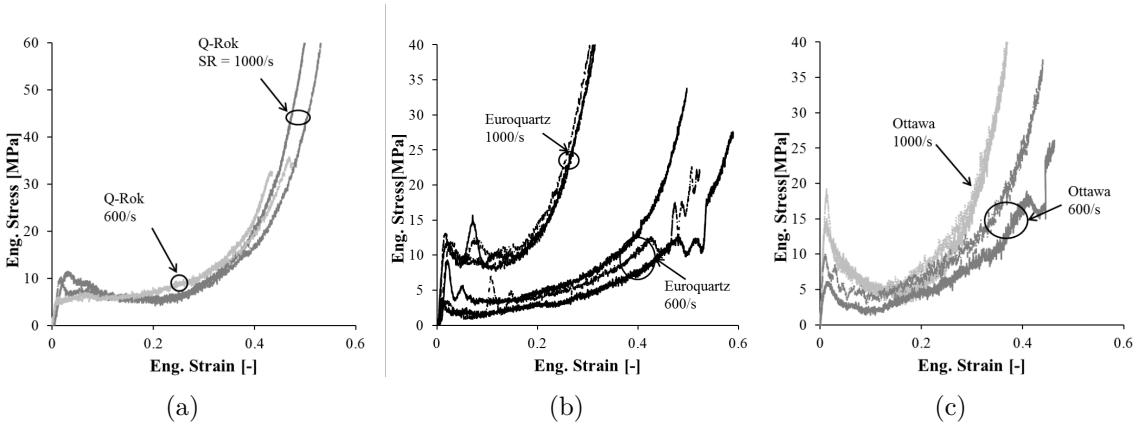
Figure 6.21: Salient values of stress and strain of the three types of sand in a deformable confinement

In conclusion, the variation of the type of confinement heavily modified the mechanical behaviour of granular materials. The adoption of deformable containers allowed for lateral deformation, thus producing test conditions similar to those obtained in quasi-uniaxial stress conditions. The effect of using a highly deformable confinement was evident in zone 3 and zone 4 of the stress-strain curves (Figure 6.20). In zone 3, the response deviated from the lock-up behaviour shown in the case of rigid confinements. As the level of confining pressure reduced, the soil sustained less axial stress. At large strains, a steep increase in the levels of stresses was observed. A comparison of the three types of sand, in quasi-uniaxial stress conditions, confirmed the effect of the shape of the grains on the mechanical behaviour of sand.

6.3.5 Combined effect of strain rate, shape and confinement

This section presents the combined effects of strain rate and grain morphology on the mechanical response of different types of sand in deformable confinements. To understand the effects of the strain rate on the mechanical behaviour of sand, each material investigated in the present study was tested at two different strain rates, in

quasi-uniaxial stress conditions. Figure 6.22a shows that the effect of the strain rate on the compressive mechanical response of Q-Rok sand, contained in a deformable confinement, was negligible. However, the apparent yield stress increased noticeably with the strain rates, as outlined in Figure 6.23.



(a) (b) (c)

Figure 6.22: Effect of the strain rate on the mechanical behaviour of (a) dense Q-Rok, (b) Euroquartz and (c) Ottawa sand in deformable containers

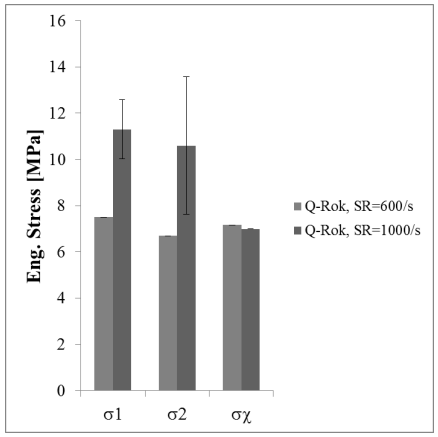


Figure 6.23: Example showing the effect of the strain rate on the values of stress of dense Q-Rok sand in deformable containers

Figure 6.22b shows the effect of the strain rate on Euroquartz sand constrained in a deformable confinement. It is evident that the increase of strain rate produced a stronger mechanical response. Figure 6.22c shows the rate dependence of Ottawa sand characterised using the same type of confinement. The variation due to the strain rate is less evident than for Euroquartz sand. Nevertheless, also in this case,

the increase of strain rate produced a slightly higher mechanical response. Figure 6.24 compares the results obtained on the three types of sand at a strain rate of $600s^{-1}$, thus confirming the influence of the grain shape on the mechanical behaviour of sand enclosed in deformable containers.

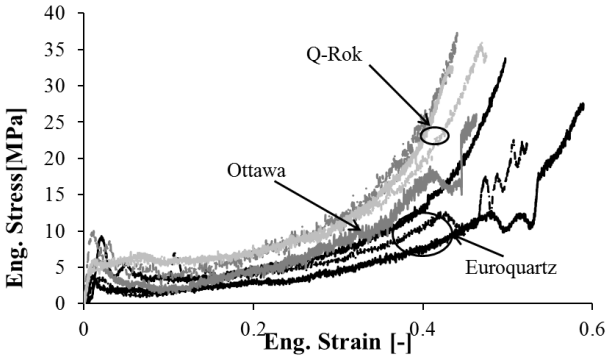


Figure 6.24: Combined effects of shape and confinement at a lower strain rate

In conclusion, an increase in the strain rate was always accompanied by an increment of strength in the mechanical response of sand confined in deformable containers. However, the observed rate dependence was different for different types of sand (i.e. for different grain shapes). The compressive behaviour of sand is strongly dependent upon the rearrangement of grains and on their fracture. The variation of the measured stress-strain curves with the rate of deformation and with grain shape demonstrated the strong influence of both these parameters on grain fracture and rearrangement.

6.3.6 Effect of water content

Dry sand can be considered a two-phase material composed of solid particles and air, which fills the interstitial voids. The addition of water adds a third phase. The water is much stiffer than air when compressed. If the specimen is loaded quasi-statically, the air and water in the pores are displaced and escape from the volume (drained condition). When the rate of deformation is high, the water and air remain trapped in the voids (undrained conditions), thus stiffening the mechanical response of the material [46]. In this study, the effect of the water content was analysed for

Euroquartz, Ottawa and Q-Rok sand. The samples were in an initially dense configuration, confined in a rigid container, and compressed at high strain rates (undrained quasi-uniaxial strain compression). The specimens were prepared according to the procedure detailed in Section 6.2.4.

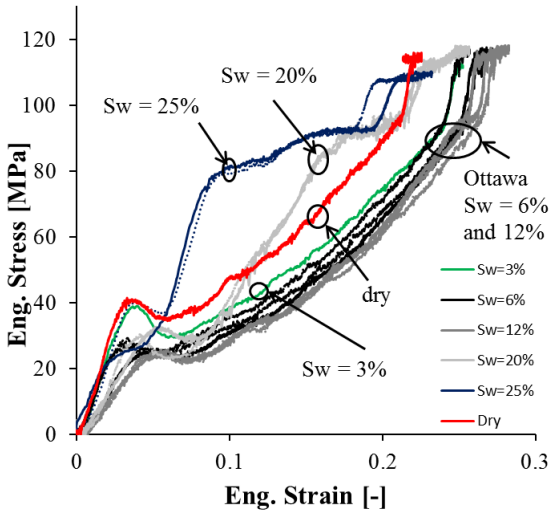
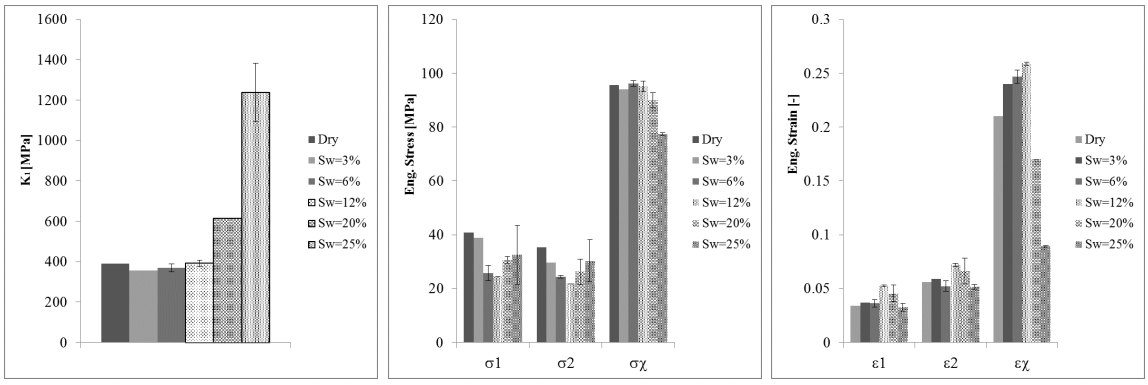


Figure 6.25: Moisture effect on initially dried, dense Euroquartz sand at high strain rate



(a) (b) (c)

Figure 6.26: Effect of the moisture content on (a) confined modulus, (b) stress and (c) strain of dense Euroquartz sand at high strain rate

Figure 6.25 shows how the moisture content affected the compressive response of Euroquartz sand. Five different gravimetric water contents were adopted: 3%, 6%, 12%, 20% and 25%. The confined modulus for partially saturated samples decreased

with respect to the dry response, as the moisture content goes from 3% to 12%. Conversely, it increased for water contents above 12% reaching its maximum for fully saturated samples (25%). Figure 6.26 summarises these conclusions. The maximum compressive strain obtained during high rate testing increased with the water content up to $S_w = 12\%$. A drastic decrease of the maximum measured compressive strain was observed when further increasing Sw (Figure 6.26c).

Analogous experiments were conducted on Ottawa sand. The water content of specimens was varied between 3% and 20%. The corresponding results are shown in Figure 6.27.

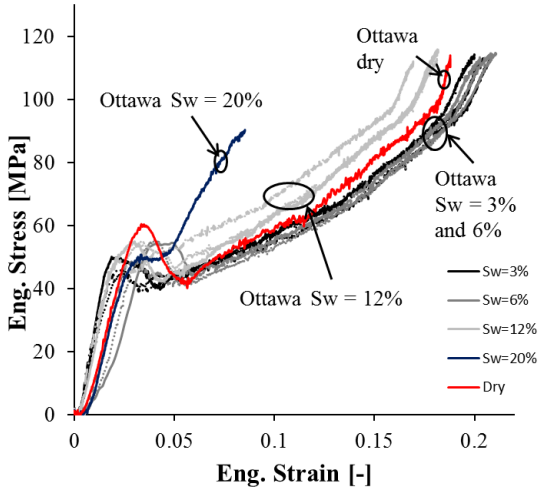
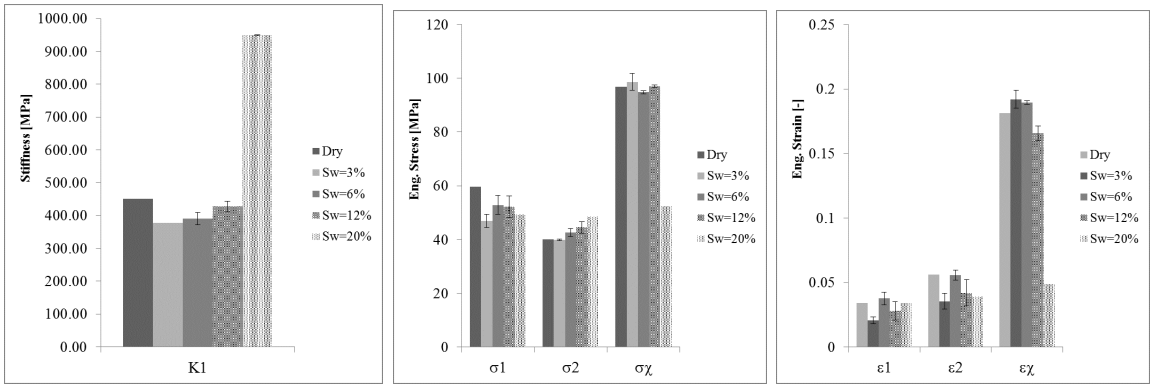


Figure 6.27: Effect of the moisture content on initially dried, dense Ottawa sand at high strain rate

Wet Ottawa sand was slightly more compliant than its dry counterpart for water contents equal to 3% and 6%. Conversely, an increase in the confined modulus was measured for moisture contents above 12%. Fully saturated conditions were achieved, in this case, at $S_w = 20\%$. Figure 6.28a summarises the results obtained on Ottawa sand in terms of confined modulus. Also in this case the variation of ε_χ and, consequently, of the maximum compressive strain shows an opposite trend than the confined modulus, as summarized in Figure 6.28c.

The effect of the moisture, for low values of gravimetric water content, can be

explained by the lubrication of inter-granular and grains-wall contacts caused by the presence of water [46]. In unsaturated conditions, it is reasonable to think that water occupies only the contact areas between grains, reducing the friction while enabling the pore air to displace within the sample. At high moisture contents, the water actively carries most of the load and the saturation of the pores prevent the free movement of air, thus stiffening the behaviour of sand.



(a) (b) (c)

Figure 6.28: Effect of the moisture content on the confined modulus of dense Euroquartz sand at high strain rate

6.3.6.1 Combination of the effects of morphology and water content

Q-Rok sand and Ottawa sand were extensively tested in dry conditions and with 6% gravimetric water content to study the concurrent effects of moisture and grains morphology on their mechanical response (Figure 6.29).

The effect of the water content was consistent for both types of sand. The unsaturated Q-Rok and Ottawa sands were more compliant than their corresponding dry configurations, when compressed in a rigid confinement. Figure 6.30a shows the reduction of confined modulus due to the presence of water for both types of sand.

Figure 6.30b and Figure 6.30c show, respectively, the influence of the water content on the measured stresses and strains; σ_1 and σ_2 were both reduced as a consequence of the addition of water to the sample, whilst σ_χ remained essentially unaffected by the moisture content.

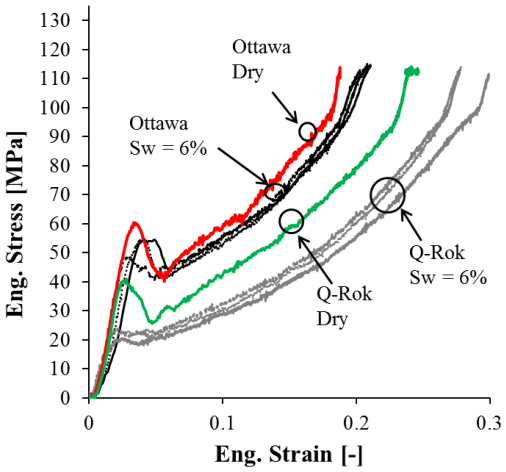
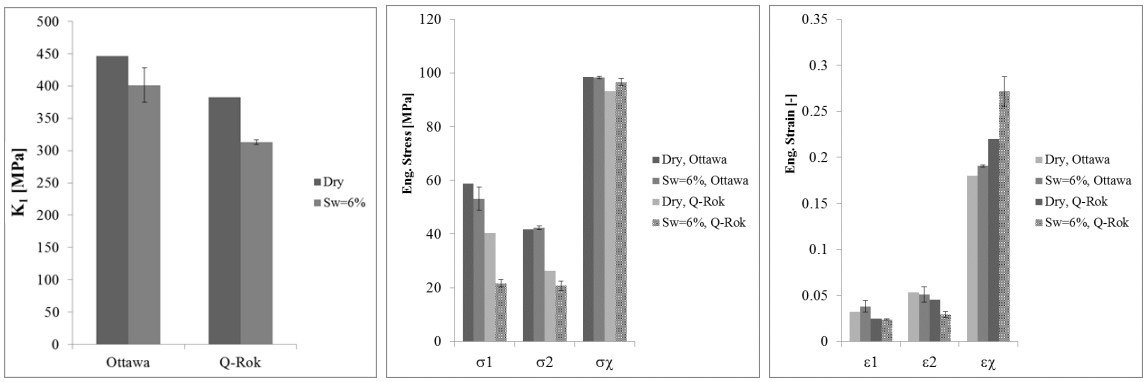


Figure 6.29: Effect of the moisture - comparison between Ottawa and Q-Rok dense sand at high strain rate



(a) (b) (c)

Figure 6.30: Effect of the moisture content on the confined modulus of dense Ottawa and Q-Rok sand at high strain rate

The reduction of stress and the increase in the maximum compressive engineering strain, due to the water content, were more evident for Q-Rok sand than for Ottawa sand. This confirmed the concurrent influence of grain morphology and moisture on the physical phenomena. The spherical grains (Ottawa sand) can roll and rearrange more easily then polyhedral grains when subjected to external compressive loading. The rolling friction is generally much lower than the sliding friction. Therefore, the inter-particles friction is much higher for polyhedral grains than for spherical particles. The water reduces the inter-granular friction acting as a lubricant. The effect of

lubrication is more evident where the sliding friction is predominant (Q-Rok sand). This explains the considerable difference in the mechanical response of Ottawa and Q-Rok sand in low water content conditions.

6.4 Summary

The research herein presented provides a comprehensive study of the effects of several parameters and their cross-interaction on the mechanical response of sand under dynamic uniaxial loading conditions. The effects of initial consolidation state, confining pressure, water content, strain rate, intergranular friction and morphology were investigated. All experiments were carried out using the Long Split Hopkinson Pressure Bar apparatus, thus allowing for the achievement of longer pulse durations and higher strains.

The effect of initial consolidation state was assessed using three different preparation procedures to obtain loose, intermediate and dense samples. Three different types of sand were tested at two different strain rates to determine any possible interaction between initial compaction, grain shape and strain rate. The results showed a noticeable stiffening of the stress-strain curves with the increase of the initial density, regardless the grain shape and the strain rate. The concurrent effects of grain morphology and strain rate were observed comparing the mechanical response of Ottawa sand (with quasi-spherical particles) and Q-Rok (with polyhedral grains) at two different strain rates. The sand composed of spherical grains was characterised by a higher stress-strain relationship when compared to sands composed of polyhedral grains. This is thought to be a consequence of the grain fracturing mechanisms, which, in turn, depend upon the grain shape. Additionally, for the first time in literature, the effect of intra-granular friction on the mechanical response of granular materials has been showed by comparing the behaviour of naturally occurring and coated Euroquartz sand. The effect of the coating depended considerably upon the initial consolidation state. When the sand was tightly packed, the variation of sur-

face properties did not seem to influence its mechanical response. The effect of the coating was more evident in loose configurations where the grains, when compressed, had more freedom of movement. The increase of friction due to the coating enhanced the inter-granular locking, hence increasing the stiffness of the material and reducing the maximum compressive strains. The effect of the confining pressure was also analysed. The adoption of latex confinements allowed the sand to expand radially because of their very low resistance to radial stresses. During testing, this configuration generated quasi-uniaxial stress conditions. The initial pseudo-elastic response was not affected by the confining pressure. The type of container affected, instead, the confined modulus. This indicated a strong effect of the confining pressure on the reorganisation of the grains and on their fracture during uniaxial compression. The strain rate sensitivity of the sand in quasi-uniaxial stress condition was strongly dependent upon the shape of the grains. An increase in the strain rate always yielded a stronger material response and a higher apparent yield point when testing sand in deformable containers. This demonstrated the interdependence of confining pressure and grains morphology on their fracture and rearrangement.

The effect of the water content was investigated for Euroquartz, Ottawa and Q-Rok sands. The samples were in an initially dense configuration, confined in a rigid container, and compressed at high strain rate. The results showed that unsaturated samples were more compliant than dry sand. Such behaviour was observed on any kind of sand regardless the morphology. The effect of water content on unsaturated samples can be explained by the lubrication of inter-granular and grains-wall contacts due to the presence of water. A further increase of the water content led to the saturation of the pores. This prevented the free movement of air volumes, thus stiffening the behaviour of the sand.

This chapter attempts to fill some of the gaps identified in literature. However, it does not provide any verification of the rate sensitivity of granular materials. This topic will be the core of the next chapter.

Chapter 7

The development of sound measurements for the evaluation of the rate sensitivity of granular materials

The experimental characterisation of granular materials, presented in the previous chapter, proved the influence and inter-dependency of many parameters on their high rate behaviour. Nevertheless, it was not possible to isolate and observe relevant variations in their mechanical response when varying the rate of deformation from $1600/s$ to about $600-800/s$. Even the literature (Section 2.3.2) provides contradictory observations on the rate dependency of granular materials. For both the aforementioned reasons, further experimental studies are carried out. In particular, the current chapter addresses three main questions:

1. is the mechanical behaviour of granular materials affected by the variation of the rate of loading?

2. what is the role of grain crushing and inter-granular friction on the rate dependent behaviour of sand and on its mechanical response?

3. could the grains fracture be localised in time, during the execution of uniaxial compression tests?

Typically, Non Destructive Techniques (NDT) are used to obtain *real-time* measurements of phenomena happening within the material during the application of the loading. A detailed literature review is available in Section 2.5. One of the most used NDT in soil and rock mechanics is the Acoustic Emission (AE) technique. However, it presents several drawbacks when used to detect emissions at the grain level (e.g. inter-granular sliding and grain crushing can not be distinguished).

Initially, a new NDT called *Sound Measurements* (SM), based on acoustics, is defined and calibrated against microscopy images taken during in-situ compression tests on single sand grains and small assemblies. Later, the new technique is applied to study the rate effects and role of grains fracture on the mechanical response of granular materials subjected to uniaxial loading, thus attempting to answer the identified open questions.

7.1 Sound Measurements and imaging of sand grains failure during in-situ compression tests

Sand grain fracture is identified as one of the main mechanisms governing the mechanical response of granular media [211, 212]. Within a granular assembly, any applied force in the system is transmitted through contact forces, commonly referred to as force chains. Crushing happens when tensile intra- and trans-granular cracks develop around the contact area of highly loaded particles because of point loading [80, 213]. Constitutive parameters, such as normal compression line of sand [78], yield surface [214], and friction angle [215] are related to this phenomenon. In addition, porosity and permeability of the granular media are drastically affected by grains comminution since particle crushing induces a reduction in the mean particle size of an assembly [86, 216]. Grain crushing, together with intragranular friction, is also responsible for the rate sensitivity of granular materials [41, 217, 218]. Therefore, a better understanding of single particle fragmentation would clarify its effect on, for example, soil crushability and on the overall mechanical response of sand.

In order to address some of the aforementioned issues and since part of the AE events frequency spectrum falls in the audible range, the present study proposes a new technique, herein defined as Sound Measurement, which adopts airborne sensors (i.e. microphones) to capture the events generated exclusively by grain fracture. Firstly, the SM technique is defined and, then, calibrated against in-situ observations of the fracture of single sand grains and of arrangements of grains. Moreover, this work provides a combined audio-visual analysis of the failure of sand grains, showing the effects of chemical composition, morphology, and grain sizes on it.

7.2 Experimental procedure

7.2.1 Proposed method

Sound Measurement, with underlying physical principles that come from the acoustics, has been thought to be an alternative non-destructive technique that can be used to study granular materials. It relies on the ability to record sounds originated during fracture, which travel through the air as compressive waves. The main difference between SM and AE is the frequency range of the signals in which they work. While AE provides a very wide range of frequencies (1 kHz-1 MHz), SM works within the audible spectrum (20 Hz - 20 kHz). To compensate this, SM requires a simpler set-up with less costly sensors (microphones) and a much easier installation, since they do not need to be coupled with the surface of the body under examination.

7.2.2 Materials and experimental set-up

Three types of sand were tested to show the effect of grain shape, size and material on the single grain failure mechanics: Crystalline Silica Ottawa sand with round grain shape, Crystalline Silica Q-Rok sand with polyhedral grain shapes, and amorphous volcanic ashes. Ottawa and Q-Rok sand were described and characterised in Section 6.1.1. The volcanic sand was collected during the paroxysm of December 2014 from the South East Flank of Mount Etna. The size distribution of Ottawa and Q-Rok

sand are reported in Figure 6.1a-b, whilst the volcanic one is displayed in Figure 7.1. The size distribution of the volcanic sand was obtained through sieving. It passed #14 sieve (sieve opening = 1.4 mm), and was retained on #120 sieve (sieve opening = 0.125).

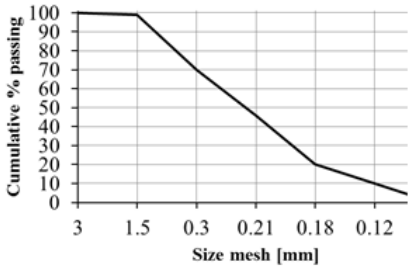
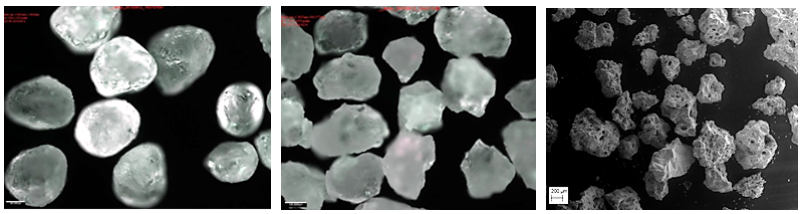


Figure 7.1: Size distribution of Volcanic sand

Table 6.1 provides details for the chemical composition of the two types of quartz sand: Q-Rok and Ottawa. Ottawa is a naturally occurring sand, whilst Q-Rok sand is obtained by crushing. Etnean Volcanic ash, instead, is mainly composed of two minerals: cristobalite and anorthite. The former is characterised by the same chemical composition of silica (Table 6.1) but it has a distinct crystal structure; the latter ($CaAl_2Si_2O_8$) is omnipresent in all rocks of Mount Etna. These ashes are characterised by the presence of abundant vesicles inducing an inherent porosity and a vitreous phase formed as a result of the very rapid cooling lava undergoes after the eruption.

Figure 7.2 shows SEM images of Ottawa, Q-Rok sand and Volcanic sand grains, where the different geometries and features can be identified.



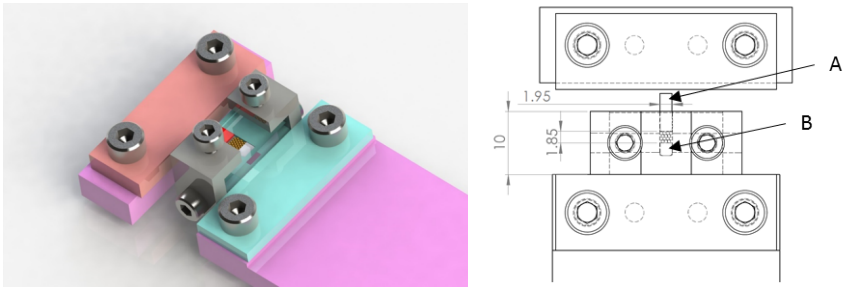
(a) (b) (c)

Figure 7.2: Grain shapes for Ottawa (a), Q-Rok (b), and Volcanic sand (c) with 20X magnification

Further sieving was carried out to obtain controlled overall grain sizes for the

three types of sand, to investigate the effects of morphology and chemical composition. Therefore, grains with average diameter size comprised between 0.425 and 0.5 mm were selected. Ottawa grains with size smaller than 0.425 mm were adopted to evaluate the size effect. In-situ observations of the fracture dynamics of single grains and of arrangements of sand grains were carried out in combination with sound measurements.

A stainless steel container, with a thick transparent glass cover (Figure 7.3), was designed to confine the grains. It was, then, inserted in a 5 kN Deben UK stage that was used to perform the mechanical tests.



(a) (b)

Figure 7.3: Metallic container and glass cover for in-situ tests on sand (dimensions in mm)

During the tests, each particle and assembly of particles were placed between two flat stainless steel platens (labelled A and B and shown in Figure 7.3b). The platen A was in charge of transmitting the load from the moving cross-head to the specimens. Uniaxial compression tests, at ambient conditions, were carried out in a displacement-controlled manner with a cross-head speed of 0.5 mm/min and a preload of 1 N. The load was measured with a load-cell of 150 N, whilst displacement of the platens was measured by means of a linear voltage displacement transducer (LVDT) mounted on the side of the metallic container. Images and videos (with an acquisition frame rate of 15 fps) were taken using an Alicona Infinite Focus 3D profilometer with a $5X$ magnification lens. The sound was recorded using a desktop microphone placed close to the container with an acquisition rate of 96 kHz.

Audio and video were recorded concurrently during testing in order to produce real-time measurements, which were then compared in the post-processing phase (Figure 7.4). The audio recordings were de-noised to improve the Signal-to-Noise (SNR) ratio. The de-noising procedure was done using the built-in functionality of the acquisition software Audacity, which is based on the so-called *spectral noising gating* technique [219].

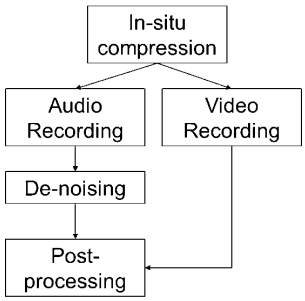
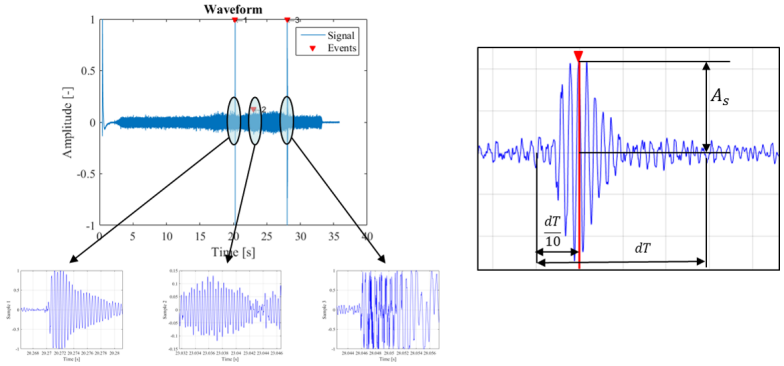


Figure 7.4: In-situ testing procedure

7.2.3 Post processing protocol

The SM analysis is based on the estimation of several characteristic parameters that help the researcher to infer mechanical features and properties of a medium during the application of an external load. The parameters herein defined were similar to those used in Acoustic Emissions analysis. The post-processing was carried out by employing the Signal Analysis toolbox of Matlab 2015b.



(a) (b)

Figure 7.5: Extraction of the fracture events from the waveform of the signal (a) and definition of an event (b)

Once the waveform of the signal was de-noised, the failure events needed to be identified. An amplitude threshold was set equal to 10% of the maximum amplitude of the signal to separate acoustic events from background noise. An SM event, as shown in Figure 7.5, started when the signal exceeded the prescribed threshold. Each event had a duration set equal to $dt = 10$ ms (with a tail of the signal of duration equal to $0.1dt$). In the time domain, each event was characterised by:

1. Counts per event (CE): defined as the number of times that a signal went above a fixed threshold (equal to one tenth of the maximum amplitude A_s) in a particular event.

2. Cumulative counts per event (CC): that measures the evolution of the emissions during the fracture and it was equal to the sum of the counts per event over time.

   Both parameters are shown in Figure 7.6.

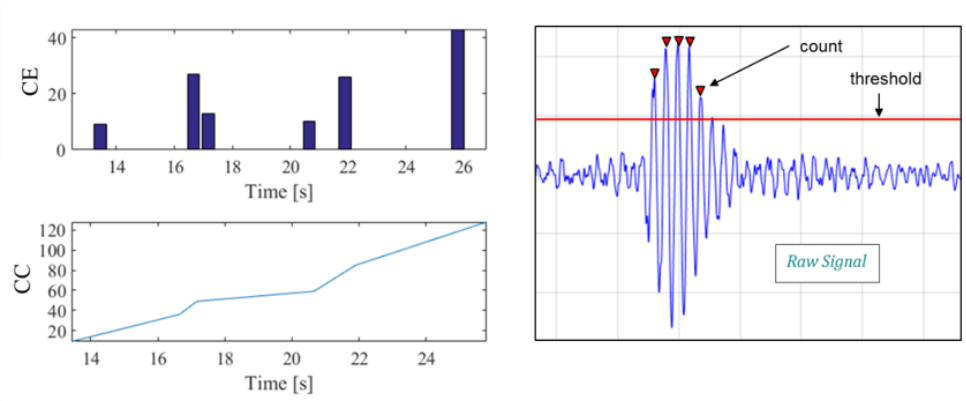


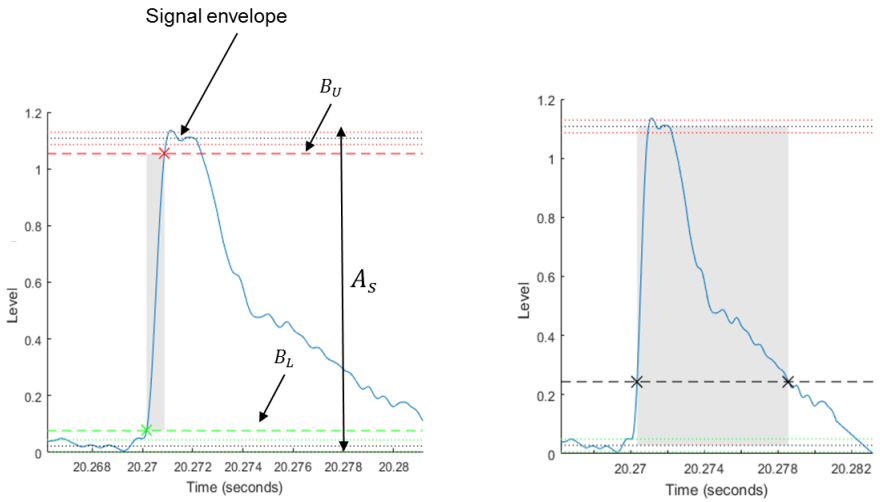
Figure 7.6: Definition of counts per event (Hits) and cumulative counts per event

3. Event amplitude: this is the maximum signal level reached during an event.

4. Duration: It was computed on the signal envelope (Figure 7.7a); the duration is strongly dependent upon the choice of the threshold amplitude A_t. However, there is not any guideline for choosing the threshold. One and only one value

of A_t was adopted among different tests to obtain meaningful comparisons (in these analyses $A_t = 0.2A_S$).

5. Rise Time: It represented the time needed to the signal to go from the Lower bound (B_L) to the Upper bound (B_U), where $B_L = 0.05A_S$ and $B_U = 0.95A_S$. It measured the speed at which the energy was released during the cracking events (Figure 7.7b).



(a) (b)

Figure 7.7: Typical examples of rise time (a) and duration (b) of a burst event

Additional details can be obtained by exploring the frequency spectrum of the signal. In the Acoustic Emission theory, the spectrum of a signal is believed to be strictly correlated to events happening during the fracturing process of a body. Additionally, it is less affected by testing conditions when compared against time domain characteristics. The signals are converted from time domain to frequency domain by applying FFT methods. The energy spectral density, defined in eq. (7.1), is generally employed in case of transient signals having a finite total energy [220].

$$ESD = \int_{-\infty}^{+\infty} |x(t)|^2 dt \tag{7.1}$$

In this case, Parseval's theorem [221] gives an alternate expression for the energy of the signal in terms of its Fourier transform, as reported in eq. (7.2).

$$ESD = \int_{-\infty}^{+\infty} S_{xx}(f)df \tag{7.2}$$

The integrand $S_{xx}(f)$ can be interpreted as a density function measuring the energy of the signal per unit frequency. Moreover, in order to discretise between the characteristic frequencies of relevant events from the spurious ones, due to background noise coming from the loading device (in-situ compression stage), the Frequency-time distribution was computed [222]. It represented the time-varying spectral components of non-stationary signals. An example of the Frequency-time distribution is shown in Figure 7.8.

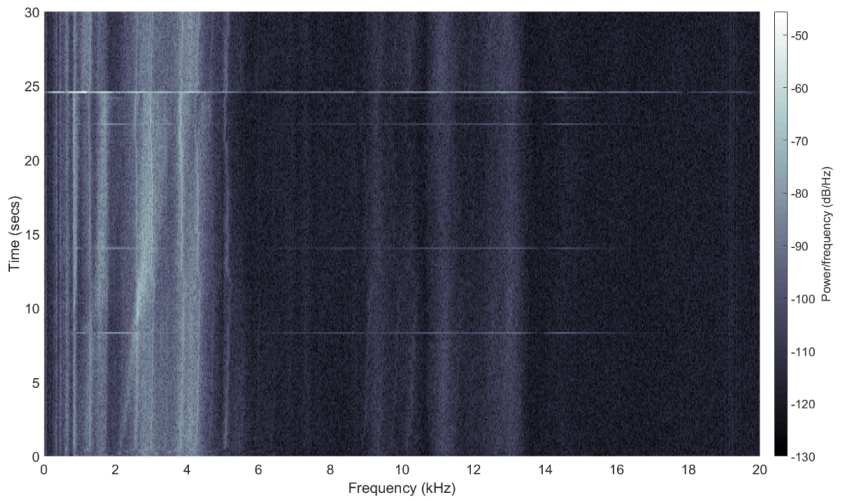


Figure 7.8: Example of Frequency-Time distribution analysis

7.3 Results and discussion

The results are based on the analysis of five different sets of tests aimed at understanding the effects of grain size, shape and chemical composition on the single grain fracture. On average, five tests per configuration were carried out to generate statistics and check the reproducibility of the results.

7.3.1 Mechanical characterisation

This section summarises forces and displacements at failure, measured for all types of sand, during the in-situ compression tests on single grains. The results are shown in form of box and whisker plots with median values marked by a red line.

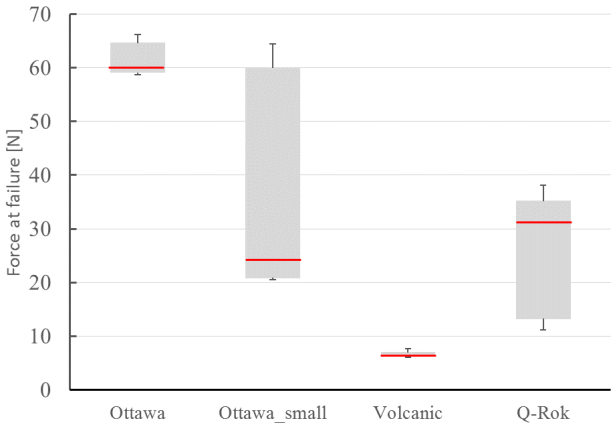


Figure 7.9: Box plot of force at failure for different types of sand grains

Figure 7.9 shows how the force at failure changes for different types of sand grains. The size effect on the fracture of single sand grains can be analysed by comparing Ottawa sand grains with two different diameters (Ottawa and Ottawa small in Figure 7.9). It is clearly seen that bigger grains can withstand higher loads before failure, thus confirming the results reported in [210]. The observed positive trend in the *Force at failure vs. size* could be justified by assuming a single-crystalline microstructure for Ottawa sand. In this case, the failure would be caused by the development of trans-granular cracks. Bigger grains would require higher forces to yield the levels of stress needed for fracture. On the other hand, in case of polycrystalline grains, the outbreak of inter-granular cracks (which notoriously require less activation energy) would produce an opposite *Force at failure vs. size* relationship, as smaller grains would contain fewer grain boundaries thus opposing more resistance to fracture.

The effect of grain shape, shown in Figure 7.9, can be seen by comparing Ottawa and Q-Rok sand grains. In this case, the average grain size and chemical composition are the same for both types of sand. Q-Rok sand breaks at lower values of applied

force, because of stress concentration happening at the edges and corners of Q-Rok sand grains. Finally, the Volcanic sand exhibits much lower values of force at failure than all the other types of sand. This is thought to be a direct consequence of chemical composition and porous microstructure of the Volcanic sand grains (Section 7.2.2), which enhance their friability. As a matter of fact, it is widely recognised that the presence of vesicles (open or closed pores), their shapes, and relative density strongly enhance the friability of the material [223].

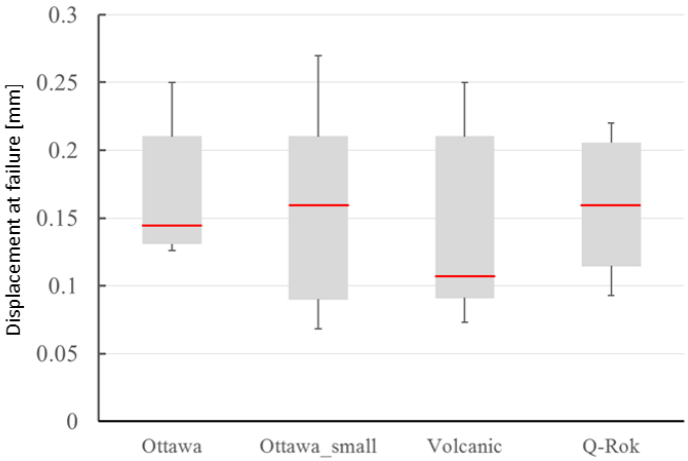


Figure 7.10: Box plot of displacement at failure for different types of sand grains

For a more comprehensive understanding of the single grain fracture, Figure 7.10 summarises the values of the displacement measured at the onset of failure. It is evident that, in this case, there is not a clear trend. All values fall within $0.07 - 0.28$ mm range. However, in case of brittle failure, the knowledge of displacement (d_f), force at failure (F_f), and the assumption of a linear relationship between the two (Figure 7.11) allow us to infer the elastic energy (E_r in eq. (7.3)) released during fracture for the materials under examination.

$$E_r \propto F_f d_f \tag{7.3}$$

With the displacement similar for all types of sand, as previously stated, E_r can be seen as directly proportional to the measurements of force at failure, shown in

Figure 7.9. Therefore, we could conclude, qualitatively, that higher elastic energy is released in case of Ottawa sand, followed by Q-Rok and Volcanic sand.

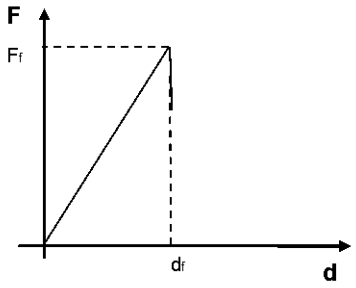


Figure 7.11: Typical force - displacement curve for brittle materials

7.3.2 Correspondence of bursts and cracking events

Two representative tests were carried out to show the ability of the proposed method to capture all cracking events taking place during uniaxial compression of single Ottawa sand grains. Three measurement methods were employed and compared to identify the fracture of grains: (i) SM, (ii) visual inspection through microscopy, and (iii) drops in the force-time curves. In the first test, an almost spherical Ottawa particle (Figure 7.12a) with a diameter equal to 0.425 mm was used.

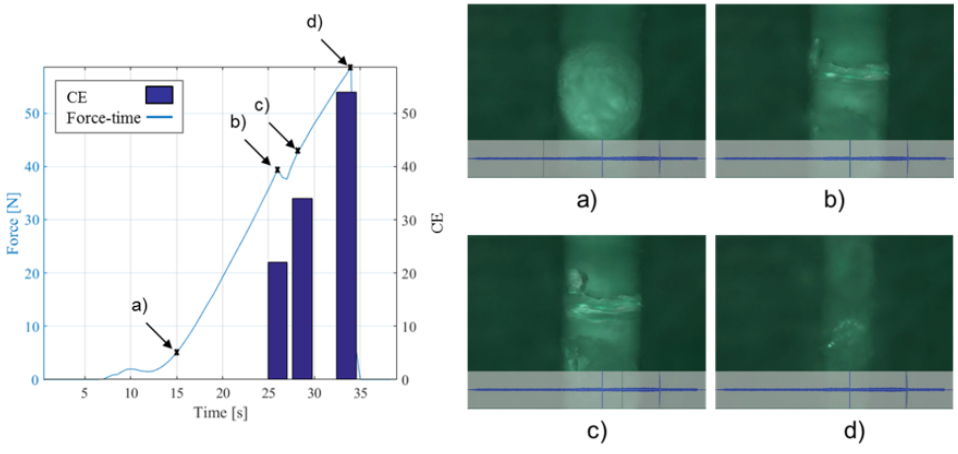


Figure 7.12: Test 1 - Ottawa sand grain. Comparison between SM, force-time curve (left), and microscopy (right): initial configuration (a), subsequent fractures (b and c) and complete crushing (d)

After an initial elastic compression phase, a diametral crack developed in between

the two loading points causing a drop in the force-time curve and shown in Figure 7.12b. Nevertheless, the particle was still able to carry load. A second minor crack, not recognisable in the force-time curve, was recorded by both SM (blue histogram in Figure 7.12, showing the number of counts per event) and microscopy (Figure 7.12c). Finally, a catastrophic failure happened at a load of about 58 N (Figure 7.12d). It was successfully detected by all techniques: a drop in the load, a visible burst event, and an acoustic event.

A second test was conducted on an Ottawa sand grain with roundness lower than the previous particle, but having similar sizes (Figure 7.13a).

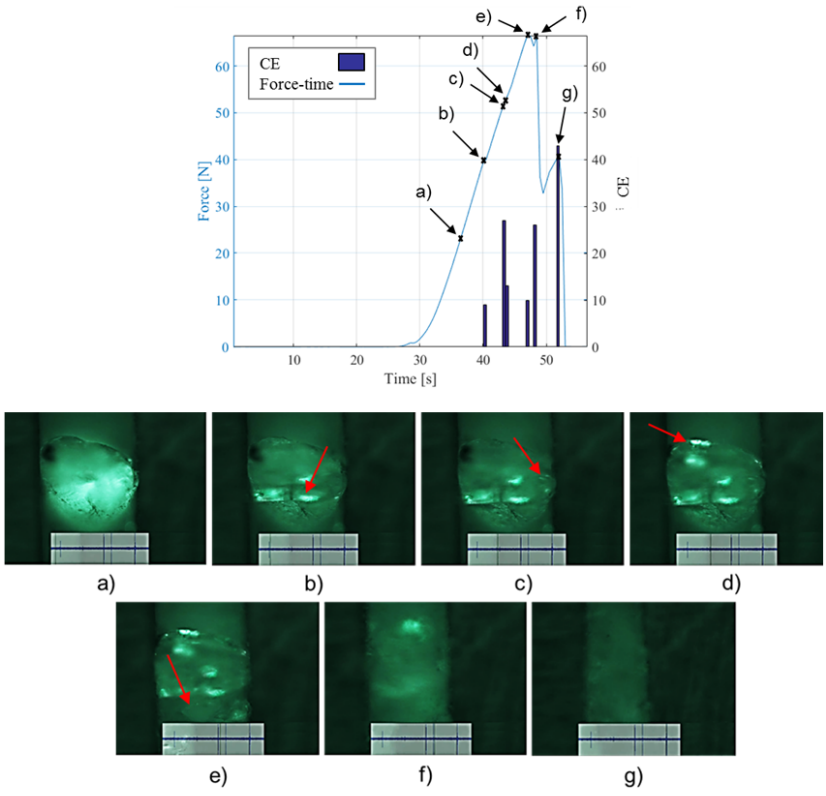


Figure 7.13: Test 2 - Ottawa sand grain. Comparison between SM, force-time curve (top) and microscopy (bottom): initial configuration (a), subsequent fractures (arrows in b - f), and complete crushing (g)

In this case, after the appearance of an initial diametrical crack (Figure 7.13b), multiple micro-cracks developed along the loading direction (Figure 7.13c - Figure

7.13e). Most of these cracking events, were *not visible* in the force-time curve, but they were successfully detected by the SM, as shown in Figure 7.13 (blue histogram). In this case, the grain was able to carry the load up to 65 N. At that stage, the movement of the fragments yielded a drastic drop in the load (Figure 7.13f). A final burst event, characterised by the highest number of counts, corresponded to the total pulverisation of the grain (Figure 7.13g) at a load of about 40 N.

These results unequivocally proved the correspondence between sound measurements and fracture of the grain and showed the ability of the proposed method to capture even those events hardly recognisable from the force-time curves.

7.3.3 Time domain characteristics

Information about the fracture events can also be obtained in both time and frequency domains. The signals were post-processed by adopting the procedure presented in Section 7.2.3. A time-domain analysis was carried out for Test 1 (presented in Section 7.3.2).

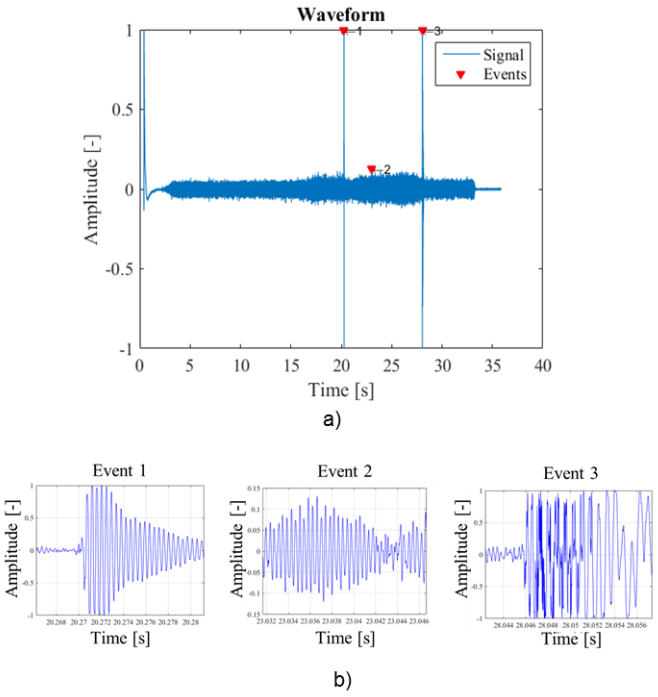


Figure 7.14: Test 1 - Waveform (a) and extraction of SM events (b)

In spite of being strongly dependent upon testing conditions [98], duration, rise time and amplitude can be used to estimate the energy released during cracking. The SM events (Figure 7.14b) were isolated from the waveform of the signal (Figure 7.14a) and analysed. Here, the amplitude was normalised against the maximum amplitude measured during the test. Figure 7.15a shows that the first and third events produced an acoustic signal of higher amplitude than the second one. The second event, because of its low amplitude and long rise time, was the one with the slowest and smallest release of energy (Figure 7.15c). The third event lasted for longer than the first one (Figure 7.15b) and presented a shorter rise time (Figure 7.15c). Therefore, it is not unreasonable to conclude that most of the energy was released during the last cracking event. This conclusion agrees with the images and videos taken with the microscope, as they show that more fracture surfaces (cracks) are generated during the last event (complete crushing of the grain as shown in Figure 7.12).

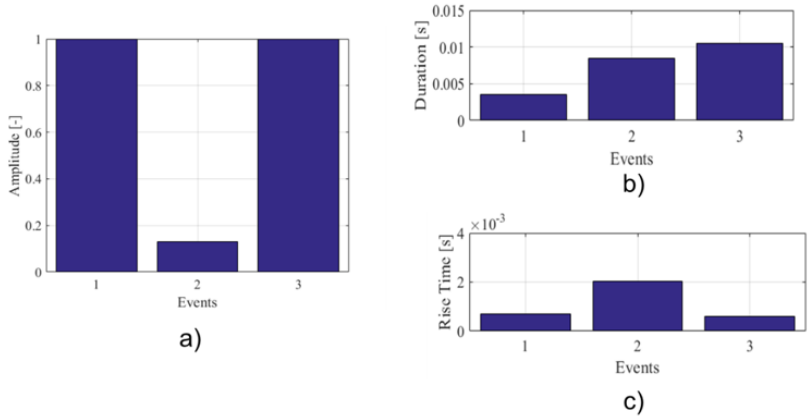


Figure 7.15: Amplitude (a), duration (b) and rise time (c) of the three events

7.3.4 Single grains cracking versus sliding/rotations

The acoustic emissions applied to granular materials are notoriously sensible to both sliding between particles and crushing [99]. Therefore, complex post-processing analysis was required to distinguish the emissions due to those mechanisms. The in-situ test reported below allowed us to prove the insensibility of SM to rotation and sliding of the grains. Again, force-time curve, sound measurements and microscopy

images were compared to identify the cracking events. The heart-shaped Ottawa sand grain (Figure 7.16a) elastically deformed until a major diametrical crack developed, splitting it into two halves (Figure 7.16b). This event induced a drop in the load that was successfully measured by the SM (blue bar corresponding to point b in the top graph of Figure 7.16). The measured emissions matched all the drops in the force-time curve (Figure 7.16d - Figure 7.16g) except the one marked by point c. In fact, even though the force-time curve showed a drastic drop (point c in the top graph of Figure 7.16), no SM events were detected.

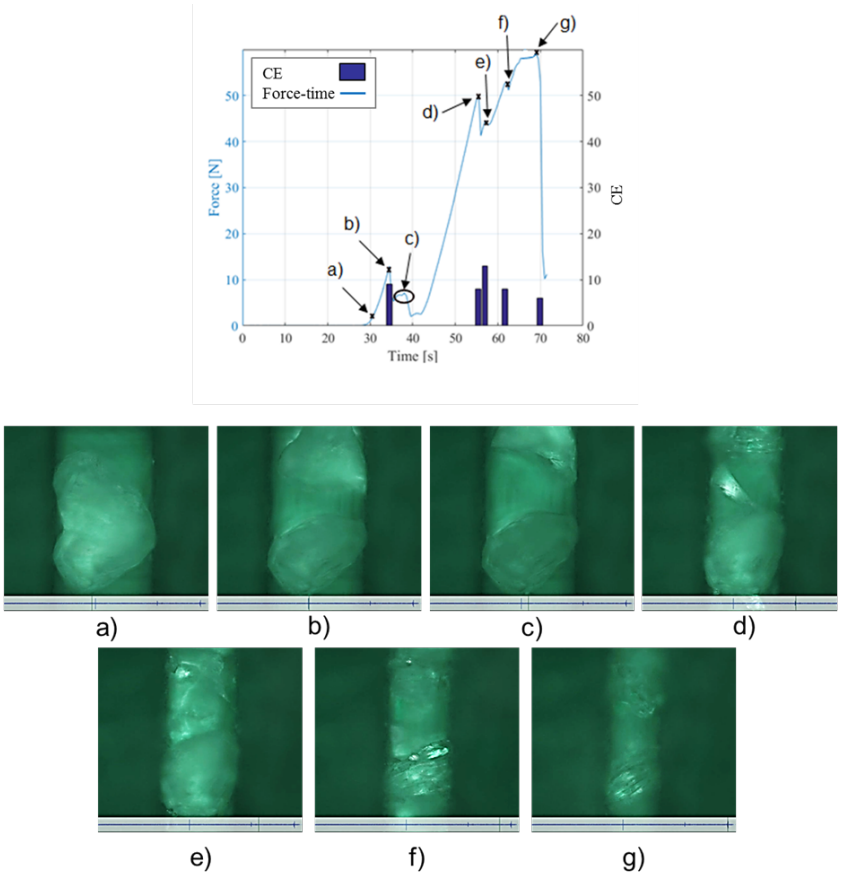


Figure 7.16: Test 3 - Insensitivity of SM to rotations during uniaxial compression test. Comparison between SM, force-time curve (top) and microscopy (bottom): initial configuration (a), subsequent fractures (b - f) and final crushing (g)

By comparing Figure 7.16b and Figure 7.16c, it can be seen that the drop was only due to the rotation of one of the fragments, thus proving that sliding and rigid

rotations of the grains are not captured by the proposed technique. The insensitivity of SM to sliding and rotations can be explained by the very low amplitude emissions connected to these phenomena, which fall within the noise range. Therefore, all sounds recorded are unequivocally associated with the failure of the grains. Consequently, such method can be applied to isolate the effect of fracture on the behaviour of granular materials (i.e. time sensitivity, etc.).

7.3.5 Effect of size, material and shape on single grain fracturing: frequency domain

In AE theory, the frequency analysis is widely adopted as it is less dependent upon testing conditions [98]. In particular, the dominant frequency of a phenomenon is often used for source mode identification, since AE are simultaneously affected by crushing and sliding of the grains. Previous experimental studies on rocks, concrete and sandstones confirmed that high-stress levels and subsequent relevant cracking events are featured by high-frequency elastic waves [98, 224]. In this study, all frequencies with a corresponding energy spectral density higher than 50% of its maximum (to include as many frequencies as possible) were arbitrarily considered dominant frequencies. Moreover, since we showed that SM signals were exclusively due to grains fracture, the analysis of the frequency domain was used to determine the influence of grain size, material and shape on the single grain fracture. In particular, information on the effect of grain shape was collected by comparing the dominant frequencies of Ottawa and Q-Rok sand grains. An example of uniaxial compression of Q-Rok sand grain is shown in Figure 7.17.

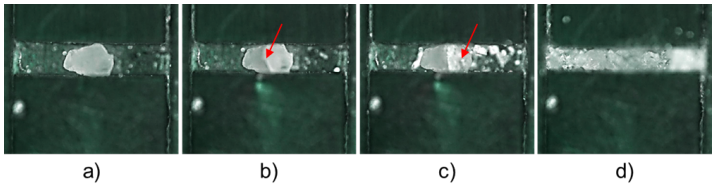


Figure 7.17: Uniaxial compression of Q-Rok sand grain: initial configuration (a), subsequent fractures (b and c) and final crushing (d)

Here it is noted that the two types of sand presented the same chemical composition but different shape as detailed in Section 7.2.2. The effect of chemical composition and grains shape was studied by comparing the dominant frequencies across the different types of sand. Figure 7.18 shows the uniaxial compression of a single Volcanic sand grain.

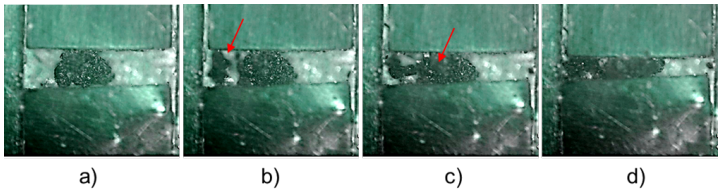


Figure 7.18: Uniaxial compression of Volcanic sand grain: initial configuration (a), subsequent fractures (b and c) and final crushing (d)

Finally, the effect of the grain size on the mechanics of fracture is evaluated by testing smaller single Ottawa sand grains. For this purpose, two different sets of grains with diameters respectively equal to 0.5 mm and 0.35 mm were used.

The signals measured during the tests were post-processed by adopting the procedure presented in Section 7.2.3. Consequently, the relevant frequencies across all experiments are presented in Figure 7.19. The effect of the grain shape can be clearly seen by comparing Ottawa (quasi-spherical) and Q-Rok (polyhedral) sand in Figure 7.19. It resulted in a higher scatter in the range of dominant frequencies ($1-6$ KHz) for quasi-spherical particles with respect to what measured for polyhedral grains ($1-3$ kHz). The Q-Rok sand grains showed a cluster of relevant frequencies at about 16 kHz.

The effect of chemical composition, evaluated by comparing Volcanic sand with the other two types of quartz sand in Figure 7.19, resulted in a smaller range of variation for the dominant frequencies, with a maximum value of about 9 kHz and with clusters around 1 and 4 kHz. Finally, the effect of grain size is shown in Figure 7.20. It can be seen that smaller grains generated a wider range of dominant frequencies, with clusters between $1-4$ kHz and peak values of 19 kHz.

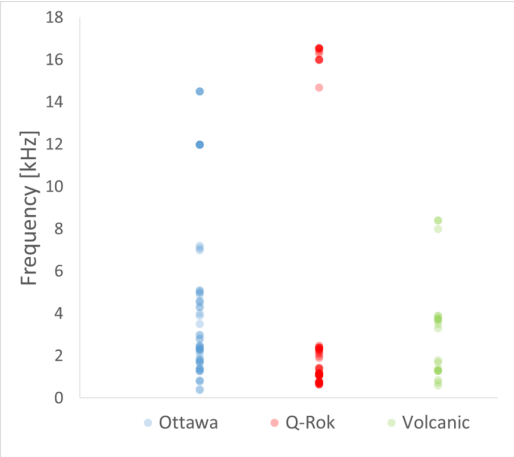


Figure 7.19: Effect of grain shape and chemical composition on the fracture of single sand grains

It is not possible to compare the obtained results with the ones available in literature because of the different frequency response of the acoustic devices used in the present work (as explained in Section 7.2.1). Nevertheless, the consistency of the results among multiple tests and the visual validation obtained through microscopy ensure the validity of the results.

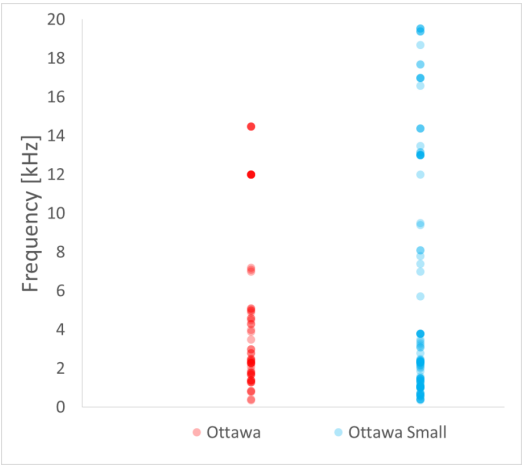


Figure 7.20: Effect of the grain size on the fracture of single sand grains

7.3.6 SM applied to granular assemblies: limitations of the technique

The applicability of SM to large-scale problems required its calibration using granular assemblies with a low number of grains. An in-situ uniaxial compression test on

an assembly containing 11 grains of comparable size (diameter of $\simeq 0.5$ mm) was carried out to check the one to one correspondence between SM measures and cracking events detected through microscopy. Figure 7.21 portraits the initial assembly of grains. The load was applied on the top anvil, whilst the bottom one was fully constrained.

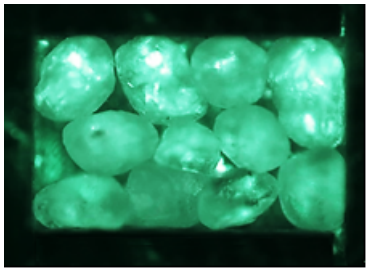


Figure 7.21: Initial assembly of Ottawa sand grains

Once again, even in the case of assemblies, the images and the drops in the force-time curve (Figure 7.22) confirm the ability of SM to identify the fracture of grains.

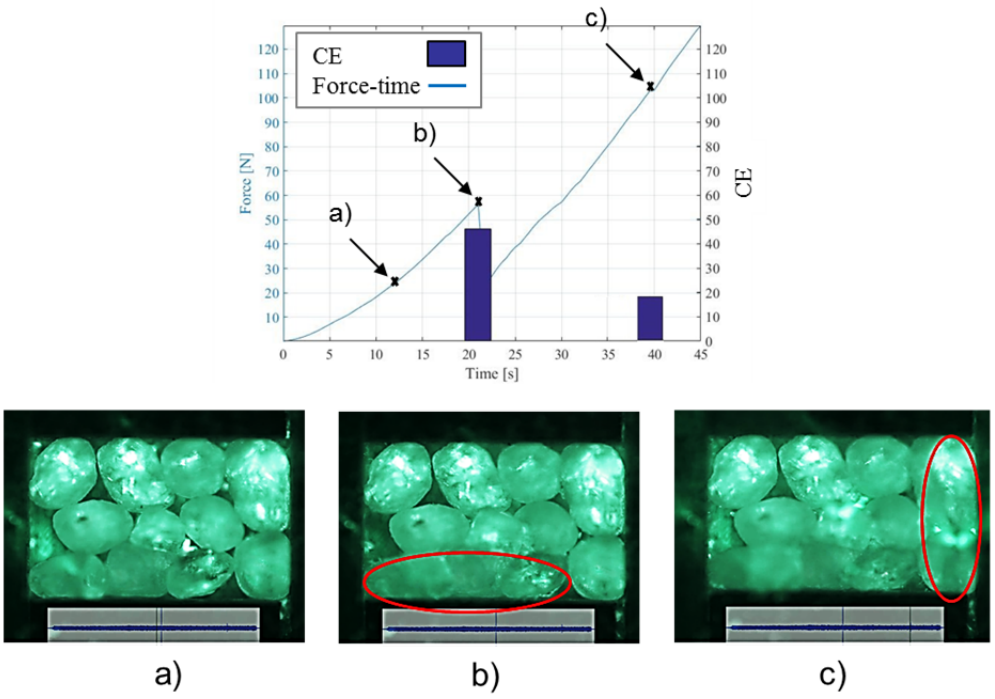


Figure 7.22: Assembly - Comparison between SM, force-time curve (top) and microscopy (bottom): initial configuration (a), subsequent fractures (b and c)

The two events detected in this example by SM involve simultaneous fractures of multiple grains (Figure 7.22b and Figure 7.22c). Therefore, in the case of assemblies, the possibility of multiple cracking happening at the same time invalidate the relation between the number of SM events and the number of failed grains. Nevertheless, the technique can still be applied to detect the onset of cracking events in the domain. The idea of undercounting the cracking events, known as *masking effect*, is widely accepted in AE and it has been proposed to be a consequence of clustering of acoustic events [86]. Our observations unequivocally confirm this assumption.

7.4 Sound Measurements on sand assemblies at different rates of loading

Once the new technique has been calibrated, it can be applied to RVEs of sand to study the rate dependency of their mechanical response. Understanding the effect of the strain rate on the overall mechanical behaviour of granular materials is fundamental to explain, predict or control a wide range of dynamic phenomena (earthquakes, mine explosions, projectile penetration, etc.). However, as already mentioned, the existing literature provides conflicting points of view on the existence of rate dependency for granular materials and on their possible causes. In other words, it is not clear whether the sand shows any rate dependency and which time-dependent parameter (i.e. inter-granular friction during grains rearrangement or grain crushing) plays a major role in their hypothetical rate dependency. Even the role of grain crushing on the mechanical response of granular materials during uniaxial compression tests represents an open question. As a matter of fact, the literature recognises the existence of 4 main zones in a typical uniaxial compression stress-strain relationship (Figure 6.6), one of which (i.e. Zone 4) should be mainly due to grain fragmentation. However, there is not yet any experimental evidence that proves this assumption.

The next sections attempts to fill the existing gaps by providing an insight into the effect of the grain crushing and inter-granular friction on the rate dependent behaviour

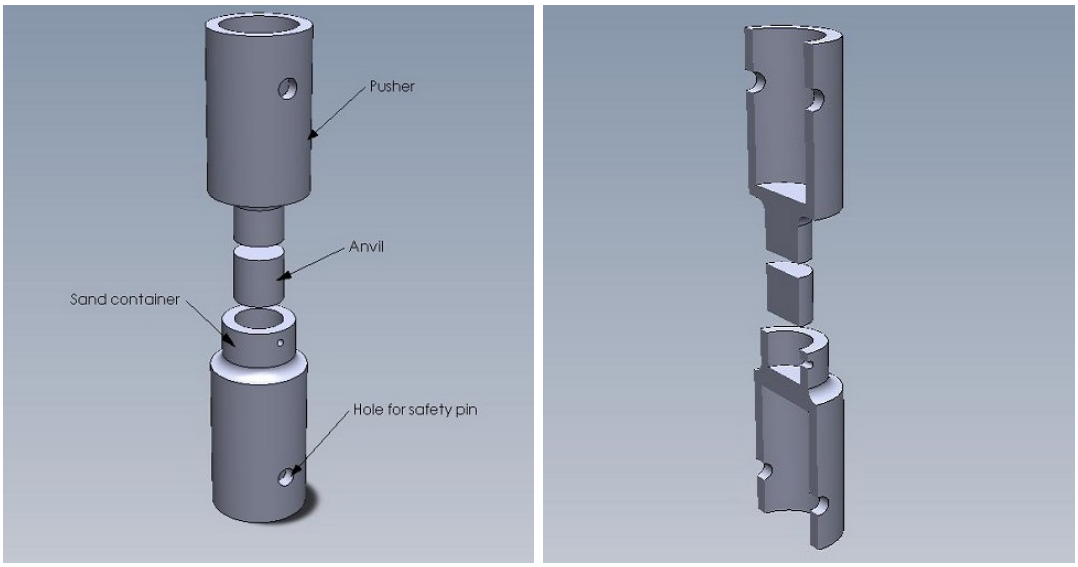
of sand and on the time localisation of the grains failure during uniaxial compression tests. In order to do so, the chosen granular materials are mechanically compressed at several decades of rate of deformation (from $10^{-3}/s$ to $10^{1}/s$). The mechanical tests are carried out together with Sound Measurements. Two types of sand with different grain shapes, in two different initial consolidation states, are chosen to demonstrate the possible interdependent effect of grain shape and consolidation state on their rate dependent behaviour.

7.4.1 Materials and containers

Dry Ottawa and Q-Rok silica sand, in an initially dense and loose state, are used to prove the existence of strain rate effects. Chemical composition, size distribution and microscopy images of grains shape are reported in Section 6.1.1.

The samples, whose sizes are chosen following the numerical procedure detailed in Chapter 5, are cylinders with 20 mm diameter and 6 mm height.

The sand is tested in a quasi-uniaxial strain condition by adopting a bespoke stainless steel container, providing a stiff lateral confinement and fitting the test space and the supports of the testing machine.



(a) (b)

Figure 7.23: Assembly of the different components of the container (a) and cross-sectional view (b)

Figure 7.23 shows the different parts composing the container. The compressive load is applied by the testing machine cross-head on the *pusher* and transmitted through the *anvil* onto the sample, which is placed in the cavity of the *sand container*. Both top and bottom part are hollow to allow for a tight fit with the Instron connectors. Two water quenched steel pins are used to secure the bottom and upper part of the fixture to the connectors of the testing machine. Diameter and material of the pins are chosen to ensure their failure in case a maximum admissible load (maximum stress of 80 MPa) is exceeded. This is done to preserve the load cell from any potential damage during the compression tests.

Both types of sand are tested in an initially dense and loose consolidation state. The samples are prepared following the procedures reported in Section 6.2. The respective void ratio values are summarised in Table 7.1.

Sand	e
Ottawa dense	0.57
Ottawa loose	0.80
Q-Rok dense	0.69
Q-Rok loose	1.00

Table 7.1: Void ratios for Ottawa and Q-Rok sand

To prepare the samples, the bottom part of the fixture is detached from the testing machine by removing the correspondent pin. Once the sample is prepared, the anvil is secured with a grub-screw to constrain and seal the sand. The screw is removed, before the execution of the test, once anvil and pusher are in contact.

7.4.2 Experimental set-up

The displacement-controlled uniaxial compression tests are carried out by employing an Hydraulic Axial-Torsion Instron 8854 System (Figure 7.24).



Figure 7.24: Axial-torsion hydraulic Instron 8854 testing device

The specimens are compressed at different displacement rates, to ensure the achievement of several decades of strain rate, as reported in Table 7.2.

Displacement rate	**Strain rate**
0.02 mm/s	$10^{-3}s^{-1}$
2.00 mm/s	$10^{-1}s^{-1}$
20.00 mm/s	$10^{0}s^{-1}$

Table 7.2: Displacement rates applied to the samples and corresponding strain rates

Two axis Dynacell with integral accelerometers (conforming to $ISO7500$) are used for force measurement. The measures of engineering strains are obtained from the Instron machine readings and from *digital image correlation* (DIC). In the latter case 180 frames, recorded using the Kirana high speed camera (924 x 768 pixels, at 10^5 fps), are analysed with the DIC Gom software Aramis.

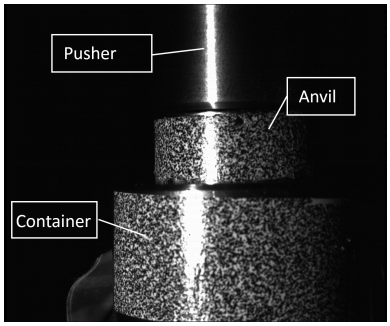


Figure 7.25: Example of speckle pattern used for DIC on anvil and sand container

The DIC strains are obtained by tracking the relative displacement between the anvil and the container of the sand (Figure 7.25). Since the strains measured using

the cross-head of the Instron machine are affected by the deformation of frame and fixture of the machine, the DIC strains are used to compute accurate stress-strain curves.

Concurrently to the mechanical tests, Sound Measurements are conducted. A desktop microphone, placed close to the container, with an acquisition rate of 96 kHz is adopted. The background noise is removed using the *spectral noising gating* technique.

The acquisition of mechanical readings and sound is synchronised to guarantee meaningful comparisons between the two measurements.

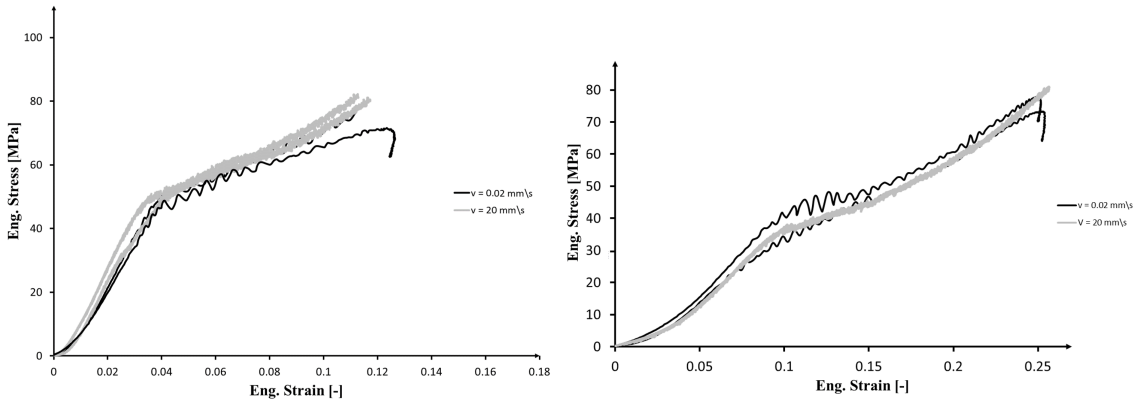
7.4.3 Results and observations

7.4.3.1 Mechanical characterisation

The uniaxial compression stress-strain curves of Q-Rok and Ottawa sand in loose and dense initial consolidation state at different strain rates are herein presented.

A series of at least 5 tests per configuration was carried out. However, for the sake of clarity, only few representative curves are reported in the next figures.

Figure 7.26 shows the absence of any noticeable effect of the strain rate on Ottawa sand, regardless of the initial consolidation state. Indeed, the curves corresponding to higher strain rates fall within the range of experimental responses at lower rates.



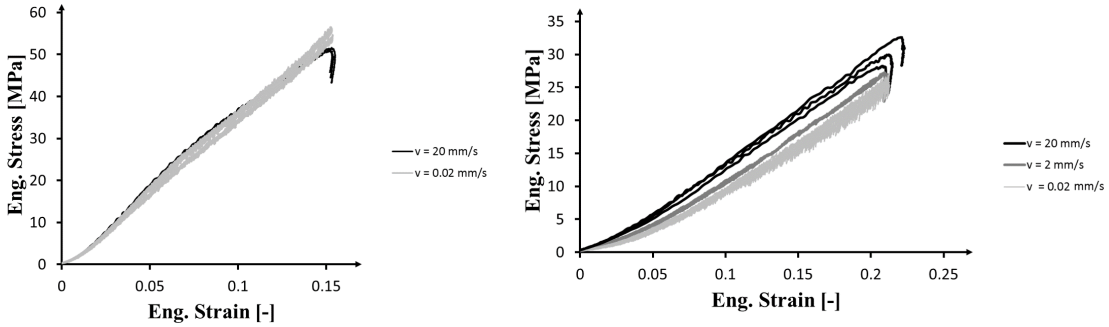
(a) (b)

Figure 7.26: Effect of the strain-rate on dense (a) and loose (b) Ottawa sand

The spurious oscillations in the stress-strain curves, at relatively low speeds, are thought to be a consequence of a non optimal choice of the PID controller parameters and pre-control servovalve of the hydraulic machine for the quasi-static tests.

Figure 7.27 shows the effect of the strain rate on the mechanical response of Q-Rok sand.

In this case, the consolidation state plays a crucial role in the rate dependency of the material. A positive rate effect can be only seen for loose Q-Rok sand (Figure 7.27b).



(a) (b)

Figure 7.27: Effect of the strain-rate on dense (a) and loose (b) Q-Rok sand

7.4.3.2 Sound measurements

The sound measurements technique defined in this chapter has been proven to detect exclusively grain crushing events. Any sound coming from the testing device and surrounding environment is filtered during the signal analysis. Therefore, its adoption during uniaxial compression tests on Q-Rok and Ottawa samples allowed for the estimation of the effect of grain breakage on the overall mechanical response of the sand and on its time dependency.

All the burst events recorded were post-processed following the procedure detailed in Section 7.2.3. However, in the following analysis only the total number of *counts per event* is used to make comparisons between the different test cases.

Figure 7.28 shows the total counts per event - in logarithmic scale - measured

during uniaxial compression of Ottawa sand, in dense and loose initial consolidation states, at different decades of loading rate. Despite the absence of any evident strain rate dependence in the mechanical behaviour of Ottawa sand (Figure 7.26), a negative trend in the counts per event with respect to the loading rate was measured. This confirms the time dependent nature of the grain fracture process foreseen in Section 2.3.2.

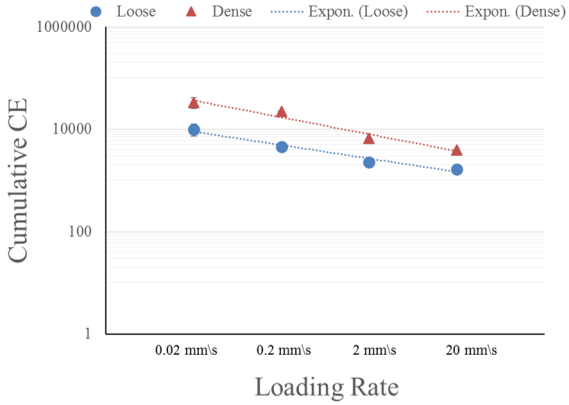


Figure 7.28: Cumulative counts per event (logarithmic scale) on Ottawa sand in dense and loose consolidation states at different loading rates

The trend of the *counts per event vs. loading rate curve* is similar regardless of the initial consolidation state. However, the number of events increases in dense samples. This is thought to be related to the higher coordination number in denser specimens yielding, in turn, higher chances of grain failure.

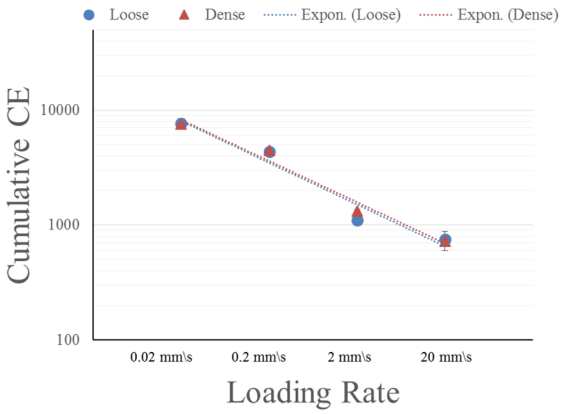


Figure 7.29: Cumulative counts per event (logarithmic scale) on Q-Rok sand in dense and loose consolidation states at different loading rates

Figure 7.29, instead, shows the total number of counts per event measured for Q-Rok sand at different loading rates.

The Q-Rok sand exhibits similar trend and nearly equal values of counts per event for both loose and dense samples. Once again, a negative trend in the SM-loading rate is observed. This result is not in correlation with the mechanical results (Figure 7.27), as Q-Rok sand in its dense state did not show any rate dependence whilst loose Q-Rok sand showed a minimal influence of the strain rate on its mechanical response.

The histograms used to measure the number of counts per event (Figure 7.29-7.33) are highly affected by the definition of the *bin sizes* used for the sampling of the acoustic events in time. Obviously, such decision should take into consideration the different speed at which the samples are compressed. Higher deformation speed should require smaller bin sizes. In the present work, an inverse proportional relationship between rate of deformation and bin size was used. In order to confirm the results, further investigations should focus on the estimation of optimal correct bin sizes to be used in experiments at different loading rates.

In conclusion, the lack of correlation between time dependency of the comminution of the grains and of the overall mechanical response demonstrates, for the first time in literature, the existence of alternative *key phenomena* (i.e. different from grains comminution) leading the rate dependency of granular materials. These predominant entities could be, for instance, the grains rearrangement and intergranular friction.

Ad-hoc experiments, able to measure the rate effects on the intergranular friction in granular media, would be required to unequivocally prove this conclusion.

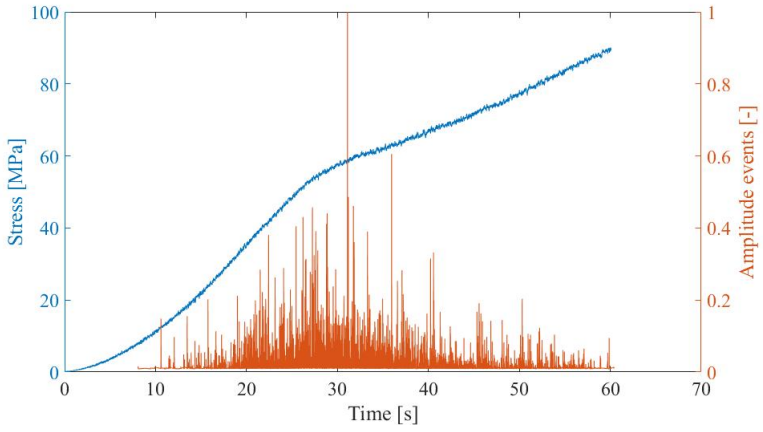
7.4.3.3 Time location of grain crushing during uniaxial compression tests

The synchronisation between sound measurements and mechanical testing allow for the timing of the cracking events during the uniaxial compression of sand.

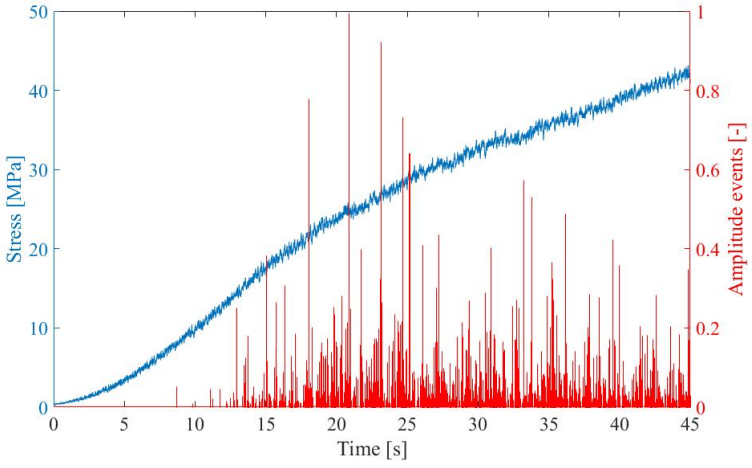
Given the high reproducibility of the results, both in terms of stress-strain relationship and sound measurements, one representative example per sample configuration

is herein presented to show key findings resulting from the analysis of the tests.

All figures show the stresses (in blue) and the amplitude of the cracking events (in red) over time. The amplitudes are normalised dividing by the maximum value measured during the test. Each red bar locate a cracking event in time. Figure 7.30 shows a comparison between dense (a) and loose (b) Ottawa sand at a displacement rate equal to $v = 0.02\ mm/s$.



(a)



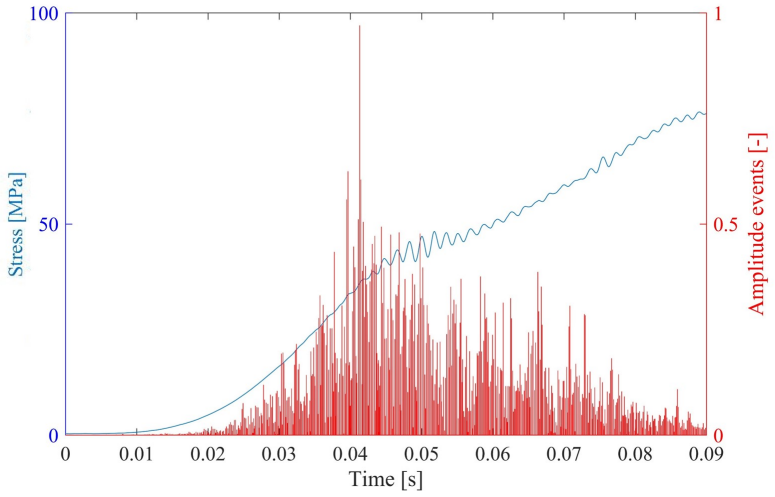
(b)

Figure 7.30: Grains fracture location in dense (a) and loose (b) Ottawa sand at $v = 0.02\ mm/s$

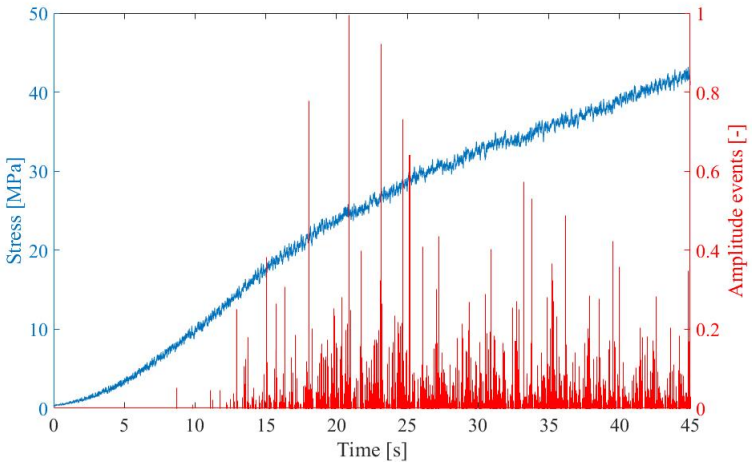
In both cases, no cracking events were detected for relatively low values of stress (below 15 MPa). A clustering of high amplitude events (with intensity above 40% of their maximum value) was recorded in the dense sample at the inflection point of

the stress-time history ($\simeq 29s$), whilst a more uniform distribution of cracking events was measured in the loose sample.

Figure 7.31 shows the effect of the strain rate on the localisation of grain fracture events by comparing the response of loose Ottawa sand samples compressed, respectively, at $v = 20\ mm/s$ and $v = 0.02\ mm/s$.



(a)



(b)

Figure 7.31: Grains fracture location in loose Ottawa sand at (a) $v = 20\ mm/s$ and (b) $v = 0.02\ mm/s$

Once again, it is evident the total absence of cracking events at low stresses (below 10 MPa). Both configurations presented a similar clustering of high amplitude events

(above 60% of their maximum value) at the inflection point of the stress distribution.

A comparison between Q-Rok and Ottawa sand is presented in Figure 7.32. Both types of sand are in an initially dense configuration and compressed at $v = 0.02\ mm/s$ (quasi-static condition).

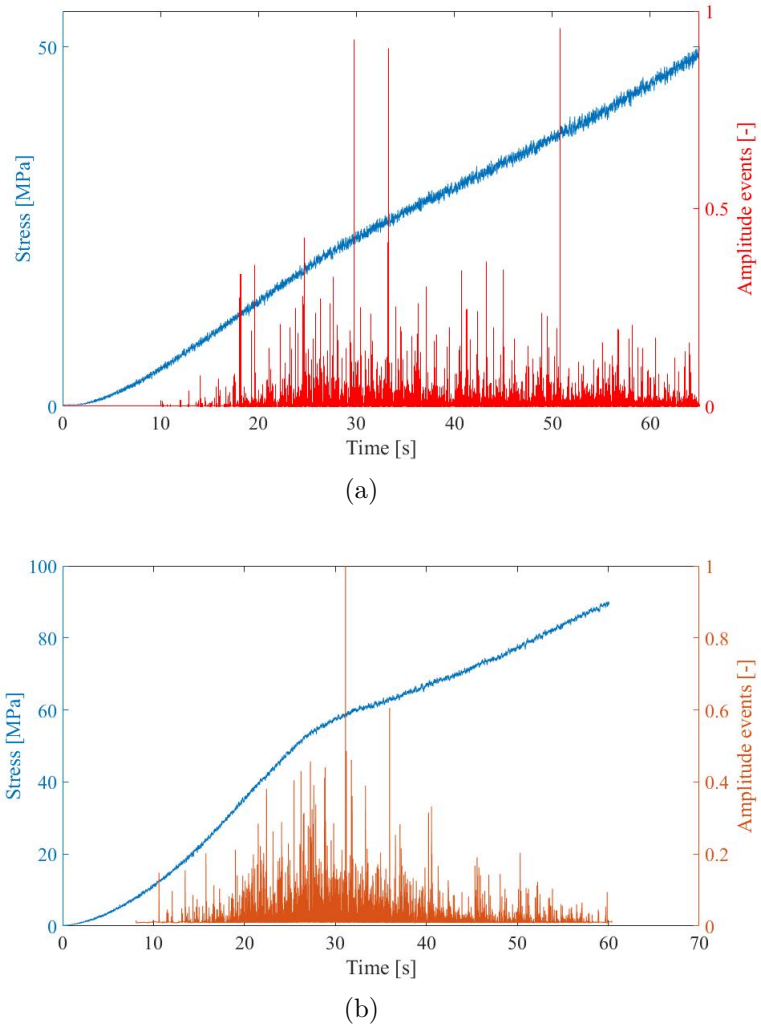


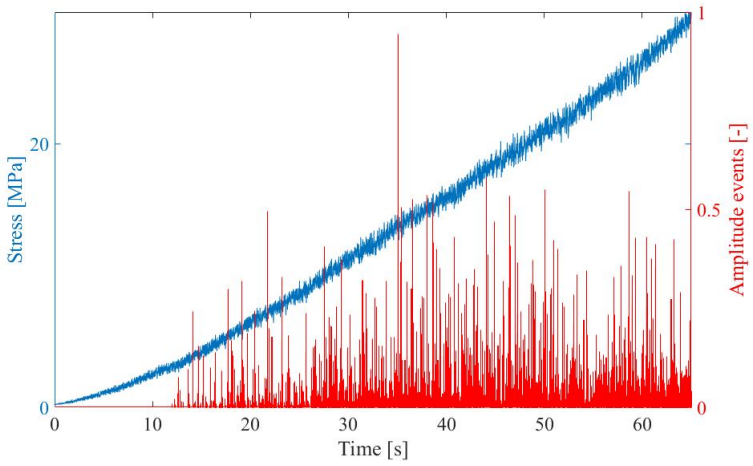
Figure 7.32: Grains fracture location in dense (a) Q-Rok and (b) Ottawa sand at $v = 0.02\ mm/s$

A more uniform distribution of cracking events over time is measured for Q-Rok sand. This can be seen as a proof of the effect of the grain shape on the fracture, similarly to what proved for single sand grains - in terms of frequency print - in Section 7.3.5.

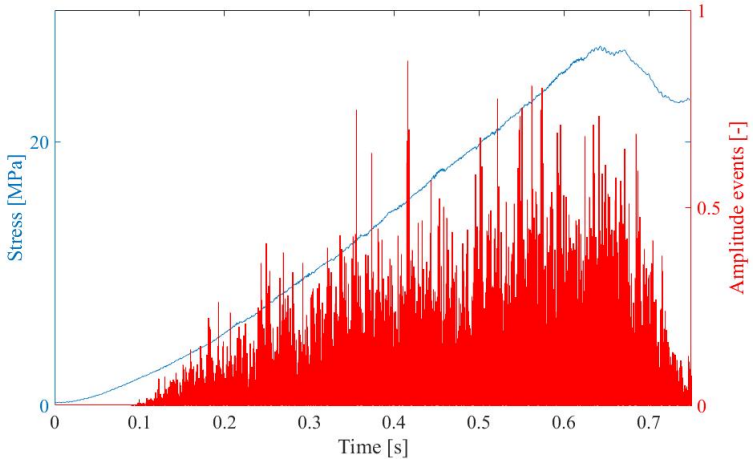
Finally, Figure 7.33 shows the strain rate effect of the time location of fracture for

Q-Rok sand in loose configuration. This is the only sample configuration exhibiting rate dependence on its mechanical response (Figure 7.27b).

The visual comparison between Figure 7.33a and Figure 7.33b shows, for samples deformed at higher speed, a clustering of high amplitude events delayed in time (happening at higher values of stress). This could be one of the reasons behind the rate dependency of loose Q-Rok sand.



(a)



(b)

Figure 7.33: Grains fracture location in loose Q-Rok sand at (a) $v = 0.02\ mm/s$ and (b) $v = 2\ mm/s$

In other words, the stiffer mechanical response measured for samples compressed at higher rates of deformation could be explained, not only by the variation in the

number of the grains failure events (see Section 7.4.3.2), but also by the modification of their time location.

It is worth mentioning that the total deformation of the sample is enhanced by the comminution of the particles (as the fragments can fill the interstitial voids, allowing for further reorganisation and compaction of the remaining grains). Therefore, the clustering of SM at higher values of stress means a delayed occurrence of grains failure, which in turn yields a stiffer response up to the onset of grains failure. Subsequently, when comminution occurs, the void ratio rapidly reduces producing an even stiffer response (and higher confined modulus, as explained in Section 6.3.1) in zone 4 of the stress-strain curve.

In conclusion, the sound measurements showed the evident effect of consolidation state, loading rate and grain shape on the time of occurrence of grain fracture. It has been shown, for the first time in literature, that no events are detected for low stresses, thus confirming that zone 1 and zone 2 in a typical stress-strain curve (Figure 6.6) are manly due to elastic deformation and rearrangement of the grains. Moreover, the results herein presented contradict the widely accepted assumption (see Section 6.3) that zone 4 of the stress-strain curve is mainly ruled by grain fracture since cracking events have also been measured in zone 3.

7.5 Summary

This chapter presented a Sound Measurement technique, based on the use of air-borne acoustic sensors, to monitor the process of fragmentation of single sand grains and grain assemblies. A post-processing analysis in the time and frequency domain was also proposed. The sound measurements were validated against microscopy images captured during in-situ compression tests and compared against the force-time curves. Additionally, bespoke sand containers have been designed to test RVEs under several decades of loading rate in an hydraulic testing machine, thus checking the effect of grains fracture on the rate dependency of sand and locating the cracking

events in time. Based on the results presented in this study, it can be concluded that:

- Differently from AE, SM was not sensible to rotations and sliding of the grains. This entailed that all sounds recorded were unequivocally associated with grain failure. Consequently, such method could be applied to isolate the distinct effect of fracture on the behaviour of granular materials.

- The technique was also successfully applied to detect grain failure in granular assemblies. However, the images confirmed the existence of the masking effect, with multiple concurrent grains fracturing at the same time, which invalidated the unequivocal relationship between the number of SM events and the number of failed grains.

- The analysis of the dominant frequencies for the three different types of sand and different grain sizes demonstrated the influence of granulometry, chemical composition and grain shape on the fracture mechanics of single sand grains.

- The uniaxial compression tests carried out on Ottawa and Q-Rok sand in dense and loose consolidation states proved the existence of a light positive rate dependency only for loose Q-Rok samples. In all other cases, it was not possible to draw the same conclusion despite a common negative trend in the counts per event vs rate of loading that confirmed the time dependent nature of the grain crushing.

- The sound measurement technique allowed for the time location of the grains comminution, demonstrating that cracking events are very common in both zone 3 and 4 of the typical stress-strain curve shown in Figure 6.6, whereas they are totally absent in zone 1.

- Grain shape, consolidation state and rate of loading not only affect the amount of fracture events but also their time location. The rate sensitivity measured

for loose Q-Rok sand, for instance, can be justified by the combination of the previous parameters on the location of the failure during uniaxial compression.

Chapter 8

Concurrent adaptive mass-conserving comminution of granular materials using rigid elements

The previous chapter clearly identified the role of the grain fracture on the mechanical response of granular media. Therefore, the failure of the single sand grains needs to be correctly modelled when simulating the uniaxial compression of sand to capture their correct mechanical behaviour. Section 2.6.2.2 of this thesis proved the validity of the DEM to model granular materials and summarised the existing numerical approaches to successfully simulate grains comminution during mechanical loading. In particular, it showed the advantages of adopting the *multigenerational approach* over the use of grain clusters. However, it also identified the absence of multigenerational algorithms able to preserve the mass of the mother particles after failure. This limitation results to be particular severe when simulating grains fracture in dynamic phenomena. The aim of this chapter is to present a novel multigenerational method able to overcome the issue of mass loss without imposing any overlap to the particles.

8.1 Implementation

This section presents the implementation of the proposed numerical approach. When the failure condition is reached within a particle, the domain is decomposed using a Laguerre-Voronoi tessellation technique, which automatically generates polyhedral cells containing the failed particle and part of the surrounding voids (without the need for additional void search). These cells are then filled by a dense agglomerate of tangent, non-overlapping particles, generated with the geometrical packing algorithm presented in Section 3.2. Since the polyhedral cells are, by construction, bigger than the failed particle, the developed approach allows for a drastic - if not complete - reduction of the mass loss within a time efficient, concurrent simulation of the comminution process.

8.1.1 Spawning Method

This method relies entirely on the adoption of three dimensional spheres for representing both mother and daughter particles. Figure 8.1 summarises the main steps of the spawning method presented in this work. Initially, the stress state within each grain in the domain needs to be monitored. The particle is flagged when the stress value reaches a prescribed threshold. Further details on the choice of the stress formulation are reported in Section 8.1.2. The domain surrounding the flagged particles is tessellated by means of a Laguerre Voronoi method, as explained in Section 8.1.3, and the failed particle is removed. Finally, the new daughter particles are inserted by adopting an extended version of the 3D-clew method presented in Section 3.2.

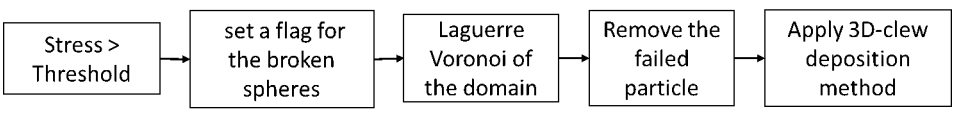


Figure 8.1: Flowchart showing the spawning method

8.1.2 Failure Criterion

The failure criterion is a limit condition after which the mother particle ceases to exist and it is replaced by daughter particles. A variety of particle failure criteria, applied to the multigenerational approach, have been used in literature. Sometimes, this condition is directly related to the maximum allowed contact force applied to the particle [121]. In some other cases, either very complex formulations [120] or a much simplistic averaged particle stress tensor [225] can be used. The latter is used in the present work and defined as follows

$$\sigma_{i,j} = -\frac{1}{V}\sum_{N_c} x_i F_j \tag{8.1}$$

where V is the volume of the particle, N_c is the number of contacts, x_i the location of the contact point and F_j the force acting on the particle. However, the algorithm presented hereby can be used with any failure criterion.

8.1.3 Laguerre Voronoi Tessellation of the domain

Once the failed particle is identified, the surrounding volume is tessellated by using the Laguerre Voronoi diagram [180, 181]. Let $G = \{c_1, c_2, ..., c_n\}$ be a set of n spheres in the domain, and let r_i and $P_i = (x_i, y_i, z_i)$ be the radius and the centre of each sphere. For each sphere c_i and a generic point P, let us define their weighted distance

$$d_L(P, c_i) = d(P, P_i)^2 - r_i^2 \tag{8.2}$$

Each Laguerre Voronoi cell is defined as

$$R_L(G, c_i) = P \in \Re^3 \mid d_L(P, c_i) < d_L(P, c_j), j \neq i \tag{8.3}$$

The Laguerre Voronoi tessellation has been generated using the open-source software TetGen [226] and a representation of the obtained domain is shown in Figure

8.2.

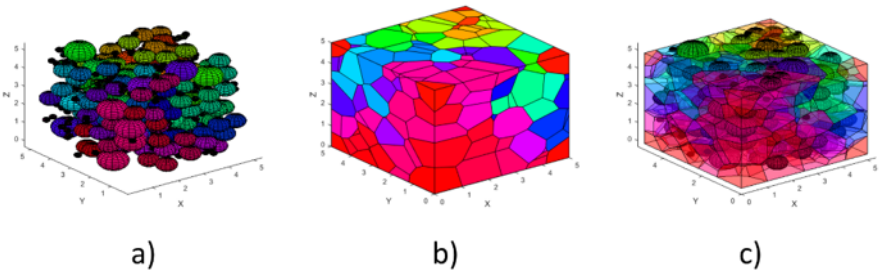


Figure 8.2: Laguerre Voronoi tessellation: a) granular packing, b) corresponding tessellation of the domain, c) superimposition of packing and tessellation

The Laguerre Voronoi tessellation (or weighted Voronoi) has been preferred to the classical Voronoi tessellation since it takes into consideration the different sizes of the particles within the domain. If modelling a monodisperse packing, the Laguerre Voronoi will degenerate into a classical Voronoi tessellation.

8.1.4 Generation and arrangement of new fragments

After having tessellated the domain, the failed particle is removed from the packing, whilst the corresponding Voronoi cell defines the volume within which the daughter particles are positioned. The method adopted for packing the daughter particles is the *3D-clew approach* (Section 3.2). It allows for the adoption of user-defined size distributions (i.e. obtained by post-mortem studies on the fragments). The method, represented in Figure 8.3, can be briefly summarised as follows:

- The radii distribution is pre-assigned;
- The first daughter particle is placed in the position originally occupied by the mother particle;
- Each new particle is added imposing the tangency with two already existing particles, creating a spiral-spool of spheres;
- The distance between every newly added particles and the ones already existing is checked to avoid overlap.

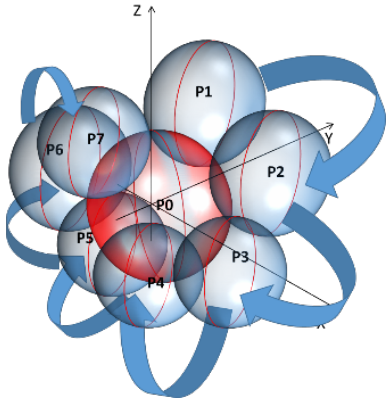


Figure 8.3: Representation of the 3D-clew deposition method for the spawning of daughter particles

In this case the *4 sphere-tangency condition* has not been adopted to reduce the computational cost of the packing.

Each added daughter particle has not to overlap with any of the Laguerre cell boundaries.

When computing the position of the newly added particle P_i (of radius R_i) with respect to each boundary of the cell, six different situations can happen, as shown in Figure 8.4.

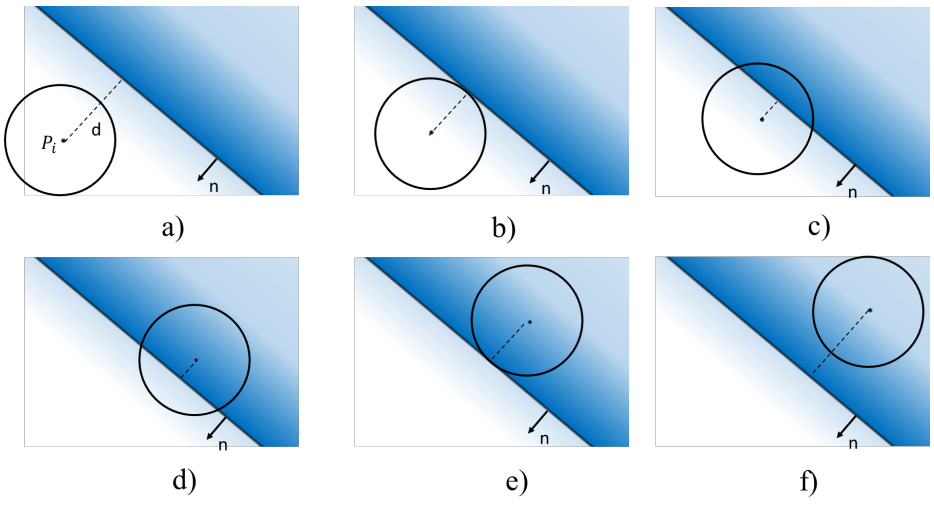


Figure 8.4: Different cases for the point-to-plane distance d_i; the white colour indicates the portion of volume within the cell

In the last three cases (d-f) of Figure 8.4, the particle P_i is discarded as its centre falls outside the cell. Among the remaining cases (Figure 8.4a-c), only the conditions

a) and b) allow for the deposition of the daughter particle P_i as their point-to-plane distance d_i is bigger or equal than the radius R_i.

In order to concurrently measure the point-to-plane distance and establish whether a particle is inside the cell, the concept of signed distance D_i needs to be introduced.

Let ℓ be the list of vertices (connectivity) v_i of each face Γ_i of the selected Voronoi cell such that

$$\ell = \left\{ v_1, v_2, ..., v_n \in \Re^3 \right\} \tag{8.4}$$

where $v_i = (x_i, y_i, z_i)$ and $\ell \in \Gamma_i$.

Taken one random vertex v_i in ℓ, the signed distance between P_i and Γ_i is:

$$D_i = \hat{n}_i \cdot (P_i - v_i) \tag{8.5}$$

with $\hat{n}_i$ being the unit normal of each Γ_i.

Given three random vertices v_i, v_j and v_k in ℓ, the unit normal of the face Γ_i is

$$\hat{n}_i = \frac{(v_j - v_i) \times (v_k - v_i)}{|(v_j - v_i) \times (v_k - v_i)|} \tag{8.6}$$

The sign of D_i depends on the direction of $\hat{n}_i$. It is positive only when $\hat{n}_i$ points inwards (Figure 8.4).

The direction of $\hat{n}_i$ is, in turn, a consequence of the connectivity ℓ of the face Γ_i. The ℓ can either be clockwise (Figure 8.5b) or anti-clockwise (Figure 8.5a) and it is a result of the Laguerre tessellation of the domain and, in most cases, not controllable by the user.

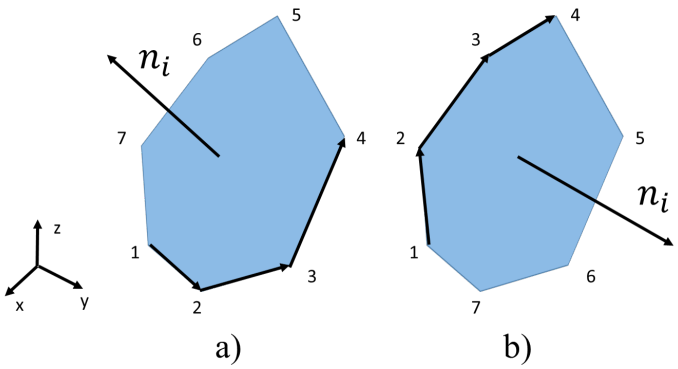


Figure 8.5: Clockwise and anti-clockwise connectivity of the face and consequent direction of the normal

To control the orientation of the normal of each face Γ_i, the concept of point-to-surface signed distance D_i can be applied to the centre of the mother particle, which corresponds to the centroid of the cell (i.e. it surely falls within the Laguerre cell). The sign of D_i can be stored in a vector S of dimension $[N \times 1]$, with N equal to the number of faces of the cell. S gives information on the direction of $\hat{n}_i$ of each face Γ_i:

- $\hat{n}_i > 0$ if it points towards the mother cell (inside the cell); S_i is set equal to 1.
- $\hat{n}_i < 0$ if it points outwards; S_i is set equal to -1.

At this point, the signed distance D_i of the newly added daughter particle with respect to each Γ_i of the cell needs to be multiplied by S_i to take into consideration the different orientations of their normals. This gives a new array of signed distances Ds of dimensions $[N \times 1]$:

$$Ds = D. * S \tag{8.7}$$

where the operator $.*$ represents the element-wise product between the two arrays.

The particle falls within the cell only when $Ds_i > 0$ (Figure 8.4a-c).

If the smallest of the point-to-plane distances Ds_i is bigger than its radius R_i, no overlap is detected (Figure 8.4a or Figure 8.4b) and the daughter particle is added.

When the centre of the daughter particle falls within the cell and it overlaps with one of the boundaries (Figure 8.4c), it can be rescaled and translated to be concurrently tangent to the neighbouring particles and the closest boundary of the cell.

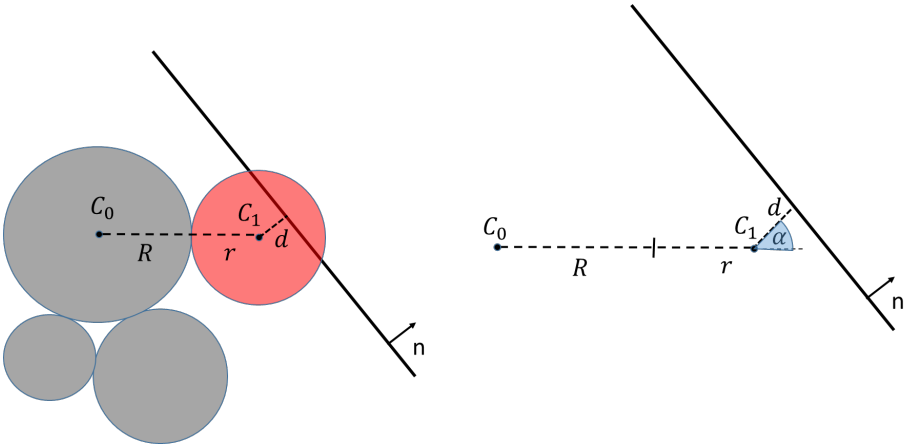


Figure 8.6: Example of daughter particle intersecting the boundary (left) and geometrical definition of the deposition angle α (right)

Figure 8.6 shows an example of daughter particle intersecting the closest boundary of the Laguerre cell. The grey circles are a 2D representation of the already placed daughter particles, whilst the red circle (C_1) represents the last attempt to place a new daughter particle that overlaps with the boundary. C_0 is the central particle of the 3D-clew deposition with respect to which C_1 (or any new scaled particle) has to be tangent.

To rescale and translate the new daughter particle C_n and to minimise the computational effort of the rescaling procedure, the deposition angle α is kept constant and it is computed as:

$$\cos\alpha = \frac{\overrightarrow{C_1 - C_0} \cdot \hat{n}_i}{\|\overrightarrow{C_1 - C_0}\|} \tag{8.8}$$

The radius x of the new daughter particle C_n (Figure 8.7) needs to be defined.

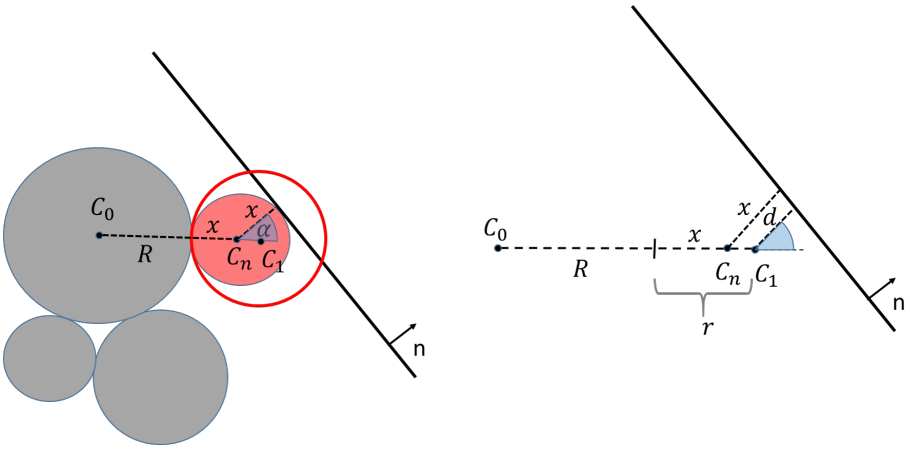


Figure 8.7: Example of scaling of the daughter particle (left) and definition of the new radius x of the scaled particle C_n (right)

Figure 8.7 and Figure 8.8 show the geometrical construction used to estimate x.

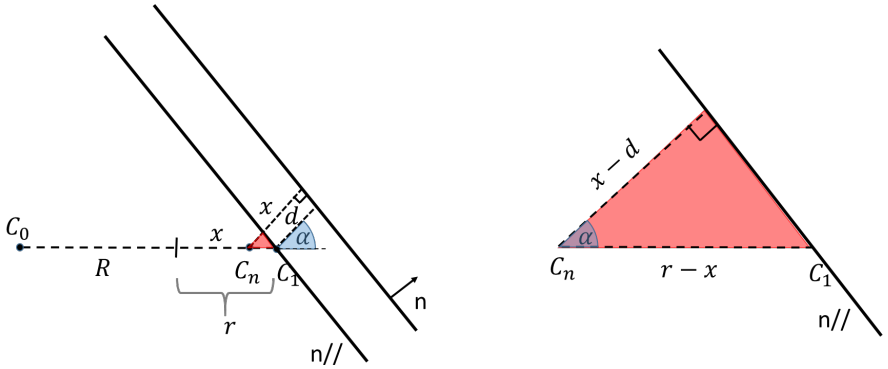


Figure 8.8: Estimation of the position x of C_n (left) and zoom-in of the geometrical construction (red triangle) used to estimate x (right)

Considering the right-angled triangle (in red in Figure 8.8) obtained using a plane $n_{\|}$ parallel to the closest boundary of the cell and passing through C_1, the new radius x of C_n is computed as:

$$(x-d) = (r-x)\cos\alpha \tag{8.9}$$

From here:

$$x = \frac{r\cos\alpha + d}{1+\cos\alpha} \tag{8.10}$$

If the final radius x of the scaled daughter particle C_n is within a desirable range of sizes, the particle is added at a distance $R+x$ from the centre of the previously added daughter particle C_0, at an angle α (direction of deposition).

Additionally, every time that a new particle is added, the total mass of the daughter particles has to be updated. Knowing the bulk density ρ of the medium and the radius of the new daughter particle, the increment of mass δm is:

$$\delta m = \frac{4}{3}\pi R_i^3 \rho \tag{8.11}$$

Therefore, the total mass M can be computed as:

$$M = M_{prev} + \delta m \tag{8.12}$$

where M_{prev} is the total mass of the cluster corresponding to the last addition of a daughter particle.

New particles are added until either their total mass equals the mass of the mother particle or it is not possible to add more particles without avoiding the overlap with existing spheres or boundaries.

Figure 8.9 shows some of the packings obtained for different cells shapes. The red spheres represent the mother particles, while the blue ones are the daughter particles. This figure demonstrates the ability of the method to adapt to every type of shape, thus exploiting the voids surrounding the particle.

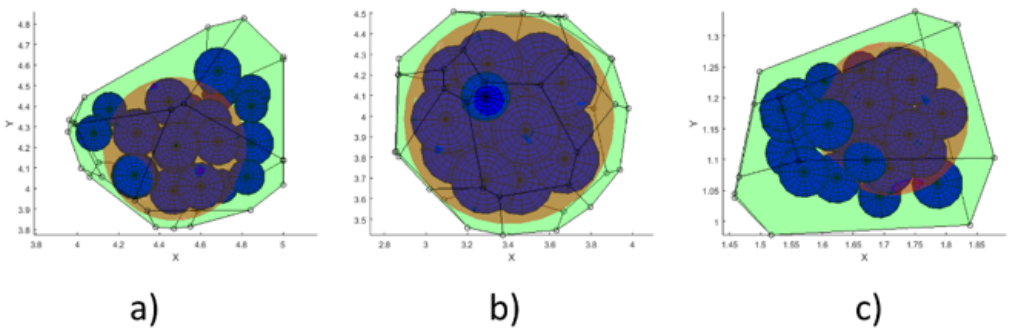


Figure 8.9: Examples of spawning in Voronoi cells: a) polyhedral shape, b) spherical shape, c) elongated shape

8.2 Examples and Results

In this section some results are collected to prove the effectiveness of the presented method. In particular, the mass loss and number of daughter particles adopted in this study are compared against another multigenerational method based on the adoption of Apollonian sphere packings [117]. Moreover, the effect of the size of the daughter particles on the previous quantities is analysed. The failure of every particle within the packing is imposed (Figure 8.10) in order to generate statistics and to reproduce any possible scenario during mechanical loading.

8.2.1 Mass loss and number of daughter particles: comparison with other existing methods

The daughter particles adopted in this study have dimension equal to a third of the diameter of each mother particle. Possible variation of the daughter particle size is imposed by the re-scaling procedure (they are forced to be not smaller than 70% of the initial daughter particle's radius). The same packing is studied in two different consolidation states: with high relative density, which represents a limiting case for the proposed method (less intergranular voids available) and with low relative density (loose packing).

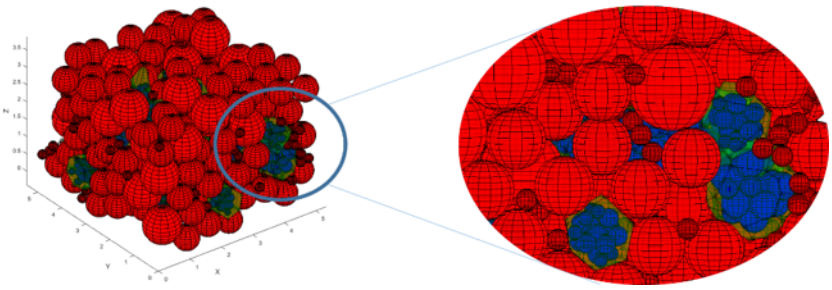


Figure 8.10: Example of packing with fractured particles

Figure 8.11 shows that the number of particles for both loose and dense configuration has a median equal to 24, with a standard deviation of 5 for the dense configuration and 3.1 for the loose one. The mass loss, instead, has a median equal

to 9.66% for dense sand and 7.31% for loose sand. This confirms a low variation of both variables with the consolidation state, thus proving the effectiveness of the method. Moreover, [117] presents a minimum mass loss of 37% when adopting a packing of 57 balls; by adopting the presented method, instead, the mass loss drops to 10% by just adopting 24 particles. If needed, additional particles can be placed in the surrounding cells, completely removing the mass loss. The reduced number of particles adopted for the comminution, with respect to what exist in literature [117], is beneficial to the computational cost of the DEM simulation since less particles means bigger fragments, and consequently, bigger time steps.

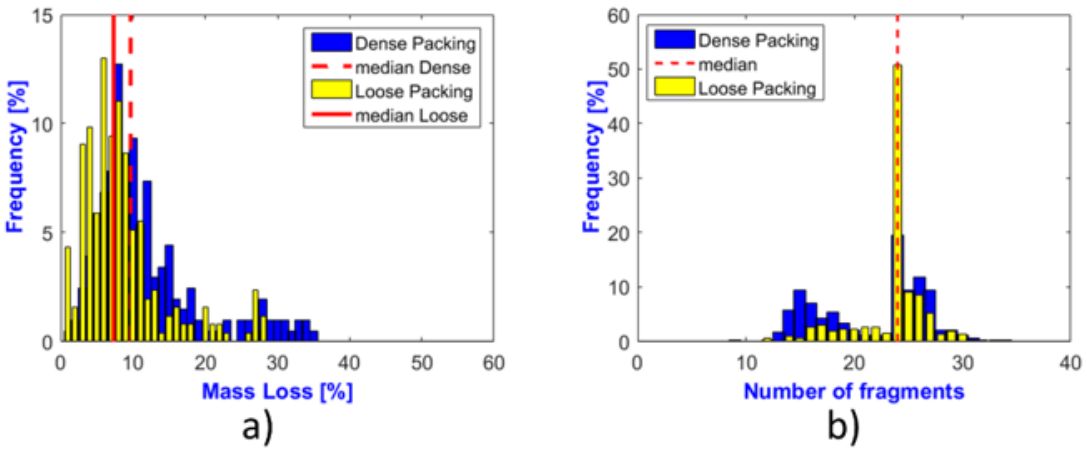


Figure 8.11: Number of particles with certain mass loss a) and number of daughter particles b) for different consolidation states

8.2.2 Effect of the size of the daughter particles

In this section, the effect of the size of the daughter particles on both mass loss and number of daughter particles is checked. Two different radii are adopted, respectively equal to one third and one fourth of the radius of the mother particle (Figure 8.12).

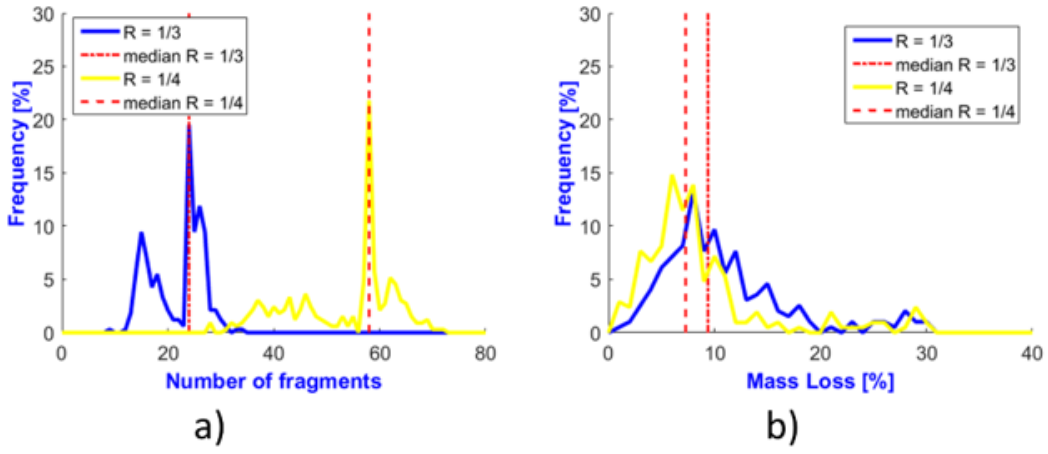


Figure 8.12: Number of particles with certain mass loss a) and number of daughter particles b) for different radii of the daughter particles

As expected, the adoption of smaller radii induces a reduction of mass loss but, consequently, a relevant increase in the number of daughter particles, as reported in the following table.

Radius Ratio	**Mass Loss**	**Number of particles**
$R = 1/4$	7.3 ± 6.2	58 ± 10.1
$R = 1/3$	9.4 ± 6	24 ± 5

Table 8.1: Median and standard deviation of mass loss and number of daughter particles for different radius ratios

8.3 Summary

This work presents a multigenerational method for reproducing the comminution of particles in DEM simulations based on the Laguerre Voronoi tessellation of the domain - thus exploiting the surrounding voids without performing any local search - and able to *reduce the mass loss* induced by the substitution of the failed grains with a cluster of non-overlapping daughter particles.

The adoption of ad-hoc geometrical packing approaches for the spawning of daughter particles results in user controlled size distributions of the fragments that can reproduce those measured through experiments. Moreover, the time efficient and

scalable packing method enhance the effectiveness of such numerical approach.

The results presented show a relevant reduction of mass loss even adopting a considerable lower number of daughter particles. In summary, the adoption of the proposed approach *extends* the range of application of multigenerational DEM to *dynamic* simulations of grains comminution. In future applications, this method will be employed in DEM and multi-scale simulations of dynamic compression tests of sand to be calibrated against the experimental results presented in this thesis.

Chapter 9

Conclusions and suggestions for future work

The work presented in this thesis addressed most of the open questions identified in literature, regarding the behaviour of granular materials subjected to impact loading. A number of contributions were made increasing further the understanding of the basic physics and science behind the dynamic phenomena happening on granular media.

In particular, new numerical algorithms for the modelling of statistically representative granular assemblies were introduced, together with a new numerical approach for the estimation of Representative Volume Elements to be used in experiments and in multiscale frameworks. Moreover, a comprehensive experimental campaign adopting be-spoke apparatus, pulse-shaping and sample sizes, identified the role and inter-dependency of all parameters controlling the mechanical behaviour of granular materials at high strain rates. The definition of an alternative NDT, named Sound Measurements, allowed for the identification of the role of grain comminution on the mechanical behaviour and rate sensitivity of granular materials. Finally, a new numerical method for the modelling of mass-conserving grains comminution extended the range of applicability of DEM to high rate applications.

The main conclusions drawn from each chapter of this thesis and directions for future work are summarised in the following sections.

9.1 Generation and packing of statistically representative granular samples

Two novel methods for the generation of mono- and poly-disperse packings of spheres, based on geometrical tangency conditions and able to concurrently assign radii distribution and total number of particles, were presented in Chapter 3. The two methods can efficiently generate dense packings with properties comparable to those obtained through gravity assisted simulations. For instance, values of compaction close to the theoretical limit for monodisperse assemblies were reached by adopting the *planar* approach. Moreover, it was shown that a wide range of experimental compaction states can be achieved by combining the proposed geometrical algorithms with subsequent mechanical methods. A reduction of the total computational cost up to 2.5 times was obtained when running gravity assisted simulations starting from pre-geometrically-packed samples (obtained with the proposed algorithms) instead of randomly placing the particles within the considered domain. The presented results showed the ability of the method to reproduce valid consolidation states, size distributions and coordination numbers.

A complete statistical characterisation of the numerical assemblies through spatial statistical metrics (e.g. nearest neighbour distance and orientations, pair correlation function, etc.) will be a topic for future studies.

Chapter 4 introduced a numerical technique to model the shape of the grains. The proposed method modifies the typical Hardcore Voronoi tessellation technique by means of two user-controlled parameters: the *hardcore radius* and the *stretching parameter*. It is able to correctly reproduce the grains shape and size distributions of a wide range of natural and synthetic granular media. A method for the geometrical packing of the obtained particles was also proposed. The polyhedral grains were enclosed in their bounding spheres and assembled using the packing algorithms presented in Chapter 3. This enabled the achievement of relatively dense initial geo-

metrical packing to be used in subsequent mechanical simulations, thus drastically reducing the total computational cost.

However, the present work did not fully addressed the mechanical consolidation of polyhedral packings. It will be examined in a future study. Additionally, given the ability to reproduce the shapes of particles, inclusions and voids, the proposed method could be also used to generate representative models of granular based materials such as foams, concrete and granular composites.

9.2 Definition of Representative Volume Elements for granular materials

The statistically representative samples, generated by means of the aforementioned numerical methods, were then used to evaluate the sizes of the Representative Volume Elements (RVE) for granular media. The proposed RVE was based on the phenomenological observation of the importance of the initial consolidation state of granular materials measured by the void ratio parameter. Chapter 5 presented an iterative numerical procedure, based on Discrete Element Methods (DEM), to estimate the RVE sizes for Ottawa sand in a dense and loose initial compaction state. An experimental verification consisting in testing different sample sizes of sand in a SHPB under uniaxial loading conditions proved, for the first time, the existence of a lower limit on the dimensions of the specimens to be used in high rate experiments. This work demonstrated that it is not possible to use arbitrarily small samples in the experiments, as specimens smaller than the RVE do not statistically represent the desired consolidation state of the medium. Moreover, the adoption of samples with dimensions comparable to the RVE yielded better repeatability and improved dynamic equilibrium than what generally available in the open literature.

Future studies on this topic should focus on the definition of RVEs for polyhedral packings and on the evaluation of the effect of the moisture content (addition of a third phase) on the estimated RVEs.

9.3 Characterisation of the mechanical response of sand to impact loading

In Chapter 6, a comprehensive experimental characterisation of granular materials was carried out by means of a Long Split Hopkinson Pressure Bar (LSHPB). The new adopted set-up allowed for the achievement of higher strain rates, longer pulses durations and, in turn, higher maximum strains than what presented in literature to date. Additionally, the sample sizes were defined according to the procedure reported in Chapter 5 thus drastically enhancing the repeatability of the tests and the dynamic equilibrium within the samples. The effects of initial consolidation state, confining pressure, water content, morphology and inter-granular friction and their inter-dependency were addressed.

Three different preparation procedures were used to recreate distinct initial consolidation states. Three types of quartz sand, with different grains shapes but similar size distribution, were used to verify the effect of the grain morphology on the mechanical behaviour of granular materials.

The results showed a noticeable stiffening of the stress-strain curves with the increase of the initial density regardless the grain shape and the strain rate. In other words, higher consolidation states lead to a lock-up behaviour due to a higher difficulty of relative movement between grains.

The effect of the grain morphology resulted in a stiffer and higher stress-strain relationship for sand composed of spherical grains with respect to the one with polyhedral grains. This was thought to be a consequence of the different grain fracturing mechanisms happening when varying the grains shape.

For the first time in literature, the influence of the intra-granular friction on the mechanical response of granular materials was identified. This was achieved by testing and comparing the behaviour of naturally occurring and epoxy-resin-coated Euroquartz sand. A striking effect of inter-granular friction and its strong dependency

upon the initial consolidation state of the considered medium was shown.

Moreover, the use of different containers (radially deformable latex confinements and fully rigid stainless steel containers) allowed for the achievement of quasi-uniaxial stress and strain conditions respectively. The initial pseudo-elastic response was not affected by the confining pressure. On the contrary, a strong dependence on the type of container was measured for the confined modulus, proving the strong effect of the confining pressure on the reorganisation and fracture of the grains.

Finally, the effect of the water content was investigated for the three types of sand. The results showed that unsaturated samples, because of the lubrication of inter-granular and grains-wall contacts, were more compliant than dry sand. Such behaviour was observed on all types of sand regardless their morphology. Further increase in the water content led to the saturation of the pores. This prevented the free movement of air volumes, thus stiffening the behaviour of the sand.

The presented results quantified *material and confining state parameters* which have significant effect on the high strain rate mechanical response of granular materials for future integration into rate dependent constitutive models.

Nevertheless, the results obtained using the LSHPB neither unequivocally proved the existence of rate dependency in the tested materials nor identified its possible driving forces. To achieve this, a new alternative NDT, called *Sound Measurements*, was proposed and calibrated against in-situ compression tests on single sand grains and small granular assemblies in Chapter 7.

SM was proved not to be sensible to rotations and sliding of the grains but only to grain failure. Time and frequency domain analysis allowed for the identification of complementary features in the complex mechanical behaviour of granular materials. The proposed method was applied to study the effects of chemical composition, morphology and grain sizes on the failure mechanics of sand grains. Once calibrated, it was used during uniaxial compression tests executed at several decades of loading rate to investigate the existence of rate sensitivity in granular materials. On one

hand, a common negative trend in the *counts per event vs. rate of loading* was observed, confirming the time dependent nature of the crushing phenomenon. On the other hand, the mechanical tests identified a slightly positive rate dependency only for Q-Rok sand in a loose consolidation state.

Thanks to the possibility to time-locate cracking events, offered by the SM, an unusual time distribution of cracking events was found for Q-Rok sand in loose state when compared against all other cases. This observation could demonstrate that not only the outbreak of cracking events but also their time location play a major role in the rate dependency of granular materials. Finally, it was proved that single grains failure not only happens, as previously thought, in the lock-up phase of an uniaxial compression test but even at earlier stages (from strains above 5%).

Therefore, it can be concluded that the experiments presented in Chapter 7 provided valuable insight into the effect of grain crushing on the mechanical response of sand and its rate dependency.

Future studies will aim at conducting larger experimental campaigns, based on the adoption of SM during mechanical compression tests, to definitely prove the reported findings. Moreover, SM should be used to identify the effect of the moisture content on the mechanics of fracture of single sand grains.

9.4 Discrete modelling of the comminution process during uniaxial compression of granular materials

The experimental observations presented in this thesis proved the marked influence of grain fracture on the overall mechanical response of granular materials. As a result, there is a need for the correct representation of the grains failure into DEM simulations. The multigenerational approach has been extensively used in literature and it has been proved to be able to simulate, in DEM, the grains comminution during mechanical loading of grain assemblies. Its only limit is the loss of mass induced by the

substitution of the mother particle with the daughter ones, which makes it unsuitable for dynamic simulations where the total momentum of the system should be conserved to get meaningful results.

Chapter 8 presented a mass-preserving algorithm that replaces the failed mother particle with on-the-fly, randomly generated assemblies of fragments. This method is based on the Laguerre Voronoi tessellation of the domain. It exploits, for spawning the daughter particles, the empty space surrounding the failed particle, thus reducing the total mass loss with respect to what existed in literature.

The spawning approach entirely relies on the 3D clew deposition method presented in Section 3, which was demonstrated to be scalable and efficient and to be able to reproduce ad-hoc size distributions of fragments. This noticeably enhanced the effectiveness of the presented approach.

In future applications, this approach will be used in large distinct element models to include, at the mesoscale, the grains comminution into dynamic simulations.

References

[1] R. Guises. *Numerical Simulation and Characterisation of the Packing of Granular Materials*. PhD thesis, Department of Earth Sciences and Engineering, Imperial College London, U.K., 2008.

[2] L. Bates. The need for industrial education in bulk technology. *Bulk Solids Handling*, 26:461–473, 2006.

[3] Pierce county: Road/foundation debris. `https://www.co.pierce.wa.us/3944/RoadFoundation-Debris`.

[4] Healtalso. `http://www.healthalso.com/tag/hypertension/`.

[5] Emaze. `https://www.emaze.com/@AOCITRIW/spain-and-cuba`.

[6] Emap: Mountaintop removal. `http://www.energymining.org/`.

[7] Indiana department of homeland security: Earthquakes. `https://www.in.gov/dhs/2792.htm`.

[8] C Glößner, S Moser, R Külls, S Heß, S Nau, M Salk, D Penumadu, and N Petrinic. Instrumented projectile penetration testing of granular materials. *Experimental Mechanics*, 57(2):261–272, 2017.

[9] Gang Lu and Efthimios Kaxiras. An overview of multiscale simulations of materials. *arXiv preprint cond-mat/0401073*, 2004.

[10] B Andreotti, Y Forterre, and O Pouliquen. *Granular Media: Between Fluid and Solid*. Cambridge University Press, 2013.

[11] JC Santamarina and GC Cho. Soil behaviour: The role of particle shape. In *Advances in geotechnical engineering: The skempton conference*, volume 1, pages 604–617. Thomas Telford, 2004.

[12] Hakon Wadell. Volume, shape, and roundness of rock particles. *The Journal of Geology*, pages 443–451, 1932.

[13] P. J. Barrett. The shape of rock particles, a critical review. *Sedimentology*, 27(3):291–303, 1980.

[14] Elisabeth T Bowman, Kenichi Soga, and W Drummond. Particle shape characterisation using fourier descriptor analysis. *Geotechnique*, 51(6):545–554, 2001.

[15] John-Paul Latham, Antonio Munjiza, Xavier Garcia, Jiansheng Xiang, and Romain Guises. Three-dimensional particle shape acquisition and use of shape library for dem and fem/dem simulation. *Minerals Engineering*, 21(11):797–805, 2008.

[16] Ivan Vlahinić, Edward Andò, Gioacchino Viggiani, and José E Andrade. Towards a more accurate characterization of granular media: extracting quantitative descriptors from tomographic images. *Granular Matter*, 16(1):9–21, 2014.

[17] N Chawla, VV Ganesh, and B Wunsch. Three-dimensional (3D) microstructure visualization and finite element modeling of the mechanical behavior of sic particle reinforced aluminum composites. *Scripta Materialia*, 51(2):161–165, 2004.

[18] R. F. Craig. *Craig's Soil Mechanics*. Spon Press, 2004.

[19] N. Mitarai and F. Nori. Wet granular materials. *Advances in Physics*, 55:1–45, 2006.

[20] J Michael Duncan, Stephen G Wright, and Thomas L Brandon. *Soil strength and slope stability*. John Wiley & Sons, 2014.

[21] Poul V Lade and Moon K Kim. Single hardening constitutive model for soil, rock and concrete. *International Journal of Solids and Structures*, 32(14):1963–1978, 1995.

[22] J.M Zhang. Transient shear strength of saturated sand under cyclic loading considering strain-rate effect. *Soil and Foundations*, 34:51–65, 1994.

[23] J An. *Soil behaviour under blast loading.* 2010.

[24] J.P. Borg and T.J. Vogler. An experimental investigation of the a high velocity projectile penetrating sand. Orlando, Florida, USA, 2008.

[25] WW Chen and B Song. Split - hopkinson (kolsky) bar: design; testing and applications. *Springer*, 2011.

[26] JE Field, SM Walley, WG Proud, HT Goldrein, and CR Siviour. Review of experimental techniques for high rate deformation and shock studies. *International Journal of Impact Engineering*, 30:725–775, 2004.

[27] H Kolsky. An investigation of the mechanical properties of materials at very high rates of loading. *Proceedings of the Physical Society. Section B*, 62(11):676, 1949.

[28] Herbert Kolsky. *Stress waves in solids*, volume 1098. Courier Corporation, 1963.

[29] ASM International. *ASM Handbook, Vol. 8, Mechanical Testing and Evaluation.*, 2000.

[30] R Gerlach, C Kettenbeil, and N Petrinic. A new split - hopkinson tensile bar design. *International Journal of Impact Engineering*, 50:63–67, 2012.

[31] W.A. Charlie, C.A. Ross, and S.J. Pierce. Split-hopkinson pressure bar testing of unsaturated sand. *Geotechnical Testing Journal*, 13 (4):291–300, 1990.

[32] D. J.and Forrestal Frew and W Chen. Pulse shaping techniques for testing brittle materials with a split - hopkinson pressure bar. *Experimental Mechanics*, 42(1):93–106, 2002.

[33] C.E. Frantz, P.S. Follansbee, and W.J. Wright. New experimental techniques with the split Hopkinson pressure bar. In *Presented at the 8th Intern. Conf. on High Energy Rate Fabrication, San Antonio, 17-21 Jun. 1984*, 1984.

[34] Paul S Follansbee. The hopkinson bar. *Metals handbook*, 8(9):198–217, 1985.

[35] Robert Gerlach, Sivasubramaniam K Sathianathan, Clive Siviour, and Nik Petrinic. A novel method for pulse shaping of split hopkinson tensile bar signals. *International Journal of Impact Engineering*, 38(12):976–980, 2011.

[36] RJ Christensen, SR Swanson, and WS Brown. Split-hopkinson-bar tests on rock under confining pressure. *Experimental Mechanics*, 12(11):508–513, 1972.

[37] S Ellwood, LJ Griffiths, and DJ Parry. Materials testing at high constant strain rates. *Journal of Physics E: Scientific Instruments*, 15(3):280, 1982.

[38] M. Scheidler, J. Fitzpatrick, and R. Kraft. Optimal pulse shapes for shpb tests on soft materials. In *Proceedings of the 2011 SEM Annual Conference and Exposition on Experimental and Applied Mechanics, Uncasville, CT, 13-16 June 2011*, 2011.

[39] J.D Parry, A.G Walker, and P. R Dixon. Hopkinson bar pulse smoothing. *Meas. Sci. Technol.*, 443:443–446, 1995.

[40] XJ Wu and DA Gorham. Stress equilibrium in the split hopkinson pressure bar test. *Le Journal de Physique IV*, 7(C3):C3–91, 1997.

[41] M. Omidvar, M. Iskander, and S. Bless. Stress-strain behavior of sand at high strain rates. *International Journal of Impact Engineering*, 49:192–213, 2012.

[42] A.M. Bragov, G.M. Grushevsky, and A.K. Lomunov. Use of the kolsky method for confined tests of soft soils. *Experimental Mechanics*, 36(3):237–242, 1996.

[43] AM Bragov, VV Balandin, AK Lomunov, and AR Filippov. Determining the impact compressibility of soft soils from inversed test results. *Technical physics letters*, 32:487–488, 2006.

[44] Eduardo Suescun-Florez, Sina Kashuk, Magued Iskander, and Stephan Bless. Predicting the uniaxial compressive response of granular media over a wide range of strain rates using the strain energy density concept. *Journal of dynamic behavior of materials*, 1:330–346, 2015.

[45] M. E. Kabir, Bo Song, B. E. Martin, and W. Chen. Compressive behavior of fine sand. Technical report, Sandia National Laboratories, Albuquerque, New Mexico 87185 and Livermore, California 94550, 2010.

[46] B. E. Martin, W. Chen, B. Song, and Akers S. A. Moisture effects on the high strain-rate behavior of sand. *Mechanics of Material*, 41(6):786–798, 2009.

[47] Bo Song, Weinong Chen, and Vincent Luk. Impact compressive response of dry sand. *Mechanics of Materials*, 41:777–785, 2009.

[48] S. Pierce. High intensity compressive stress wave propagation through unsaturated sands. Master's thesis, Colorado State University, Fort Collins, Co., 1989.

[49] C. W. Felice, E. S. Gaffney, and J. A. Brown. Extended split hopkinson bar analysis for attenuating materials. *Jal of Engineering Mechanics, ASCE*, 117:1119–1135, 1991.

[50] G. E. Veyera and C. A. Ross. High strain rate testing of unsaturated sands using a split-hopkinson pressure bar. In *Proc. 3rd International Conference on*

Recent Advances in Geotechnical Earthquake Engineering and Soil Dynamics, 1995.

[51] A.D. Barr, S.D. Clarke, M. Petkovski, A. Tyas, S.E. Rigby, J. Warren, and S. Kerr. Effects of strain rate and moisture content on the behaviour of sand under one-dimensional compression. *Experimental Mechanics*, 56:1625–1639, 2016.

[52] John V Farr and Richard D Woods. A device for evaluating one-dimensional compressive loading rate effects. 1988.

[53] Stephen A Akers. *Uniaxial strain response of Enewetak Beach sand*. US Army Engineer Waterways Experiment Station, 1986.

[54] Kenneth L Lee, Harry Bolton Seed, and Pamela Dunlop. The effect of transient loading on the strength of sand. Highway Research Board, 1966.

[55] JE Roberts and JM De Souza. *The compressibility of sands*. Massachusetts Institute of Technology, 1958.

[56] GR McDowell and O Harireche. Discrete element modelling of soil particle fracture. *GEOTECHNIQUE-LONDON-*, 52(2):131–136, 2002.

[57] Robert V Whitman, Edmond T Miller, and Peter J Moore. Yielding and locking of confined sand. *Journal of Soil Mechanics & Foundations Div*, 90(Proc. Paper 3966), 1964.

[58] Jerry A Yamamuro and Poul V Lade. Effects of strain rate on instability of granular soils. 1993.

[59] M Matsushita. Time effects on the prepeak deformation properties of sands. In *Proc. Second Int. Conf. on Pre-Failure Deformation Characteristics of Geomaterials, IS Torino'99*, volume 1, pages 681–689. Balkema, 1999.

[60] John V Farr. Loading rate effects on the one-dimensional compressibility of four partially saturated soils. Technical report, DTIC Document, 1986.

[61] V. N. Georgiannou, J. B. Burland, and D. W. Hight. The undrained behaviour of clayey sands in triaxial compression and extension. *Geotechnique*, 40(3):431–449, 1990.

[62] S. Leroueil and P.R. Vaughan. The general and congruent effects of structure in natural soils and weak rocks. *Geotechnique*, 40(3):467–488, 1990.

[63] A.M. Freudenthal. *The Inelastic Behavior of Engineering Materials and Structures*. John Wiley & Sons, 1950.

[64] Z. Hashin. Analysis of composite materials - a survey. *ASME J. Appl. Mech.*, 50:481–505, 1983.

[65] S. Graham and N. Yang. Representative volumes of materials based on microstructural statistics. *Scripta Mater.*, 48:269–274, 2003.

[66] T. Kanit, S. Forest, I. Galliet, V. Mounoury, and D. Jeulin. Determination of the size of the representative volume element for random composites: statistical and numerical approach. *Int. J. Solids Struct.*, 40:3647–3679, 2003.

[67] D.M. Nielsen. *Practical Handbook of Environmental Site Characterization and Ground-Water Monitoring, Second Edition*. Taylor & Francis, 2005.

[68] P. Evesque and F. Adjemian. Stress fluctuations and macroscopic stick-slip in granular materials. *Eur. Phys. J.*, 9:253–259, 2002.

[69] Z. Y. Ren and Q. S. Zheng. A quantitative study of minimum sizes of representative volume elements of cubic polycrystals - numerical experiments. *Journal of the Mechanics and Physics of Solids*, 50:881–893, 2002.

[70] M. Stroeven, H. Askes, and L. J. Sluys. Numerical determination of representative volumes for granular materials. *Comput. Methods Appl. Mech. Engrg.*, 193:3221–3238, 2004.

[71] H. Lu, H. Luo, and R. Komaduri. Dynamic compressive response of sand under confinements. In *Proceedings of the SEM Annual Conference, Society of Experimental Mechanics Inc.*, 2009.

[72] Q. B. Zhang and J. Zhao. A review of dynamic experimental techniques and mechanical behaviour of rock materials. *Rock Mech Rock Eng*, pages 1–68, 2013.

[73] Justin L Brown, Tracy J Vogler, Lalit C Chhabildas, William D Reinhart, and Tom F Thornhill. Shock response of dry sand. 2007.

[74] C. W. Felice. *The response of soil to impulse loads using the S.H.P.B technique.* PhD thesis, University of Utah, Salt Lake City, 1985.

[75] J. Meunier. *Contribution a l'etude des ondes et des ondes de choc dans les sols.* PhD thesis, Grenoble University, 1974.

[76] A.D. Salaman and D.A. Gorham. The fracture of glass spheres. *Powder technol.*, 107:179–185, 2000.

[77] A. R. Russel and I. Einav. Energy dissipation from particulate systems undergoing a single particle crushing event. *Granular Matter*, 15:299–314, 2013.

[78] G.R. McDowell and M.D. Bolton. On the micromechanics of crushable aggregates. *Geotechnique*, 48:667–679, 1998.

[79] Y. Nakata, H. Masayuki, A.F.L. Hyde, K. Yoshinori, and H. Murata. Microscopic particle crushing of sand subjected to high pressure one-dimensional compression. *Journal of the Japanese Geotechnical Society : soils and foundation*, 41:69–81, 2001.

[80] S.L. Karner, F.M. Chester, A.K. Kronenberg, and J.S Chester. Subcritical compaction and yielding of granular quartz sand. *Tectonophysics*, 377:357–381, 2003.

[81] Y. D. Zhang, G. Buscarnera, and I. Einav. Grain size dependence of yielding in granular soils interpreted using fracture mechanics, breakage mechanics and weibull statistics. *Géotechnique*, 66:149–160, 2016.

[82] F. Kim, D. Penumadu, J. Gregor, N. Kardjilov, and I. Manke. High-resolution neutron and x-ray imaging of granular materials. *Journal of Geotechnical and Geoenvironmental Engineering*, 139(5):715–723, 2013.

[83] N.B. Parab, B. Claus, M.C. Hudspeth, J.T. Black, A. Mondal, J. Sun, K. Fezzaa, X. Xiao, S.N. Luo, and W. Chen. Experimental assessment of fracture of individual sand particles at different loading rates. *International Journal of Impact Engineering*, 68:8–14, 2014.

[84] S.A. Hall, M. Bornert, J. Desrues, Y. Pannier, N. Lenoir, G. Viggiani, and P. Besuelle. Discrete and continuum analysis of localised deformation in sand using x-ray and volumetric digital image correlation. *Geotechnique*, 60:315–322, 2010.

[85] Z.X. Yang, R.J. Jardine, B.T. Zhu, P. Foray, and C.H.C. Tsuha. Sand grain crushing and interface shearing during displacement pile. *Geotechnique*, 60:469–482, 2010.

[86] R. H. Brzesowsky, C.J. Spiers, C.J. Peach, and S.J.T. Hangx. Time-independent compaction behavior of quartz sands. *Journal of Geophisical research: Solid Earth*, 119:936–956, 2014.

[87] M.B. Cil and K.A. Alshibli. 3D assessment of fracture of sand particles using discrete element. *Geotechnique Letters*, 2:161–166, 2012.

[88] E. Ando', S.A. Hall, G. Viggiani, J. Desrues, and P. Besuelle. Grain-scale experimental investigation of localised deformation in sand: a discrete particle tracking approach. *Acta Geotechnica*, 7:1–13, 2012.

[89] B Zhao, J Wang, MR Coop, G Viggiani, and M Jiang. An investigation of single sand particle fracture using x-ray micro-tomography. *Géotechnique*, 65(8):625–641, 2015.

[90] G. Michlmayr, D. Cohen, and D. Or. Sources and characteristics of acoustic emissions from mechanically stressed geologic granular media — a review. *Earth-Science Reviews*, 112:97–114, 2012.

[91] D. Lockner. The role of acoustic emission in the study of rock fracture. *International Journal of Rock Mechanics and Mining Sciences & Geomechanics Abstracts*, 30:883–899, 1993.

[92] W.A. Olsson and D.J. Holcomb. Compaction localization in porous rock. *Geophysical research letters*, 27:3537–3540, 2000.

[93] M. Ohtsu and H. Watanabe. Quantitative damage estimation of concrete by acoustic emission. *Construction and Building Materials*, 15:217–224, 2001.

[94] I.M. De Rosa, C. Santulli, and F. Sarasini. Acoustic emission for monitoring the mechanical behaviour of natural fibre composites: A literature review. *Composites Part A: Applied Science and Manufacturing*, 40:1456–1469, 2009.

[95] A. Smith, N. Dixon, P. Meldrum, E. Haslam, and J. Chambers. Acoustic emission monitoring of a soil slope: comparisons with continuous deformation measurements. *Géotechnique Letters*, 4:255–261, 2014.

[96] CL Jiaa and DA Dornfeld. Experimental studies of sliding friction and wear via acoustic emission signal analysis. *Wear*, 139(2):403–424, 1990.

[97] V. Salinas, Y. Vargas, J. Ruzzante, and L. Gaete. Localization algorithm for acoustic emission. pages 863–871, Santiago de Chile, 2010.

[98] W. Mao and I. Towhata. Monitoring of single-particle fragmentation process under static loading using acoustic emission. *Applied Acoustics*, 94:39–45, 2015.

[99] B. Caicedo and L. Martinez, A.: Vallejo. Assessing of crushing in granular materials using acoustic emission. Toronto, Ontario, Canada, 2011.

[100] Y. Fan, F. Gu, and A. Ball. Modelling acoustic emissions generated by sliding friction. *Wear*, 268:811–815, 2010.

[101] Jean Lemaitre and Jean-Louis Chaboche. *Mechanics of solid materials*. Cambridge university press, 1994.

[102] Wei Wu and Erich Bauer. A simple hypoplastic constitutive model for sand. *International Journal for Numerical and Analytical Methods in Geomechanics*, 18(12):833–862, 1994.

[103] Eduardo E Alonso, Antonio Gens, Alejandro Josa, et al. Constitutive model for partially saturated soils. *Géotechnique*, 40(3):405–430, 1990.

[104] Anne Mangeney-Castelnau, François Bouchut, JP Vilotte, E Lajeunesse, A Aubertin, and Marina Pirulli. On the use of saint venant equations to simulate the spreading of a granular mass. *Journal of Geophysical Research: Solid Earth*, 110(B9), 2005.

[105] Antonio A Munjiza. *The combined finite-discrete element method*. John Wiley & Sons, 2004.

[106] P. A. Cundall. A discrete numerical model for granular assemblies. *Geotechnique*, 29:47–65, 1979.

[107] GT Nolan and PE Kavanagh. Random packing of nonspherical particles. *Powder technology*, 84(3):199–205, 1995.

[108] He Tao, Baosheng Jin, Wenqi Zhong, Xiaofang Wang, Bing Ren, Yong Zhang, and Rui Xiao. Discrete element method modeling of non-spherical granular flow in rectangular hopper. *Chemical Engineering and Processing: Process Intensification*, 49(2):151–158, 2010.

[109] Romain Guises, Jiansheng Xiang, John-Paul Latham, and Antonio Munjiza. Granular packing: numerical simulation and the characterisation of the effect of particle shape. *Granular Matter*, 11(5):281–292, 2009.

[110] Sinan Kockara, Tansel Halic, Coskun Bayrak, K Iqbal, and Richard Rowe. Contact detection algorithms. *JCP*, 4(10):1053–1063, 2009.

[111] Heinrich Hertz. On the contact of elastic solids. *J. reine angew. Math*, 92(156-171):110, 1881.

[112] Algis Džiugys and Bernhard Peters. An approach to simulate the motion of spherical and non-spherical fuel particles in combustion chambers. *Granular matter*, 3(4):231–266, 2001.

[113] E Rougier, A Munjiza, and NWM John. Numerical comparison of some explicit time integration schemes used in dem, fem/dem and molecular dynamics. *International journal for numerical methods in engineering*, 61(6):856–879, 2004.

[114] Nikica Petrinic. *Aspects of discrete element modelling involving facet-to-facet contact detection and interaction*. 1996.

[115] NS Weerasekara, MS Powell, PW Cleary, Luís Marcelo Tavares, M Evertsson, RD Morrison, Johannes Quist, and RM Carvalho. The contribution of dem to the science of comminution. *Powder technology*, 248:3–24, 2013.

[116] S. Lobo-Guerrero, L. E. Vallejo, and L. F Vesga. Visualization of crushing evolution in granular materials under compression using dem. *Internation Journal of Geomechanics*, 6:195–200, 2006.

[117] M. O. Ciantia, M. Arroyo, F. Calvetti, and A. Gens. An approach to enhance efficiency of dem modelling of soils with crushable grains. *Geotechnique*, 65:91–110, 2015.

[118] O. Ben-Nun, I. Einav, and A. Tordesillas. Force attractor in confined comminution of granular materials. *Phys. Rev. Lett.*, 104:108001, 2010.

[119] J. Bruchmuller, B. G. M. Van Wachem, S. Gua, and K. H. Luo. Modelling discrete fregmentation of brittle particles. *Powder Technology*, 208:731–739, 2011.

[120] G. R. McDowell and J. P. De Bono. On the micro mechanics of one dimensional normal compression. *Geotechnique*, 63:895–908, 2013.

[121] J. A. Astrom and H. J. Hermann. Fragmentation of grains in a two-dimensional packing. *Eur. Phys. J. B.*, 5:551–554, 1998.

[122] A. C. F. Cocks and I. C. Sinka. Constitutive modelling of powder compaction - i. theoretical concepts. *Mechanics of materials*, 39:392–403, 2007.

[123] G. J. Weltje and L. J.H. Alberts. Packing states of ideal reservoir sands: Insights from simulation of porosity reduction by grain rearrangement. *Sedimentary Geology*, 242:52–64, 2011.

[124] L. Liu and Y. Yuan. Dynamic simulation of powder compact by random packing of monosized and polydisperse particles. *Journal of Materials Science Letters*, 19:841–843, 2000.

[125] D. Mostofinejad and M. Reisi. A new DEM based method to predict packing density of coarse aggregates considering their grading and shapes. *Construction and Building Materials*, 35:414–420, 2012.

[126] H. W. Sheng, W. K. Luo, F. M. Alamgir, J. M. Bai, and E. Ma. Atomic packing and short-to-medium-range order in metallic glasses. *Nature*, 439:419–425, 2006.

[127] T. M. Truskett, S. Torquato, and P. G. Debenedetti. Towards a quantification of disorder in materials: Distinguishing equilibrium and glassy sphere packings. *Physical Review E.*, 62:993–1001, 2000.

[128] M. D. Rintoul and S. Torquato. Computer simulations of dense hardsphere systems. *The Journal of Chemical Physics*, 105, 1996.

[129] P.H. Gaskell, H. Beck, and H.J. Guntherodt. Glassy metals II. *Topics in Applied Physics*, 53:5, 1983.

[130] Randall M German. *Particle packing characteristics*. Metal Powder Industries Federation, 1989.

[131] M. Gan, N. Gopinathan, and X. Jia. Predicting packing characteristics of particles of arbitrary shapes. *KONA*, 22:82–93, 2004.

[132] Bing Ren Yong Zhang Rui Xiao He Tao, Xiaofang Wang. Discrete element method modeling of non-spherical granular flow in rectangular hopper. *Chemical Engineering and Processing: Process Intensification*, 49:151–158, 2010.

[133] SR Buechler and SM Johnson. Efficient generation of densely packed convex polyhedra for 3 D discrete and finite-discrete element methods. *International Journal for Numerical Methods in Engineering*, 94(1):1–19, 2013.

[134] C. F. Gauss. Untersuchungen ioeber die eigenschaften der positiven ternioeren quadratischen formen von ludwig. *Gioettingische Gelehrte Anzeigen*, 1831.

[135] T.C. Hales. A proof of the Kepler conjecture. *Annals of Mathematics*, 162:1065–1185, 2005.

[136] A. Donev, I. Cisse, D. Sachs, E. A. Variano, F. H. Stillinger, R. Connelly, S. Torquato, and P. M. Chaikin. Improving the density of jammed disordered packings using ellipsoids. *Science*, 303(5660):990–993, 2004.

[137] S. Torquato, T. M. Truskett, and P. G. Debenedetti. Is random close packing of spheres well defined? *Physical Reviewe Letters*, 84(10):2064–2067, 2000.

[138] G. E. Mueller. Numerical simulation of packed beds with monosized spheres in cylindrical containers. *Powder Technology*, 92:179–183, 1997.

[139] J. Garai. Upper bound on the disordered density of sphere packing and the Kepler conjecture. *eprint arXiv:1001.1714*, 2010.

[140] R. P. Zou and A. B. Yu. Evaluation of the packing characteristics of mono-sized non-spherical particles. *Powder Technology*, 88:71–79, 1996.

[141] W. M. Visscher and M. Bolsterli. Random packing of equal and unequal spheres in two and three dimensions. *Nature*, 239:504–507, 1972.

[142] A. Wouterse, S. R. Williams, and A. P. Philipse. Effect of particle shape on the density and microstructure of random packings. *Journal of Physics: Condensed Matter*, 19(40), 2007.

[143] N. D. Aparicio and A. C. F. Cocks. On the representation of random packings of spheres for sintering simulations. *Acta metall. mater.*, 43(10):3873–3884, 1995.

[144] S. H. Lo and W. X. Wang. Generation of tetrahedral mesh of variable element size by sphere packing over an unbounded 3D domain. *Computer Methods in Applied Mechanics and Enigneering*, 194:5002–5018, 2005.

[145] O. Haggstrom and R. Meester. Nearest neighbour and hard sphere models in continuum percolation. *Random Struct. Algor.*, 9:295–315, 1996.

[146] D. Stoyan. Random sets: Models and statistics. *International Statistical Review*, 66(1):1–27, 1998.

[147] J. F. Jerier, V. Richefeu, D. Imbault, and F. V. Donze'. Packing spherical discrete elements for large scale simulations. *Computer Methods in Applied Mechanics and Engineering*, 199:1668–1676, 2010.

[148] R. M. O'Connor, J. R. Torczynskiz, D. S. Preece, J. T. Klosek, and J. R. Williams. Discrete element modeling of sand production. *Int. J. Rock Mech. & Min. Sci.*, 34, 1997.

[149] G. Mollon and J. Zhao. Realistic generation and packing of DEM sand samples. *ICGE Conference*, 2012.

[150] L. Martinez, R. Andrade, E. G. Birgin, and J. M. Martinez. Packmol: A package for building initial configurations for molecular dynamics simulations. *Journal of Computational Chemistry*, 30(13):2157–2164, 2009.

[151] AE R_ Westman and HR Hugill. The packing of particles. *Journal of the American Ceramic Society*, 13(10):767–779, 1930.

[152] R. K. McGeary. Mechanical packing of spherical particles. *Journal of the American Ceramic Society*, 44:513–522, 2006.

[153] F. De Cola, S. Falco, E. Barbieri, and N. Petrinic. New 3D geometrical deposition methods for efficient packing of spheres based on tangency. *International Journal for Numerical Methods in Engineering*, pages 1–24, 2015.

[154] Leo Rothenburg and Richard J Bathurst. Numerical simulation of idealized granular assemblies with plane elliptical particles. *Computers and geotechnics*, 11(4):315–329, 1991.

[155] Umang Agarwal and Fernando A Escobedo. Mesophase behaviour of polyhedral particles. *Nature materials*, 10(3):230–235, 2011.

[156] Paul A Langston, Mohammad A Al-Awamleh, Feras Y Fraige, and Basel N Asmar. Distinct element modelling of non-spherical frictionless particle flow. *Chemical Engineering Science*, 59(2):425 – 435, 2004.

[157] Benjamin Nassauer, Thomas Liedke, and Meinhard Kuna. Polyhedral particles for the discrete element method. *Granular Matter*, 15(1):85–93, 2013.

[158] John R Williams and Alex P Pentland. Superquadrics and modal dynamics for discrete elements in interactive design. *Engineering Computations*, 9(2):115–127, 1992.

[159] K Han, YT Feng, and DRJ Owen. Polygon-based contact resolution for superquadrics. *International journal for numerical methods in engineering*, 66(3):485–501, 2006.

[160] Guilhem Mollon and Jidong Zhao. 3D generation of realistic granular samples based on random fields theory and Fourier shape descriptors. *Computer Methods in Applied Mechanics and Engineering*, 279:46–65, 2014.

[161] D Buscombe and DM Rubin. Advances in the simulation and automated measurement of well-sorted granular material: 2. direct measures of particle properties. *Journal of Geophysical Research: Earth Surface (2003–2012)*, 117(F2), 2012.

[162] P Siegkas, V Tagarielli, and N Petrinic. Modelling stochastic foam geometries for FE simulations using 3D Voronoi cells. *Procedia Materials Science*, 4:221–226, 2014.

[163] F. Aurenhammer. Voronoi diagrams - a survey of fundamental geometric data structure. *ACM Computer Surveys*, 23(3), 1991.

[164] Susmit Kumar and Stewart K Kurtz. Simulation of material microstructure using a 3d voronoi tesselation: Calculation of effective thermal expansion coefficient of polycrystalline materials. *Acta metallurgica et materialia*, 42(12):3917–3927, 1994.

[165] F. Fritzen, T. Böhlke, and E. Schnack. Periodic three-dimensional mesh generation for crystalline aggregates based on voronoi tessellations. *Computational Mechanics*, 43(5):701–713, 2008.

[166] Simone Falco, Petros Siegkas, Ettore Barbieri, and Nik Petrinic. A new method for the generation of arbitrarily shaped 3D random polycrystalline domains. *Computational Mechanics*, 54(6):1447–1460, 2014.

[167] Qiang Du, Vance Faber, and Max Gunzburger. Centroidal voronoi tessellations: applications and algorithms. *SIAM review*, 41(4):637–676, 1999.

[168] Claudia Lautensack and Sergei Zuyev. Random Laguerre tessellations. *Advances in Applied Probability*, 40(3), 2008.

[169] Jan Elias. Simulation of railway ballast using crushable polyhedral particles. *Powder Technology*, 264:458 – 465, 2014.

[170] Y.T. Feng, K. Han, and D.R.J. Owen. Filling domain with disks: an advancing front approach. *International Journal for Numerical Methods in Engineering*, 56:699–713, 2003.

[171] P. Moon and D.E. Spencer. *Field Theory Handbook, Including Coordinate Systems, Differential Equations, and Their Solutions*. 1988.

[172] M. Parrinello and A. Rahman. Crystal structure and pair potentials: A molecular-dynamics study. *Phys. Rev. Lett.*, 45:1196–1199, Oct 1980.

[173] B. Henrich, A. Wonisch, T. Kraft, M. Moseler, and H. Riedel. Simulations of the influence of rearrangement during sintering. *Acta Materialia*, 55(2):753 – 762, 2007.

[174] D. Penumadu and R. Zhao. Triaxial compression behavior of sand and gravel using artificial neural networks (ann). *Computers and Geotechnics*, 24(3):207 – 230, 1999.

[175] Maya Muthuswamy and Antoinette Tordesillas. How do interparticle contact friction, packing density and degree of polydispersity affect force propagation in particulate assemblies? *Journal of Statistical Mechanics: Theory and Experiment*, 2006(09):P09003, 2006.

[176] Leonardo E Silbert, Deniz Ertaş, Gary S Grest, Thomas C Halsey, and Dov Levine. Geometry of frictionless and frictional sphere packings. *Physical Review E*, 65(3):031304, 2002.

[177] J Kozicki and FV Donzé. A new open-source software developed for numerical simulations using discrete modeling methods. *Computer Methods in Applied Mechanics and Engineering*, 197(49):4429–4443, 2008.

[178] H Teufelsbauer, Y Wang, SP Pudasaini, RI Borja, and W Wu. Dem simulation of impact force exerted by granular flow on rigid structures. *Acta Geotechnica*, 6(3):119–133, 2011.

[179] Romain Quey, PR Dawson, and Fabrice Barbe. Large-scale 3D random polycrystals for the finite element method: Generation, meshing and remeshing. *Computer Methods in Applied Mechanics and Engineering*, 200(17):1729–1745, 2011.

[180] F. Aurenhammer. Power diagram - properties, algorithms and applications. *SIAM J. Comput*, 16:78–96, 1987.

[181] H. Imai, M. Iri, and K. Murota. Voronoi diagram in the Laguerre geometry and its applications. *SIAM J. Comput*, 14:93–105, 1985.

[182] William Christian Krumbein. Measurement and geological significance of shape and roundness of sedimentary particles. *Journal of Sedimentary Research*, 11(2), 1941.

[183] Jigang Wang, Predrag Neskovic, and Leon N. Cooper. Bayes classification based on minimum bounding spheres. *Neurocomput.*, 70(4-6):801–808, 2007.

[184] Emo Welzl. Smallest enclosing disks (balls and ellipsoids). In *Results and New Trends in Computer Science*, pages 359–370. Springer-Verlag, 1991.

[185] J. D'Errico. A suite of minimal bounding objects, January 2012.

[186] A. Semechko. Exact minimum bounding spheres/circles, December 2014.

[187] Bernd Gärtner. Fast and robust smallest enclosing balls. In *Proceedings of the 7th Annual European Symposium on Algorithms*, ESA '99, pages 325–338, London, UK, UK, 1999. Springer-Verlag.

[188] Leonid G Khachiyan. Rounding of polytopes in the real number model of computation. *Mathematics of Operations Research*, 21(2):307–320, 1996.

[189] Nima Moshtagh. Minimum volume enclosing ellipsoid. 2005.

[190] C Bradford Barber, David P Dobkin, and Hannu Huhdanpaa. The quickhull algorithm for convex hulls. *ACM Transactions on Mathematical Software (TOMS)*, 22(4):469–483, 1996.

[191] GH Bagheri, Costanza Bonadonna, Irène Manzella, and P Vonlanthen. On the characterization of size and shape of irregular particles. *Powder Technology*, 270:141–153, 2015.

[192] Simon J Blott and Kenneth Pye. Particle shape: a review and new methods of characterization and classification. *Sedimentology*, 55(1):31–63, 2008.

[193] Chun-Yi Kuo, Raymond S Rollings, and Larry N Lynch. Morphological study of coarse aggregates using image analysis. *Journal of materials in civil engineering*, 10(3):135–142, 1998.

[194] Caroline A Schneider, Wayne S Rasband, and Kevin W Eliceiri. Nih image to imagej: 25 years of image analysis. *Nature methods*, 9(7):671, 2012.

[195] R. Blumenfeld, S. F. Edwards, and R. C. Ball. Granular matter and the marginal rigidity state. *Journal of Physics: Condensed Matter*, 17:2481–2487, 2005.

[196] J. W. Landry, G. S. Grest, L. E. Silbert, and S. J. Plimpton. Confined granular packings: Structure, stress, and forces. *Physical Review E*, 67(4), 2003.

[197] W. Man, A. Donev, F. H. Stillinger, M. T. Sullivan, W. B. Russel, D. Heeger, S. Inati, S. Torquato, and Chaikin P. M. Experiments on random packings of ellipsoids. *Physical Review Letters*, 94(19), 2005.

[198] D. J. Cumberland and R. J. Crawford. *The packing of particles*. Elsevier Science Pub. Co. Inc., 1987.

[199] S. Faure, A. Lefebvre-Lepot, and B. Semin. Dynamic numerical investigation of random packing for spherical and nonconvex particles. *ESAIM: Proceedings*, 28:13–32, 2009.

[200] M. M. Hagerty, D. R. Hite, C. R. Ullrich, and D. J. Hagerty. One-dimensional high-pressure compression of granular media. *Geotech. Engrg.*, 119(1):1–18, 1993.

[201] Vandewalle, N., Lumay, G., Gerasimov, O., and Ludewig, F. The influence of grain shape, friction and cohesion on granular compaction dynamics. *Eur. Phys. J. E*, 22(3):241–248, 2007.

[202] A. Zavaliangos. A numerical study of the development of tensile principal stresses during die compaction. *Particulate Science and Technology*, 21(2):105–115, 2003.

[203] E. Olsson and P.-L. Larsson. On the Effect of Particle Size Distribution in Cold Powder Compaction. *Journal of Applied Mechanics*, 79(5):051017, 2012.

[204] Olle Skrinjar and Per-Lennart Larsson. On discrete element modelling of compaction of powders with size ratio. *Computational Materials Science*, 31:131–146, 2004.

[205] MR Razavi, B Muhunthan, and O Al Hattamleh. Representative elementary volume analysis of sands using x-ray computed tomography. *Geotechnical Testing Journal*, 30(3), 2006.

[206] Ralph Brazelton Peck, Walter Edmund Hanson, and Thomas Hampton Thornburn. *Foundation engineering*, volume 10. Wiley New York, 1974.

[207] H.E White and S.F Walton. Particle packing and particle shape. *J. Am. Ceram. Soc.*, 20, 1937.

[208] Poul V Lade, CD Liggio, and Jerry A Yamamuro. Effects of non-plastic fines on minimum and maximum void ratios of sand. *Geotechnical Testing Journal*, 21:336–347, 1998.

[209] A. Pellegrino, F. De Cola, K. Dragnevski, and N. Petrinic. The dynamic response of etnean sand and the effect of its impingement on Ti-6Al-4V alloy. *Journal of Dynamic Behavior of Materials*, pages 1–14, 2016.

[210] R.H. Brzesowsky, C.J. Spiers, C.J. Peach, and S.T.J. Hangs. Failure behaviour of single sand grains: theory versus experiment. *Journal of geophysical research*, 116, 2011.

[211] M.R Coop. The influence of particle breakage and state on the behavior of sands. pages 19–57, Yamaguchi, Japan, 1999.

[212] k.l. Lee and J Farhoomand. Compressibility and crushing of granular soils in anisotropic triaxial compression. *Canadian Geotechnical J.*, 4:68–86, 1967.

[213] J.S. Chester, S.C. Lenz, F.M. Chester, and R.A. Lang. Mechanisms of compaction of quartz sand at diagenetic conditions. *Earth Planet. Sci. Lett.*, 220:435–451, 2004.

[214] Y.P Cheng, M.D. Bolton, and Y. Nakata. Crushing and plastic deformation of soils simulated using dem. *Geotechnique*, 54:131–141, 2004.

[215] P.V. Lade and J.A. Yamamuro. Undrained sand behavior in axisymmetric tests at high pressures. *J Geotech Eng*, 122:120–129, 1996.

[216] C. Ovalle, C. Dano, P.Y. Hicher, and M. Cisternas. Experimental framework for evaluating the mechanical behavior of dry and wet crushable granular materials based on the particle breakage ratio. *Canadian Geotechnical Journal*, 52:587–598, 2015.

[217] P.V. Lade and H. Karimpour. Static fatigue controls particle crushing and time effects in granular materials. *Soils and foundations*, 50:573–583, 2010.

[218] P.V. Lade and H. Karimpour. Stress drop effects in time dependent behavior of quartz sand. *International Journal of Solids and Structures*, 87:167–182, 2016.

[219] Audacity: Noise reduction.

[220] A. V. Oppenheim and G.C. Verghese. *Signals, Systems & Inference*. Prentice Hall College Div, 2015.

[221] J.Y. Stein. *Digital Signal Processing: A Computer Science Perspective*. Wiley, 2000.

[222] B. Boashash. *Time-Frequency Signal Analysis and Processing*. Academic press, Elsevier, 2015.

[223] L.J. Munkholm. Soil friability: A review of the concept, assessment and effects of soil properties and management. *Geoderma*, 167 - 168:236 – 246, 2011.

[224] P.J. De Groot, P.A. Wijnen, and R.B. Janssen. Real-time frequency determination of acoustic emission for different fracture mechanisms in carbon/epoxy composites. *Compos. Sci. Technol.*, 55:717–728, 1995.

[225] C. O'Sullivan. Particle-based discrete element modelling: a geomechanics perspective. Hoboken, New York, USA, 2011. Taylor and Francis.

[226] S Hang. Tetgen, a delaunay-based quality tetrahedral mesh generator. *ACM Trans. on Mathematical Software*, 41:11, 2015.